

	June 5, 1999	Final Report 10/1/93-9/30/98	
Title: New Theories for Erosion-Corrosion		Funding Numbers: N00014-93-I-0056	
Author: Mark E. Orazem			
Address: Department of Chemical Engineering PO Box 116005 University of Florida Gainesville, FL 32611-6005			
Sponsor: Department of the Navy Office of Naval Research Materials Division Office of Chief of Naval Res. Arlington, VA 22217-5000			
Distribution: Unlimited			
<p>Abstract:</p> <p>The erosion-corrosion of copper and copper-nickel alloys in synthetic seawater was investigated using an impinging jet. Video microscopy, corrosion potential monitoring, and impedance spectroscopy were used to investigate the state of the system and the reactivity of the electrode surface. Shear-induced removal of salt films was observed and found to be associated with significant increases in surface reactivity. Direct shear-induced removal of oxide films, however, was not observed. Nevertheless, the protective oxide layer showed sensitivity in passively aerated seawater to large fluid velocities and to small perturbations in potential. The films were stable under all conditions tested in continuously aerated seawater. The present work supports the argument that localized corrosion of copper alloys is caused by galvanic coupling between different regions of a metal coupon. Thus, cathodic protection may be used to prevent such corrosion. A modeling and experimental study was conducted to show the conditions under which non-uniform current distributions influence the impedance response of a disk electrode. Measurement model tools were developed to identify the stochastic and experimental bias errors. This information was used to filter data, design experiments, and assess the validity of regression assumptions and the confidence intervals of the resulting parameters.</p>			
Subject Terms: erosion-corrosion, copper, copper-nickel alloys, impedance spectroscopy, impinging jet, models			# pages 125
Unlimited	Unlimited	Unlimited	Unlimited

19990624015

1999 0615 103

## TABLE OF CONTENTS

<b>TABLE OF CONTENTS .....</b>	<b>2</b>
<b>SUMMARY OF RESULTS.....</b>	<b>3</b>
Variable-Amplitude Galvanostatically Modulated Impedance Spectroscopy.....	3
Preliminary Interpretation of Data .....	3
Experimental Study of Shear-Induced Removal of Films.....	4
Influence of Current Distribution on Impedance Response of a Disk Electrode.....	4
Development of Statistical Tools for Interpretation of Spectroscopy Data .....	4
<b>PUBLICATIONS AND PRESENTATIONS .....</b>	<b>5</b>
Refereed Publications .....	5
Conference Proceedings.....	6
Presentations .....	6
Dissertations .....	7
<b>REFEREED PUBLICATIONS<sup>1</sup> .....</b>	<b>8</b>

---

<sup>1</sup> Copies of refereed publications are presented in this section.

## SUMMARY OF RESULTS

The contract supported the dissertation research of Paul T. Wojcik and Madhav Durbha. The objective of Paul's research was to investigate the corrosion of copper and copper-nickel alloys under high-shear flow of synthetic seawater. The principle accomplishments of this research include:

### Variable-Amplitude Galvanostatically Modulated Impedance Spectroscopy

An algorithm was developed described in which galvanostatic regulation of electrochemical impedance measurements was conducted with an amplitude of current perturbation adjusted at each frequency to yield a desired variation in potential. Measurements of three previous frequencies were used to estimate the value of the impedance at the target frequency. The algorithm was implemented using a graphically-based general interfacing software on a personal computer. Experimental results illustrated artifacts that can arise as a result of galvanostatic measurement with fixed current amplitude or as a result of potentiostatic measurements for systems with a changing corrosion potential. A demonstration is presented of the use of variable-amplitude galvanostatically modulated impedance spectroscopy to monitor the corrosion of copper in synthetic seawater. This approach provided a critical step in developing a method to monitor the natural evolution of a corroding system without changing the system behavior.

### Preliminary Interpretation of Data

A methodology was developed to allow use of the measurement model approach to quantify differences in surface reactivity in the absence of specific process models.<sup>2</sup> The interpretation of the spectra presented here followed: a) identification of the frequency-dependent stochastic component of the error structure following the method presented by Agarwal *et al.*<sup>3</sup> This information was used to weight subsequent regressions; b) identification of the portion of the spectrum that is consistent with the Kramers-Kronig relations following the method presented by Agarwal *et al.*;<sup>4,5</sup> and c) regression of the measurement model to the part of the spectrum found to be consistent with the Kramers-Kronig relations. The regressed parameter values were used to extrapolate to the zero-frequency limit and Monte Carlo simulations were performed using the standard deviations of the regressed parameters to estimate the confidence interval for the extrapolation. The polarization impedance was obtained by subtracting the regressed solution resistance from the extrapolated zero-frequency value. This approach allowed extraction of reactivity data in the absence of a specific model for the corrosion of copper in seawater.

---

<sup>2</sup> M. E. Orazem, P. T. Wojcik, M. Durbha, I. Frateur, and L. H. García-Rubio, "Application of Measurement Models for Interpretation of Impedance Spectra for Corrosion," *Materials Science Forum*, **289-292** (1998), 813.

<sup>3</sup> P. Agarwal, O. D. Crisalle, M. E. Orazem, and L. H. García-Rubio, *Journal of the Electrochemical Society*, **142** (1995), 4149-4158.

<sup>4</sup> P. Agarwal, M. E. Orazem, and L. H. García-Rubio, *Journal of the Electrochemical Society*, **142** (1995), 4159-4168.

<sup>5</sup> P. Agarwal, M. E. Orazem, and L. H. García-Rubio, *Electrochemical Impedance: Analysis and Interpretation*, J. Scully, D. Silverman, M. Kendig, Editors, American Society for Testing and Materials, Philadelphia, 1993, 115-139.

## **Experimental Study of Shear-Induced Removal of Films**

The erosion-corrosion of copper and copper-nickel alloys in synthetic seawater was investigated using an impinging jet. Video microscopy, corrosion potential monitoring, and impedance spectroscopy were used to investigate the state of the system and the reactivity of the electrode surface. Shear-induced removal of salt films was observed and found to be associated with significant increases in surface reactivity. Direct shear-induced removal of oxide films, however, was not observed. Nevertheless, the protective oxide layer showed sensitivity in passively aerated seawater to large fluid velocities and to small perturbations in potential. The films were stable under all conditions tested in continuously aerated seawater. The present work supports the argument that localized corrosion of copper alloys is caused by galvanic coupling between different regions of a metal coupon. The potential difference driving the galvanic couple could originate from localized shear-induced removal of salt films as well as from non-uniformly distributed oxygen transport rates.

## **Influence of Current Distribution on Impedance Response of a Disk Electrode**

As the impinging jet cell used impedance spectroscopy to monitor reactivity, a key question was whether the non-uniform current distribution seen at some potentials could influence the impedance response, and thereby influence the interpretation of the data. A mathematical model was developed which accounts for the influence of nonuniform current distribution on the impedance response of a rotating disk electrode. Results obtained using this two-dimensional model were compared against those using the one-dimensional model for impedance developed by Tribollet and Newman. The one-dimensional model was found to be adequate when kinetic limitations cause the current to be uniformly distributed. Significant differences between the one-dimensional and two-dimensional models were seen for fast reaction kinetics where the nonuniform ohmic potential distribution is balanced by a nonuniform concentration overpotential.

## **Development of Statistical Tools for Interpretation of Spectroscopy Data**

Interpretation of impedance spectra requires, in addition to an adequate quantitative deterministic model, quantitative assessment of measurement characteristics. An important factor, often ignored or understated in electrochemical impedance spectroscopy, is the nature of the error structure associated with the measurements. The importance of the error structure has been neglected, in part, because the inability to replicate impedance measurements has made it difficult to distinguish among stochastic, experimental bias, and fitting errors. The recent development of measurement model tools for impedance spectroscopy has made it possible to identify the stochastic and experimental bias errors and to use this information to filter data, design experiments, and assess the validity of regression assumptions and the confidence intervals of the resulting parameters.

In spite of the stochastic character of impedance measurements, a definite structure has been resolved for impedance errors. Impedance measurements were found to be heteroskedastic (in the sense that the standard deviations are functions of frequency). The standard deviations for the real and imaginary parts of the impedance were found to be equal, even at frequencies sufficiently high or low that the imaginary part of the impedance asymptotically approaches zero. This result has been observed even for systems with very large leading resistances and has been shown to be a consequence of the Kramers-Kronig relations. The general nature of this result was



confirmed by analyzing the frequency-dependent complex viscosity of viscoelastic fluids. For measurements that satisfied the Kramers-Kronig relations, the standard deviations for real and imaginary parts of the viscosity were found to be equal.

Knowledge of the error structure plays a critical role in interpreting spectroscopic measurements. An assessment of the stochastic (or noise) component of the errors allows refinement of regression strategies and can guide design of experiments to improve signal-to-noise ratios. Assessment of consistency of data with the Kramers-Kronig relations is also important because inconsistencies can be attributed to experimental bias errors that must be accounted for during interpretation of measurements.

## **PUBLICATIONS AND PRESENTATIONS**

The following publications and presentations resulted from this contract. Copies of the refereed publications are attached.

### **Refereed Publications**

1. P. T. Wojcik, P. Agarwal, and M. E. Orazem, "A Method for Maintaining a Constant Potential Variation during Galvanostatic Regulation of Electrochemical Impedance Measurements," *Electrochimica Acta*, **41** (1996), 977-983.
2. P. Agarwal, M. E. Orazem, and L. García-Rubio, "The Influence of Error Structure on Interpretation of Impedance Spectra," *Electrochimica Acta*, **41** (1996), 1017-1022.
3. M. E. Orazem, P. Agarwal, C. Deslouis, and B. Tribollet, "Application of Measurement Models to Electro-Hydrodynamic Impedance Spectroscopy," *Journal of the Electrochemical Society*, **143** (1996), 948-960.
4. M. E. Orazem, T. El Moustafid, C. Deslouis, and B. Tribollet, "The Error Structure of Impedance Spectroscopy Measurements for Systems with a Large Ohmic Resistance with Respect to the Polarization Impedance," *Journal of the Electrochemical Society*, **143** (1996), 3880-3890.
5. M. Durbha, M. E. Orazem, and L. H. García-Rubio, "Spectroscopy Applications of the Kramers-Kronig Relations: Implications for Error Structure Identification," *Journal of the Electrochemical Society*, **144** (1997), 48-55.
6. P. T. Wojcik and M. E. Orazem, "Variable-Amplitude Galvanostatically-Modulated Impedance Spectroscopy as a Tool for Assessing Reactivity at the Corrosion Potential without Distorting the Temporal Evolution of the System," *Corrosion*, **54** (1998) 289-298.
7. M. E. Orazem, P. T. Wojcik, M. Durbha, I. Frateur, and L. H. García-Rubio, "Application of Measurement Models for Interpretation of Impedance Spectra for Corrosion," *Materials Science Forum*, **289-292** (1998), 813.
8. M. Durbha and M. E. Orazem, "Current Distribution on a Rotating Disk Electrode Below the Mass-Transfer Limited Current: Correction for Finite Schmidt Number and Determination of Surface Charge Distribution," *Journal of the Electrochemical Society*, **145** (1998) 1940-1949.
9. M. Durbha, B. Tribollet, and M. E. Orazem, "A Mathematical Model for the Radially-Dependent Impedance of A Rotating Disk Electrode," *Journal of the Electrochemical Society*, in press.

10. M. E. Orazem, M. Durbha, C. Deslouis, H. Takenouti, and B. Tribollet, "Influence of Surface Phenomena on the Impedance Response of a Rotating Disk Electrode," *Electrochimica Acta*, in press.

### Conference Proceedings

1. M. Durbha, M. E. Orazem, and L. H. García-Rubio, "Propagation of Spectroscopy Errors Through the Kramers-Kronig Relations: A Common Ground for Interpretation of Measurements," in *New Directions in Electroanalytical Chemistry*, J. Leddy and R. M. Wightman, editors, Electrochemical Society, Inc., Pennington, N.J., 1996, 385-397.
2. P. T. Wojcik and M. E. Orazem, "Variable-Amplitude Galvanostatically Modulated Impedance Spectroscopy as a Non-Invasive Tool for Assessing Reactivity at the Corrosion Potential," Paper #97-282, National Association of Corrosion Engineers, Houston, Texas, 1997.
3. P. T. Wojcik and M. E. Orazem, "Experimental Study of the Erosion-Corrosion of Copper and Copper-Nickel Alloys Using a Submerged Impinging Jet," Paper #97-435, National Association of Corrosion Engineers, Houston, Texas, 1997.
4. P. T. Wojcik, E. Charrière, and M. E. Orazem, "Experimental Study of the Erosion-Corrosion of Copper and Copper-Nickel Alloys at the Corrosion Potential and at Anodic Potentials," *Proceedings of the Tri-Service Conference on Corrosion*, November 17-21, 1997.
5. M. Durbha and M. E. Orazem, "A Mathematical Model For The Radially Dependent Impedance Of A Rotating Disk Electrode," in *Advances in Modeling and Simulation of Electrochemical Processes and Oxygen Depolarized Cathodes and Activated Cathodes for Chlor-Alkali and Chlorate Processes*, J. W. van Zee, T. F. Fuller, P. C. Foller, and F. Hine, editors, PV-98-10, Electrochemical Society, Inc., Pennington, N.J., 1998, 106-131.

### Presentations

1. P. T. Wojcik, P. Agarwal, and M. E. Orazem, "A Method for Maintaining a Constant Potential Variation during Galvanostatic Regulation of Electrochemical Impedance Measurements," presented at the Third International Symposium on Electrochemical Impedance Spectroscopy, Ysermonde, Belgium, May 7-12, 1995.
2. P. T. Wojcik, P. Agarwal, and M. E. Orazem, "Variable-Amplitude Galvanostatically Modulated Impedance Spectroscopy as a Non-Invasive Tool for Assessing Reactivity at the Corrosion Potential," presented at the 2nd Workshop on Quantitative Methods for Predicting Coating Performance, Annapolis, Maryland, November 1-3, 1995.
3. M. Durbha, M. E. Orazem, and L. García-Rubio, "Propagation of Spectroscopy Errors through the Kramers Kronig Relations," presented at the 189th Meeting of the Electrochemical Society, Los Angeles, California, May 8, 1996.
4. P. T. Wojcik and M. E. Orazem, "Evaluation of Corrosion under Controlled Flow by Variable-Amplitude Galvanostatically Modulated Impedance Spectroscopy and Video Microscopy," presented at the 190th Meeting of the Electrochemical Society, San Antonio, Texas, October 10, 1996.
5. P. T. Wojcik and M. E. Orazem, "Variable-Amplitude Galvanostatically Modulated Impedance Spectroscopy as a Non-Invasive Tool for Assessing Reactivity at the Corrosion

Potential," paper 97-282 presented at Corrosion/97, New Orleans, Louisiana, March 9-14, 1997.

6. P. T. Wojcik and M. E. Orazem, "Experimental Study of the Erosion-Corrosion of Copper and Copper-Nickel Alloys Using a Submerged Impinging Jet," paper 97-435 presented at Corrosion/97, New Orleans, Louisiana, March 9-14, 1997.
7. M. Durbha, M. E. Orazem, C. Deslouis, H. Takenouti, and B. Tribollet, "The Influence of Current Distribution on the Reduction of Ferricyanide on a Pt Disk Electrode below the Mass-Transfer Limited Current," presented at the 191<sup>st</sup> Meeting of the Electrochemical Society, Montreal, Canada, May 6, 1997.
8. M. E. Orazem and L. H. García-Rubio, "The Influence of Error Structure on the Interpretation of Impedance Spectra," (invited lecture) presented at the 191<sup>st</sup> Meeting of the Electrochemical Society, Montreal, Canada, May 8, 1997.
9. M. E. Orazem, C. Deslouis, and B. Tribollet, "Comparison of Impedance Models for Mass Transfer to a Disk Electrode," (invited lecture) presented at the 191<sup>st</sup> Meeting of the Electrochemical Society, Montreal, Canada, May 6, 1997.
10. M. E. Orazem, P. T. Wojcik, I. Frateur, and L. H. García-Rubio, "Application of Measurement Models for Interpretation of Impedance Spectra for Corrosion," (keynote lecture) presented at Electrochemical Methods for Corrosion Research, EMCR 97, Trento, Italy, August 25-29, 1997.
11. P. T. Wojcik, E. Charrière, and M. E. Orazem, "Experimental Study of the Erosion-Corrosion of Copper and Copper-Nickel Alloys at the Corrosion Potential and at Anodic Potentials," presented at the Tri-Service Conference on Corrosion, November 17-21, 1997.
12. M. Durbha, S. L. Carson, A. H. Kalajian, M. J. Lazzara, M. E. Orazem, and L. H. García-Rubio, "Common Features of Electrochemical and Mechanical Spectroscopy Measurements," presented at the AIChE Meeting, Los Angeles, California, November 16-21, 1997.
13. M. E. Orazem, "A Tutorial on Impedance Spectroscopy," (invited lecture) presented at Corrosion/98, San Diego, California, March 22-27, 1998.
14. M. Durbha, M. E. Orazem, C. Deslouis, H. Takenouti, and B. Tribollet, "Influence of Current and Potential Distribution on the Faradaic Impedance below the Mass-Transfer-Limited Current for a Rotating Disk Electrode," presented at the 193<sup>rd</sup> Meeting of the Electrochemical Society, San Diego, May 3-8, 1998.
15. M. E. Orazem, M. Durbha, C. Deslouis, H. Takenouti, and B. Tribollet, "Influence of Surface Phenomena on the Impedance Response of a Rotating Disk Electrode," presented at the 4th International Symposium on Electrochemical Impedance Spectroscopy, Rio de Janeiro, Brazil, August 2-7, 1998.

## Dissertations

1. Paul T. Wojcik, *The Electrochemical Behavior of Copper and Copper Nickel Alloys in Synthetic Seawater*, University of Florida, August, 1997.
2. Madhav Durbha, *Influence of Current Distributions on the Interpretation of the Impedance Spectra Collected For Rotating Disk Electrode*, Ph.D. dissertation, University of Florida, August, 1998.

## REFEREED PUBLICATIONS

Copies of the following refereed publications are presented in this section.

---

P. T. Wojcik, P. Agarwal, and M. E. Orazem, "A Method for Maintaining a Constant Potential Variation during Galvanostatic Regulation of Electrochemical Impedance Measurements," *Electrochimica Acta*, **41** (1996), 977-983.

P. Agarwal, M. E. Orazem, and L. García-Rubio, "The Influence of Error Structure on Interpretation of Impedance Spectra," *Electrochimica Acta*, **41** (1996), 1017-1022.

M. E. Orazem, P. Agarwal, C. Deslouis, and B. Tribollet, "Application of Measurement Models to Electro-Hydrodynamic Impedance Spectroscopy," *Journal of the Electrochemical Society*, **143** (1996), 948-960.

M. E. Orazem, T. El Moustafid, C. Deslouis, and B. Tribollet, "The Error Structure of Impedance Spectroscopy Measurements for Systems with a Large Ohmic Resistance with Respect to the Polarization Impedance," *Journal of the Electrochemical Society*, **143** (1996), 3880-3890.

M. Durbha, M. E. Orazem, and L. H. García-Rubio, "Spectroscopy Applications of the Kramers-Kronig Relations: Implications for Error Structure Identification," *Journal of the Electrochemical Society*, **144** (1997), 48-55.

P. T. Wojcik, E. Charrière, and M. E. Orazem, "Experimental Study of the Erosion-Corrosion of Copper and Copper-Nickel Alloys at the Corrosion Potential and at Anodic Potentials," *Proceedings of the Tri-Service Conference on Corrosion*, November 17-21, 1997.

P. T. Wojcik and M. E. Orazem, "Variable-Amplitude Galvanostatically-Modulated Impedance Spectroscopy as a Tool for Assessing Reactivity at the Corrosion Potential without Distorting the Temporal Evolution of the System," *Corrosion*, **54** (1998) 289-298.

M. E. Orazem, P. T. Wojcik, M. Durbha, I. Frateur, and L. H. García-Rubio, "Application of Measurement Models for Interpretation of Impedance Spectra for Corrosion," *Materials Science Forum*, **289-292** (1998), 813.

M. Durbha and M. E. Orazem, "Current Distribution on a Rotating Disk Electrode Below the Mass-Transfer Limited Current: Correction for Finite Schmidt Number and Determination of Surface Charge Distribution," *Journal of the Electrochemical Society*, **145** (1998) 1940-1949.

M. Durbha, B. Tribollet, and M. E. Orazem, "A Mathematical Model for the Radially-Dependent Impedance of A Rotating Disk Electrode," *Journal of the Electrochemical Society*, in press.

M. E. Orazem, M. Durbha, C. Deslouis, H. Takenouti, and B. Tribollet, "Influence of Surface Phenomena on the Impedance Response of a Rotating Disk Electrode," *Electrochimica Acta*, in press.



## A METHOD FOR MAINTAINING A CONSTANT POTENTIAL VARIATION DURING GALVANOSTATIC REGULATION OF ELECTROCHEMICAL IMPEDANCE MEASUREMENTS

PAUL T. WOJCIK, PANKAJ AGARWAL<sup>1</sup> and MARK E. ORAZEM\*

Department of Chemical Engineering, University of Florida, Gainesville, Florida 326111, U.S.A.

(Received 8 May 1995)

**Abstract**—An algorithm is described in which galvanostatic regulation of electrochemical impedance measurements is conducted with an amplitude of current perturbation that is adjusted at each frequency to yield a desired variation in potential. Measurements at previous frequencies are used to estimate the value of the impedance at the target frequency. The algorithm was implemented using LabView for Windows® on an IBM-compatible computer. Experimental results illustrate artifacts which can arise as a result of galvanostatic measurement with a fixed current amplitude or as a result of potentiostatic measurements for systems with a changing corrosion potential.

**Key words:** corrosion, experimental techniques, linearity, impedance spectroscopy.

### INTRODUCTION

Electrochemical impedance measurements are usually performed under potentiostatic regulation. In these measurements the potential is a fixed value with a superimposed (often sinusoidal) perturbation of fixed amplitude. This approach is attractive because linearity in electrochemical systems is controlled by potential. For example, a Taylor series expansion for current density at the open-circuit condition using the Butler-Volmer equation (1)

$$i = i_0 \{ e^{(\alpha_a F \eta_s / RT)} - e^{(-\alpha_c F \eta_s / RT)} \} \quad (1)$$

yields

$$i = i_0 \left\{ (\alpha_a + \alpha_c) \frac{F \eta_s}{RT} + \frac{(\alpha_a^2 - \alpha_c^2)}{2} \left( \frac{F \eta_s}{RT} \right)^2 + \frac{(\alpha_a^3 + \alpha_c^3)}{6} \left( \frac{F \eta_s}{RT} \right)^3 + O(\eta_s^4) \right\} \quad (2)$$

where  $\alpha_a$  and  $\alpha_c$  are the apparent transfer coefficient for the anodic and cathodic reactions, respectively,  $\eta_s$  is the surface overpotential,  $F$  is Faraday's constant,  $R$  is the gas constant, and  $T$  is absolute temperature. For typical parameter values for a symmetric reaction ( $\alpha_a = \alpha_c = 0.5$ ) and for  $T = 298$  K, the second term is equal to zero, and the third term is equal to 1% of the first (linear) term for potentials of roughly  $13.0 \text{ mV s}^{-1}$ . Potential perturbations of  $5\text{--}20 \text{ mV s}^{-1}$  are often used. Potentiostatic regulation is usually used even for measurement of the impedance at the corrosion potential, a measurement which should, in

principle, be conducted galvanostatically (with a time-averaged current density set equal to zero). The potential is set to the value of the corrosion potential at the beginning of the measurement and the potential is perturbed by a value sufficiently small to ensure linearity [2, 3]. This approach is successful if the corrosion potential does not change during the course of the measurement.

Galvanostatic regulation is required, however, when the system is to be studied under constant current density. For example, the evaluation of the resistance of skin to iontophoresis is typically done under constant current because the delivery of therapeutic drugs is more directly governed by current density than by potential [4]. Galvanostatic control is also preferred for the use of impedance spectroscopy as a non-invasive tool for periodically observing the condition of a metal coupon held at the corrosion potential for a long period of time. A drift in the corrosion potential during the course of the measurement of a impedance spectrum will, in the case of potentiostatic regulation, result in application of a potential that is anodic or cathodic to the true open-circuit potential, thus perturbing the long-term measurement at the zero-current condition. Under galvanostatic control, the desired zero-current condition is maintained throughout the impedance measurement.

The difficulty with galvanostatic measurements with a fixed amplitude for the current perturbation is that such measurements can result in severe swings in potential, especially at low frequencies where the impedance is large. The amplitude of the potential variation  $\Delta \bar{V}$  associated with a perturbation amplitude of current  $\Delta \bar{I}$  is given by

$$\Delta \bar{V} = \Delta \bar{I} |Z(\omega)| \quad (3)$$

<sup>1</sup> Current Address: Materials Department, Swiss Federal Institute of Technology (Lausanne), MX-C Ecublens, Lausanne, Switzerland.

\* Author to whom correspondence should be addressed.



A current perturbation as small as  $10\ \mu\text{A}$  can result in potential swings of 1 V for systems with a polarization resistance of  $10^5\ \Omega$ , a value typical of many membranes and some slowly corroding systems. Nonlinear behavior of skin has, for example, been reported for impedance measurements conducted under galvanostatic regulation.

An algorithm was developed in which galvanostatic regulation is conducted with an amplitude of current perturbation that is adjusted at each frequency to yield a desired variation in potential. Measurements at previous frequencies are used to estimate the value of the impedance at the target frequency. The current perturbation to be used is given by

$$\Delta \tilde{I}(\omega) = \frac{\Delta \tilde{V}_{\text{target}}}{|Z(\omega)|_{\text{estimated}}} \quad (4)$$

where  $\Delta \tilde{I}(\omega)$  is the current perturbation at a given frequency,  $\Delta \tilde{V}_{\text{target}}$  is the desired potential perturbation at the surface of the electrode, and  $|Z(\omega)|_{\text{estimated}}$  is the magnitude of the impedance taken from the preceding measurement[5]. The value of the current perturbation obtained from equation (4) is also used to guide automated selection of the current measuring resistor. Automated selection of current measuring resistors is not new, but its implementation is an essential feature of the algorithm.[6] Several changes of the current measuring resistor are often needed because the current perturbation may vary over several orders of magnitude during a scan. An initial guess of  $|Z(\omega)|_{\text{estimated}}$  is necessary for the first frequency of an impedance scan. The estimated solution resistance provides a good initial guess for impedance scans made from high frequency to low. The algorithm described above was implemented using LabView for Windows® on an IBM-compatible computer.

### COPPER IN SYNTHETIC SEA-WATER

Two experimental set-ups were used for this work. The first consisted of a 0.635 cm diameter cylindrical 99.90% copper working electrode held vertically in a stagnant solution of ASTM D-1141 synthetic sea water. Approximately 4 cm of the 5.5 cm rod was submerged. The copper rod annealed at  $750^\circ\text{C}$  in an Argon atmosphere for 3.75 h and oven cooled. The electrochemical cell was a 300 ml Pyrex® H-cell filled with approximately 200 ml of solution. A  $2.5 \times 2.5\ \text{cm}$  ( $25\ \text{cm}^2$  active area) Pt foil counter electrode was placed in one side reservoir of the H-cell and a saturated calomel reference electrode was placed in the other. The electrolyte had a pH of approximately 8.3 and was exposed to the atmosphere. The temperature of the cell was held constant at  $25^\circ\text{C}$ . A PAR 273 potentiostat and a Solartron 1260 Frequency Response Analyzer were used to obtain the impedance data.

The second system consisted of a 0.635 cm diameter copper rod embedded in epoxy such that only the face of the rod is exposed to electrolyte. The electrolyte properties and the instrumentation were the same as described above. The disk electrode was

exposed to well-defined flow from a submerged impinging jet that was axisymmetric with the disk. The cell geometry was selected to ensure that the disk is within the stagnation regime of the flow pattern.

### RESULTS AND DISCUSSION

The copper/synthetic sea-water system chosen to illustrate the benefits of the variable amplitude potentiostatic algorithm is strongly affected by the formation of salt and oxide films. The corrosion potential of a freshly polished copper electrode submerged in electrolyte changes rapidly at first due to the formation of films[6], then reaches a pseudo steady-state condition after a period of several hours or days. Impedance spectroscopy can be used as a non-invasive tool for assessing the reactivity of the copper electrode during a long-term measurement of the corrosion potential if the amplitude of the perturbation is sufficiently small and if the measurement does not perturb the baseline condition of the electrode.

The disruption caused by the variable-amplitude galvanostatic impedance scan developed in this work is compared in Fig. 1 to the disruption caused by the more traditional use of impedance measurements at the open-circuit potential in which the potential is held at the corrosion potential measured before the scan and a fixed-amplitude potential perturbation is applied. The measured corrosion potential is shown in Fig. 1 as a function of time. The points at which the potentiostatic measurement is made (with a  $10\ \text{mV s}^{-1}$  amplitude perturbation) are characterized by roughly a  $15\ \text{mV s}^{-1}$  perturbation of potential which decays slowly to the baseline value. The perturbation in corrosion current associated with this set of experiments is shown in Fig. 2. In contrast, the variable-amplitude galvanostatic impedance measurements show a much smaller perturbation of potential (roughly  $2\ \text{mV s}^{-1}$  from an extension of the baseline), and there was no perturbation from the zero-current condition.

Potentiostatic experiments, due to their nature, do not contain a zero current condition throughout an experiment in which the corrosion potential changes with time. For a potentiostatic experiment, the corrosion potential is manually or automatically reset and a potential bias of that value is applied. The sinusoidal perturbation of an impedance scan is then superimposed over the potential bias. If the open circuit potential is stable, the set bias will yield zero or near zero current. If, however, the open circuit potential changes during the course of an experiment, in the latter stages of the measurement the bias potential will drive a anodic or cathodic current. This phenomena is illustrated in Fig. 2. The corrosion potential of the system was determined and a potential bias of the same value was applied the potentiostatic mode. After the bias was applied the resulting current was measured and a current on the order of  $-0.002\ \text{mA}$  resulted from the applied bias. The values for the pre-scan current measurements are represented by the circles in Fig. 2. After the completion of each impedance scan



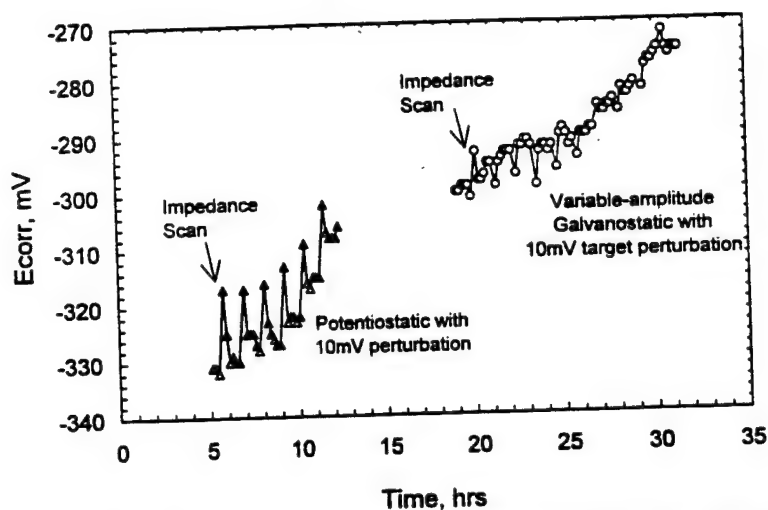


Fig. 1. Corrosion potential for a cylindrical copper electrode in synthetic sea-water measured as a function of time from immersion. Impedance scans were conducted at regular intervals (potentiostatic from 5–13 h and variable-amplitude galvanostatic from 19–32 h). The first impedance of each series is marked.

which typically took from 5–6 min, the current was again measured and these measurements are represented by the squares in Fig. 2. Polarization currents after the scan were on the order of 0.35 mA which can be attributed to a shift in the corrosion potential during the scan.

It is clear that potentiostatically regulated impedance measurements are invasive for systems that have a changing corrosion or open-circuit potential. For such systems, the zero-current condition can be assured only through use of galvanostatic control. For conventional galvanic experiments, however, has a fixed current amplitude is used which can lead to poor signal-to-noise ratios, non-linearity, or both. Use of a single fixed value for the current perturbation is inappropriate for the typical electrochemical systems characterized by a magnitude of the impedance which varies over several orders of magnitude with frequency. For the copper cylinder system used in this work the magnitude with fre-

quency. For the copper cylinder system used in this work the magnitude of the impedance changed almost three orders of magnitude over the measured frequency range.

As shown in Fig. 3, a large change in the impedance magnitude can yield significant experimental design problems. For example, a sweep from 20 kHz to 0.05 Hz with a fixed current perturbation of 0.035 mA resulted in a  $10 \text{ mV s}^{-1}$  potential perturbation at the electrode surface at low frequency. This is a desirable potential perturbation value which did not cause non-linearity in this system, however, the potential perturbation at the surface at high frequency was on the order of  $0.1 \text{ mV s}^{-1}$ . A low value of the potential response causes signal-to-noise problems. The poor signal-to-noise ratio at high frequencies was alleviated by increasing the amplitude of the current perturbation to 0.5 mA, but the potential perturbations on the order of  $300 \text{ mV s}^{-1}$  at low frequency far exceed usual linearity constraints (see

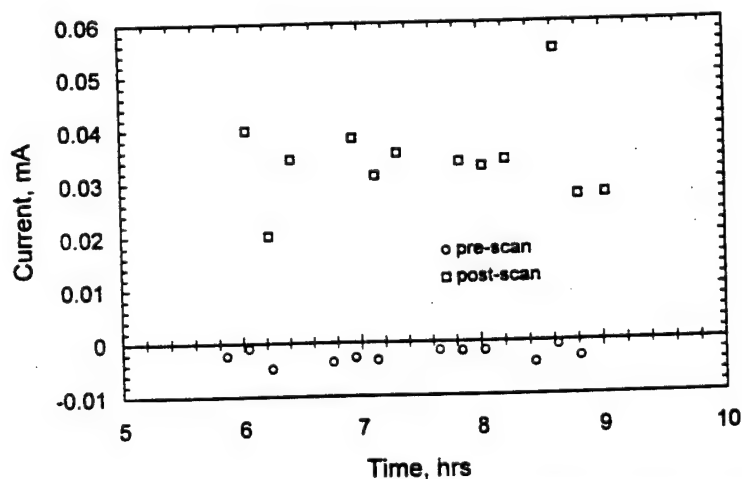


Fig. 2. Polarization current measured before and after the potentiostatic impedance measurements shown in Fig. 1.

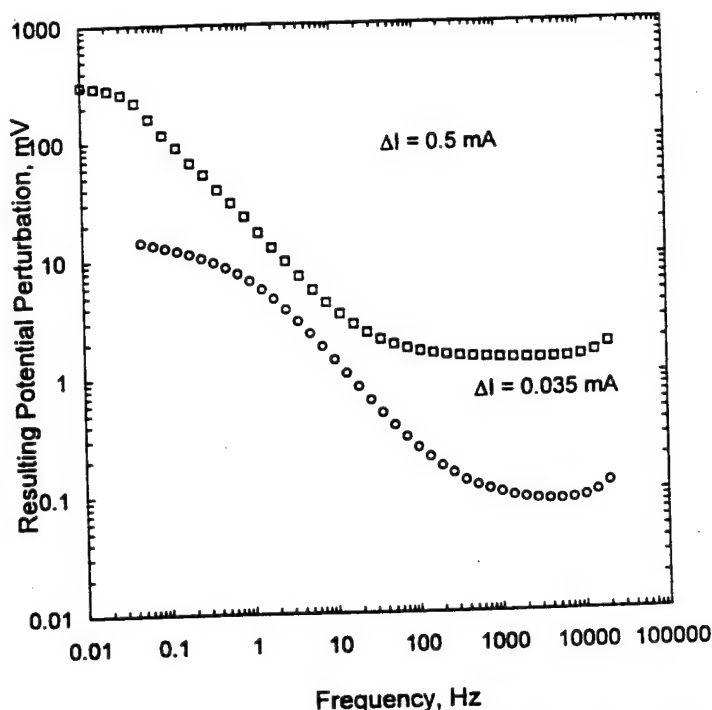


Fig. 3. Amplitude of the frequency-dependent potential response associated with the current perturbation of a fixed current amplitude galvanostatic impedance measurement. Data were collected for the copper cylinder electrode in synthetic sea-water.

equation (1)). While linearity can be assured by using galvanostatic modulation with a fixed current amplitude that is sufficiently small, the penalty for such an experimental approach is (as shown in Fig. 4) that the time required for the measurement is increased significantly. Even at an amplitude of 0.1 mA for which the maximum potential perturbation was

$43 \text{ mV s}^{-1}$ , the time required to conduct an impedance scan was more than twice the time required to conduct the same experiment with the variable-amplitude galvanostatic impedance method.

As shown in Fig. 5, the applied current perturbation in the variable-amplitude galvanostatic algorithm is changed at each frequency according to

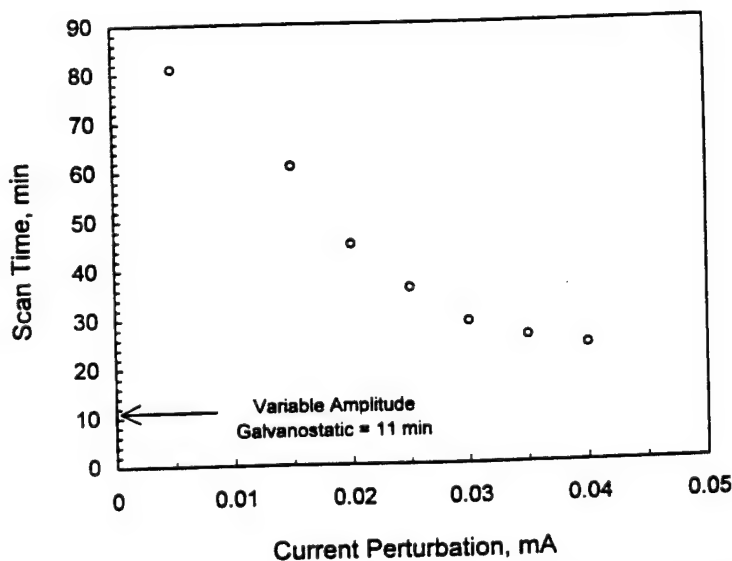


Fig. 4. The time required for a complete impedance measurement as a function of the current perturbation of fixed-amplitude galvanostatic impedance measurements. The corresponding time required for the variable-amplitude galvanostatic measurements was 11 min.

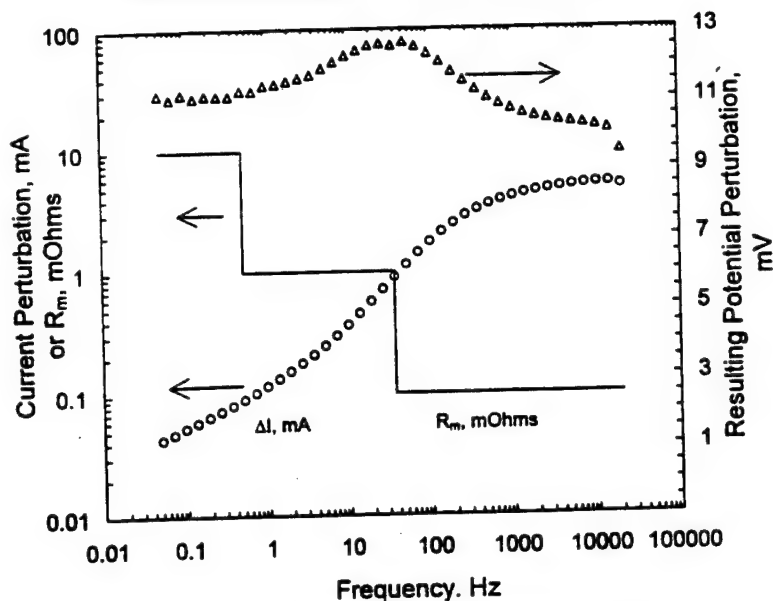


Fig. 5. Characteristic behavior of the variable-amplitude galvanostatic impedance measurement. The amplitude of the current perturbation changes over two orders of magnitude, triggering a corresponding change in the current measuring resistor. The measured amplitude of the potential perturbation is within 20% of the target  $10 \text{ mV s}^{-1}$  amplitude.

equation (4). In this case, impedance measurements were conducted from high frequency to low. The target potential was  $10 \text{ mV s}^{-1}$ , and the resulting potential perturbation ranged between 10 and  $12 \text{ mV s}^{-1}$ . A better correspondence between the target and measured potential perturbation should in principle be achieved if a better prediction for the impedance were used. The solid line in Fig. 5 represents the value of the currents measuring resistor as a function of frequency.

Seven sets of impedance spectra collected using the variable-amplitude galvanostatic method over a period of approximately 3.5 h are shown in Fig. 6. The high degree of repeatability suggests the extent to which the measurement did not adversely disturb the system. A comparable set of conventional galvanostatic data sets of different current amplitudes are shown in Fig. 7. These data are much more scattered due to noise, and disturbances to the system by the measurement. Furthermore, these spectra show

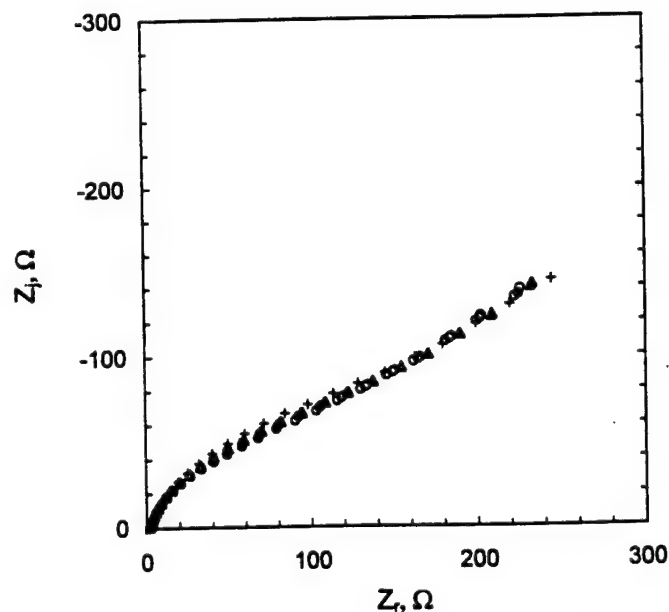


Fig. 6. Typical impedance plane plot for repeated data collected using the variable-amplitude galvanostatic impedance measurement algorithm with a  $10 \text{ mV s}^{-1}$  target potential perturbation. Data were collected for the copper cylinder electrode in synthetic sea-water.

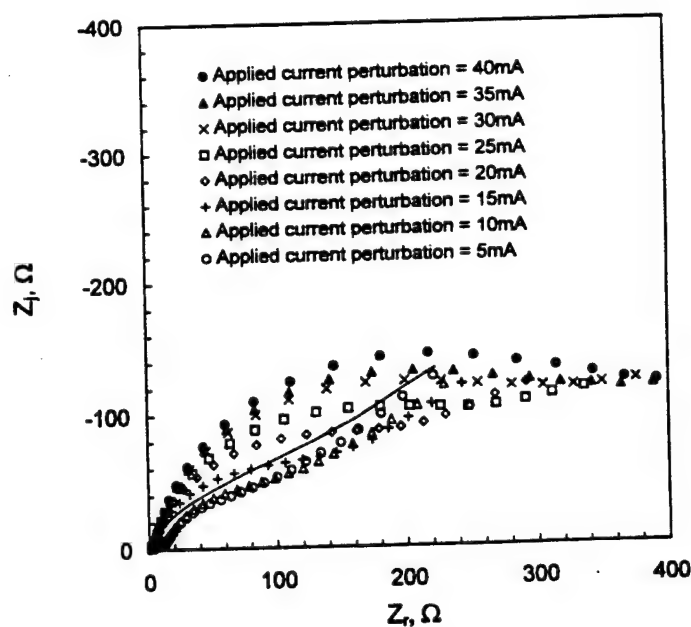


Fig. 7. Typical impedance plane plot for repeated data collected using the conventional galvanostatic method. The data are compared to the results of the variable-amplitude galvanostatic impedance measurement algorithm with a  $10 \text{ mV s}^{-1}$  target potential perturbation (solid line). Data were collected for the copper cylinder electrode in synthetic sea-water.

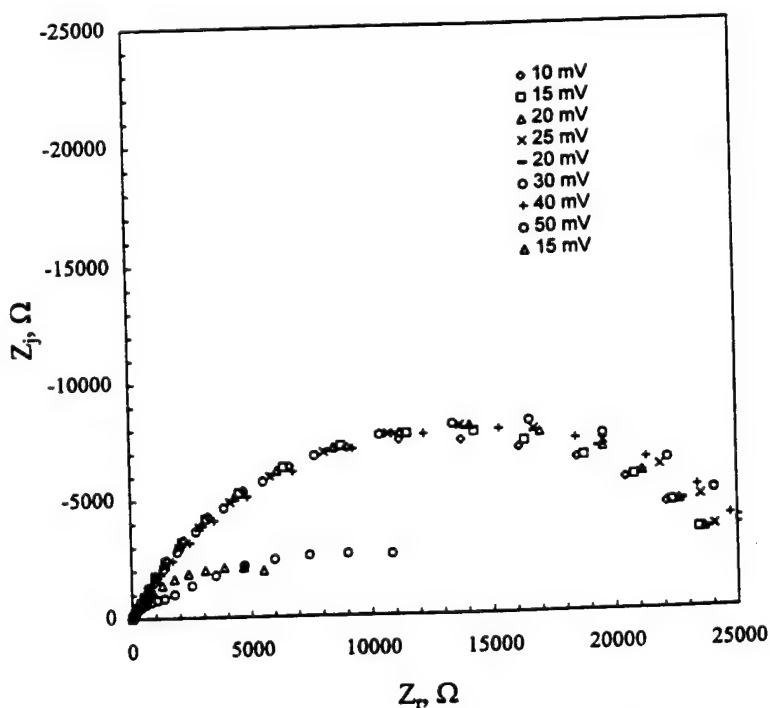


Fig. 8. Typical impedance plane plot for repeated data collected sequentially using the variable-amplitude galvanostatic impedance measurement algorithm. Data were collected for the copper disk electrode subjected to an axisymmetric impinging jet of synthetic sea-water. Note that the experiments are repeatable until the electrode was subject to impedance scans using a  $50 \text{ mV s}^{-1}$  target potential perturbation. The subsequent measurement at a  $15 \text{ mV s}^{-1}$  amplitude shows a significant increase in the reactivity of the copper electrode.

features that differ significantly from the spectra collected using the variable-amplitude galvanostatic method.

The variable-amplitude galvanostatic method addresses the need for monitoring corrosion systems at the open-circuit condition with impedance techniques that are non-invasive and that maintain linearity. It should be emphasized that for some systems, violation of linearity constraints can also perturb significantly the experimental system. The results of repeated variable-amplitude galvanostatic scans are presented in Fig. 8 for a copper disk subjected to flow from a submerged impinging jet. The data were collected after the corrosion potential, polarization resistance, and optical images showed no further change in system properties (6 days). The impedance scans taken with target potentials of 10–40 mV s<sup>-1</sup> show rough agreement corresponding to a modest degree of non-linearity. This behavior was reversible, since scans taken at a target potential of 20 mV s<sup>-1</sup> and separated by a series of measurements at 25 and 30 mV s<sup>-1</sup> showed good agreement. The impedance scan obtained with a target potential of 50 mV s<sup>-1</sup> shows a strikingly lower polarization resistance, and a subsequent measurement at a target potential of 15 mV s<sup>-1</sup> did not recover the large polarization resistance seen in previous scans. The nonlinear behavior associated with a large potential variation for copper in synthetic sea-water can therefore be reversible if the potential variation is small, but irreversible changes to the system were associated with a potential perturbations as small as 50 mV s<sup>-1</sup>.

### CONCLUSIONS

Impedance spectroscopy can be used for a non-invasive evaluation of properties, but, in order for

this technique to be non-invasive, the perturbation must be small and the modulation must not change the steady state characteristics. Galvanostatic regulation is ideally suited for the use of impedance spectroscopy as a non-invasive tool for periodically observing the condition of a metal held at the corrosion potential for a long period of time. While galvanostatic measurements with a fixed amplitude for the current perturbation can result in severe swings in potential, the algorithm described here provides a good means for adjusting the modulation amplitude for current so as to prevent large perturbations to the system.

*Acknowledgements*—This research was supported by the Office of Naval Research under Grant Number N00014-89-J-1619; Dr A. J. Sedriks was the program monitor.

### REFERENCES

1. J. A. V. Butler, *Trans. Faraday Soc.*, **19**, 729–734 (1924).
2. EG&R Princeton Applied Research, *Model 273 Potentiostat/Galvanostat*, operation manual (1985).
3. Schlumberger, *1260 Impedance/Gain-Phase Analyser*, operation manual (1993).
4. J. B. Phipps, J. R. Gyory, *Advanced Drug Delivery Reviews*, **9**, 137–176 (1992).
5. P. Agarwal, *Application of Measurement Models to Impedance Spectroscopy*, Ph.D. Dissertation, University of Florida, Gainesville, Florida, 1994.
6. M. W. Kendig, A. I. Allen, and F. Mansfield, *J. Electrochem. Soc.*, **131**, 935–936 (1984).
7. F. LaQue, *Marine Corrosion: Causes and Prevention*, John Wiley and Sons, NY, 1975.
8. P. T. Wojcik, *Velocity Enhanced Corrosion of Copper and Copper Alloys in Synthetic Sea Water*, Ph.D. Dissertation, University of Florida, Gainesville, Florida, in preparation.



## THE INFLUENCE OF ERROR STRUCTURE ON INTERPRETATION OF IMPEDANCE SPECTRA

PANKAJ AGARWAL,\* MARK E. ORAZEM† and LUIS H. GARCIA-RUBIO‡

Department of Chemical Engineering, University of Florida, Gainesville, FL 32611, U.S.A.

‡ Department of Chemical Engineering, University of South Florida, Tampa, FL 33620, U.S.A.

(Received 8 May 1995)

**Abstract**—The influence of error structure on interpretation of impedance measurements is demonstrated for electro-hydrodynamic impedance spectra. The stochastic component of the error structure was determined through use of measurement models, and a three-parameter model for the error structure was identified. The measurement model was also used to identify portions of the impedance spectra that were not corrupted by bias errors. Regression employing weighting by the stochastic component of the error structure yielded unambiguous values for physical properties such as the Schmidt number, whereas significant ambiguity was observed using modulus or proportional weighting.

**Key words:** electro-hydrodynamic impedance, impedance spectroscopy, modeling, mass transfer, statistics.

### INTRODUCTION

The objective of impedance measurements is identification of physical processes or parameter values appropriate for a given system. Interpretation of impedance spectra requires, in principle, identification of a model which provides a physical description of the system under study. In addition to an adequate deterministic model, however, interpretation of impedance spectra requires a quantitative assessment of the fundamental characteristics of the measurement. An important factor, often ignored or understated in electrochemical impedance spectroscopy, is the nature of the error structure associated with the measurements.

The concept that the error structure plays an important role in the interpretation of experimental data is, in fact, well established in the scientific literature[1]. As an example of its application to a class of spectroscopic measurements, knowledge of the error structure has been shown to allow enhanced interpretation of light scattering measurements in terms of particle size distribution or even particle classification[2, 3].

Identification of the error structure for most radiation-based spectroscopic measurements such as light scattering can be accomplished by calculating the standard deviation of replicate measurements. The error analysis approach has been successful for light spectroscopy measurements because these systems lend themselves to replication and, therefore, to the independent identification of the different errors that contribute to the total variance of the measurements. In contrast, the stochastic contribu-

tion to the error structure of electrochemical impedance spectroscopy measurements cannot be obtained from the standard deviation of replicated measurements because the inherently non-stationary character of electrochemical systems introduces a non-negligible time-varying bias contribution to the error.

The discussion of the stochastic error structure in impedance spectroscopy has, therefore, been limited to *a priori* predictions of measurement noise based on instrument noise[4] and to standard assumptions concerning the error structure such as constant or proportional errors[5-7]. Zoltowski reported an experimental assessment of the stochastic noise at selected frequencies which showed that the standard deviation of the real and imaginary parts of the impedance (and admittance) are correlated[8]. This result was used to defend the use of modulus weighting for regression of models to experimental data[8-10]. Attempts to weight regressions by standard deviations determined from repeated impedance scans (*eg* Ref. [11]) have not been very successful because the standard deviation obtained in this way includes both bias and stochastic contributions to the error structure.

The importance of bias errors in impedance spectroscopy has led to development of tools to assess the consistency of spectra with the Kramers-Kronig relations[12-25]. Recently, a measurement model concept was introduced which can be used to determine both stochastic and bias components of the error structure of impedance measurements[26-33]. The objective of this communication is to review the status of the development of the error structure for impedance measurements and to demonstrate, through an example, the role that knowledge of the error structure can play in enhancing interpretation of impedance measurements. Electro-hydrodynamic impedance spectra[34-37] were selected for this dis-

\* Current Address: Materials Department, Swiss Federal Institute of Technology (Lausanne), MX-C Ecublens, Lausanne, Switzerland.

† Author to whom correspondence should be addressed.



cussion because an accurate deterministic model is available for reduction of ferricyanide on a Pt disc in a 1 M KCl supporting electrolyte[38]. A detailed discussion of this work is presented in Ref.[39].

### CLASSIFICATION OF MEASUREMENT ERRORS

The residual errors that arise when a model is regressed to experimental data can be described as being composed of deterministic (systematic) and stochastic (randomly distributed) contributions,  $\epsilon_{\text{sys}}$  and  $\epsilon_{\text{stoch}}$ , respectively. Thus, at any given frequency, the residual error is given by

$$Z - \hat{Z} = \epsilon_{\text{sys}} + \epsilon_{\text{stoch}} \quad (1)$$

where the caret signifies the model value for the complex impedance  $Z$ . In this work, the systematic errors that result from model inadequacies are distinguished from the experimental errors that are propagated through the model and that could arise from a changing baseline or from instrumental artifacts. Systematic errors are therefore defined to consist of contributions from the lack of fit of the model to the data ( $\epsilon_{\text{lof}}$ ) and a bias ( $\epsilon_{\text{bias}}$ ) in the experiment, *ie*

$$\epsilon_{\text{sys}} = \epsilon_{\text{lof}} + \epsilon_{\text{bias}} \quad (2)$$

In principle, improvement of a stationary model will reduce the error associated with a lack of fit, but non-stationary behavior ( $\epsilon_{\text{ns}}$ ) and instrumental artifacts ( $\epsilon_{\text{ins}}$ ) can still contribute to the bias errors, *ie*

$$\epsilon_{\text{bias}} = \epsilon_{\text{ns}} + \epsilon_{\text{ins}} \quad (3)$$

The error structure for impedance measurements is defined in this work to include the stochastic and experimental bias errors, but does not include errors associated with model inadequacies.

### IDENTIFICATION OF ERROR STRUCTURE

The method for assessing the stochastic part of the error structure was based on using a measurement model to filter non-replicacy of impedance data. A model composed of Voigt elements in series with a solution resistance has been shown to be a useful and general measurement model (see Fig. 1 in Ref. [26])[26–33]. The measurement model can be described as being a superposition of line-shapes in which each RC element of the Voigt model constitutes a line-shape. While the line-shape parameters may not be unequivocally associated with a set of deterministic or theoretical parameters for a given system, the measurement model approach has been shown to represent adequately the impedance spectra obtained for a large variety of electrochemical systems[26]. The line-shape models represent the low frequency (as compared to the noise frequency) stationary components of the impedance spectra (in a Fourier sense). Regardless of their interpretation, the measurement model representation can be used to filter and thus identify the non-stationary (drift) and high frequency (noise) components contained in the same impedance spectrum[32, 33].

### Stochastic contributions to the error structure

The approach taken to assess the error structure of impedance data was to identify the measurement characteristics experimentally rather than to assess the noise level from the published specifications of the component instrumentation. Pseudo-replicate impedance scans were obtained. The measurement model was regressed to each data set using the maximum number of parameters that could be resolved from the data. The measurement model parameters differed slightly for each data set because the system changed slightly from one experiment to the other. Hence, by regressing the measurement model to individual data sets separately, the effects of the change of the experimental conditions from one experiment to another were incorporated into the measurement model parameters. The standard deviations of the real and imaginary residual errors could therefore be obtained as a function of frequency, and these provided a good estimate for the standard deviation of the stochastic noise in the measurement.

Following the experimental observation that standard deviation for the noise in the real part of the impedance obtained in this way was indistinguishable from the noise in the imaginary part of the impedance, a preliminary model for the error structure was obtained for systems with a negligible ohmic resistance[28, 29, 32]:

$$\sigma_j = \sigma_r = \sigma = \alpha |Z_j| + \beta |Z_r| + \gamma \frac{|Z|^2}{R_m} \quad (4)$$

where  $\alpha$ ,  $\beta$ , and  $\gamma$  were adjustable parameters, and  $R_m$  was the value for the current measuring resistor. The parameters  $\alpha$ ,  $\beta$ , and  $\gamma$  were found to be dependent on the instruments used and on the experimental parameters employed. For example, the parameters obtained under potentiostatic control using a Solartron 1250 frequency response analyzer and a PAR 273 potentiostat were different than those obtained using the same frequency response analyzer coupled with a Solartron 1286 potentiostat[28, 29]. The validity of the model for the error structure is supported by the fact that a three-parameter model provides a good agreement for solid state systems as well as for electrochemical systems, for data collected under a wide variety of experimental conditions, and for errors ranging from mΩ to MΩ[24, 25, 27].

The error structure model for the electrohydrodynamic impedance measurements discussed here was found to be[39]

$$\sigma_j = \sigma_r = \sigma = \alpha |Z_j| + \beta |Z_r| + \delta \quad (5)$$

where  $\delta$  is a constant. This model was found to apply for a wide range of rotation rates for both oxidation and reduction reactions[39].

### Bias contributions to the error structure

A quantitative measure of the consistency with the Kramers–Kronig relations provides evidence of the extent to which a given data set was affected by non-stationary behavior or by instrumental artifacts. The Kramers–Kronig relations have not found widespread use in the analysis and interpretation of elec-

trochemical impedance spectroscopy data due to difficulties with their application. Explicit integration of the relations requires data for frequencies ranging from zero to infinity, whereas the obtainable experimental frequency range is often constrained by instrumental limitations or by the instability of the electrode. Here, measurement models were used to check for the consistency of the experimental data with the Kramers-Kronig relations[27, 29, 33]. The methodology takes advantage of the fact that electrical circuits composed of passive elements must satisfy the Kramers-Kronig relations. Since, by including a sufficient number of line-shapes, a measurement model can provide an adequate fit to stationary electrochemical impedance data, an inability to fit an impedance spectrum can be attributed to the failure of the data to conform to the assumptions of the Kramers-Kronig relations rather than the failure of the model. No direct integration of the Kramers-Kronig relations is required.

### APPLICATION TO ELECTRO-HYDRODYNAMIC IMPEDANCE SPECTROSCOPY

The application of the error structure to interpretation of impedance data is illustrated for evaluation of the Schmidt number using electro-hydrodynamic impedance spectroscopy. Electro-hydrodynamic impedance spectroscopy (EHD) is a technique in which sinusoidal modulation of a disc rotation rate drives a sinusoidal current or potential response[35-37]. The technique has been applied to surface or electrode processes that are under mass transport control, and it has been proposed to be a sensitive tool for measurement of diffusion coefficients of ionic species. Ionic diffusivities are obtained by regressing a model to the EHD data. A process model for this system was given by Tribollet and Newman[38]

$$\frac{I}{\bar{\Omega}} = \frac{2A_0 z_p \left( Sc^{1/3} \frac{\omega}{\bar{\Omega}_0} \right)}{j\omega R_e C + 1} \quad (6)$$

where  $z_p$  is a tabulated function for the electro-hydrodynamic impedance which includes corrections for a finite Schmidt number,  $A_0$  is the impedance at zero frequency,  $Sc$  is the Schmidt number ( $Sc = \nu/D$ ), and  $R_e C$  is a lumped parameter which contains the electrode capacitance  $C$  and ohmic resistance  $R_e$ . The error structure for EHD measurements was identified for a platinum disc electrode rotating in solutions with a 0.01 M ferri/ferro cyanide redox couple in a 1 M KCl supporting electrolyte. Experimental details are provided in Ref.[39]. Typical results are presented in Fig. 1.

The error structure obtained by using the measurement model to filter lack of replicacy is compared in Fig. 2 to the modulus and to the standard deviations of the replicate measurements. The line given in Fig. 2 is the fitted model for the error structure (see equation (5)). The stochastic noise of the EHD measurements is clearly not proportional to the modulus of the impedance. The standard deviation of the real and imaginary parts of the noise are

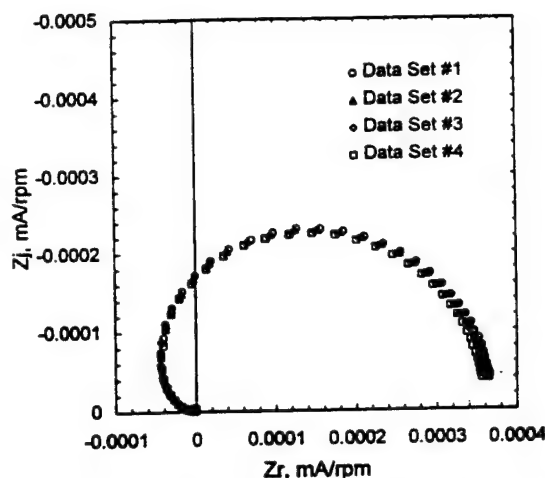


Fig. 1. The results of four sequential electro-hydrodynamic impedance experiments in the impedance plane. The mean rotation rate was 200 rpm, the applied potential was 0 V (sce), and analog filtering of input signals to the FRA was not employed.

equal, a result that is consistent with observations made for EIS[28, 29, 32]. The results presented in Fig. 2 also suggest that the noise level becomes a significant fraction of the signal at higher frequencies, a characteristic that influences regression of models to EHD data. It is worth noting that the error structure obtained under the assumption that the repeated measurements are replicate over-predicts the filtered standard deviation by as much as an order of magnitude, and that the standard deviations for the real and imaginary components appear to be correlated but are not equal. This result is presented in greater detail in Ref. [39].

Modulus weighting has, in the past, been used to regress the EHD model to the data. The use of

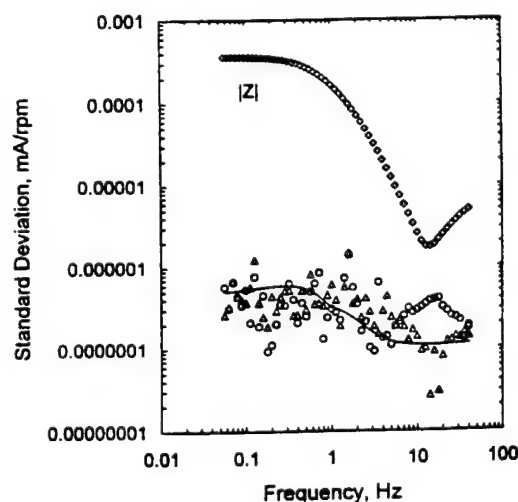


Fig. 2. The error structure identified for the EHD measurements shown in Fig. 1. The open circles and triangles represent the real part and imaginary parts, respectively, of the standard deviation filtered by the measurement model. The diamonds represent the mean modulus. The solid line is the fitted model for the error structure (equation (5)).

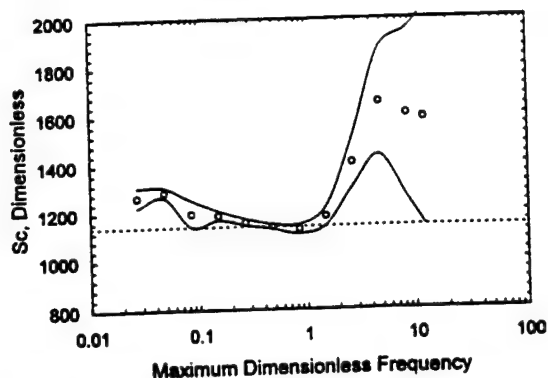


Fig. 3. Regressed values for the Schmidt number obtained under modulus weighting as a function of the upper value for the dimensionless frequency range. The regressed frequency range for any open circle was 0.0168 to the maximum dimensionless frequency given for that point. The first data set shown in Fig. 1 was used for the regression. The solid lines represent the 95% confidence interval for the regressed parameter and the dashed line represents the value reported in this work. Similar ambiguity was seen for  $A_0$  and  $R_s C$ .

modulus implies that the stochastic noise is proportional to the modulus of the impedance, an assumption that is shown in Fig. 2 to be incorrect. It has been reported that inclusion of noisy high fre-

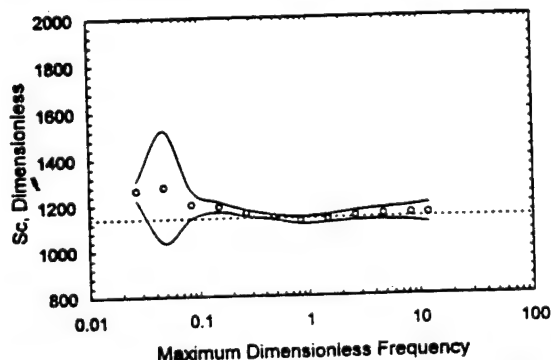


Fig. 4. Regressed values for the Schmidt number obtained under error structure (see equation (5)) weighting as a function of the upper value for the dimensionless frequency range. The regressed data was the same as reported in Fig. 3.

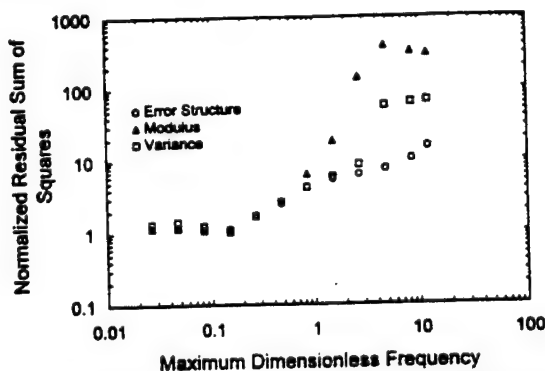


Fig. 5. The residual sum of squares normalized by the sum of squares of the standard deviation given by equation (5) for the fits obtained under modulus, apparent standard deviation, and error structure weighting (see Fig. 2).

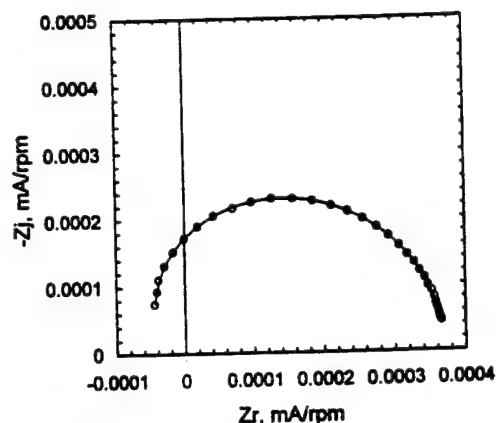


Fig. 6. Results of the regression of the process model (equation (6)) to the first of the data sets shown in Fig. 1. The circles represent the experimental data and the solid lines represent the corresponding model fit. The frequency range of the regression was that shown to be free of non-stationary bias errors.

quency data in regression under modulus weighting leads to unrealistic values for the Schmidt number [11]. The problem of high frequency noise has, in the past, been addressed by deleting high frequency points. Unfortunately, elimination of high

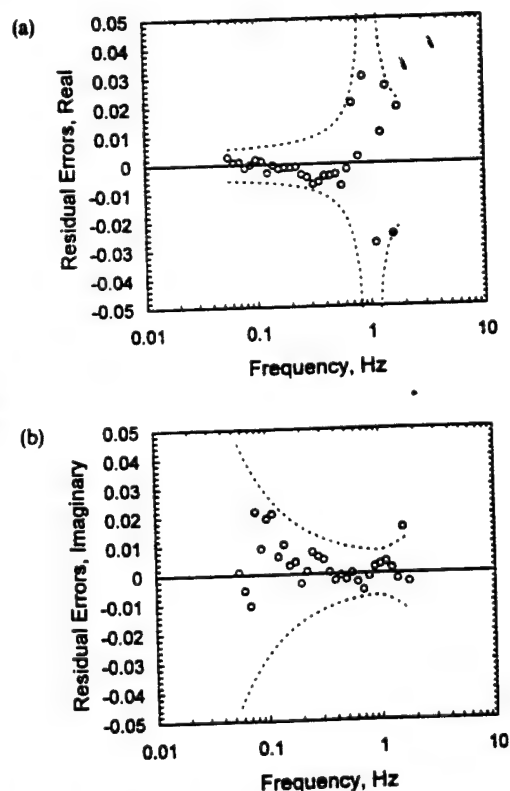


Fig. 7. The relative (dimensionless) residual errors for the fit presented in Fig. 6. (A value of 0.01 corresponds to a 1% relative residual error.) The dashed line represents the 95.4% ( $2\sigma$ ) confidence interval (or noise level) for the measurement as determined by the measurement model approach: (a) real part; (b) imaginary part.

frequency data from the regression leads to ambiguity in determination of the Schmidt number because, as shown in Fig. 3, the resulting value for  $Sc$  depends on the number of data points included in the regression. The 95% confidence interval for the parameter estimate presented in Fig. 3 as upper and lower solid lines also reflects the large uncertainty in the estimate for  $Sc$ . Similar ambiguity is seen when the standard deviation of repeated measurements is used to weight the regression. As shown in Fig. 4, use of the measured error structure for the EHD measurements to weight the regression (the solid line in Fig. 2) eliminated ambiguity in the identification of the Schmidt number, and the confidence interval for the estimate was improved. The regressed values for  $A_0$  and  $R_p C$  showed similar ambiguity when modulus weighting is employed, and an unambiguous value was obtained when the error structure is used in the regression.

The sum of squares of the residual error for this series of regressions, normalized by the sum of squares of the standard deviation, is given in Fig. 5. The use of error structure weighting improved the regression statistic, but the value was significantly larger than one when high frequency data were included. The large normalized residual error seen when high frequency data were included could be attributed to an inadequacy of the process model or to the influence of non-stationary phenomena. A change in the electrode properties was suggested by departures from ideal behavior of the modulus (see Fig. 2) and phase angle at high frequencies [40, 41]. Inconsistency due to non-stationary behavior may be expected for high frequency data since the time required for the measurement increased greatly at high frequencies. To explore the role of non-stationarity, the methods of Ref. [33] were used to evaluate the consistency of the data with the Kramers-Kronig relations. The data within the range of 0.0561–1.8 Hz were found to be consistent with the Kramers-Kronig relations to within the 95.4% confidence interval of the measurement model. Data in the range 1.8–40 Hz were rejected as being inconsistent and presumably influenced by non-stationary bias errors.

As shown in Fig. 6, the process model (equation (6)) provided a good fit to the data over the consistent frequency range. Residual errors, presented in Fig. 7, fell within the error structure for the measurement. The values for Schmidt number obtained on freshly polished electrodes under error structure weighting for frequency ranges found to be consistent with the Kramers-Kronig relations were in good agreement with published values. The value for the Schmidt number, however, increased with the time of exposure of the electrode, and the value obtained for  $R_p C$  was an order of magnitude larger than expected. These results suggest that the blocking phenomena changes the values for  $Sc$  and  $R_p C$ .

## CONCLUSIONS

The development and application of mathematical models for the interpretation of electrochemical impedance data requires both physical insight and a

quantitative assessment of the fundamental characteristics of the measurement. The example presented here illustrates that synergistic implementation of experiment, measurement model and process model can enhance the information content of impedance spectra in terms of physically meaningful parameters. The measurement model provides a means of characterizing the measurement characteristics for electro-hydrodynamic impedance spectroscopy as well as electrochemical impedance spectroscopy. Regression employing weighting by the stochastic component of the error structure yielded unambiguous values for physical properties such as the Schmidt number, whereas significant ambiguity was observed using modulus or proportional weighting. Through use of the measurement model, the influence of non-stationary processes on the data could be distinguished from the influence of surface blocking. The influence of surface phenomena on the transport properties could be observed clearly under the use of error structure weighting.

**Acknowledgements**—The work performed at the University of Florida (PA and MEO) was supported by the Office of Naval Research. The work performed at the University of South Florida (LHGR) was supported by the National Science Foundation under Grants No. RII-8507956 and INT-8602578. The example given here to illustrate the influence of error structures is based on work conducted at the UPR, 15 du CNRS "Physique des Liquides et Electrochimie", Paris, France in collaboration with Drs C. Deslouis and B. Tribollet and presented in Ref. [39].

## REFERENCES

1. G. E. P. Box and N. R. Draper, *Empirical Model-Building and Response Surfaces*. John Wiley & Sons, Inc., New York (1987).
2. R. W. Christy, *Am. J. Physics* 40, 1403 (1972).
3. A. Jutan and L. H. Garcia-Rubio, *Process Control and Quality* 4, 235–243 (1993).
4. G. Spinolo, G. Chioldelli, A. Moghistris and U. A. Tamburini, *J. Electrochem. Soc.* 135, 1419 (1988).
5. J. R. Macdonald and L. D. Potter, Jr., *Solid State Ionics* 23, 61 (1987).
6. J. R. Macdonald, *Electrochim. Acta* 35, 1483 (1990).
7. J. R. Macdonald and W. J. Thompson, *Commun. Statist. Simula.* 20, 843 (1991).
8. P. Zoltowski, *J. Electroanal. Chem.* 178, 11 (1984).
9. P. Zoltowski, *J. Electroanal. Chem.* 260, 269 (1989).
10. P. Zoltowski, *J. Electroanal. Chem.* 260, 287 (1989).
11. B. Robertson, B. Tribollet and C. Deslouis, *J. Electrochem. Soc.* 135, 2279 (1988).
12. M. Kendig and F. Mansfield, *Corrosion* 39, 466 (1983).
13. M. K. Brachman and J. R. Macdonald, *Physica* 20, 141 (1956).
14. D. D. Macdonald and M. Urquidi-Macdonald, *J. Electrochem. Soc.* 132, 2316 (1985).
15. F. Mansfield, M. W. Kendig and W. J. Lorenz, *J. Electrochem. Soc.* 132, 290 (1985).
16. M. Urquidi-Macdonald, S. Real and D. D. Macdonald, *J. Electrochem. Soc.* 133, 2018 (1986).
17. M. C. H. McKubre, D. M. Macdonald and J. R. Macdonald, in *Impedance Spectroscopy, Emphasizing Solid Materials and Systems* (Edited by J. R. Macdonald) p. 274, John Wiley & Sons, New York (1987).
18. C. Haili, MS Thesis, University of California, Berkeley (1987).

19. M. Urquidi-Macdonald, S. Real and D. D. Macdonald, *Electrochim. Acta* 35, 1559 (1990).
20. D. D. Macdonald and M. Urquidi-Macdonald, *J. Electrochem. Soc.* 137, 515 (1990).
21. D. Townley, *J. Electrochem. Soc.* 137, 3305 (1990).
22. M. Urquidi-Macdonald and D. D. Macdonald, *J. Electrochem. Soc.* 137, 3306 (1990).
23. J. M. Esteban and M. E. Orazem, *J. Electrochem. Soc.* 138, 67 (1991).
24. M. E. Orazem, J. M. Esteban and O. C. Moghissi, *Corrosion* 47, 248 (1991).
25. B. J. Dougherty and S. Smedley, in *Electrochemical Impedance: Analysis and Interpretation*, ASTM, STP 1188 (Edited by J. Scully, D. Silverman and M. Kendig). American Society for Testing and Materials, Philadelphia (1993).
26. P. Agarwal, M. E. Orazem and L. H. Garcia-Rubio, *J. Electrochem. Soc.* 139, 1917 (1992).
27. P. Agarwal, M. E. Orazem and L. H. Garcia-Rubio, in *Electrochemical Impedance: Analysis and Interpretation*, ASTM, STP 1188 (Edited by J. Scully, D. Silverman and M. Kendig), p. 115. American Society for Testing and Materials, Philadelphia (1993).
28. M. E. Orazem, P. Agarwal, A. N. Jansen, P. T. Wojcik and L. H. Garcia-Rubio, *Electrochim. Acta* 38, 1903 (1993).
29. P. Agarwal, PhD dissertation, University of Florida, Gainesville (1994).
30. B. A. Boukamp and J. R. Macdonald, *Solid State Ionics* 74, 85 (1994).
31. B. A. Boukamp, *J. Electrochem. Soc.* 142, 1885 (1995).
32. P. Agarwal, O. D. Crisalle, M. E. Orazem and L. H. Garcia-Rubio, *J. Electrochem. Soc.* 142, 4149 (1995).
33. P. Agarwal, M. E. Orazem and L. H. Garcia-Rubio, *J. Electrochem. Soc.* 142, 4159 (1995).
34. S. Bruckenstein, M. I. Bellavance and B. Miller, *J. Electrochem. Soc.* 120, 1351 (1973).
35. B. Miller and S. Bruckenstein, *J. Electrochem. Soc.* 121, 1558 (1974).
36. C. Deslouis and B. Tribollet, *Advances in Electrochemical Science and Engineering*, 2, 205 (1991).
37. B. Robertson, B. Tribollet and C. Deslouis, *J. Electrochem. Soc.* 135, 2279 (1988).
38. B. Tribollet and J. Newman, *J. Electrochem. Soc.* 130, 2016 (1983).
39. M. E. Orazem, P. Agarwal, C. Deslouis and B. Tribollet, *J. Electrochem. Soc.*, in press.
40. A. Caprani, C. Deslouis, S. Robin and B. Tribollet, *J. Electroanal. Chem.* 238, 67 (1987).
41. R. S. Silva, O. E. Barcia, O. R. Mattos and C. Deslouis, *J. Electroanal. Chem.* 365, 133 (1993).



Reprinted from JOURNAL OF THE ELECTROCHEMICAL SOCIETY  
Vol. 143, No. 3, March 1996  
Printed in U.S.A.  
Copyright 1996

# Application of Measurement Models to Electrohydrodynamic Impedance Spectroscopy

Mark E. Orazem\* and Pankaj Agarwal\*\*<sup>a</sup>

*Department of Chemical Engineering, University of Florida, Gainesville, Florida 32611, USA*

Claude Deslouis\* and Bernard Tribollet\*

*UPR 15 du CNRS, Laboratoire "Physique des Liquides et Electrochimie," Université Pierre et Marie Curie,  
75252 Paris Cedex 05, France*

## ABSTRACT

The measurement model concept was used to assess both the stochastic and bias contributions to the error structure of electrohydrodynamic (EHD) impedance spectra. The stochastic component of the error structure was determined, and a model for the error structure was identified. Regression employing weighting by the stochastic component of the error structure yielded unambiguous values for physical properties such as the Schmidt number, whereas significant ambiguity was observed using other weighting strategies. The influence of surface phenomena on the impedance response could, through use of the measurement model for assessing consistency with the Kramers-Kronig relations, be distinguished from nonstationary effects. The measurement model provided a quantitative means for assessing the utility of input signal filtering. The noise level in the measured impedance was found to be unaffected by use of input filters and, surprisingly, the time required to collect the data was increased slightly by using the filters. The estimated parameter values and their standard deviations were comparable whether or not filtering was used. The use of the measurement model to assess stochastic and bias components of the error structure extends the useful frequency range for EHD measurements and should enhance the application of EHD for assessing surface phenomena.

The development and application of mathematical models for the interpretation of electrochemical impedance data requires quantitative assessment of the fundamental characteristics of the measurement as well as quantitative identification and evaluation of the physics and chemistry of the system under study. An important factor, often ignored or understated in electrochemical impedance

spectroscopy (EIS), is the nature of the error structure associated with the measurements. The importance of the error structure is neglected in spite of the fact that electrochemical impedance measurements are recognized as being, in general, heteroskedastic in frequency and time varying. Identification and quantification of the measurement-error structure is essential for filtering data, designing experiments, assessing the validity of regression assumptions, and determining the confidence intervals or the relevance of the resulting parameters.

In previous work,<sup>1-9</sup> a measurement model based upon a superposition of line shapes was shown to provide a satis-

\* Electrochemical Society Active Member.

\*\* Electrochemical Society Student Member.

<sup>a</sup> Present address: Swiss Federal Institute of Technology, Materials Department, Metallurgical Chemistry, MX-C Ecublens, Lausanne, Switzerland.



factory fit to the impedance response of typical electrochemical systems. The ability of the measurement model to fit general electrochemical data makes it a useful tool for identifying the error structure of impedance data, for screening impedance data for instrumental artifacts and nonstationary behavior, and for guiding development of an appropriate process model. In effect, the measurement model becomes a vehicle for a sophisticated statistical analysis of impedance spectra. The process model, which provides a mathematical description of the system-specific physics and chemistry, can then be regressed to the data to extract physically meaningful parameters.

While the measurement model has proved to be useful in the analysis of impedance data based on modulation and measurement of current and potential, the object of this work was to explore the utility of the measurement model for interpretation of data obtained by the "transfer function" techniques based on modulation of other system variables.<sup>10,11</sup> The system chosen for this study was electrohydrodynamic impedance spectroscopy (EHD), which is described in Ref. 12-19. EHD involves modulating the rotation speed of a disk electrode and measuring the resulting current. To a first approximation, this approach isolates the influence of mass transfer. Transport properties are obtained by regressing process models to the EHD impedance spectra. EHD can, in principle, provide accurate determination of the diffusivities of species that cannot be measured in other ways. An advantage of this technique is that an accurate process model is available that treats the convective diffusion to a disk electrode. The major limitation of the technique has been that noise in the measurement causes ambiguity in the regression, and the resulting uncertainty in the value for  $Sc$  can be 30% or more.

In this work it is shown that the measurement model can be applied for identification of the error structure for EHD and that regression of a process model with error structure weighting, coupled with identification of bias errors in the measurement, eliminates ambiguity in the determination of the values of the physical parameters.

### Principles of EHD

In the usual application of electrochemical impedance spectroscopy, a complex impedance is calculated as the ratio of potential to current under a small perturbation of current (galvanostatic regulation) or potential (potential regulation). The impedance is measured as a function of the frequency of the perturbation, and regression of models to the resulting spectra yields values for physical properties. In recent years generalized impedance techniques have been introduced in which a nonelectrical quantity such as pressure, temperature, magnetic field, or light intensity is modulated to give a current or potential response.<sup>10,11</sup> EHD is one such generalized impedance technique in which sinusoidal modulation of disk rotation rate drives a sinusoidal current or potential. The technique has been applied to surface or electrode processes that are under mass-transport control, and it has been used to obtain diffusion coefficients of ionic species from determination of the Schmidt number ( $Sc = (\nu/D)$ ).<sup>12-22</sup>

The relationship between EIS and EHD has been developed from the perspective of a transfer function analysis.<sup>16</sup> EHD has an advantage over EIS for measurement of the Schmidt number (or ionic diffusivities) because the measurements can be made at the mass-transfer limited current plateau, whereas an EIS measurement must be made on the slope below the limiting current plateau. Unrealistically large values of the Schmidt number are obtained below the limiting current plateau by either EIS or EHD, and this discrepancy can be as large as 200% or more.<sup>24,25</sup> Preliminary work suggested that this discrepancy may be caused by the nonuniform current, concentration, and overpotential seen at the disk electrode for currents below the limiting current plateau.<sup>26</sup> The EHD method employs a sinusoidal perturbation of the disk rotation rate while the electrode is held at a constant potential at the mass-transfer limited current. The resulting sinusoidal current is

measured, and the ratio of the complex current and the amplitude of the disk rotation gives the EHD transfer function. As the measurement is conducted at the limiting current, the current distribution and, hence, the concentration of reacting species, is uniform along the surface of the disk electrode.

The sensitivity of EHD to surface processes makes it useful for studying the influence of surface films and of blocking phenomena.<sup>16,17,21,22</sup> It should be noted that, while dc experiments at the current plateau can give good answers for the mass-transfer limited current, a nice diffusion plateau is not enough to calculate the diffusion coefficient. Additional information (electrode surface area and solute concentration) is needed, and the plateau may be influenced by blocking. An example of the use of EHD to explore the influence of blocking is given in Ref. 27. If blocking is present, the EIS measurement is also affected, but the effect is generally coupled with the effect of kinetics and is therefore less easily distinguished.

### EHD Experiments

A series of EHD experiments was conducted on a rotating platinum disk electrode. A wide range of experimental conditions was used in order that a generalized model for the error structure of the data could be obtained.

The disk was rotated by a high-speed low-inertia rotating disk apparatus developed at the CNRS.<sup>23</sup> The rotator was rated at a power of 115 W. This high power is necessary to obtain modulation over a large frequency range without attenuation. The rise time of the rotator between 0 and 1000 rpm when a stepwise potential is applied was less than 2 ms (indicating a low inertia). The long-term stability and accuracy of the rotation speed was 0.2% from 100 to 1000 rpm (the range corresponding to the experiments presented here). The tachometer had 24 poles, and the electro-mechanical constant was 3 mV/rpm. The amplitude of modulation was set to 10% of the average rotation rate.

The potentials and currents were measured and controlled by a P.G.Stat.Z1 potentiostat. A Solartron 1250 frequency-response analyzer (FRA) was used to apply the sinusoidal perturbation and to calculate the transfer function. A matched two-channel Kemo Type VBF8 48 dB low-pass Butterworth analog filter was used to reduce the noise level of the input signals to the FRA. The high-frequency cutoff was set to three times the measurement frequency. When the analog filter was in use, the perturbation and the response were both filtered to reduce the influence of the instrument phase shift. The analog filter gain was set to maximize the signal without causing clipping. This meant that, for the experimental conditions used here, the filter gain was set to times 10 for experiments at 200 and 400 rpm and to times 1 for experiments conducted at 800 rpm. Experiments were performed with the analog filter on and off-line to explore its influence on the noise of the resulting impedance and on the measurement time.

A ferri/ferrocyanide redox couple in KCl supporting electrolyte was used as the experimental system. The electrochemical reaction kinetics for this system on conditioned Pt are very fast as compared to mass transfer; therefore, this system is suitable for the comparison of diffusion measurements. Equimolar (0.01 M) concentrations of potassium ferricyanide and potassium ferrocyanide were dissolved in a 1 M potassium chloride solution. Before the start of each experiment, the electrode was wet polished on a 1200 grit emery cloth and rinsed in distilled water. The electrode diameter was 5 mm, yielding a surface area of 0.1963 cm<sup>2</sup>. The temperature was controlled at 25.0 ± 0.1°C.

The data were collected frequency-by-frequency from the low frequency (0.05 Hz) to the maximum frequency with measurements taken at 20 logarithmically spaced frequencies per decade. The first measurement at 0.05 Hz was discarded in the analysis because the start-up transient often influenced the value of impedance reported by the instrumentation. The long (1% closure error) autointe-

gration option of the frequency-response analyzer was used, and the channel used for integration was that corresponding to current. The time required to collect a complete frequency scan was roughly 90 min. The solution was not deaerated, but experiments were performed at a polarization potential of 0 V (SCE) in order to minimize the influence of oxygen on the reduction of ferricyanide. FraCom software developed in-house at CNRS by H. Takenouti was used to control the experiments and collect the data. Replicate runs were performed at each experimental condition. Data were collected at rotation rates of 200, 400, and 800 rpm with the analog filter on and off-line.

A typical set of four successive EHD measurements is shown in Fig. 1 for a rotation rate of 200 rpm with the analog filter disconnected, for a frequency range of 0.05 Hz (where the real part approaches a low-frequency asymptote of about 0.36  $\mu\text{A}/\text{rpm}$ ) to 40 Hz (where both the real and imaginary components approach zero). In contrast to the usual presentation of EHD data in dimensionless form, the data are presented here in units of  $\mu\text{A}/\text{rpm}$  to emphasize the physical nature of the experiment, to emphasize that the modulus at zero frequency (the normalizing parameter used to make such plots dimensionless) is a fitted parameter, and to emphasize that, since the parameters for the model for the error structure to be developed later are not all dimensionless, the units of the measurement are important. Close examination of Fig. 1 reveals a lack of replicacy. As is discussed in a subsequent section, the high-frequency behavior evident in Bode plots of Fig. 1 can be associated with gradual poisoning or blocking of the Pt surface.

### Measurement Model Analysis

This work is intended to demonstrate the applicability of the measurement model concept to EHD data and to determine the stochastic component of the error structure of EHD data. A generalized model for the error structure was then used to weight regression of the process model for this system.

*Applicability of the measurement model concept to EHD data.*—The measurement model<sup>1-9</sup> used for determination of the error structure of the EHD data was given by a generalized Voigt model, i.e.

$$Z(\omega) = Z_0 + \sum_k \frac{\Delta_k}{(1 + j\tau_k\omega)} \quad [1]$$

It is worth noting that Eq. 1 represents a superposition of line shapes (i.e., a series arrangement of circuits involving dissipative elements  $\Delta_k$  in parallel with oscillating elements with time constants  $\tau_k$ ) that has been applied in the fields of optics, solid mechanics, rheology ( $\Delta_k$  are then viscosities), and electrochemistry (where, for ac impedance,  $\Delta_k$  are resistances and  $Z_0$  is the ohmic potential drop resistance). In the particular case of EHD impedance, the  $\Delta_k$  are dimensioned as electrical charges, and  $Z_0$  is equal to zero.

To illustrate the applicability of Eq. 1 as a measurement model for EHD impedance, Eq. 1 was regressed to the first EHD data set shown in Fig. 1. The error structure for the measurement, presented in a subsequent section, was used to weight the regression. The frequency range for this regression was 0.0561 to 1.774 Hz (31 data points). This frequency range was that determined by the measurement model analysis (shown later) to be consistent with the Kramers-Kronig relations. As shown in Fig. 2, the measurement model provided a good fit to EHD data with the high frequency limit ( $Z_0$  in Eq. 1) set to zero as suggested by the theory for EHD. Two line shapes (four parameters) were obtained from the regression, which was weighted by the model for the error structure to be developed in a subsequent section. The residual sum of squares for this regression, normalized by the sum of squares of the noise, was 1.50, which compares favorably to the value of 2.60 obtained by the best fit of the process model over the same frequency range. As shown in (Fig. 3), the residual errors for the regression fall well within the measured 95.4% ( $2\sigma$ )

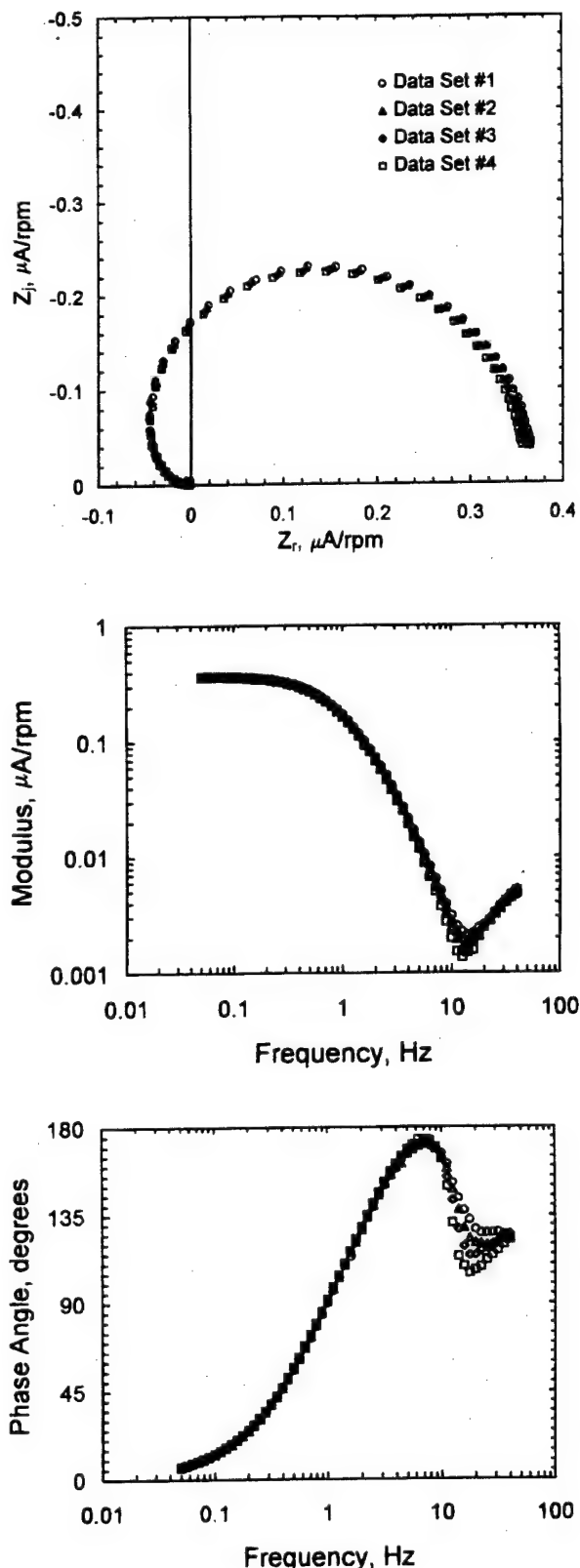


Fig. 1. The results of four sequential electrohydrodynamic impedance experiments. The mean rotation rate was 200 rpm, and the analog filter was not employed.

error structure for the measurement. Note that the residual errors and the error structure given in Fig. 3 are on a relative fractional basis. Thus, the residual errors and the confidence interval for the data tend toward infinity at large frequencies where both the real and imaginary parts

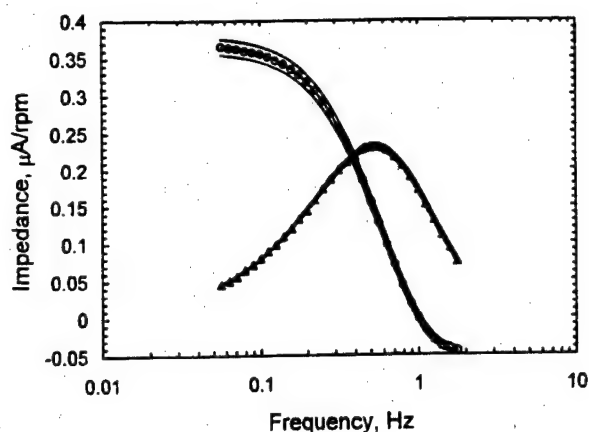


Fig. 2. Results of the regression of a measurement model containing two Voigt elements to both real and imaginary parts of the first of the data sets shown in Fig. 1. The circles represent the real part of the experimental data, the triangles represent the negative imaginary part of the experimental data, and the solid lines represent the corresponding model fit. The frequency range of the regression is that shown to be free of nonstationary bias errors.

of the impedance tend toward zero. The residual errors and confidence interval for the real part of the impedance also approach infinity at a frequency of 1 Hz, where the real part crosses the imaginary axis.

It is perhaps surprising that the impedance response of a Voigt circuit serves so well as a measurement model for

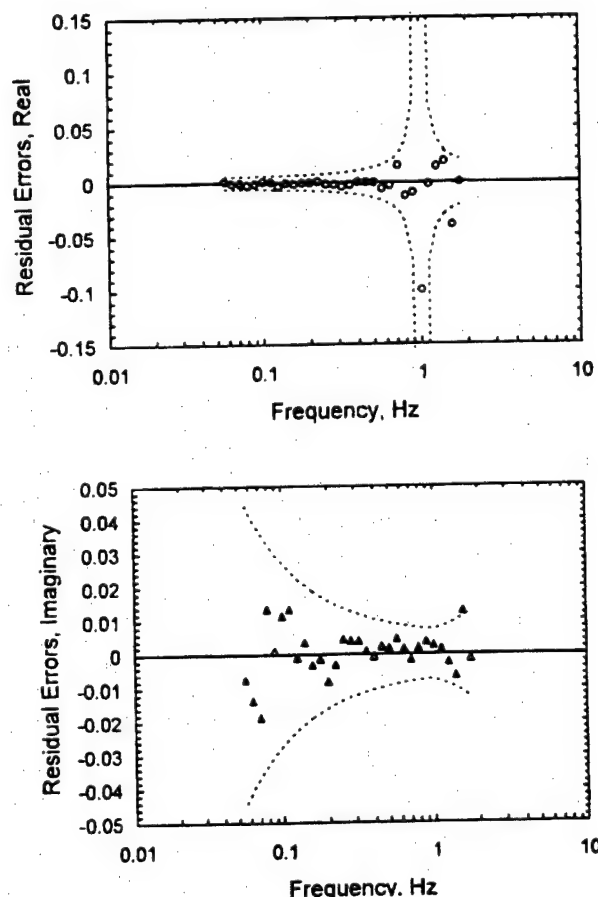


Fig. 3. The fractional residual errors for the fit presented in Fig. 2. The dashed line represents the 95.4% ( $2\sigma$ ) confidence interval (or noise level) for the measurement as determined by the measurement model approach. (a, top) real part; (b, bottom) imaginary part.

EHD when Eq. 1 is not dimensionally consistent with EHD data (if the parameters  $\Delta_k$  are given their usual meaning as a circuit-element resistance). This apparent inconsistency is easily resolved if the parameters  $\Delta_k$  are given units of EHD impedance and if it is understood that the principal constraint for selection of line shapes for a measurement model is that the line shape be consistent with the Kramers-Kronig relations. The measurement model is meant only to provide a statistically adequate fit to data and is not used here for direct interpretation of data in terms of physical processes.

**The error structure of EHD data.**—The stochastic components of the errors for the EHD data were determined using the procedure described in Ref. 4, 6, and 8, in which the measurement model served as a filter for the nonreproducibility of sequential impedance measurements. Such nonreproducibility is evident in Fig. 1 and is typical of electrochemical data. The results of the analysis for the data at 200 rpm with the analog filter disconnected are compared in Fig. 4 to the modulus and to the standard deviation of the repeated measurements. The open circles and triangles represent the real part and the imaginary part, respectively, of the standard deviation in which the lack of replicability was filtered by the measurement-model technique. The corresponding closed symbols represent the standard deviations of the repeated measurements. The line given in Fig. 4 is the fitted model for the error structure which is discussed in a subsequent section. The stochastic noise of the EHD measurements is clearly not proportional to the modulus of the impedance. The standard deviation of the real and imaginary parts of the noise are equal, a result that is consistent with observations made for EIS.<sup>4,6,8</sup> The results presented in Fig. 4 also suggest that the noise level becomes a significant fraction of the signal at higher frequencies, a characteristic that influences regression of models to EHD data. From the perspective of motivating the measurement model analysis of the error structure, perhaps the most compelling result shown in Fig. 4 is that the error structure obtained under the assumption that the repeated measurements are replicate (filled symbols) over-

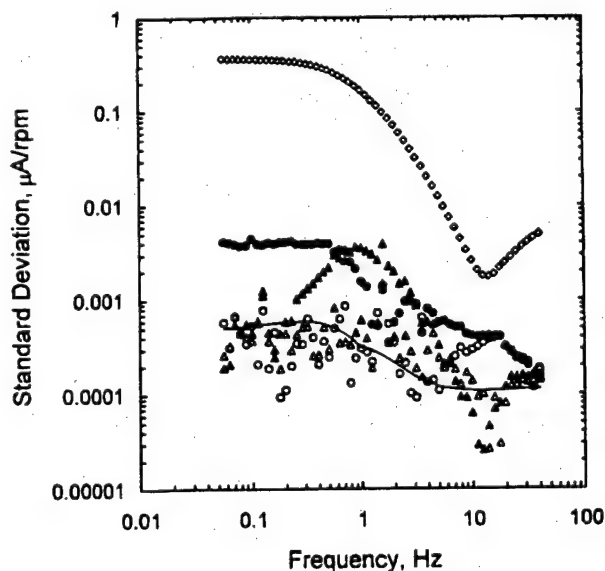


Fig. 4. The error structure identified for EHD measurements. The mean rotation rate was 200 rpm, and the analog filter was not employed. The open circles and triangles represent the real part and imaginary part of the standard deviation filtered by the measurement model. The closed circles and triangles represent the real part and imaginary part of the standard deviation calculated directly from repeated measurements. The diamonds represent the modulus. The solid line is the fitted model for the error structure (Eq. 3) with parameter values given in Table I.

Table I. Regressed values for the error structure of the electrohydrodynamic impedance measurements. Regression was weighted by a five point moving averaged value for the apparent variance of the standard deviation filtered using the measurement model. The data were detrended to ensure that the mean residual error was equal to zero.

Parameters	Std. dev. (percent)
$\alpha = 1.26 \pm 0.05 \times 10^{-3}$	3.8
$\beta = 9.4 \pm 0.3 \times 10^{-4}$	2.9
$\delta = 1.01 \pm 0.02 \times 10^{-4} \mu\text{A/rpm}$ ( $5.1 \pm 0.1 \times 10^{-4} \mu\text{A/cm}^2 \text{ rpm}$ )	1.9

predicts the standard deviation by as much as an order of magnitude, and that the standard deviations for the real and imaginary components are seen to be correlated but are not equal. This result has important consequences for the use of the standard deviation of repeated measurements to weight regression procedures, as was used, for example, in Ref. 23.

**Model for the error structure for EHD data.**—The generalized model previously developed for the stochastic noise of electrochemical impedance measurements was of the form

$$\sigma_r = \sigma_j = \alpha|Z_i| + \beta|Z_r| + \gamma \frac{|Z|^2}{R_m} \quad [2]$$

where  $\sigma_r$  and  $\sigma_j$  are the real and imaginary parts, respectively, of the standard deviation of the complex impedance  $Z$ ;  $R_m$  is the value of the current-measuring resistor; and  $\alpha$ ,  $\beta$ , and  $\gamma$  are dimensionless parameters which were found to be constants for a given instrumental system. A similar model was found for the stochastic contribution of the error structure for EHD data, *i.e.*

$$\sigma_r = \sigma_j = \alpha|Z_i| + \beta|Z_r| + \delta \quad [3]$$

where  $Z_i$  and  $Z_r$  are the imaginary and real parts of the EHD transfer function, respectively, and  $\alpha$ ,  $\beta$ , and  $\delta$  are parameters which were found by regression to the set of standard deviations obtained using the measurement model technique described in Ref. 8. The parameter values so determined are presented in Table I. These parameter values could be used, in accordance with Eq. 3, to describe the error structure for all rotation rates studied, for both

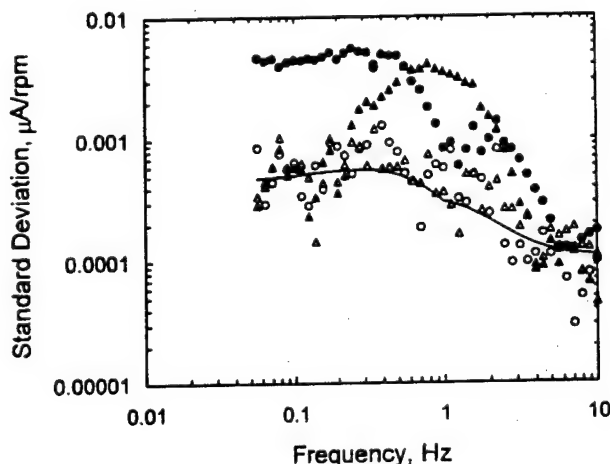


Fig. 5. The error structure identified for EHD measurements. The mean rotation rate was 200 rpm, and the analog filter was employed. The open circles and triangles represent the real part and imaginary part of the standard deviation filtered by the measurement model. The closed circles and triangles represent the real part and imaginary part of the standard deviation calculated directly from repeated measurements. The solid line is the fitted model for the error structure (Eq. 3) with parameter values given in Table I.

oxidation of ferrocyanide at +0.4 V(SCE) and reduction of ferricyanide at 0 V(SCE), and for the data collected with and without analog filtering. It is important to note that, while  $\alpha$  and  $\beta$  are dimensionless,  $\delta$  has units of EHD impedance, dimensioned as a charge and given here in units of  $\mu\text{A/rpm}$ .

The error structure obtained using the analog filter at 200 rpm is presented in Fig. 5. Similar results were obtained for the experiments conducted at 400 and 800 rpm with the analog filter disconnected and active, respectively. The solid line shown in Fig. 4 and 5 is the fitted model for the error structure developed in the next section with the same model parameters. It is evident that the use of the filter does not influence the error structure of the measurement. This result perhaps reflects the efficiency of the long (1% closure error) integration feature of the frequency-response analyzer as a filter for noise. This result also serves to emphasize the importance of the measurement model as an approach for assessing the noise level in the final output of the instrumentation. The matched analog filters were observed by oscilloscope to reduce significantly the noise level of the signals input into the frequency-response analyzer. The reduction of the stochastic noise in the input signal did not, in this case, result in a reduced noise level of the electrohydrodynamic impedance.

As the analog filter did not reduce the noise level of the measurement, it is worth asking whether matched input signal analog filters can be used to reduce the time required to collect impedance measurements. The time required per measurement is presented as a function of frequency in Fig. 6 for a rotation rate of 200 rpm. Similar results were obtained at 400 rpm. The error bars correspond to one standard deviation of 4 to 14 repeated measurements. The dashed lines correspond to the time required for integration of 3, 5, and 10 cycles, and the value associated with each line is given by the intercept of the dashed lines with the frequency axis. In making an impedance calculation, the frequency-response analyzer integrates over an integral number of cycles, with the smallest number of cycles being 3. At low frequencies, the time required per measurement corresponds to 3 to 5 cycles. At higher frequencies, where the signal-to-noise ratio is worse, more time is required to achieve the 1% closure error criterion of the long integration feature of the FRA. It is evident that, for this application, use of an analog filter does not reduce the time required per measurement, and, in fact, the time required per measurement was increased slightly. In one experiment, the filter was found to reduce the time required to collect data in the frequency range of 1 to 40 Hz at 800 rpm. This experiment was characterized by an input signal that was badly matched to the analog filter in that, while the signal was very weak, use of the times 10 filter gain caused clipping at low frequencies. The values for the  $Sc$  number obtained by regression to the resulting data were unreliable.

The role of input filters was irrelevant in the present case because the FRA used makes correlations with six significant digits. While the noise rejection properties of this FRA were found to be adequate for the signal-to-noise ratio of the measurements presented in this work, it should be noted that not all commercially available instruments have the same noise rejection properties and that the signal-to-noise ratio can be very small for some measurements. In situations where the signal-to-noise ratio is very poor, prefiltering of signals can be essential. In our laboratory, for example, EHD measurements for the same experimental system reported here but below the limiting current could not be obtained without use of the analog filters described in this work.

### Process Model for EHD

Electrohydrodynamic impedance experiments are performed by modulating the angular velocity  $\Omega$  of the rotating disk electrode with a fixed amplitude of perturbation  $\Delta\Omega$  around a mean angular velocity  $\Omega_0$ . The perturbation



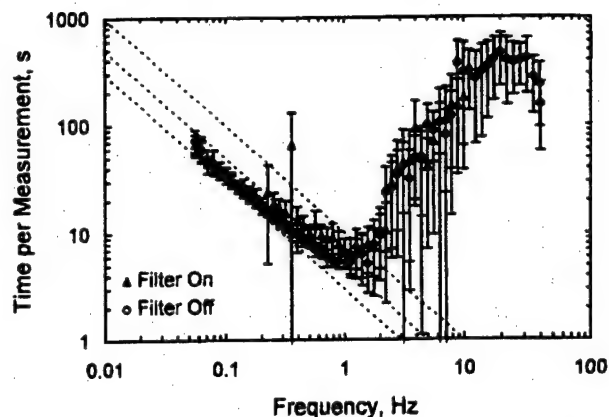


Fig. 6. A comparison of the time required per measurement at a mean rotation rate of 200 rpm when the input filter is employed ( $\Delta$ ) or disconnected ( $\circ$ ). The error bars represent  $\pm 1$  standard deviation for the successive experiments. The dashed lines represent (bottom to top) the time required per measurement for 3, 5, or 10 cycles.

frequency  $\omega$  is varied to obtain the widest possible range. The angular velocity can thus be written as

$$\Omega = \Omega_0 + \Delta\Omega \cos(\omega t) \quad [4]$$

The resulting current  $I$ , at fixed potential, can be expressed as

$$I = I_0 + \Delta I \cos(\omega t + \phi) \quad [5]$$

where  $I_0$  is the average current,  $\Delta I$  is the amplitude of the sinusoidal current response, and  $\phi$  is the phase shift. These equations can be introduced into the differential equations that describe the physics and chemistry of the system to calculate explicitly the transfer function for the system. Tribollet and Newman<sup>28</sup> have developed a theoretical transfer function for the system which can be written as

$$\frac{\bar{I}}{\Omega} = \frac{2A_0 z_p(u)}{\left\{ \frac{R_c}{Z_d(0)z_d(u)} + j\omega R_c C \left( \frac{R_t}{Z_d(0)z_d(u)} + 1 \right) + \frac{R_t}{Z_d(0)z_d(u)} + 1 \right\}} \quad [6]$$

where

$$u = Sc^{1/3} \frac{\omega}{\Omega_0}$$

$z_p(u)$  and  $z_d(u)$  are tabulated functions for the electrohydrodynamic impedance and the convective diffusion impedance, respectively, which include corrections for a finite Schmidt number.  $2A_0$  and  $Z_d(0)$  are the respective moduli for the impedance at zero frequency, and  $Sc$  is the Schmidt number. The terms  $R_t/Z_d(0)$  and  $R_c/Z_d(0)$  correspond to corrections for kinetic and ohmic resistance, respectively, normalized by the zero frequency limit for the convective Warburg impedance. The surface capacitance appears in the lumped parameter  $R_c C$ . The correction terms  $R_t/Z_d(0)$ ,  $R_c/Z_d(0)$ , and  $j\omega R_c C$  are generally considered to be negligible as compared to unity if the electrode kinetics are fast. Robertson *et al.*<sup>23</sup> for example, neglected these terms altogether in their regression. In this work, only one correction term [ $R_t/Z_d(0)$ ,  $R_c/Z_d(0)$ , or  $R_c C$ ] could be resolved for any given regression. The smallest residual errors were obtained when  $R_c C$  was retained. This result is consistent with the order-of-magnitude analysis of Tribollet and Newman<sup>28</sup> which suggested that  $R_c C$  should be the most important correction term to account for high frequency processes on the limiting current plateau. Thus, the process model for this system was given by

$$\frac{\bar{I}}{\Omega} = \frac{2A_0 z_p(u)}{j\omega R_c C + 1} \quad [7]$$

Equation 7 was regressed to the experimental data to obtain the values for  $A_0$ ,  $R_c C$ , and  $Sc$ .

### Regression of the Process Model to the Data

The issue of weighting is recognized as being critical to regression of models to impedance data,<sup>28-32</sup> but lack of information on the error structure has prevented weighting in accordance to the stochastic noise. While Robertson *et al.*<sup>23</sup> weighted their regressions by the experimentally measured variance of repeated measurements, modulus weighting has been generally used to regress the EHD model to data.<sup>28</sup> The use of modulus weighting implies that the stochastic noise is proportional to the modulus of the impedance, an assumption that is shown in Fig. 4 to be incorrect.

Inclusion of noisy high frequency data in regression under modulus and apparent variance weighting were reported as giving unrealistically large values for the Schmidt number.<sup>23</sup> The problem of high frequency noise has, therefore, been addressed by deleting high frequency points. Unfortunately, elimination of high frequency data from the regression leads to ambiguity in determination of the Schmidt number because the regressed frequency range is somewhat arbitrarily selected on the basis of the reasonableness of the resulting values.

To identify the influence of weighting strategy on the value of physical parameters obtained, regressions were made under modulus, apparent variance, and error structure weighting with frequency ranges that excluded different numbers of high frequency data. The analysis presented here is for the first spectrum taken at a rotation rate of 200 rpm with the analog filter disconnected. Very similar results were obtained for the other rotation rates and with the analog filter connected and disconnected.

The results of the regression of the process model under modulus weighting to the first data set collected at a mean rotation rate of 200 rpm with the analog filter disconnected are shown in Fig. 7 as a function of the maximum dimensionless frequency ( $p = \omega/\Omega_0$ ) included in the regression. The dashed line, included as a reference, is the value obtained under error-structure weighting for the frequency range determined to be free of nonstationary errors. The dimensionless frequency is used here to allow easy comparison to the maximum dimensionless frequency of 0.3 used in the regressions of Robertson *et al.*<sup>23</sup> The regressed frequency range was, therefore, 0.0168 (0.0561 Hz) to the value reported on the ordinate. The value obtained for all parameters depended on the number of data points included in the regression. The 95% confidence interval for the parameter estimate presented in Fig. 7 as upper and lower solid lines reflects large uncertainty in the estimate for  $Sc$  and large uncertainty in the estimate of  $A_0$  when dimensionless frequencies above 1 are included. The value of  $R_c C$  was even more uncertain. The confidence interval for this parameter included zero when the maximum dimensionless frequency was less than 0.5 (ten complex data points) or greater than 5 (50 data points). A similar ambiguity was seen when the variance calculated directly from the successive measurements was used to weight the regression.

Use of the measured error structure to weight the regression of models to the EHD measurements greatly reduced the ambiguity in the determination of the Schmidt number. The results are shown in Fig. 8. Examination of the results shows that the ambiguity in the estimation of  $Sc$  has been reduced except when too few points are used in the regression resulting in the loss of information. The confidence interval for the estimates is also seen to improve, although it increases slightly when all the high frequency data are included in the analysis.

The residual sum of squares for these regressions, normalized by the residual sum of squares for the measurement noise, is given in Fig. 9. The regression statistic

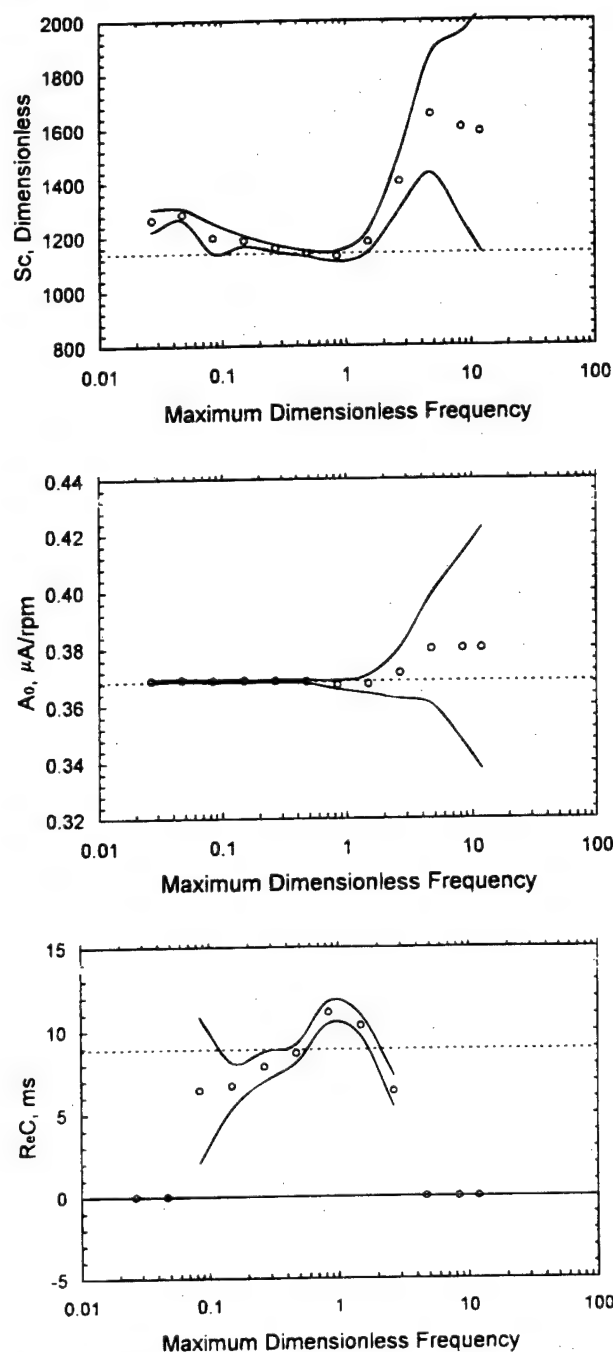


Fig. 7. Regressed values for the first data set collected at 200 rpm without analog filtering obtained under modulus weighting for process model parameters as a function of the upper value for the dimensionless frequency range. The solid lines represent the 95% confidence interval for the regressed parameter and the circles represent the regressed parameter value. The dashed lines represent the value reported in this work. (a, top) Schmidt number; (b, middle) the low-frequency asymptotic value for the modulus of the EHD impedance; and (c, bottom) the capacitive correction term (see Eq. 7).

seems to be roughly equivalent for the three weighting strategies except when frequencies above a dimensionless value of 1 are included in the regression. In all cases, the use of error structure weighting yielded the smallest value for the residual error.

The large normalized residual error seen when high frequency data were included could be attributed to an inadequacy of the process model or to the influence of nonstationary phenomena. A change in the electrode properties is

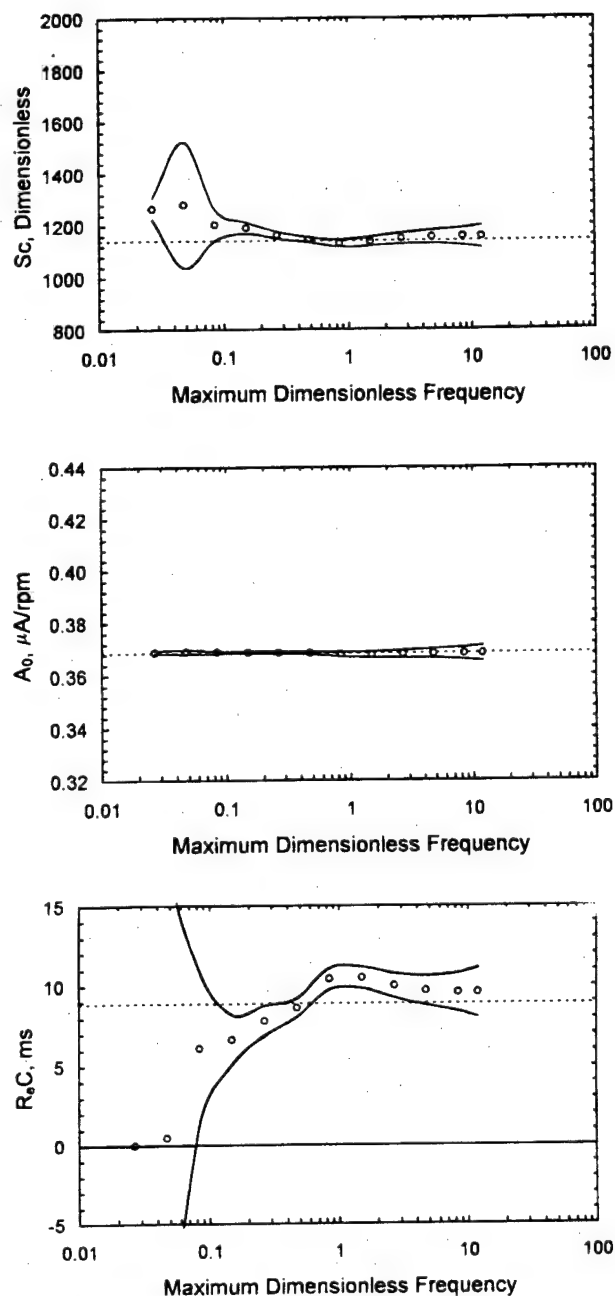


Fig. 8. Regressed values for the first data set collected at 200 rpm without analog filtering obtained under error structure weighting (see Eq. 3) for process model parameters as a function of the upper value for the dimensionless frequency range. The solid lines represent the 95% confidence interval for the regressed parameter, and the circles represent the regressed parameter value. The dashed lines represent the value reported in this work. (a, top) Schmidt number; (b, middle) the low-frequency asymptotic value for the modulus of the EHD impedance; and (c, bottom) the capacitive correction term (see Eq. 7).

suggested by the departure of the modulus and phase angle from ideal behavior at high frequency. This effect is reflected in a reduction of the low frequency asymptote in the impedance plane (see Fig. 1 and Ref. 33, 34).

To explore the role of nonstationarity, the methods of Ref. 3 and 9 were used to evaluate the consistency of the data with the Kramers-Kronig relations. This procedure is illustrated by the regression of a measurement model to the imaginary component of the first data set of Fig. 1 as presented in Fig. 10. Three line shapes were obtained from



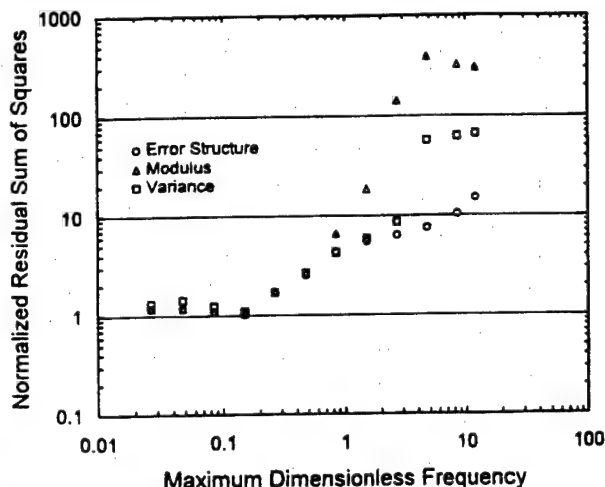


Fig. 9. The residual sum of squares normalized by the sum of squares of the standard deviation given by Eq. 3 for the fits obtained under modulus weighting (Fig. 7), apparent variance weighting, and error structure weighting (Fig. 8).

the regression, and the resulting residual errors fall within the  $2\sigma$  limits for the measurement errors (see Fig. 11). The model parameters were used to predict the real part of the measurement, and a Monte Carlo simulation was used to determine the  $2\sigma$  confidence interval of the model, shown as the upper and lower solid lines in Fig. 12. The comparison between the predicted real part of the impedance and the 95.4% confidence interval is seen more clearly in Fig. 13. The real part of the EHD impedance can be calculated from the imaginary at low frequencies, but at frequencies above 1.8 Hz ( $p = 0.54$ ), the residual errors fall outside the 95.4% confidence interval for the prediction. The data within the range of 0.0561 to 1.8 Hz are shown to be consistent with the Kramers-Kronig relations to within the 95.4% confidence interval of the measurement model, and data in the range 1.8 to 40 Hz are shown to be inconsistent and presumably influenced by nonstationary bias errors. Inconsistency due to nonstationary behavior is expected for high frequency data since the time required for the measurement increased greatly at high frequencies (see Fig. 6).

As shown in Fig. 14, the process model (Eq. 7) provided a good fit to the data over the consistent frequency range. Residual errors, presented in Fig. 15, fall within the error structure for the measurement. The results obtained under

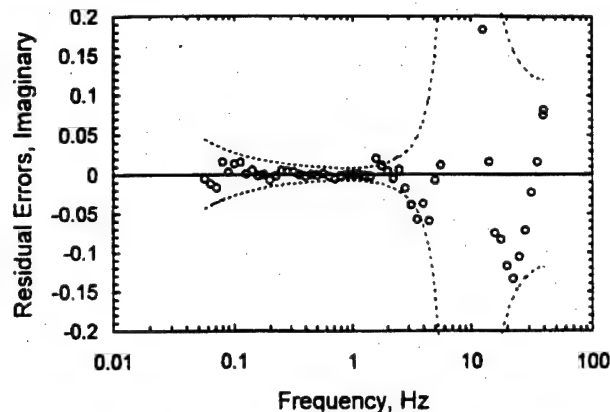


Fig. 11. The residual errors as a function of frequency for the regression shown in Fig. 10. The dashed lines represent the 95.4% ( $2\sigma$ ) value for the noise of the measurement.

error-structure weighting for frequency ranges found to be consistent with the Kramers-Kronig relations are presented in Table II. These results are in good agreement with published values for the Schmidt numbers.<sup>23</sup>

### Discussion

The topics covered in this section include the influence of weighting strategies on regression of impedance data, the interpretation of the resulting process model parameters, and the extent to which high frequency EHD data can be used.

**Influence of weighting strategies.**—This work should be viewed in the context of the careful study presented by Robertson *et al.*<sup>23</sup> In their work, replicate EHD measurements were obtained, and the squares of the residuals were weighted by the reciprocal of the variances of five successive measurements. The difference between the work presented by Robertson *et al.*<sup>23</sup> and this work is that, in this work, the measurement model was used as a filter for lack of replicacy in the assessment of stochastic measurement noise.

It has been demonstrated that the weighting used can have a significant effect on the information obtained by regression of a model to impedance data.<sup>4,29-32</sup> While weighting by the variance of the measurement is a preferred regression approach, the variance calculated directly from successive impedance measurements includes con-

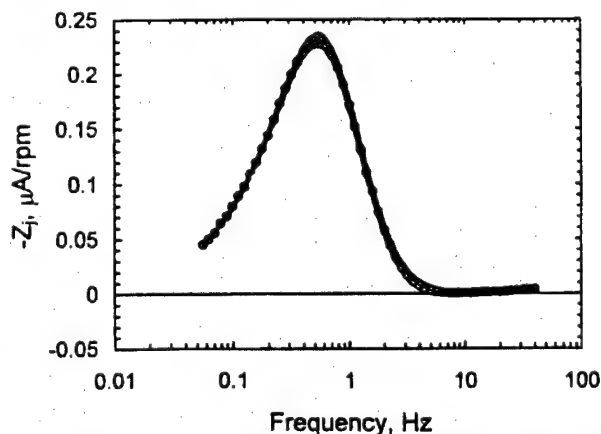


Fig. 10. The fit of a measurement model containing three Voigt elements to the imaginary part of the first spectrum obtained at 200 rpm without analog filtering. The upper and lower lines represent the 95.4% confidence interval for the model.

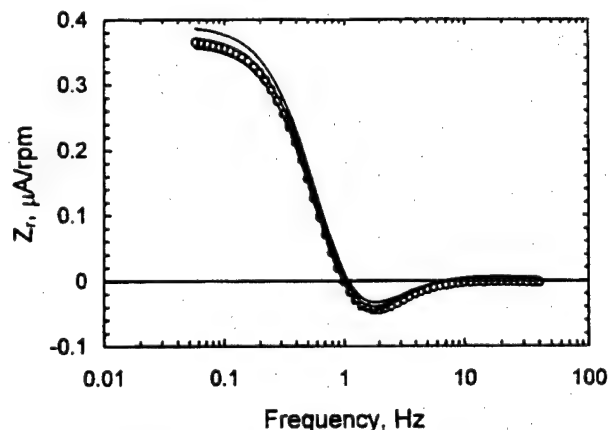


Fig. 12. The real part of the impedance obtained at 200 rpm without analog filtering. The center line is the value predicted by the measurement model fit to the imaginary part of the first spectrum. The upper and lower lines represent the 95.4% confidence interval for the model.

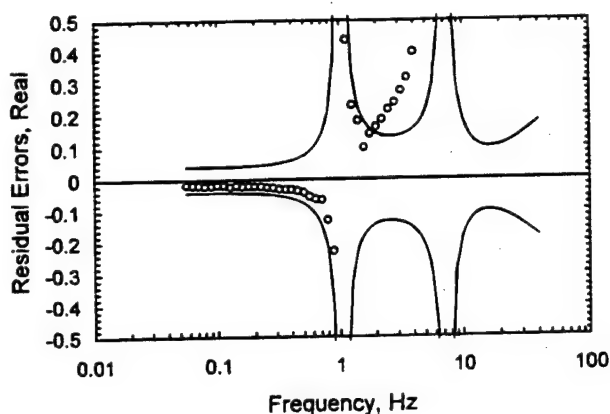


Fig. 13. The residual errors for the prediction shown in Fig. 12. The upper and lower lines represent the 95.4% confidence interval for the model.

tributions from lack of replicacy as well those associated with stochastic errors. The measurement model approach yielded bias-free estimates for the standard deviation of the impedance measurements, and regression using this as the error structure for weighting gave more unambiguous results for parameter estimates. The reason for the importance of weighting can be seen in Fig. 16, where different weighting strategies are compared to error structure weighting for the data collected at 400 rpm. As compared to use of the error structure for weighting, the no-weighting option under weights the data at low frequencies and over weights the high-frequency data. The discrepancy in weighting of high and low frequency data, however, is only one order of magnitude. In contrast, modulus weighting over weights the data at low frequency and under weights the data in regions where the modulus approaches zero (at roughly 2 Hz and at high frequency). The discrepancy in weighting of high and low frequency data can be many orders of magnitude. Because the variance calculated

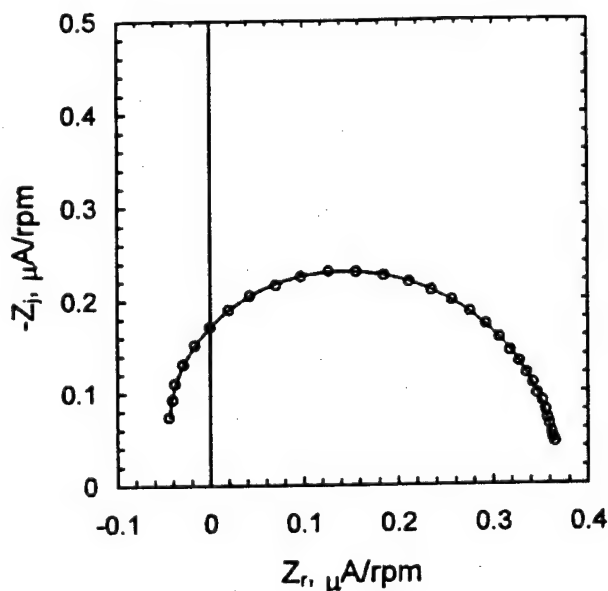


Fig. 14. Results of the regression of the process model to the first of the data sets shown in Fig. 1. The circles represent the experimental data, and the solid lines represent the corresponding model fit. The frequency range of the regression is that shown to be free of nonstationary bias errors.

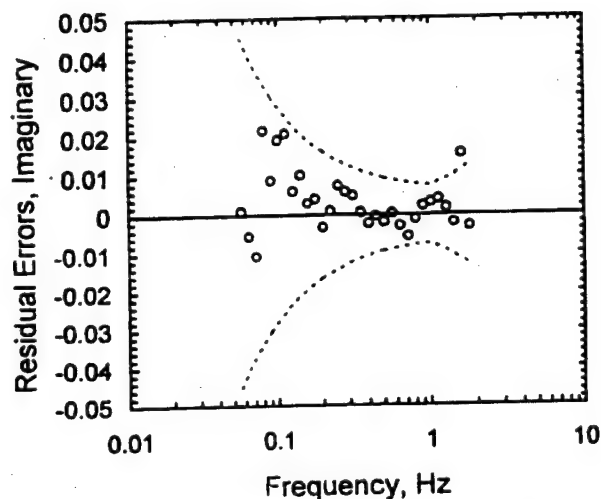
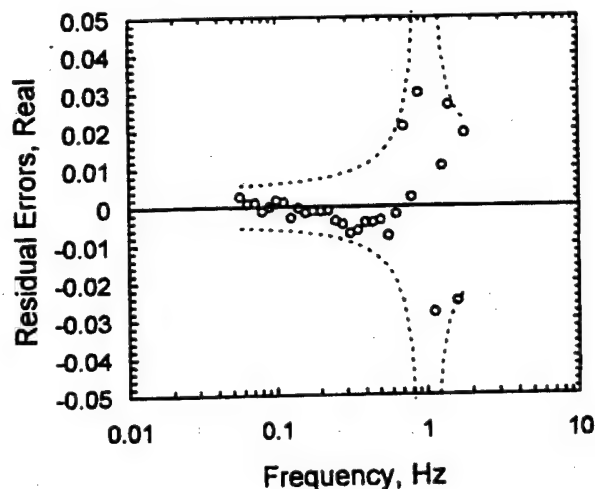


Fig. 15. The fractional residual errors for the fit presented in Fig. 14. The dashed line represents the 95.4% ( $2\sigma$ ) confidence interval (or noise level) for the measurement as determined by the measurement model approach: (a, top) real part; (b, bottom) imaginary part.

directly from repeated measurements does not yield equal standard deviations for the real and imaginary components of the impedance, the weighting by the apparent variance applies grossly different weights to the real and imaginary components. The high frequency data are underweighted for both real and imaginary components: the real impedance is underweighted at roughly 2 Hz, where the real impedance changes sign; and the imaginary impedance is underweighted at low frequency. Again, the discrepancy in weighting of high and low frequency data can be many orders of magnitude.

*Interpretation of process model parameters.*—The measurement model proved useful for identification of the influence of nonstationary behavior, but the large value obtained for the capacitive term and its dependence on rotation rate suggests that the process model may not account for all surface phenomena. The importance of surface processes on the determination of the Schmidt number is evident in that the Schmidt number obtained by regression to sequential measurements increased with time for every rotation rate studied and that the original values were recovered upon repolishing of the Pt electrode. The role of surface processes is also evident in that, in subsequent work, the method of surface preparation was found to influence the value of the mass-transfer-limited current density at a given rotation speed.

Table II. The model parameters obtained by regression to the first experiment after polishing of each series as compared to the values reported by Robertson *et al.*<sup>23</sup> The frequency range used in this work was that determined to be free of bias errors. The standard deviations reported are (\*) the standard deviation of the parameter estimate obtained by regression and (°) the standard deviation calculated from repeated measurements.

Rotation rate		This study (Filter off)	This study (Filter on)	Ref. 23 DC value	Ref. 23 EHD value
200 to 3200 rpm	Sc	—	—	1099.6 ± 4.0°	—
200 rpm	Sc	1141 ± 5°	1066 ± 5°	—	1109.3 ± 11.2°
	A <sub>0</sub>	0.3685 ± 0.0003	0.3510 ± 0.0004	—	—
	μA/rpm	—	—	—	—
	R <sub>c</sub> C, ms	8.9 ± 0.3	10.2 ± 0.2	—	—
	Frequency range	0.0561 to 1.774 Hz (0.0168 to 0.532)	0.0561 to 6.295 Hz (0.0168 to 1.89)	—	0.1 to 1 Hz (0.030 to 0.3)
400 rpm	Sc	1193 ± 4°	1153 ± 7°	—	1169.0 ± 34.6°
	A <sub>0</sub>	0.2645 ± 0.0001	0.2477 ± 0.0003	—	—
	μA/rpm	—	—	—	—
	R <sub>c</sub> C, ms	2.36 ± 0.09	3.07 ± 0.14	—	—
	Frequency range	0.0561 to 3.155 Hz (0.00842 to 0.473)	0.0561 to 20.0 Hz (0.00842 to 3.0)	—	0.1 to 2 Hz (0.015 to 0.3)
800 rpm	Sc	1222 ± 6°	—	—	1165.3 ± 54.0°
	A <sub>0</sub>	0.1842 ± 0.0001	—	—	—
	μA/rpm	—	—	—	—
	R <sub>c</sub> C, ms	1.15 ± 0.05	—	—	—
	Frequency range	0.0561 to 17.74 Hz (0.00421 to 1.33)	—	—	0.1 to 4 Hz (0.008 to 0.3)
Mean	Sc	1185 ± 41°	1110 ± 61°	—	1155.1 ± 43.2°

The regressed parameters are presented in Fig. 17 for the data collected at a mean rotation rate of 200 rpm without analog filtering. Figure 17 represents a change in process model parameters over a period of roughly 6 h. Because the measurements model was used to check consistency with the Kramers-Kronig relations, the portion of each spectrum used for the regression could be considered to be a pseudo-stationary realization of a slowly evolving process. As  $A_0$  is proportional to the limiting current, the change in  $A_0$  represents a 3% decrease in the limiting current over a period of 6 h. Similar results were seen in separate dc measurements. A similar nonstationary behavior was reported in Ref. 21 and 22 and attributed to rotator fatigue. The stability of the rotator used in the present work was checked by superimposing a 20% peak-to-peak speed modulation at a frequency of 20 Hz on a 1000 rpm mean speed for a period of 24 h. The phase shift was at all times lower than 0.07°, and the variation of the amplitude was less than 0.4%. The linearity of the response was checked by measuring the first harmonic, which was

found to be smaller than 0.15% of the fundamental signal. Thus, rotator fatigue can be rejected as a cause for the observed reduction in mass-transfer-limited current.

The high frequency behavior of the modulus and phase angle shown in Fig. 1 are suggestive of partial blocking (see Fig. 6 in Ref. 33). Such partial blocking has in fact been reported previously for Pt electrodes.<sup>35</sup> The decrease in  $A_0$  with measurement number and the corresponding increase in the Schmidt number are also consistent with gradual and partial blockage of the electrode surface. Partial surface blockage was not introduced in the process model used here. Blocking was addressed by a numerical approach by Caprani *et al.*,<sup>33</sup> and an analytic approach was proposed by Silva *et al.*<sup>34</sup> for highly blocked interfaces.

It can be noted that inclusion of the corrective capacitive term in Eq. 7 results in a high frequency limiting phase angle of 270° instead of 180°. However, typical values of  $R_cC$  would provide this behavior at frequencies much higher than reported in this study (about two orders of magnitude). Such an effect was observed, for instance, in systems of low conductivity where  $R_cC$  becomes large.<sup>36</sup> Comparison to the work of Caprani *et al.*<sup>33</sup> suggests that the blocking effect leads, for low and midrange frequencies, to a slight increase of the phase shift in the same way as is caused by the  $R_cC$  term. This argument could account for the unexpectedly large values for  $R_cC$  (about ten times) found in the present work.

The suggestion that  $R_cC$  is accounting for a blocking effect is supported by the analytic model Vidal and West<sup>22</sup> have presented recently for the influence of surface coverage by adsorbed species on EHD impedance. The structural form of their model (see, for example, Eq. 19 in Ref. 22) is quite similar to Eq. 7. In comparing Eq. 7 to their model,  $R_cC$  would be replaced by a constant that is a function of polarization resistance, ohmic resistance, and fractional surface coverage. A second correction term, scaled by  $1/Z_d(\omega)$ , would presumably play a significant role at high frequencies.

The Schmidt number was found to be very sensitive to inclusion of the high frequency correction term  $R_cC$ , even when the frequencies above  $p = 0.3$  were not included in the regression. As seen in Fig. 17, the value of the Schmidt number was higher when  $R_cC$  was not included in the model, and the corresponding confidence interval was larger. Neglect of the capacitive correction term influenced the value of the Schmidt number, even when high frequency data were neglected in the regression and even at the low rotation rate of 200 rpm for which the influence of the correction term should be lowest.

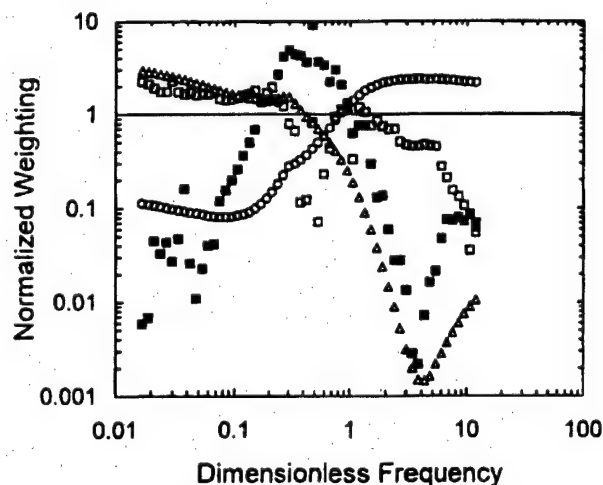


Fig. 16. A comparison of weighting strategies to the error structure weighting corresponding to Eq. 3. The strategies are normalized in this figure to provide an average weighting of one over the measured frequency range. The weighting strategies correspond to that used to obtain Fig. 8-10. Open circles correspond to use of no weighting; open triangles correspond to modulus weighting; and squares correspond to weighting by the (unfiltered) standard deviation of repeated measurements (open symbols are for the real part and closed symbols for the imaginary part).

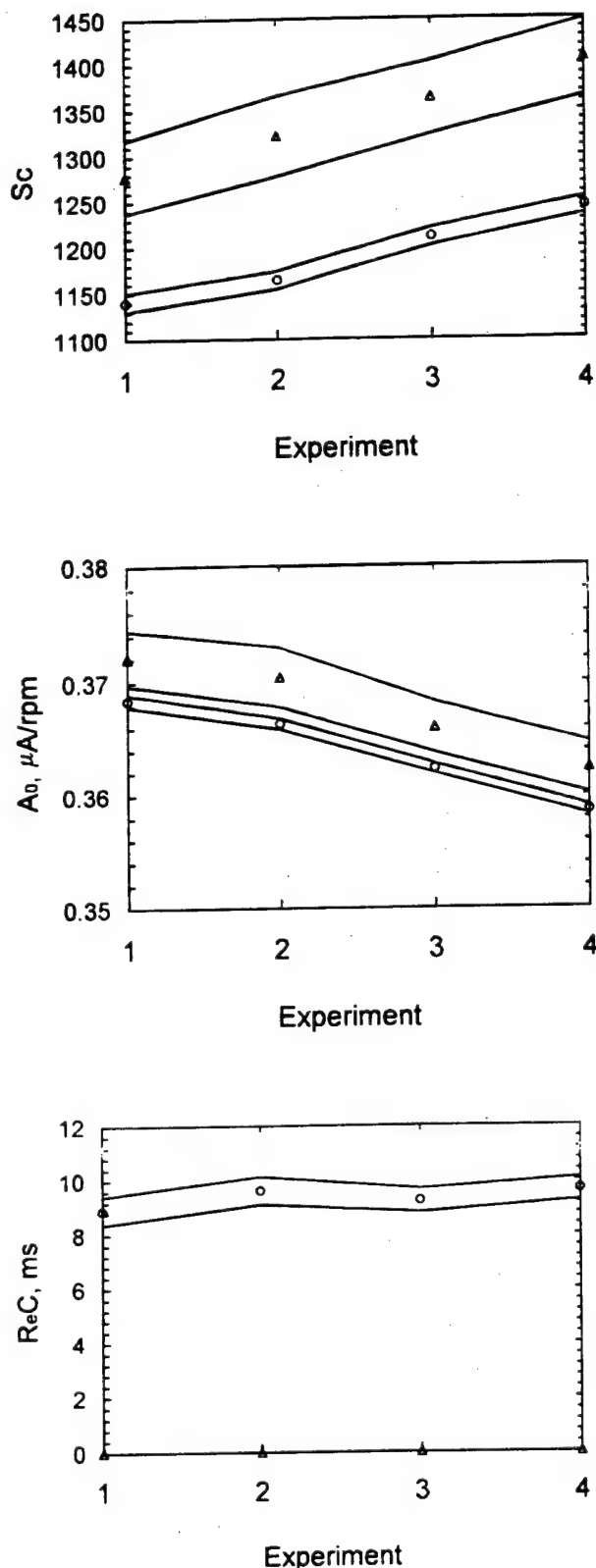


Fig. 17. Regressed values for data collected at 200 rpm without analog filtering under error structure weighting (see Eq. 3) for process model parameters as a function of the numerical order of the repeated measurements. Circles represent results obtained when the capacitive correction term was included, and triangles represent values obtained when the capacitive term was not included in the model. The lines represent the 95% confidence interval for the regressed parameter, and the circles represent the regressed parameter value. (a, top) Schmidt number; (b, middle) the low-frequency asymptotic value for the modulus of the EHD impedance; and (c, bottom) the capacitive correction term (see Eq. 7).

**The meaning of high frequency EHD data.**—The meaning of high frequency EHD data can be addressed from a qualitative and quantitative perspective. The first step in assessing the meaning would be to identify the portion of the spectrum that is free from experimental bias errors that yield inconsistencies with the Kramers-Kronig relations. The qualitative features of high frequency data can be used to suggest the presence of surface phenomena, such as the blocking effect that is apparent in Fig. 1. The quantitative analysis requires that a process model which includes the surface phenomena be regressed to the bias-free data under a suitable weighting strategy.

**Determination of Schmidt number.**—The Schmidt number is, of course, a property of the fluid and is therefore independent of surface processes. The time evolution of the apparent Schmidt number shown in Fig. 17 and attributed to the evolution of blocking phenomena shows that surface phenomena, evident in the high frequency range, can influence the apparent value of the Schmidt number if an incorrect model is used to extract the parameter. An incorrect value for the Schmidt number can be obtained even if the high frequency data are rejected.

It is common practice to reject high frequency EHD data. For example, Robertson *et al.*<sup>23</sup> noted that inclusion of data above  $p = 0.3$  (1 Hz at 200 rpm) in regressions caused the resulting value of the Schmidt number to be too high. Thus, all data above this value were dropped in the regression. Similar results were obtained by Tribollet and Newman.<sup>28</sup> The rejection of high frequency data in the above work was based, not on a quantitative evaluation of experimental bias errors, but on observation that when the high frequency data were included the regressed values were physically unreasonable.

The measurement model analysis presented here for assessing stochastic and bias errors has the advantage that a quantifiable criterion can be applied for rejection of high frequency data and that a robust weighting strategy can be used to extract physical parameters. While all weighting strategies gave roughly equivalent values for the Schmidt number when the data above  $p = 0.3$  were eliminated from the regression, the measurement model analysis indicated that the reliable (bias-free) frequency range extended in every case to frequencies above  $p = 0.3$  (see Table II).

For example, the reliable frequency range for a measurement made at 400 rpm with use of the analog filter extended to  $p = 3.0$  (20 Hz), one order of magnitude larger than the limit of 0.3 proposed in Ref. 23. As shown in Fig. 18, the value for the Schmidt number determined by regression to the entire bias-free data set was found through use of error-structure weighting to be 1152; whereas, use of modulus weighting gave a value of 1316. If data above  $p = 0.422$  were ignored, both approaches gave similar values (1162 for error structure weighting as compared to 1156 for modulus weighting).

While this work does not invalidate previous work in which other regression strategies were employed over a truncated frequency range, this work does show that high frequency data can be incorporated into the regression if a weighting strategy based on the error structure of the measurement is used. It is also clear that the ability to assess the extent to which bias errors influence impedance measurements extends the useful frequency range for EHD measurements and should enhance the application of EHD for assessing surface phenomena. The results of the fit of Eq. 7 under error structure weighting to the full frequency range for 400 rpm (filtered) are presented in Fig. 19. Equation 7 provides a good fit to the data except at frequencies above 10 Hz ( $p = 1.5$ ), in which a discrepancy is seen in the phase angle. As the phase angle values show a systematic (not random) trend, this discrepancy cannot be attributed to noise. As the measurement model approach demonstrated that the EHD data were consistent with the Kramers-Kronig relations over the entire frequency range, this discrepancy also cannot be attributed

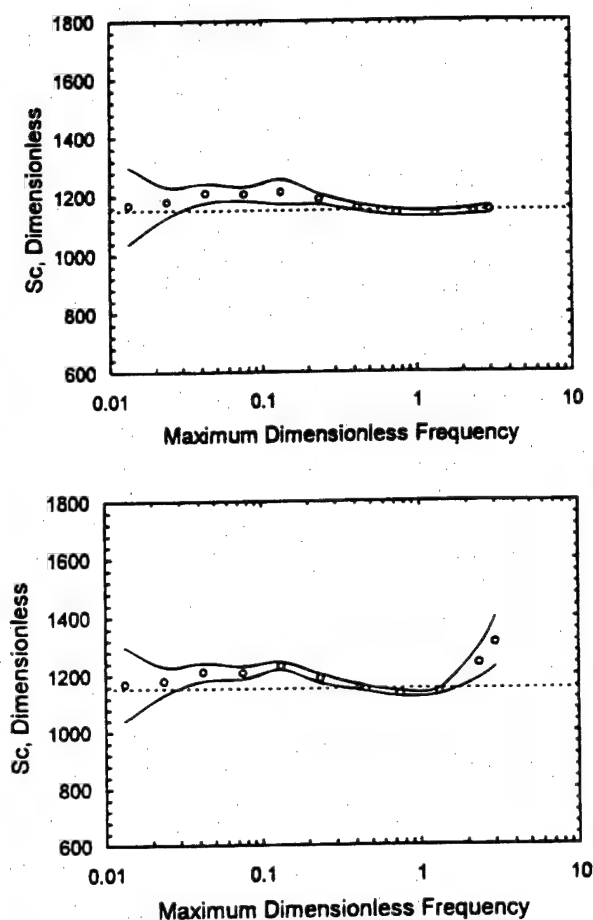


Fig. 18. Regressed values of Schmidt number for the first data set collected at 400 rpm with analog filtering as a function of the upper value for the dimensionless frequency range: (a, top) obtained under error structure weighting (see Eq. 3); (b, bottom) obtained under modulus weighting. The solid lines represent the 95% confidence interval for the regressed parameter, and the circles represent the regressed parameter value. The dashed lines represent the value reported in Table II.

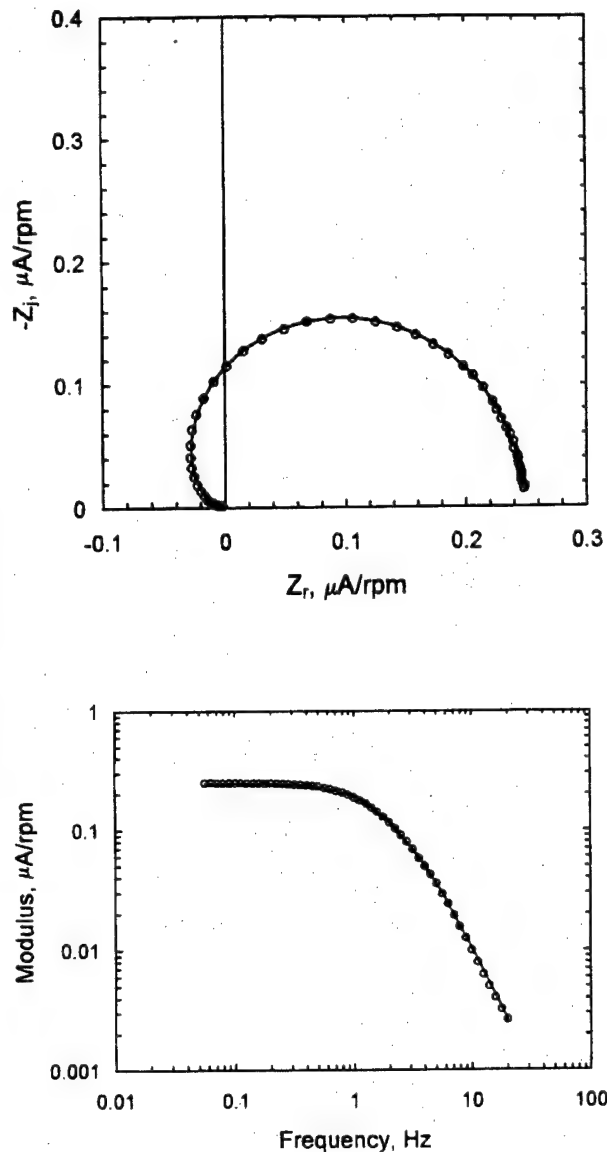


Fig. 19. (a-c) Results of the regression of the process model to the first data set collected at 400 rpm with analog filtering. The circles represent the experimental data, and the solid lines represent the corresponding model fit. The dashed lines evident in Fig. 19c (bottom) represent the 95% confidence interval for the model fit. The frequency range used was that shown to be free of nonstationary bias errors.

to nonstationary effects. Thus, the discrepancy should be addressed by further improvement of the process model, as described in the previous section.

**Quantification of surface phenomena.**—In addition to its use in evaluating Schmidt numbers, EHD measurements have been used to characterize blocking<sup>27,33,34</sup> and adsorption phenomena<sup>16,21,22</sup> at electrode surfaces and the influence of porous layers.<sup>16,17,20</sup> In the above referenced work, the experimental frequency ranges used for regression were constrained on the basis of experimental noise and perceived bias errors but without direct quantification of the error structure. As shown in the present work, unnecessary rejection of high frequency data should be avoided because the high frequency data may contain information concerning important physical processes. This caution is particularly important when information on surface processes is sought.

The absence of a quantitative assessment of the stochastic component of the error structure also compromised the regression procedure used. Although the authors often reported an excellent fit to their data, this statement must be considered to be qualitative in the absence of comparison of residual errors to measured noise levels. In the absence of a comparison of residual errors to the noise level of the measurements, there can be no indication as to



whether the data contain more information which could be obtained by refining the model.

It should be emphasized that the quantitative statistical analysis described in the present paper is used in other fields (see, e.g., Ref. 37) but is lacking in the current practice in electrochemical impedance spectroscopy. Experimental studies which employ a sophisticated experimental and modeling strategy can be compromised by the absence of quantitative statistical information. The present work provides the statistical framework needed for a quantitative assessment of the error structure of impedance data.

### Conclusions

The development and application of mathematical models for the interpretation of electrochemical impedance data requires both physical insight and a quantitative assessment of the fundamental characteristics of the measurement. The examples presented here illustrate that synergistic implementation of experiment, measurement model, and process model can enhance the information content of impedance spectra in terms of physically meaningful parameters. The measurement model provides a means of characterizing the measurement characteristics for electrohydrodynamic impedance spectroscopy as well as electrochemical impedance spectroscopy. Regression employing weighting by the stochastic component of the error structure yielded unambiguous values for physical properties such as the Schmidt number, whereas significant ambiguity was observed using modulus or proportional weighting. Through use of the measurement model, the influence of nonstationary processes on the data could be distinguished from the influence of surface blocking. The influence of surface phenomena on mass transport could be observed clearly under the use of error structure weighting.

The measurement model provided a quantitative means for assessing the utility of filtering the input to the frequency response analyzer. The noise level in the measured impedance was found to be unaffected by use of analog filters, and, surprisingly, the time required to collect the data was increased slightly by using the filters. The estimated parameter values and their standard deviations were comparable whether or not filtering was used.

Finally, this work suggests that the measurement model concept is generally applicable to impedance measurements and should, therefore, be useful for other transfer function measurements.

### Acknowledgment

The work performed at the University of Florida (P.A. and M.E.O.) was supported by the Office of Naval Research and by Gates Energy Products. This work was also supported in part by the National Science Foundation under a U.S.-France Cooperative Research Grant INT-9416713. Pankaj Agarwal acknowledges the 1993 F. M. Beckett Memorial Award of The Electrochemical Society, which supported preliminary phases of this work.

Manuscript submitted May 26, 1995; revised manuscript received Oct. 31, 1995.

The University of Florida assisted in meeting the publication costs of this article.

### REFERENCES

1. P. Agarwal, M. E. Orazem, and L. H. Garcia-Rubio, *This Journal*, **139**, 1917 (1992).
2. P. Agarwal, O. C. Moghissi, M. E. Orazem, and L. H. Garcia-Rubio, *Corrosion*, **49**, 278 (1993).
3. P. Agarwal, M. E. Orazem, and L. H. Garcia-Rubio, in *Electrochemical Impedance: Analysis and Interpretation*, ASTM STP 1188, J. Scully, D. Silverman, and M. Kendig, Editors, pp. 115-139, American Society for Testing and Materials, Philadelphia, PA (1993).
4. M. E. Orazem, P. Agarwal, A. N. Jansen, P. T. Wojcik, and L. H. Garcia-Rubio, *Electrochim. Acta*, **38**, 1903 (1993).
5. M. E. Orazem, P. Agarwal, and L. H. Garcia-Rubio, *J. Electroanal. Chem.*, **378**, 51 (1994).
6. P. Agarwal, Ph.D. Thesis, University of Florida, Gainesville, FL (1994).
7. P. Agarwal, M. E. Orazem, and L. H. Garcia-Rubio, *Electrochim. Acta*, In press.
8. P. Agarwal, M. E. Orazem, O. Crisalle, and L. H. Garcia-Rubio, *This Journal*, **142**, 4149 (1995).
9. P. Agarwal, M. E. Orazem, O. Crisalle, and L. H. Garcia-Rubio, *ibid.*, **142**, 4159 (1995).
10. C. Gabrielli, M. Keddam, and H. Takenouti, *Electrochim. Acta*, **35**, 1553 (1990).
11. C. Gabrielli and B. Tribollet, *This Journal*, **141**, 1147 (1994).
12. B. Miller, M. I. Bellavance, and S. Bruckenstein, *J. Anal. Chem.*, **44**, 1983 (1972).
13. S. Bruckenstein, M. I. Bellavance, and B. Miller, *This Journal*, **120**, 1351 (1973).
14. B. Miller and S. Bruckenstein, *ibid.*, **121**, 1558 (1974).
15. C. Deslouis and B. Tribollet, *Electrochim. Acta*, **35**, 1637 (1990).
16. C. Deslouis and B. Tribollet, in *Advances in Electrochemical Science and Engineering*, H. Gerischer and C. W. Tobias, Editors, p. 205, VCH, New York (1991).
17. A. C. West, R. D. Grimm, D. Landolt, C. Deslouis, and B. Tribollet, *J. Electroanal. Chem.*, **330**, 693 (1992).
18. C. Deslouis, *Soviet Electrochem.*, **29**, 24 (1993).
19. C. Deslouis and B. Tribollet, *ibid.*, **29**, 75 (1993).
20. O. E. Barcia, O. R. Mattos, N. Pebere, and B. Tribollet, *This Journal*, **140**, 2825 (1993).
21. R. C. Vidal and A. C. West, *ibid.*, **142**, 2689 (1995).
22. R. C. Vidal and A. C. West, *ibid.*, **142**, 2683 (1995).
23. B. Robertson, B. Tribollet, and C. Deslouis, *ibid.*, **135**, 2279 (1988).
24. C. Deslouis, I. Epelboin, M. Keddam, and J. C. Lestrade, *J. Electroanal. Chem.*, **28**, 57 (1970).
25. C. Deslouis and B. Tribollet, Paper B2-9 presented at the 35th Meeting of the International Society of Electrochemistry, Berkeley, CA, Aug. 5-10, 1984.
26. P. Appel and J. Newman, *This Journal*, **124**, 1864 (1977).
27. C. Deslouis, G. Maurin, N. Pebere, and B. Tribollet, *J. Appl. Electrochem.*, **18**, 745 (1988).
28. B. Tribollet and J. Newman, *This Journal*, **130**, 2016 (1983).
29. P. Zoltowski, *J. Electroanal. Chem. Interfac. Sci.*, **178**, 11 (1984).
30. B. A. Boukamp, *Solid State Ion.*, **20**, 31 (1986).
31. J. R. Macdonald, *Electrochim. Acta*, **35**, 1483 (1990).
32. P. Zoltowski, *J. Electroanal. Chem.*, **375**, 45 (1994).
33. A. Caprani, C. Deslouis, S. Robin, and B. Tribollet, *ibid.*, **238**, 67 (1987).
34. C. R. S. Silva, O. E. Barcia, O. R. Mattos, and C. Deslouis, *ibid.*, **365**, 133 (1993).
35. Yu. M. Povarov and P. Lukovtsev, *Electrochim. Acta*, **18**, 13 (1973).
36. C. Deslouis, O. Gil, B. Tribollet, G. Vlachos, and B. Robertson, *J. Appl. Electrochem.*, **22**, 835 (1992).
37. A. Jutan and L. H. Garcia-Rubio, *Process Control Quality*, **4**, 235 (1993).



Reprinted from JOURNAL OF THE ELECTROCHEMICAL SOCIETY  
Vol. 143, No. 12, December 1996  
Printed in U.S.A.  
Copyright 1996

# The Error Structure of Impedance Spectra for Systems with a Large Ohmic Resistance with Respect to the Polarization Impedance

Mark E. Orazem\*

Department of Chemical Engineering, University of Florida, Gainesville, Florida 32611, USA

Touriya El Moustafid, Claude Deslouis,\* and Bernard Tribollet\*

UPR 15 du CNRS, Laboratoire "Physique des Liquides et Electrochimie," Université Pierre et Marie Curie, 75252 Paris Cedex 05, France

## ABSTRACT

Electrochemical impedance spectra were obtained for polyaniline membranes in weak and strong acid electrolytes. The measurement model approach for error analysis was used to show that the standard deviation of the real and imaginary parts of the impedance were equal, even for systems containing a large solution resistance with respect to the polarization impedance. These results were confirmed using analogue RC circuits that did not require use of the measurement model approach. A model for the error structure is proposed that is in agreement with data obtained for large and small values of the solution resistance.

## Background

Interpretation of impedance spectra in terms of physical properties and processes is usually accomplished by regressing deterministic models to experimental data. While it is generally recognized that the weighting used for a regression can have a great influence on the regression results,<sup>1-5</sup> selection of a proper regression strategy is particularly important for interpretation of impedance spectra because the value of the impedance can vary by many orders of magnitude over an experimental frequency range. The importance of the weighting used for regression of impedance data has been recognized,<sup>6-15</sup> but, until recently, lack of experimental assessment of the error structure prevented weighting in accordance with the stochastic noise.

The discussion of error structures in impedance spectroscopy had, therefore, been limited to *a priori* predictions of measurement noise based on instrument noise<sup>16</sup> and to standard assumptions concerning the error structure such as constant or proportional errors.<sup>6-8</sup>

Macdonald,<sup>5,11,12</sup> Boukamp,<sup>7</sup> Zoltowski,<sup>6,9,10</sup> Orazem *et al.*,<sup>13,14</sup> and Agarwal *et al.*<sup>15,17-19</sup> have discussed the importance of selecting a proper weighting strategy for regression of models to electrochemical impedance data. A weighted least squares strategy that includes the errors in the real and imaginary parts of the impedance is given by minimization of

$$J = \sum_k \frac{Z_{r,k} - \hat{Z}_{r,k}}{\sigma_{r,k}^2} + \sum_k \frac{(Z_{j,k} - \hat{Z}_{j,k})^2}{\sigma_{j,k}^2}$$

\* Electrochemical Society Active Member.



where  $Z_{r,k}$  and  $Z_{i,k}$  represent the real and imaginary parts of the data, respectively, the caret signifies the corresponding model value, and  $\sigma_{r,k}$  and  $\sigma_{i,k}$  are the standard deviations of the real and imaginary parts of the impedance, respectively. The use of the variance to weight data ensures that data points with "low noise" content are emphasized and the data points with "high noise" content are de-emphasized. While there is general agreement that the weighting strategy should take into account the variance of the impedance, there is disagreement of the structure that this error should take. Macdonald<sup>8,11,12</sup> has been the leading advocate for use of modified proportional weighting on the basis that the stochastic noise in complex impedance measurements is likely to be proportional to the respective component of the measurement. Boukamp<sup>7</sup> supported use of modulus weighting in regression of impedance data. Use of modulus weighting implies that the real and imaginary components for the impedance measurement have the same level of stochastic noise. To support use of modulus weighting, Zoltowski performed repeated impedance measurements for a series of electrical circuits.<sup>6</sup> The calculated standard deviation of the real and imaginary parts of the impedance were found to be correlated, but not equal. Zoltowski's results, therefore, did not provide conclusive support for use of modulus weighting.

The manner in which errors propagate through the Kramers-Kronig relations suggests that it may be reasonable to assume that the real and imaginary components for the impedance measurement have the same level of stochastic noise. Macdonald presented the results of a Monte Carlo analysis with synthetic data that showed that the standard deviation of the impedance component predicted by the Kramers-Kronig relations was equal to that of the input component.<sup>20</sup> Because the Kramers-Kronig transformation of errors in synthetic data does not account for uncertainties and errors associated with measurement instrumentation, such as a potentiostat or frequency response analyzer, the result of Macdonald was considered to be a property of the Kramers-Kronig relations rather than one of experimental data. The regressions presented by Macdonald in this and subsequent papers continued to employ a modified proportional weighting strategy.<sup>20-22</sup>

The controversy over the form taken by the stochastic errors in impedance spectra should, in principle, be resolvable on experimental grounds. For example, the error structure for most radiation-based spectroscopic measurements such as absorption spectroscopy and light scattering can be readily identified.<sup>4,5</sup> The error analysis approach has been successful for some optical spectroscopy techniques because these systems lend themselves to replication and, therefore, to the independent identification of the different errors that contribute to the total variance of the measurements. In contrast, the stochastic contribution to the error structure of electrochemical impedance spectroscopy measurements cannot generally be obtained from the standard deviation of repeated measurements because even a mild nonstationary behavior introduces a nonnegligible time-varying bias contribution to the error.<sup>19</sup> Attempts to weight regressions by standard deviations determined from repeated impedance scans have not been very successful because the standard deviation obtained in this way includes both experimental bias and stochastic contributions to the error structure.<sup>23</sup>

A distinction is drawn in the present work between stochastic errors which are randomly distributed about a mean value of zero, errors caused by the lack of fit of a model, and experimental bias errors that are propagated through the model. The problem of interpretation of impedance data is therefore defined to be one of identification of experimental errors, which includes assessment of consistency with the Kramers-Kronig relations, and fitting, which entails model identification, selection of weighting strategies, and examination of residuals. The error analysis provides information that can be incorporated into regression of process models. The experimental bias errors, as referred to here, may be caused by a chang-

ing base line or by instrumental artifacts. The emphasis of the present work is on identification of stochastic experimental errors.

The measurement model approach, widely used for identification of error structures of spectroscopic measurements,<sup>4,5,24</sup> was recently used to filter experimental bias errors from estimates of the standard deviation of electrochemical impedance measurements.<sup>13,15,17-19,25</sup> In this work, the standard deviation of the real part of the impedance response was found to be equal to that of the imaginary part. Although this result was observed for a wide variety of experimental systems, the systems studied shared the common characteristic of a solution resistance that was small in comparison to the asymptotic value of the real impedance at low frequency.

The regression procedure described by Orazem *et al.*,<sup>13,14</sup> and Agarwal *et al.*<sup>15,17-19</sup> represents a weighted least squares strategy where the weighting is derived from an independent assessment of the error structure. Their approach is significantly different from the standard weighted least squares approach where modulus, proportional, or constant weighting is used because it does not rely on standard assumptions of error structures. The common weighting strategies can be described in the context of the error structure implied by the assumptions used.

Macdonald<sup>8</sup> has suggested that, when the components of the impedance are very different in magnitude, the variance of the impedance measurement should take the form

$$\begin{aligned} \sigma_r &= \sigma_r^2 = \alpha_r^2 + \beta_r^2 |\hat{Z}_r|^{2\xi_0} \\ \sigma_i &= \sigma_i^2 = \alpha_i^2 + \beta_i^2 |\hat{Z}_i|^{2\xi_0} \end{aligned} \quad [1a]$$

or, in terms of the standard deviation

$$\begin{aligned} \sigma_r &= \sqrt{\alpha_r^2 + \beta_r^2 |\hat{Z}_r|^{2\xi_0}} \\ \sigma_i &= \sqrt{\alpha_i^2 + \beta_i^2 |\hat{Z}_i|^{2\xi_0}} \end{aligned} \quad [1b]$$

where  $\alpha_r$ ,  $\beta_r$ , and  $\xi_0$  are adjustable parameters. An extreme example of a case where the components of the impedance are very different in magnitude would be provided by systems which have a solution resistance that is much larger than the polarization impedance. The standard deviations of the real and imaginary components given by Eq. 1 are not equal unless  $\beta_r = 0$ .

In contrast, use of modulus weighting suggests that

$$\sigma_i = \sigma_r = \sigma = \alpha |Z| \quad [2]$$

where  $\alpha$  is a constant, often chosen on the basis of an *a priori* estimate of noise characteristics. A value of  $\alpha = 0.03$  is commonly assumed.

Using the measurement model concept to filter lack of replicacy in repeated experiments, Orazem *et al.*<sup>13</sup> and Agarwal *et al.*<sup>15,17-19</sup> identified the standard deviation of the stochastic noise for a number of systems which had a negligibly small solution resistance. They suggested that the standard deviation of stochastic errors in impedance measurements could be modeled by

$$\sigma_i = \sigma_r = \sigma = \alpha |Z_j| + \beta |Z_i| + \gamma \frac{|Z|^2}{R_m} \quad [3]$$

where  $\alpha$ ,  $\beta$ , and  $\gamma$  are constants, and  $R_m$  is the value of the current measuring resistor. This model was modified in subsequent work applied to electrohydrodynamic impedance spectroscopy to allow for an additive constant<sup>25</sup>

$$\sigma_i = \sigma_r = \sigma = \alpha |Z_j| + \beta |Z_i| + \gamma \frac{|Z|^2}{R_m} + \delta \quad [4]$$

While parameters  $\alpha$ ,  $\beta$ ,  $\gamma$ , and  $\delta$  depend, in principle, on the experimental system and on the specific instruments used for impedance measurements, the error structure model parameters for a given instrumentation were found to be independent of the systems studied. The only exception

reported was for  $\text{LaNi}_5$  electrodes at potentials where gas evolution was favored.<sup>13,26</sup>

The significance of the assumed stochastic error structure is illustrated in Fig. 1 where experimental data are presented for an electrical circuit analogue with a solution resistance that is ten times larger than the polarization impedance. Equation 2 suggests that experimental determination of the imaginary part of the impedance response would be difficult to achieve for systems that have a large series resistance, e.g., a large solution resistance. If the noise in the measurement were characterized by a standard deviation that is 3% of the modulus value, almost all of the imaginary component would fall below the noise level, and the resulting signal-to-noise level would be very small. Even for a standard deviation of 1% of the modulus, the imaginary part of the impedance could not be resolved for frequencies lower than 3 Hz and higher than 100 Hz. The errors predicted by Eq. 3 are smaller, but still represent a significant portion of the imaginary part of the impedance response. The error structure associated with Eq. 1 with parameter values reported by Macdonald<sup>8</sup> ( $\alpha_r = 0.001$ ,  $\beta_r = 0.1$ , and  $\xi_0 = 1$ ) yields standard deviations for the real and imaginary components of the impedance that are one order of magnitude below the respective measured values.

Equations 2-4 suggest that measurement of the imaginary part of the impedance in resistive media should be extremely difficult, yet, as shown in Fig. 1, the imaginary part of the impedance can be determined experimentally in resistive media with low levels of noise. The success of such measurements supports Macdonald's argument that Eq. 1 should be used when the components of the impedance are very different in magnitude. While Eq. 1 is in conflict with experimental observation that the real and imaginary parts of the impedance have the same standard deviation,<sup>13,15,17-19,22,23</sup> these observations have been made only for systems containing a solution resistance that was small as compared to the polarization impedance.

Three results of Orazem *et al.*<sup>13,25</sup> and Agarwal *et al.*<sup>15,17-19,26</sup> are examined here in the light of experimental measurements for systems with a large series resistance as compared to the polarization impedance:

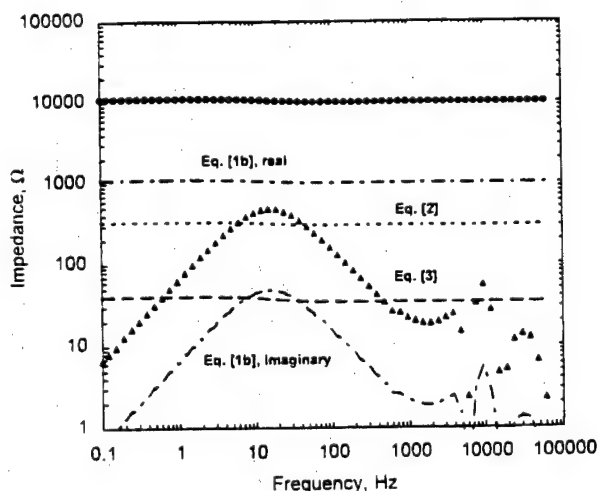


Fig. 1. A comparison of the measured impedance response of a system with a large solution resistance to three models for the standard deviation of the measurement. The circles correspond to the real component of the impedance response and the triangles represent the imaginary component. The dotted line (Eq. 2) corresponds to 3% of the modulus. The dashed line (Eq. 3) is the model for the error structure proposed by Orazem *et al.*<sup>13</sup> for a 1286 potentiostat and a 1250 frequency response analyzer. The dash-dot lines correspond to the real and imaginary parts of Eq. 1b with parameter values taken from an example given in Ref. 11.

1. The standard deviations for the real and imaginary parts of the impedance are indistinguishable.

2. The standard deviation can be represented by a three-parameter model of the form given as Eq. 3 or a four-parameter model of the form given as Eq. 4.

3. In the absence of internal sources of noise such as bubble generation, the stochastic noise is largely determined by the instrumentation. Thus, a single set of parameters  $\alpha$ ,  $\beta$ ,  $\gamma$ , and  $\delta$  should be sufficient to describe all impedance measurements conducted in a similar manner on a given instrument.

The object of this work was to explore the error structure for impedance measurements for a class of experimental systems in which the ohmic resistance is a sizable fraction of the total impedance. Results are presented for two experimental systems. The impedance response of an equilibrated freestanding polyaniline membrane is presented for a series of electrolytic environments. The error analysis presented here is an integral part of the data analysis which is to be presented in subsequent papers. The results of this work with respect to the error structure were confirmed in subsequent measurements conducted on electrical circuits.

### Freestanding Polyaniline (PANI) Membrane

As a consequence of its potential-dependent optical and electrical properties, polyaniline has potential application in electrochromic devices and in rechargeable batteries. The conductivity of polyaniline is also known to be very sensitive to the pH of the aqueous solutions with which the film has been equilibrated.<sup>27</sup> In earlier work, impedance techniques were used to study the transport and reactive properties of PANI-modified electrodes<sup>28</sup> and of freestanding PANI membranes.<sup>29</sup> The study of the freestanding films (Ref. 26) was preliminary in the sense that only graphical interpretation of spectra was presented in the absence of a quantitative model to be regressed. Following the recent development of a quantitative model for freestanding membranes,<sup>30</sup> the objective of this effort was to provide a firm statistical foundation for a more sophisticated regression-based interpretation of the impedance response of freestanding PANI films in terms of the model parameters.

**Experimental details.**—A schematic representation of the experimental system used is presented in Fig. 2. Potential was controlled by a Solartron 1186 potentiostat and driven by a Solartron 1250 frequency response analyzer. Impedance measurements were collected under galvanostatic modulation at the open-circuit condition. Impedance measurements were collected frequency-by-frequency from high frequency to low. The long integration feature of the frequency response analyzer was used, which terminated measurement at a given frequency when a 1% closure error was achieved on the potential channel. The amplitude of the perturbation was adjusted for each system to maximize the signal-to-noise ratio while staying within the linear regime.

The experimental setup parallels closely that described by Deslouis *et al.*<sup>29</sup> Polyaniline membranes were prepared by evaporation of emeraldine base solutions in an *N*-methyl-2-pyrrolidinone solvent according to the method of Angelopoulos *et al.*<sup>31</sup> The emeraldine base was dissolved in the solvent at a concentration of 20 g/liter and kept in an oven at 70°C for 2 days. The membrane was removed from the drying dish by addition of distilled water. The resulting membrane had a thickness of 20 to 100  $\mu\text{m}$ , depending on the amount of solution evaporated. After preparation, the membrane was immersed in the acid solution until it was equilibrated.

Electrolytic solutions were prepared by adding the appropriate amount of the respective reagent-grade acid to distilled water. No other ionic species were added. The cell configuration, presented in Fig. 2, was similar to that described in Ref. 20. The diameter of the membrane in contact with solution was 0.5 cm; thus the superficial exposed cross-sectional area was 0.2  $\text{cm}^2$ . The working, counter- and

reference electrodes were silver. Four-electrode galvanostatic experiments were conducted in which the impedance response was obtained from the potential difference across the membrane in response to a current perturbation.

Six repeated measurements were obtained for each electrolyte composition after the membrane was equilibrated with its environment. The time of immersion required to achieve equilibration was over 24 h. The results, presented in the subsequent section, revealed a large change in the impedance response with environment.

**Error analysis with measurement models.**—While the repeated measurements were close in value, they were not strictly replicate. The standard deviation of repeated measurements therefore contained contributions from both stochastic and experimental bias errors. The measurement model approach of Agarwal *et al.* was used to filter lack of replicacy in order to obtain estimates for the stochastic noise that were free of bias errors.<sup>19</sup> The procedure is summarized below:

1. For each experimental condition, repeated impedance measurements were obtained over identical frequency ranges. Equilibration of the membrane was assumed to have been achieved when six such measurements agreed within 3% (*i.e.*, the standard deviation for the real and imaginary components, respectively, was less than 3% of the modulus at each frequency).

2. A measurement model consisting of a Voigt series (see Fig. 1 of Ref. 32) was regressed to one of the individual spectra. The RC time constants were restricted to positive values, but the resistance for each Voigt element was allowed to have either positive or negative values. The number of parameters used in the regression (two for each Voigt element) was increased in a stepwise manner until the 95.4% ( $2\sigma$ ) confidence interval for one of the parameters included zero. The number of line shapes was then decreased by one. This procedure resulted in the maximum number of statistically significant parameters. The nonzero parameter estimate is important because, when the confidence interval for a parameter estimate includes zero, the regressed value is not statistically significant. This result could be obtained if the experimental range is insensitive to the parameter or if the stochastic or bias errors in the measurement are too large to allow parameter identification. The influence of stochastic errors on parameter estimation provides a motivation for studying the error structure of impedance measurements.

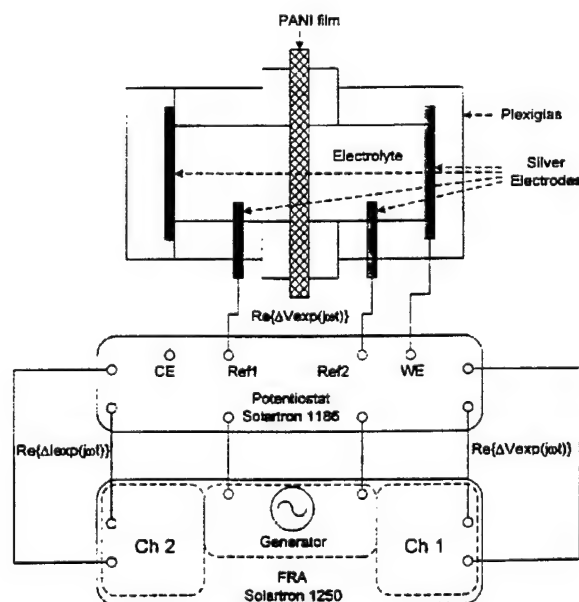


Fig. 2. Schematic illustration of the experimental system.

3. The measurement model was regressed to each of the six spectra using the same number of line shapes. If fewer line shapes could be identified for one of the spectra, the number of line shapes was reduced for all the spectra. In other words, the same number of line shapes was used for all the regressions to a given set of repeated measurements, and none of the regressions were allowed to yield parameter estimates which included zero.

4. The standard deviation of the residual errors for the regressions was calculated at each frequency. This approach was assumed to yield the bias-free standard deviation for the stochastic component of the impedance response (see Ref 17, 19, and 25).

5. Similar calculations were performed for all experimental conditions used in this work. Files containing the standard deviations calculated in the manner described above were obtained for each electrolyte and concentration. Models for the error structure were then regressed to the standard deviation files (see Ref. 17, 19, and 25). Equation 4 could not provide a good fit to the data, although a modified form given as

$$\sigma_j = \sigma_r = \sigma = \alpha|Z_i| + \beta|Z_r - R_x| + \gamma \frac{|Z_i|^2}{R_m} + \delta \quad [5]$$

was found to be satisfactory. The regression procedure is described in some detail in Ref. 19. The estimate for the solution resistance  $R_x$  used in Eq. 5 was obtained from regression of the measurement model.

**Stochastic error structure.**—While the impedance data were very sensitive to electrolytic composition, the error structure for the impedance measurements could be grouped into two classes.

**PANI in strong acids.**—The data collected in HCl, given in Fig. 3, showed a solution resistance that was roughly five times larger than the polarization impedance in the pH

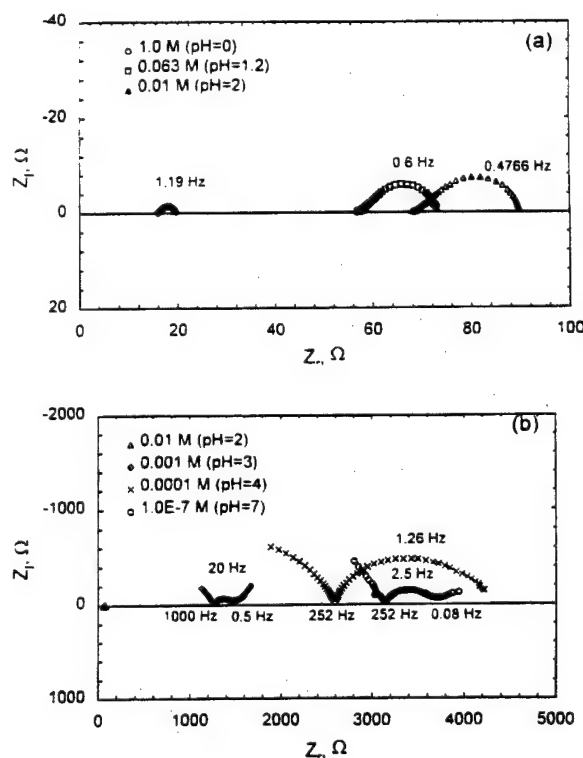


Fig. 3. Impedance plane plots collected in HCl. Characteristic frequencies are marked for peak of the impedance plane curve in (a) and for the maxima and minima of the impedance plane curves in (b).

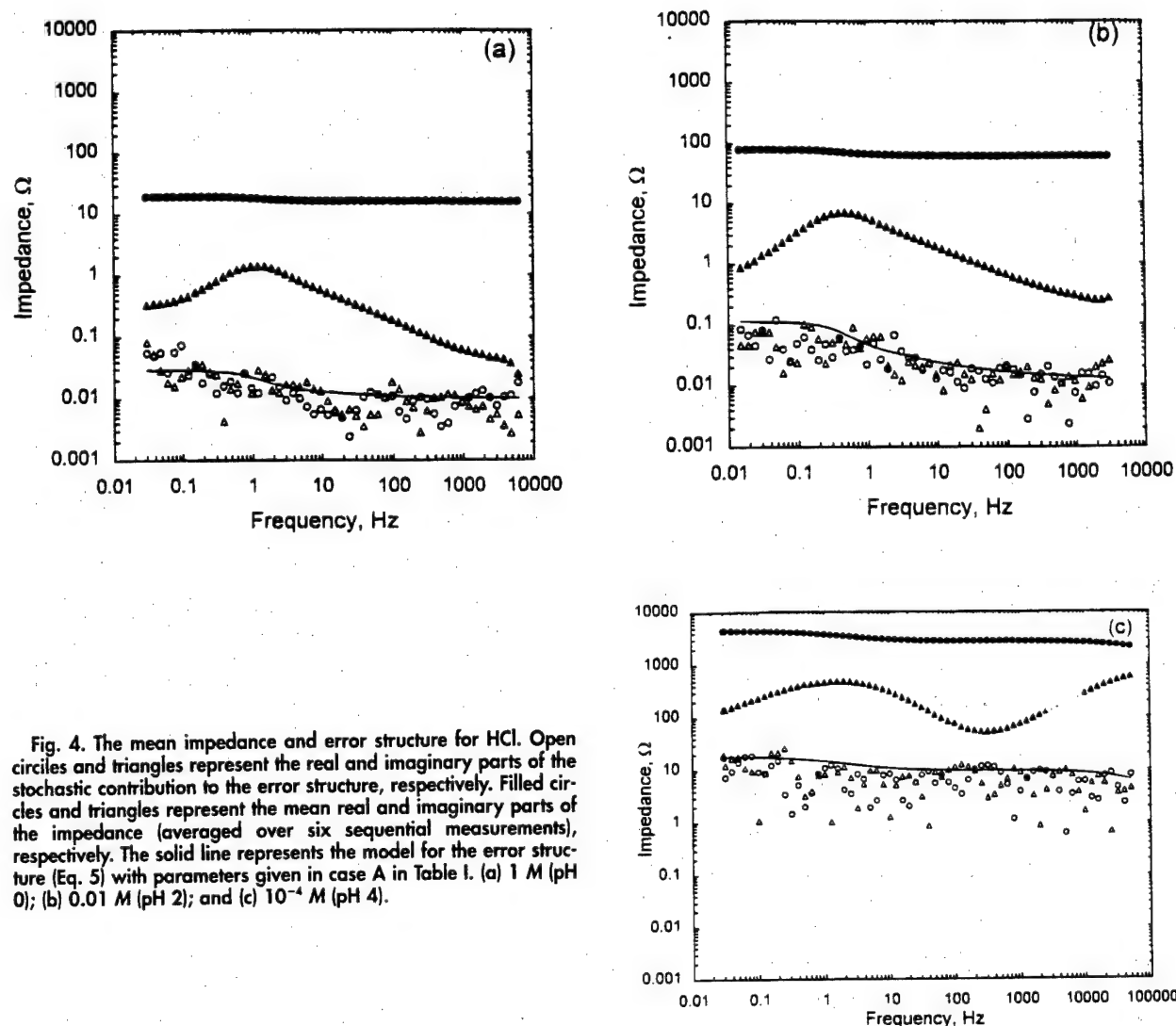


Fig. 4. The mean impedance and error structure for HCl. Open circles and triangles represent the real and imaginary parts of the stochastic contribution to the error structure, respectively. Filled circles and triangles represent the mean real and imaginary parts of the impedance (averaged over six sequential measurements), respectively. The solid line represents the model for the error structure (Eq. 5) with parameters given in case A in Table I. (a) 1 M (pH 0); (b) 0.01 M (pH 2); and (c)  $10^{-4}$  M (pH 4).

range of 0 to 2 (HCl concentration between 1 to 0.01 M). The shape of the impedance-plane curves suggests that a mass-transfer Warburg impedance corresponding to diffusion in a finite system may be present. Such a point was discussed theoretically in Ref. 30 and further applied to PANI in strong acids.<sup>33</sup> The impedance increased with increasing pH, and the characteristic time constants for the processes changed such that the high-frequency phenomena could not be resolved within instrumental constraints. The Warburg behavior was not evident at pH values between 3 and 7 (HCl concentration between  $10^{-3}$  to  $10^{-7}$  M).

While the magnitude of the impedance and the dominant phenomena were strong functions of electrolyte composi-

tion, the same model parameters in Eq. 5 could be used to fit the resulting measurement error structure. The real and imaginary parts, respectively, of the impedance response and the resulting standard deviation are presented in Fig. 4a for a PANI membrane in HCl at a pH equal to 0. Even though the real part of the impedance was several orders of magnitude larger than the imaginary part, the respective standard deviations were indistinguishable. Equality of the standard deviations for the real and imaginary parts of the impedance response was observed for all experimental conditions. The same model for the error structure was found to apply for all the data collected in HCl. Results are presented in Fig. 4b for pH 2, and in Fig. 4c for pH 4. The

Table I. Parameter values for the error structure model defined by Eq. 5.

Experimental systems	$\alpha$	$\beta$	$\gamma$	$\delta, \Omega$	$\chi^2/\nu$
A HCl: 1, 0.063, 0.01, $10^{-3}, 10^{-4}, 10^{-7}$ M	0	$5.149 \times 10^{-3}$ $\pm 0.009 \times 10^{-3}$	$2.5 \times 10^{-5}$ $\pm 0.2 \times 10^{-5}$	$9.5 \times 10^{-3}$ $\pm 0.3 \times 10^{-3}$	2.72
HClO <sub>4</sub> 1, 0.1, 0.01 M					
HNO <sub>3</sub> 1, 0.1, 0.01 M					
H <sub>2</sub> SO <sub>4</sub> 1, 0.1 M					
H <sub>3</sub> PO <sub>4</sub> 1, 0.01 M					
B H <sub>2</sub> SO <sub>4</sub> 0.01 M	$1.7 \times 10^{-2}$	0	$9 \times 10^{-5}$	$2.3 \times 10^{-1}$	1.14
H <sub>3</sub> PO <sub>4</sub> 0.1 M	$\pm 0.1 \times 10^{-2}$		$\pm 2 \times 10^{-5}$	$\pm 0.1 \times 10^{-1}$	
C H <sub>2</sub> SO <sub>4</sub> $10^{-3}, 10^{-4}, 10^{-6}$ M	$2.7 \times 10^{-3}$ $\pm 0.3 \times 10^{-3}$	$5.4 \times 10^{-4}$ $\pm 0.4 \times 10^{-4}$	0	$1.7 \times 10^{-1}$ $\pm 0.1 \times 10^{-1}$	2.19
D Circuits 1-7 (see Fig. 9)	$2.1 \times 10^{-4}$ $\pm 0.1 \times 10^{-4}$	$5.1 \times 10^{-5}$ $\pm 0.9 \times 10^{-5}$	$4.2 \times 10^{-6}$ $\pm 0.1 \times 10^{-6}$	$9.8 \times 10^{-3}$ $\pm 0.4 \times 10^{-3}$	2.65

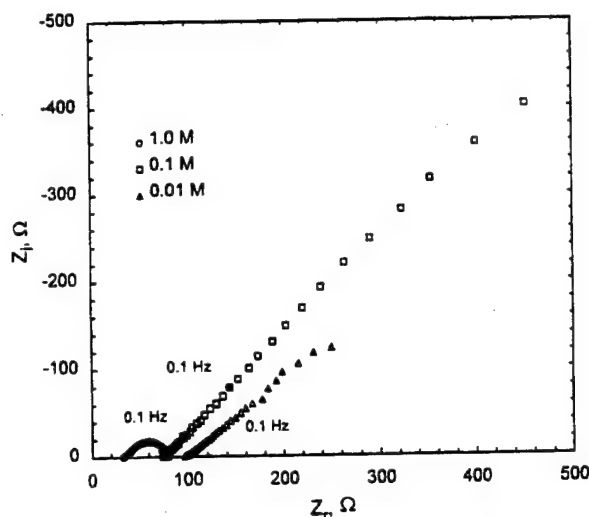


Fig. 5. Impedance plane plots for  $\text{H}_3\text{PO}_4$ . A characteristic frequency of 0.1 Hz represents the peak of the impedance plane curve for 1 M solutions. The same frequency is marked at other concentrations by a solid symbol (■ and ▲).

error structure model parameters used are given as case A in Table I. Even though the impedance response was significantly different for the different pH values (as seen in Fig. 3), the same model and the same model parameters

applied for the error structure of all data collected in the strong acids  $\text{HCl}$ ,  $\text{HClO}_4$ , and  $\text{HNO}_3$ .

**PANI in weak acids.**—While similar sensitivity to pH was observed for the weak acid  $\text{H}_3\text{PO}_4$  (Fig. 5), a single set of parameters could not be used to model the resulting error structure. As seen in Fig. 6a for the more acidic condition for  $\text{H}_3\text{PO}_4$  (1 M), the line corresponding to the error structure model parameters obtained for  $\text{HCl}$  (case A in Table I) underpredicts slightly the measured standard deviations and does not capture the peak seen between 0.1 and 1 Hz. The failure of the error structure model parameters obtained for  $\text{HCl}$  (solid line) to conform to the experimentally determined noise level was more evident at a concentration of  $10^{-1}$  M, a condition which is close to the dissociation constant for the acid (see Fig. 6b). The dashed line in Fig. 6b represents the same model for the error structure as used for the strong acids (i.e., Eq. 5), but the regressed parameters were those given as case B in Table I. The noise level returned to that given as case A for a concentration of  $10^{-2}$  M, as shown in Fig. 6c.

Similar sensitivity to concentration was observed for  $\text{H}_2\text{SO}_4$  (Fig. 7), which is also a weak acid. As seen in Fig. 8a for a concentration of  $10^{-1}$  M, the more acidic condition for  $\text{H}_2\text{SO}_4$  (1 and 0.1 M) shared the same error structure as was obtained for  $\text{HCl}$  (case A in Table I). As seen in Fig. 8b, at a concentration of 0.01 M the noise level was significantly higher than the solid line representing the error structure for strong acids. This concentration is close to the second dissociation constant for  $\text{H}_2\text{SO}_4$ . The error structure parameters corresponding to the dashed line are given as case B in Table I. At higher pH values, the noise level was less than predicted by the parameters of case A

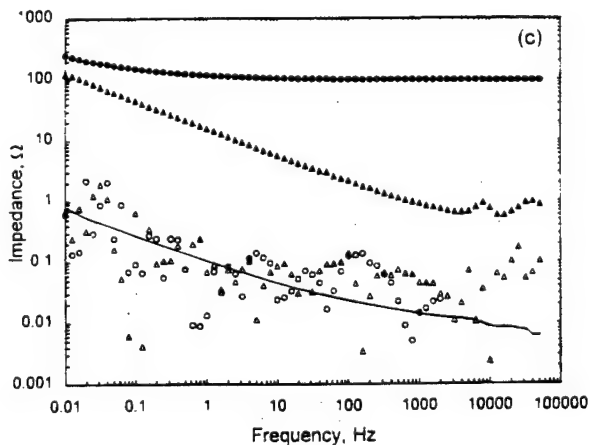
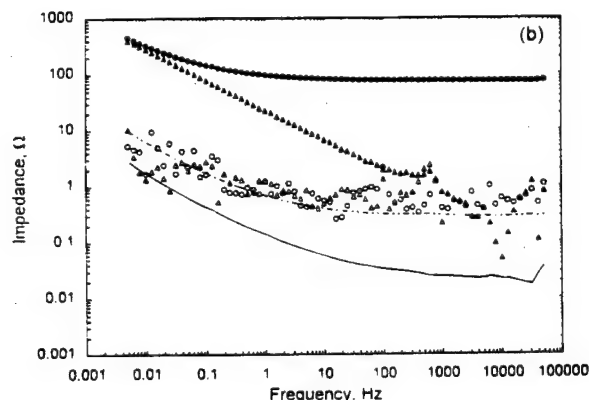
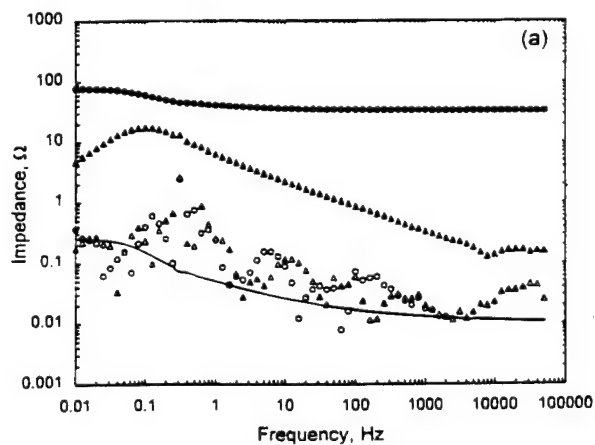


Fig. 6. The mean impedance and error structure for  $\text{H}_3\text{PO}_4$ . Open circles and triangles represent the real and imaginary parts to the stochastic contribution to the error structure, respectively. Filled circles and triangles represent the mean real and imaginary parts of the impedance (averaged over six sequential measurements), respectively. The solid line represents the model for the error structure (Eq. 5) with parameters given as case A in Table I. The dashed line in Fig. 6b represents the same model with parameters given in case B in Table I. (a) 1 M; (b) 0.1 M; (c) 0.01 M.



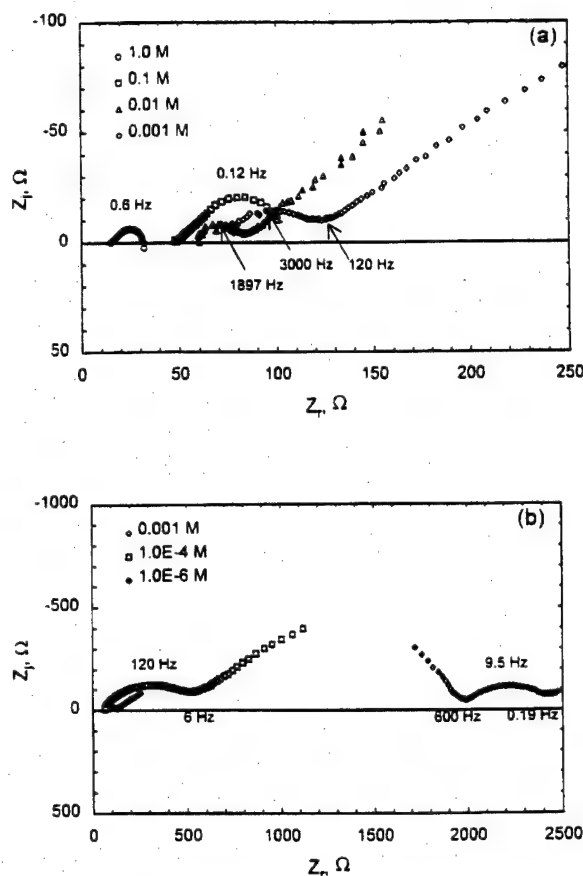


Fig. 7. Impedance plane plots for  $\text{H}_2\text{SO}_4$ . Characteristic frequencies are given for the maxima and, for concentrations below 1 M, minima of the impedance plane curves.

(see Fig. 8c). The error structure parameters given as case C in Table I applied for data collected in  $\text{H}_2\text{SO}_4$  at concentrations of  $10^{-3}$ ,  $10^{-4}$ , and  $10^{-6}$  M.

### Electrical Circuit Analogues

Experiments were conducted using electrical circuit analogues to verify that the standard deviation of the real and imaginary parts of the impedance were equal, even when the real part of the impedance was much larger than the imaginary. The stationarity of the nonelectrochemical system allowed direct calculation of the standard deviations without use of the measurement model as a filter for lack of replicacy. Thus, this work could be used to confirm that the equality of the standard deviation for real and imaginary components of the impedance was not a consequence of the measurement model filtering technique.

**Experimental details.**—Schematic representations of the circuit analogues used are presented in Fig. 9. Potential was controlled by a Solartron 1186 potentiostat and driven by a Solartron 1250 frequency response analyzer. Impedance measurements were collected under galvanostatic modulation at the open-circuit condition. Impedance measurements were collected frequency-by-frequency from high frequency to low. The long-integration feature of the frequency response analyzer was used, which terminated measurement at a given frequency when a 1% closure error was achieved on the potential channel.

**Experimental results.**—Six repeated measurements were obtained for each circuit. The standard deviations of the real and imaginary parts of the impedance were calculated directly. A single model was found to give acceptable fits to the standard deviations obtained from the different circuits. The error structure model parameters are given as case D in Table I.

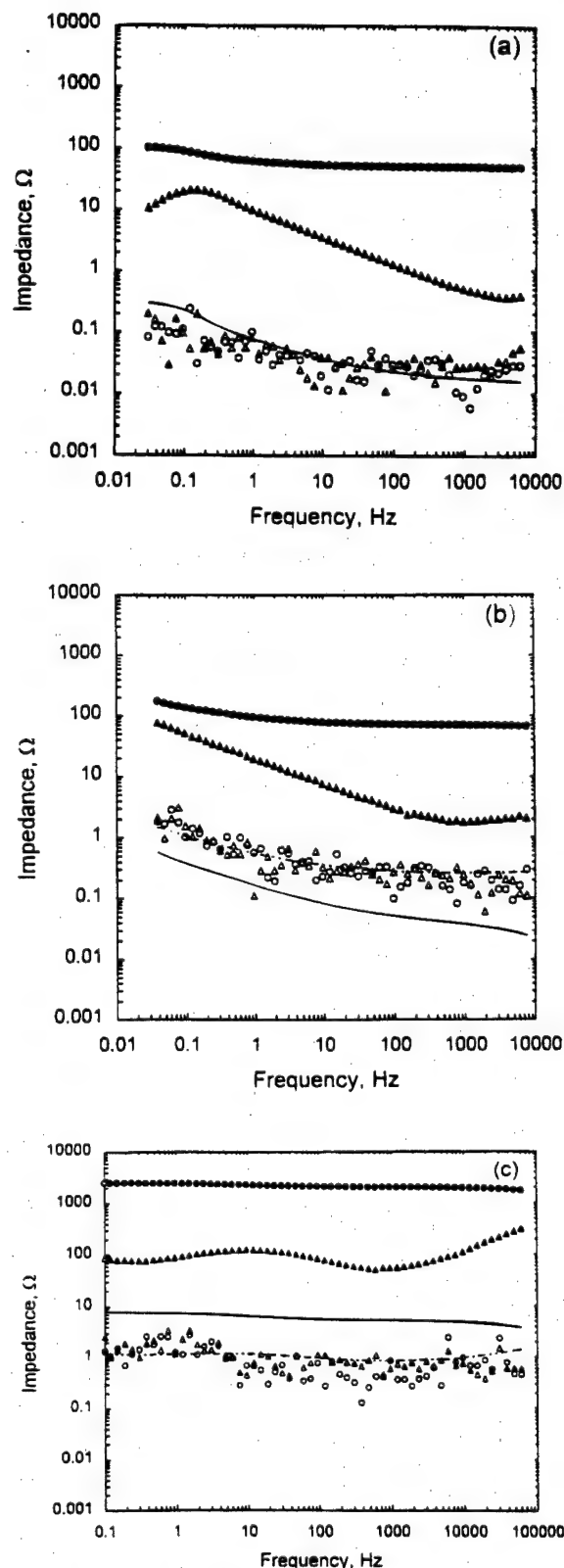


Fig. 8. The mean impedance and error structure for  $\text{H}_2\text{SO}_4$ . Open circles and triangles represent the real and imaginary parts of the stochastic contribution to the error structure, respectively. Filled circles and triangles represent the mean real and imaginary parts of the impedance (averaged over six sequential measurements), respectively. The solid line represents the model for the error structure (Eq. 5) with parameters given as case A in Table I. The dashed line in Fig. 8b represents the same model with parameters given as case B in Table I. The dashed line in Fig. 8c represents the same model with parameters given as case C in Table I. (a) 0.1 M; (b) 0.01 M; and (c)  $10^{-6}$  M.



The data obtained from circuit 1 are presented in Fig. 10a. The ratio  $R_0/R_1$  was equal to 10, which meant that the real part of the impedance was at least 20 times larger than the imaginary part of the impedance at all frequencies and was almost 2,000 times larger at the lowest frequency measured (0.1 Hz). The significant departure from RC circuit behavior seen at frequencies above 2,000 Hz was attributed to potentiostatic limitations. The data at frequencies above this point were found by the methods of Ref. 34 to be inconsistent with the Kramers-Kronig relations.

In spite of the three-orders of magnitude difference between the real and imaginary parts of the impedance, the standard deviations of the repeated measurements were indistinguishable except in two frequency regimes. The standard deviations were found to be different in value in the higher (greater than 2,000 Hz) frequency range where instrument limitations affected the measurement. The standard deviations were also found to be different in value in the frequency range between 10 and 200 Hz. In this frequency range, the calculation of the standard deviation of the real part was constrained by the five digits reported by the FRA. The dashed line in Fig. 10a represents a value corresponding to 0.5 parts in  $10^5$ . The dashed line can be interpreted as being the standard deviation one would expect if the last significant digit reported had a value of  $x + 1$  for half of the observations in an infinitely large sample. This line drops an order of magnitude at the frequency of 180 Hz where the measured real part of the impedance changes from 1000.0 to 999.99  $\Omega$ . For data points marked by an  $x$ , all five digits for six repeated measurements were identical, and a standard deviation of 0 was calculated. In other words, the standard deviations for the real and the imaginary parts of the impedance were equal unless the number of significant digits reported by the FRA were inadequate to calculate  $\sigma$ , unless potentiostatic limitations influenced the result. The solid line represents the model for the error structure obtained for the different circuits tested.

A similar result was obtained when the resistors were switched such that  $R_0/R_1$  was equal to 0.1 (Fig. 10b). The standard deviations for the real and imaginary parts were found to be indistinguishable. In this case, the potentiostatic limitations were observed at higher frequencies. The standard deviation for the real part of the impedance was very close to the round-off limit of the FRA. In the absence of a solution resistance ( $R_0/R_1 = 0$ , Fig. 10c), similar behav-

ior is seen for the standard deviations for the real solution resistance accounts well for the changes in circuit configuration. A general fit of this nature could not be seen using Eq. 1-4.

Circuits were constructed using larger resistors in order to confirm the generality of the results. As seen in Fig. 11, the standard deviations for the real and the imaginary parts of the impedance were equal unless the number of significant digits reported by the FRA were inadequate to calculate  $\sigma$ , or unless the measured values for the imaginary impedance showed that potentiostatic limitations had influenced the result. With a common set of parameters  $\beta$ ,  $\gamma$ , and  $\delta$ , the model presented here as Eq. 5 provided a good description for the error structure for all the circuits tested.

## Discussion

In conjunction with the mounting evidence obtained for systems with small solution resistances,<sup>13,15,17-19,22,23</sup> this work provides experimental verification that the standard deviations for the real and imaginary components of the impedance are equal, even when the real part of the impedance is much larger than the imaginary part. There were two exceptions to this observation.

1. The standard deviations for the real and imaginary parts were unequal when the standard deviation of the imaginary part became sufficiently small that the number of significant digits reported by the instrumentation were insufficient to calculate the standard deviation of the real part.

2. The standard deviations for the real and imaginary parts were unequal when instrumental limitations constrained the measurement.

The first condition suggests that the equality could have been achieved if a larger number of significant digits for the real part of the impedance were available. The second condition may be expected to be associated with a violation of the Kramers-Kronig relations. The work presented here suggests, not only that the standard deviation for the real and imaginary parts are equal, but that this equality may be a fundamental result associated with the manner in which errors are propagated through the Kramers-Kronig relations. The hypothesis that the propagation of errors through the Kramers-Kronig relations yields standard deviations that are equal is addressed in subsequent papers.<sup>32,33</sup>

The model for the error structure given as Eq. 4 could not describe the stochastic part of the error structure associated with systems containing large solution resistances. Equation 5 provided a satisfactory model for the error structure and, in the limit that the solution resistance tends toward zero, approaches the model proposed by Orazem *et al.*<sup>13,22</sup> and Agarwal *et al.*<sup>15,17-19,23</sup> The error structure implicit in the use of modulus or proportional weighting could not describe the observed error structure.

The previously reported observation that a single set of parameters could describe the error structure for non-gas-evolving systems was found not to be general. The present work shows, however, that broad classes of experimental systems can be found for which a single set of error structure model parameters is appropriate. In this work, the selection of groupings was by trial-and-error. As an alternative to grouping data sets, it is possible to identify separate sets of error structure parameters for each experiment, but the reduced range of impedance values makes it difficult to obtain a complete set of error structure model parameters. The resulting fit often provides a less satisfactory representation of the error structure than obtained by using a larger and more varied pool of data.

The observation that a specific system has an error structure that is much larger than other systems may provide physical insight into the processes occurring within that system. The larger noise level associated with PANI in weak acids suggests that a stochastic process within the membrane may create a noise level larger than that caused by the instrumentation. For such systems, there may be a

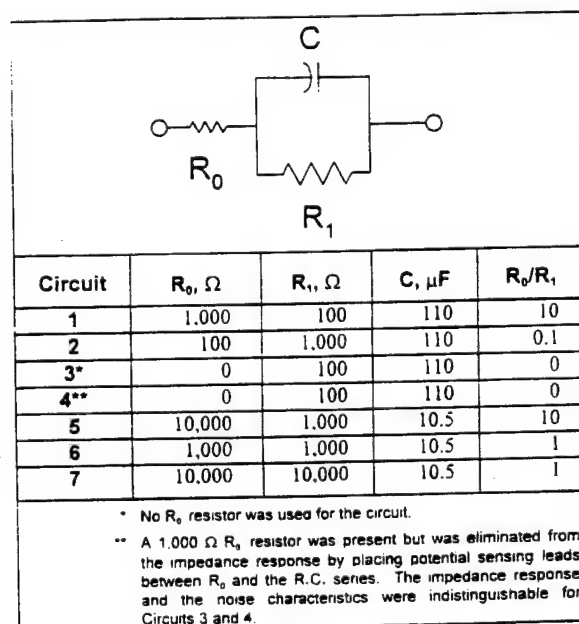


Fig. 9. Test circuit and parameter values used.

relationship between the noise of measurements conducted in the frequency domain and electrochemical noise observed in the time domain.

### Conclusions

There is now strong experimental evidence that the standard deviation of the stochastic component is the same for real and imaginary parts of the impedance response. In addition to the results presented here for PANI and an RC circuit, the equality of the standard deviations for real and imaginary parts of the impedance has been observed for the impedance response of solid-state systems (GaAs Schottky diodes, ZnO varistors, ZnS electroluminescent panels),<sup>13,18,19</sup> corrosion of copper in seawater (under either potentiostatic or galvanostatic modulation),<sup>17-19</sup> electrochemistry at metal hydride electrodes (LaNi<sub>5</sub> and mischmetal),<sup>18,26</sup> and the electrohydrodynamic impedance response for reduction of ferricyanide and oxidation of ferrocyanide on Pt rotating disks.<sup>25</sup> The error structure analysis reported here has recently been extended to measurement of the frequency-dependent complex viscosity of viscoelastic fluids, and the standard deviations for real and imaginary parts of the viscosity were found to be equal.<sup>35</sup> As the previous work was done on systems that have a negligible solution resistance, the work described in the present manuscript was undertaken to examine whether the standard deviation of the stochastic component is the same for real and imaginary parts of the impedance response even when the solution resistance is very large as compared to the polarization resistance. The

results presented here confirm that the standard deviations for the real and imaginary parts of the impedance are equal, even at frequencies sufficiently high or low that the imaginary part of the impedance asymptotically approaches zero.

The equality of the real and imaginary standard deviations has implications for the regression of models to impedance data. The fact that the information content of the imaginary part of the impedance can be obscured by noise at the asymptotic tails influences the manner in which the Kramers-Kronig relations can be applied to assess the bias contribution to the measurement. In addition, the equality of the real and imaginary standard deviations becomes a criterion for selection of appropriate weighting strategies. Among the commonly applied weighting strategies, for example, proportional weighting does not conform to this observation, but no weighting and modulus weighting do conform and may be useful weightings for preliminary regressions.

The results presented here confirm that impedance measurements are heteroskedastic (in the sense that the standard deviations are functions of frequency), though this dependence is much weaker for the galvanostatically modulated impedance data presented here than for the potentiostatically modulated data presented in Ref. 13, 17, 19, and 26. Equation 5 provides good agreement to the experimentally measured stochastic noise for the impedance data corresponding to systems with a solution resistance that is large as compared to the polarization impedance. Equation 5 approaches Eq. 4 when the solution

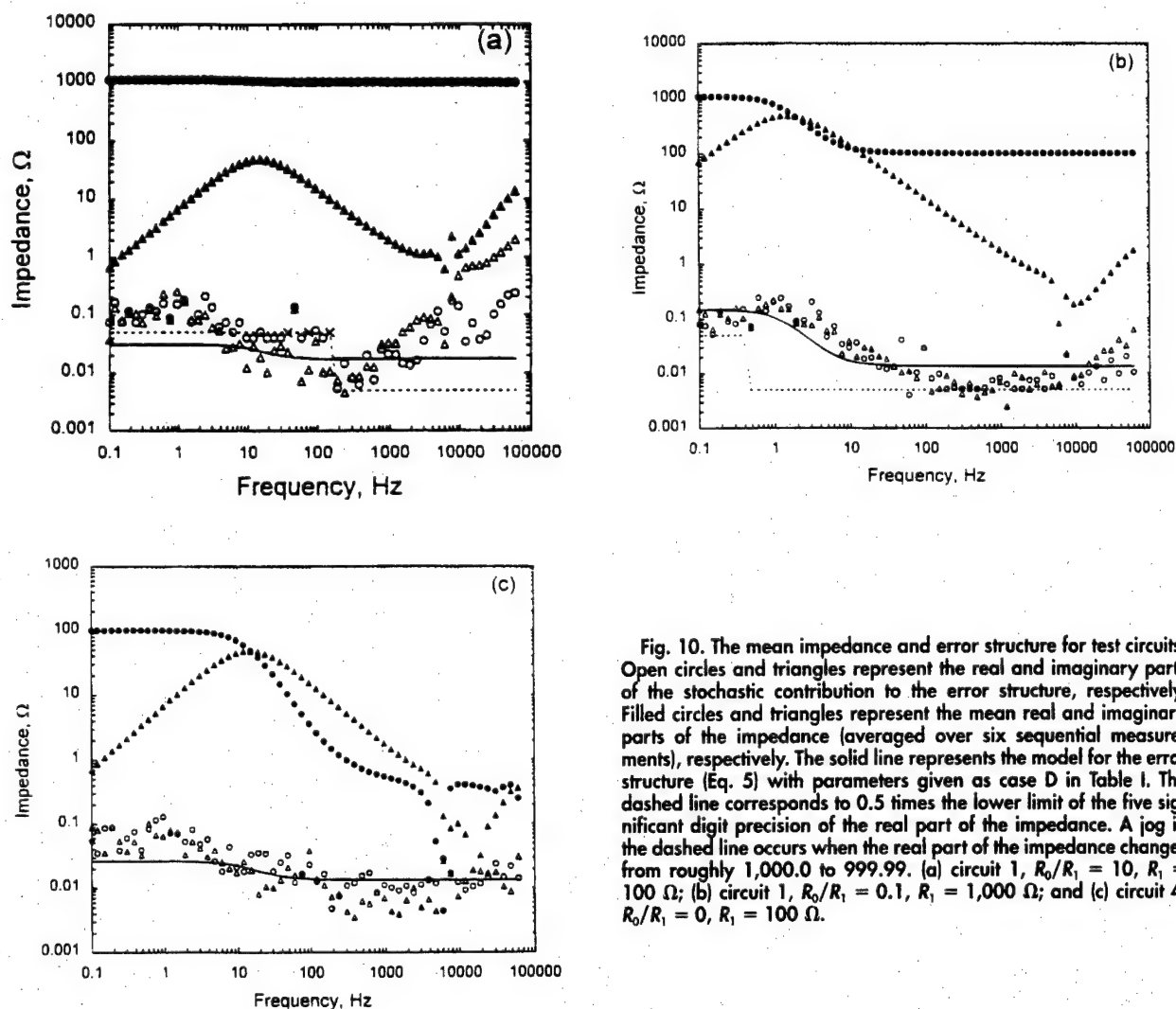


Fig. 10. The mean impedance and error structure for test circuits. Open circles and triangles represent the real and imaginary parts of the stochastic contribution to the error structure, respectively. Filled circles and triangles represent the mean real and imaginary parts of the impedance (averaged over six sequential measurements), respectively. The solid line represents the model for the error structure (Eq. 5) with parameters given as case D in Table I. The dashed line corresponds to 0.5 times the lower limit of the five significant digit precision of the real part of the impedance. A jog in the dashed line occurs when the real part of the impedance changes from roughly 1,000.0 to 999.99. (a) circuit 1,  $R_0/R_1 = 10$ ,  $R_1 = 100 \Omega$ ; (b) circuit 1,  $R_0/R_1 = 0.1$ ,  $R_1 = 1,000 \Omega$ ; and (c) circuit 4,  $R_0/R_1 = 0$ ,  $R_1 = 100 \Omega$ .

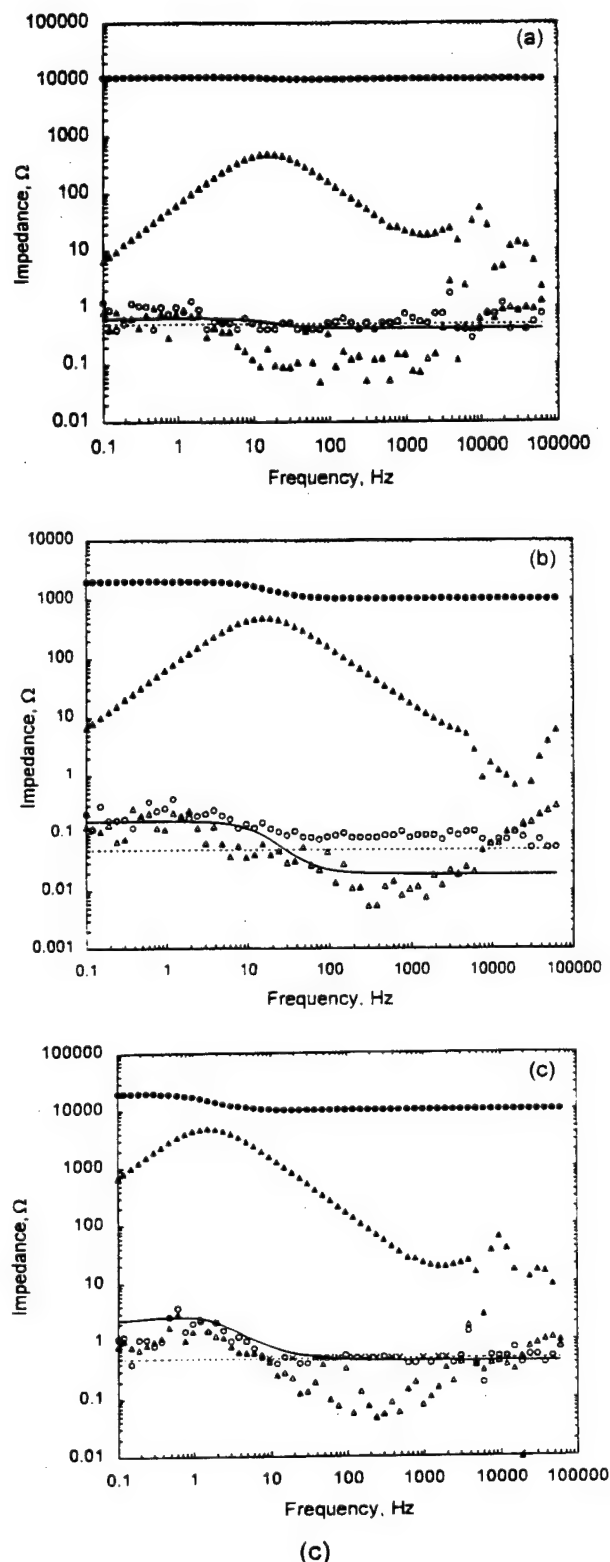


Fig. 11. The mean impedance and error structure for test circuits. Open circles and triangles represent the real and imaginary parts of the stochastic contribution to the error structure, respectively. Filled circles and triangles represent the mean real and imaginary parts of the impedance (averaged over six sequential measurements), respectively. The solid line represents the model for the error structure (Eq. 5) with parameters given as case D in Table I. The dashed line corresponds to 0.5 times the lower limit of the five significant digit precision of the real part of the impedance. (a) Circuit 5,  $R_0/R_1 = 10$ ,  $R_1 = 1,000 \Omega$ ; (b) circuit 6,  $R_0/R_1 = 10$ ,  $R_1 = 1,000 \Omega$ ; and (c) circuit 7,  $R_0/R_1 = 1$ ,  $R_1 = 10,000 \Omega$ .

resistance is negligible, and, thus, it also provides a suitable model for the error structure for the data presented in Ref. 13, 17, 19, 25, and 26. Equation 5 appears to be a suitable and general model for the stochastic part of the error structure of impedance measurements and should be useful for developing strategies for weighting regressions.

The striking extent to which the standard deviations for the real and imaginary parts of the impedance are found to be equal provides a motivation for investigating the manner in which errors are propagated through the Kramers-Kronig relations. Macdonald<sup>20</sup> presented the results of Monte Carlo simulations which showed that, when synthetic data containing additive or proportionally superimposed noise are processed through the Kramers-Kronig transforms, the standard deviation of the resulting quantity is equal to the standard deviation of the input. Similar results were obtained by García-Rubio *et al.*<sup>36</sup> While references 20 and 36 address the manner in which an assumed error structure is propagated through application of the Kramers-Kronig relations to synthetic or experimental data, an analytic approach can be used to yield an explicit relationship between  $\sigma_r$  and  $\sigma_i$  with the only requirement that the errors be stationary in the sense of replication at the measurement frequency and that the Kramers-Kronig relations be satisfied. The results of that investigation, which have direct relevance to the properties of stochastic errors in experimental data, are reported separately.<sup>37</sup>

### Acknowledgment

The work performed at the University of Florida (M.E.O.) was supported by the Office of Naval Research under Grant Numbers N0001493I0056 and N0001493I1113 (A.J. Sedriks, Program Monitor). This work was also supported in part by the National Science Foundation under a U.S.-France Cooperative Research Grant INT-9416713. Helpful discussions with Luis García-Rubio (Department of Chemical Engineering, University of South Florida) are greatly appreciated.

Manuscript submitted Feb. 28, 1996; revised manuscript received July 25, 1996.

CNRS-Laboratoire "Physique des Liquides et Electrochimie" assisted in meeting the publication costs of this article.

### REFERENCES

1. G. E. P. Box and N. R. Draper, *Empirical Model-Building and Response Surfaces*, John Wiley & Sons, Inc., New York (1987).
2. H. W. Sorenson, *Parameter Estimation: Principles and Problems*, Marcel Dekker, Inc., New York (1980).
3. G. A. F. Seber, *Linear Regression Analysis*, pp. 330-334, John Wiley & Sons, Inc., New York (1977).
4. R. W. Christy, *Amer. J. Phys.*, **40**, 1403 (1972).
5. A. Jutan and L. H. García-Rubio, *Proc. Control Qual.*, **4**, 235 (1993).
6. P. Zoltowski, *J. Electroanal. Chem.*, **178**, 11 (1984).
7. B. A. Boukamp, *Solid State Ionics*, **20**, 31 (1986).
8. J. R. Macdonald and L. D. Potter, Jr., *ibid.*, **23**, 61 (1987).
9. P. Zoltowski, *J. Electroanal. Chem.*, **260**, 269 (1989).
10. P. Zoltowski, *ibid.*, **260**, 287 (1989).
11. J. R. Macdonald, *Electrochim. Acta*, **35**, 1483 (1990).
12. J. R. Macdonald and W. J. Thompson, *Commun. Statist. Simula.*, **20**, 843 (1991).
13. M. E. Orazem, P. Agarwal, A. N. Jansen, P. T. Wojcik, and L. H. García-Rubio, *Electrochim. Acta*, **38**, 1903 (1993).
14. M. E. Orazem, P. Agarwal, and L. H. García-Rubio, *J. Electroanal. Chem.*, **378**, 51 (1994).
15. P. Agarwal, M. E. Orazem, and L. H. García-Rubio, *Electrochim. Acta*, **41**, 1017 (1996).
16. G. Spinolo, G. Chiodelli, A. Moghistris, and U. A. Tamburini, *This Journal*, **135**, 1419 (1988).
17. P. Agarwal, O. C. Moghissi, M. E. Orazem, and L. H. García-Rubio, *Corrosion*, **49**, 278 (1993).
18. P. Agarwal, Ph.D. Thesis, University of Florida, Gainesville, FL (1994).
19. P. Agarwal, O. D. Crisalle, M. E. Orazem, and L. H. García-Rubio, *This Journal*, **142**, 4149 (1995).

20. J. R. Macdonald, *Electrochim. Acta*, **38**, 1883 (1993).
21. J. R. Macdonald, *J. Electroanal. Chem.*, **378**, 17 (1994).
22. B. A. Boukamp and J. R. Macdonald, *Solid State Ionics*, **74**, 85 (1994).
23. B. Robertson, B. Tribollet, and C. Deslouis, *This Journal*, **135**, 2279 (1988).
24. L. K. DeNoyer and J. G. Good, *American Laboratory*, (March 1990). Software available from Spectrum Square Associates. Ithaca, NY 14850.
25. M. E. Orazem, P. Agarwal, C. Deslouis, and B. Tribollet, *This Journal*, **143**, 948 (1996).
26. P. Agarwal, M. E. Orazem, and A. Hiser, in *Hydrogen Storage Materials, Batteries, and Chemistry*, D. A. Corrigan and S. Srinivasan, Editors, PV 92-5, p. 120, The Electrochemical Society Proceedings Series, Pennington, NJ (1991).
27. J. C. Chiang and A. G. MacDiarmid, *Synth. Met.*, **13**, 193 (1986).
28. C. Deslouis, M. M. Musiani, M. El Rhazi, and B. Tribollet, *ibid.*, **60**, 269 (1993).
29. C. Deslouis, M. M. Musiani, and B. Tribollet, *J. Phys. Chem.*, **98**, 2936 (1994).
30. C. Deslouis, M. M. Musiani, B. Tribollet, and M. A. Vorotyntsev, *This Journal*, **142**, 1902 (1995).
31. M. Angelopoulos, A. Ray, A. G. MacDiarmid, and A. J. Epstein, *Synth. Met.*, **21**, 21 (1987).
32. P. Agarwal, M. E. Orazem, and L. H. García-Rubio, *This Journal*, **139**, 1917 (1992).
33. C. Deslouis, T. El Moustafid, M. M. Musiani, and B. Tribollet, *Electrochim. Acta*, **41**, 1343 (1996).
34. P. Agarwal, M. E. Orazem, and L. H. García-Rubio, *This Journal*, **142**, 4159 (1995).
35. M. Durbha, M. E. Orazem, and L. H. García-Rubio, in *New Directions in Electroanalytical Chemistry*, J. Leddy and R. M. Wightman, Editors, PV 96-9, p. 385, The Electrochemical Society Proceedings Series, Pennington, NJ (1996).
36. C. Bacon, L. H. García-Rubio, and M. E. Orazem, *J. Phys. D: Appl. Phys.*, Submitted.
37. M. Durbha, M. E. Orazem, and L. H. García-Rubio, *This Journal*, To be published (1997).



# Spectroscopy Applications of the Kramers-Kronig Transforms: Implications for Error Structure Identification

Madhav Durbha\* and Mark E. Orazem\*\*

*Department of Chemical Engineering, University of Florida, Gainesville, Florida 32611, USA*

Luis H. García-Rubio

*Department of Chemical Engineering, University of South Florida, Tampa, Florida 33620, USA*

## ABSTRACT

Stochastic errors were found to propagate through the Kramers-Kronig relations in such a manner that the respective standard deviations of the real and imaginary components of complex quantities at any given frequency are equal. The only requirements were that the errors be stationary in the sense of replication at each measurement frequency, that errors be uncorrelated with respect to frequency, that the derivative of the variance with respect to frequency exists, and that the Kramers-Kronig relations be satisfied. Experimental results for electrochemical and rheological systems are presented which support the conclusion that the real and imaginary components have the same variance. This result and the conclusions reported herein appear to be general and should apply for any physical system in which the real and imaginary components are obtained from the same measurement.

## Introduction

While use of weighting strategies that account for the stochastic error structure of measurements enhances the information that can be extracted from regression of spectroscopic data,<sup>1-11</sup> independent assessment of the error structure is needed. The error structure for most radiation-based spectroscopic measurements such as absorption spectroscopy and light scattering can be readily identified.<sup>12,13</sup> The error analysis approach has been successful for some optical spectroscopy techniques because these systems lend themselves to replication and, therefore, to the independent identification of the different errors that contribute to the total variance of the measurements. In contrast, the stochastic contribution to the error structure of electrochemical impedance spectroscopy measurements generally cannot be obtained from the standard deviation of repeated measurements because even a mild nonstationary behavior introduces a nonnegligible time-varying bias contribution to the error. Recent advances in the use of measurement models for filtering lack of replicacy have made possible experimental determination of the stochastic and bias contributions to the error structure for impedance measurements.<sup>14-18</sup>

The measurement model approach for identification of error structures is widely used (see, for example, Ref. 12 and 13 for applications to optical spectroscopies and Ref.

19 for general application to spectroscopy). Recently, a measurement model approach has been applied to identify the error structures of impedance spectra obtained for a large variety of electrochemical systems.<sup>14-18</sup> One striking result of application of measurement models to impedance spectroscopy has been that the standard deviation of the real and imaginary components of the impedance spectra were found to be equal, even where the two components differed by several orders of magnitude. The only exception was found when the data did not conform to the Kramers-Kronig relations or when the precision of the measurement did not allow calculation of the standard deviation of one of the components (*i.e.*, all significant digits reported by the instrumentation for the replicated measurements were equal, see Ref. 20). The objective of the present work was to explore whether the equality of the noise levels in the real and imaginary parts of electrochemical impedance spectra can be described as being a direct consequence of the manner in which errors propagate through the Kramers-Kronig relations when both real and imaginary components are obtained from the same measurement.

## Experimental Motivation

Spectroscopic measurements which yield complex variables are illustrated in hierarchical form in Fig. 1. Spectrophotometric techniques such as absorption spectroscopy and light scattering record the light intensity as a function of the wavelength of the incident radiation used

\* Electrochemical Society Student Member.  
\*\* Electrochemical Society Active Member.



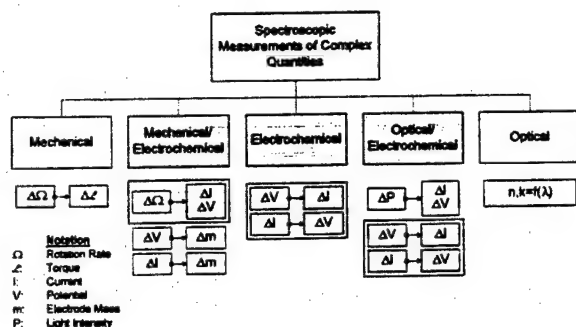


Fig. 1. Hierarchical representation of spectroscopic measurements. The shaded boxes represent measurement strategies for which the real and imaginary parts of Kramers-Kronig transformable impedance had the same standard deviation. Following completion of the analysis reported here, an experimental investigation was begun which showed that the real and imaginary parts of complex viscosity also have the same standard deviation if the spectra are consistent with the Kramers-Kronig relations.

to interrogate the sample. The frequency dependence arises from the wavelength of light employed. Electrochemical and mechanical spectroscopic techniques employ a modulation of a system variable such as applied potential, and the frequency dependence arises from the frequency of the modulation. In electrochemical, mechanical, and some spectrophotometric techniques, both real and imaginary (or modulus and phase angle) components are obtained from a single measured variable (e.g., the impedance).

To date, the equality of the standard deviations for real and imaginary components was observed for several such systems which are highlighted in Fig. 1. The equality of the standard deviation for real and imaginary components was observed for

1. Electrohydrodynamic impedance spectroscopy (EHD), a coupled mechanical/electrochemical measurement in which the rotation rate of a disk electrode is modulated about a preselected value. The impedance response at a fixed potential is given by  $\Delta I/\Delta\Omega$ .<sup>17</sup>

2. Electrochemical impedance spectroscopy (EIS). The data base now includes measurements for electrochemical and solid-state systems under both potentiostatic and galvanostatic modulation.<sup>14-16</sup> The equality of the standard deviation for real and imaginary components was observed even for systems with a very large solution resistance.<sup>20</sup>

3. Optically-stimulated impedance spectroscopy. Impedance measurements were obtained for solid-state systems under monochromatic illumination.<sup>21</sup>

The contention that the variances of the real and imaginary parts of Kramers-Kronig transformable complex variables are equal is supported by experimental evidence and has been validated statistically, as discussed in a subsequent section.

In contrast to results found for electrochemical and mechanical spectroscopies, the standard deviations for the real and imaginary components of the complex refractive index from spectrophotometric measurements were correlated but not necessarily equal.<sup>22</sup> However, for measurement of optical properties (e.g., the real and imaginary components of the complex refractive index) over a sufficiently broad range of frequencies, different instruments with their particular error structures must be used; whereas in electrochemical and mechanical spectroscopies a single instrument is used to measure both the real and imaginary components simultaneously.

For electrochemical and mechanical/electrochemical spectroscopies, the experimental evidence for the equality of the standard deviation of real and imaginary components is compelling and suggests that there may be a fundamental explanation for the observed relationship between the noise level of real and imaginary components of the impedance response.

## Application of the Kramers-Kronig Relations

The Kramers-Kronig relations are integral equations which constrain the real and imaginary components of complex quantities for systems that satisfy conditions of causality, linearity, and stability.<sup>23-26</sup> The Kramers-Kronig transforms arise from the constitutive relations associated with the Maxwell equations for description of an electromagnetic field at interior points in matter. Bode extended the concept to electrical impedance and tabulated various forms of the Kramers-Kronig relations.<sup>25</sup>

An application of the Kramers-Kronig relations to variables containing stochastic noise was presented by Macdonald, who showed, through a Monte Carlo analysis with synthetic data and an assumed error structure, that the standard deviation of the impedance component predicted by the Kramers-Kronig relations was equal to that of the input component.<sup>27</sup> The analysis was incomplete because it did not identify correctly the conditions under which the variances of the real and imaginary components of experimental impedance data are equal, and the author continued to use a weighting strategy in his regressions based on a modified proportioning error structure for which the variances of the real and imaginary components of experimental impedance data are different.<sup>27-29</sup>

The objective of the present work is to identify the error structure for frequency-dependent measurements. Herein we report an explicit relationship between the variances of the real and imaginary components of the error without *a priori* assumption of the error structure. The only requirements are that the Kramers-Kronig relations be satisfied, that the errors be stationary in the sense of replication at the measurement frequency, that the derivative of the variance with respect to frequency exists, and that the errors be uncorrelated with respect to frequency. In the subsequent section, stochastic error terms are incorporated into the derivation of Kramers-Kronig relations to examine how the errors for the real and imaginary terms are propagated.

## Absence of Stochastic Errors

The Kramers-Kronig transforms can be derived under the assumptions that the system is linear, stable, stationary, and causal. The system is assumed to be stable in the sense that response to a perturbation to the system does not grow indefinitely and linear in the sense that the response is directly proportional to an input perturbation at each frequency. Thus, the response to an arbitrary perturbation can be treated as being composed of a linear superposition of waves. The response is assumed to be analytic at frequencies of zero to infinity. The statement that the response must be analytic in the domain of integration may be viewed as being a consequence of the condition of primitive causality, i.e., that the effect of a perturbation to the system cannot precede the cause of the perturbation.<sup>30</sup>

The starting point in the analysis is that the integral around the closed loop (Fig. 2) must vanish by Cauchy's integral theorem<sup>31</sup>

$$\oint [Z_r(\infty)(x) - Z_r(\infty)]dx = 0 \quad [1]$$

where  $Z$  is the impedance response and  $x$  is the complex frequency. Equation 1 yields (see, e.g., Ref. 26)

$$Z_i(\omega) = \frac{2\omega}{\pi} \int_0^\infty \frac{Z_r(x) - Z_r(\omega)}{x^2 - \omega^2} dx \quad [2a]$$

and

$$Z_r(\omega) - Z_r(\infty) = \frac{2\omega}{\pi} \int_0^\infty \frac{-xZ_i(x) + \omega Z_i(\omega)}{x^2 - \omega^2} dx \quad [2b]$$

where only the principal value of the respective integrals is considered. The terms  $Z_r(\omega)$  and  $\omega Z_i(\omega)$  in Eq. 2a and b, respectively, facilitate numerical evaluation of the singu-



lar integrals, but do not contribute to the numerical value of the integrals as

$$\int_0^{\infty} \frac{dx}{x^2 - \omega^2} = 0 \text{ for } \omega \neq 0.^{32}$$

A similar development cannot be used to relate the real and imaginary parts of stochastic quantities because Eq. 1 is not satisfied except in an expectation sense.

### Propagation of Stochastic Errors

The stochastic error can be defined by

$$Z_{\text{ob}}(\omega) = Z(\omega) + \epsilon(\omega) = [Z_r(\omega) + \epsilon_r(\omega)] + j[Z_i(\omega) + \epsilon_i(\omega)] \quad [3]$$

where  $Z_{\text{ob}}(\omega)$  is the observed value of the impedance at any given frequency  $\omega$  and  $Z(\omega)$ ,  $Z_r(\omega)$ , and  $Z_i(\omega)$  represent the error-free values of the impedance which conform exactly to the Kramers-Kronig relations. The measurement error  $\epsilon(\omega)$  is a complex stochastic variable such that  $\epsilon(\omega) = \epsilon_r(\omega) - j\epsilon_i(\omega)$ . Clearly, at any frequency  $\omega$

$$E[Z(\omega)_{\text{ob}}] = Z(\omega) \quad [4]$$

only if

$$E[\epsilon_r(\omega)] = 0 \quad [5a]$$

and

$$E[\epsilon_i(\omega)] = 0 \quad [5b]$$

Equation 5 is satisfied for errors that are stochastic and do not include the effects of bias.

*Transformation from real to imaginary.*—The Kramers-Kronig relations can be applied to obtain the imaginary part from the real part of the impedance spectrum only in an expectation sense

$$E[Z_i(\omega)] = \frac{2\omega}{\pi} E \left[ \int_0^{\infty} \frac{Z_r(x) - Z_r(\omega) + \epsilon_r(x) - \epsilon_r(\omega)}{x^2 - \omega^2} dx \right] \quad [6]$$

It is evident from Eq. 6 that, for the expected value of the observed imaginary component to approach its true value in the Kramers-Kronig sense, Eq. 5a must be satisfied and that

$$E \left[ \frac{2\omega}{\pi} \int_0^{\infty} \frac{\epsilon_r(x)}{x^2 - \omega^2} dx \right] = 0 \quad [7]$$

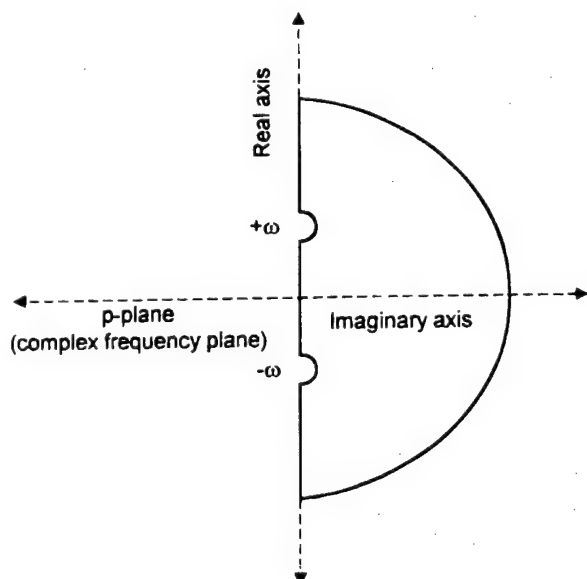


Fig. 2. Path of integration for the contour integral in the complex-frequency plane.

For the first condition to be met, the process must be stationary in the sense of replication at every measurement frequency. The second condition can be satisfied in two ways: in the hypothetical case where all frequencies can be sampled, the expectation can be carried to the inside of the integral, and Eq. 7 results directly from Eq. 5a. In the more practical case where the impedance is sampled at a finite number of frequencies,  $\epsilon_r(x)$  represents the error between an interpolated function and the "true" impedance value at frequency  $x$ . This term is composed of contributions from the quadrature and/or interpolation errors and from the stochastic noise at the measured frequencies  $\omega$ . In the latter case, Eq. 7 represents a constraint on the integration procedure. In the limit that quadrature and interpolation errors are negligible, the residual errors  $\epsilon_r(x)$  at a frequency  $x = \omega$  should be of the same magnitude as the stochastic noise  $\epsilon_r(\omega)$ .

Under the conditions that Eq. 5a and 7 are satisfied and for a given evaluation of Eq. 6

$$Z_i(\omega) + \epsilon_i^*(\omega) = \frac{2\omega}{\pi} \left\{ E \left( \int_0^{\infty} \frac{Z_r(x) - Z_r(\omega) + \epsilon_r(x) - \epsilon_r(\omega)}{x^2 - \omega^2} dx \right) + \int_0^{\infty} \frac{\epsilon_r(x)}{x^2 - \omega^2} dx \right\} \quad [8]$$

where  $\epsilon_i^*(\omega)$  represents the error in the evaluation of the Kramers-Kronig relations caused by the second integral on the right side. The variance of the transformed imaginary variable can be shown by the following development to be equal to the variance of the real variable. From Eq. 8

$$\text{var}[\epsilon_i^*(\omega)] = \left( \frac{2\omega}{\pi} \right)^2 \frac{1}{N-1} \sum_{k=1}^N \left[ \int_0^{\infty} \frac{\epsilon_{r,k}(x)}{x^2 - \omega^2} dx - \int_0^{\infty} \frac{\epsilon_{r,k}(x)}{x^2 - \omega^2} dx \right]^2 \quad [9]$$

where  $N$  is the number of replicate measurements which is assumed to be large. Under the assumption that Eq. 7 is satisfied

$$\text{var}[\epsilon_i^*(\omega)] = \frac{1}{N-1} \sum_{k=1}^N \left( \frac{2\omega}{\pi} \int_0^{\infty} \frac{\epsilon_{r,k}(x)}{x^2 - \omega^2} dx \right)^2 \quad [10]$$

As only principal values of the integrals are considered, it is appropriate to approach the point of singularity at  $x = \omega$  equally from both sides. In terms of the principal value, for specific values of  $k$ , the integral in Eq. 10 becomes

$$\frac{2\omega}{\pi} \int_0^{\infty} \frac{\epsilon_{r,k}(x)}{x^2 - \omega^2} dx = \frac{2\omega}{\pi} \int_0^{\omega^-} \frac{\epsilon_{r,k}(x)}{x^2 - \omega^2} dx + \frac{2\omega}{\pi} \int_{\omega^+}^{\infty} \frac{\epsilon_{r,k}(x)}{x^2 - \omega^2} dx \quad [11]$$

Under the transformations  $x = \omega y$  in the domain  $[0, \omega^-]$  and  $x = \omega/y$  in the domain  $[\omega^+, \infty]$

$$\frac{2\omega}{\pi} \int_0^{\infty} \frac{\epsilon_{r,k}(x)}{x^2 - \omega^2} dx = -\frac{2}{\pi} \int_0^1 \frac{(\epsilon_{r,k}(\omega y) - \epsilon_{r,k}(\omega/y))}{1 - y^2} dy \quad [12]$$

Equation 12 can be expressed in a summation sense as

$$-\frac{2}{\pi} \int_0^1 \frac{(\epsilon_{r,k}(\omega y) - \epsilon_{r,k}(\omega/y))}{1 - y^2} dy = -\frac{2}{\pi} \sum_{m=1}^M \left[ \frac{\epsilon_{r,k}(\omega y_m) - \epsilon_{r,k}(\omega/y_m)}{1 - y_m^2} W(y_m) \right] \quad [13]$$

where  $M$  is large,  $M - 1$  represents the number of intervals for the domain of integration, and  $W(y_m)$  is the weighting

factor which can be a function of the integration procedure chosen. From Eq. 10, 12, and 13

$$\text{var}[\epsilon_j^*(\omega)] = \frac{4}{\pi^2} \frac{1}{N-1} \sum_{k=1}^N \left( \sum_{m=1}^M \left[ \frac{\epsilon_{r,k}(\omega y_m) - \epsilon_{r,k}(\omega/y_m)}{1 - y_m^2} W(y_m) \right] \right)^2 \quad [14]$$

A general expression for the errors is given by  $\epsilon_{rk}(x) = P_k(0, 1)\sigma_r(x)$  where  $P_k(0, 1)$  is the  $k$ th observation of a symmetrically distributed random number with a mean value of zero and a standard deviation of 1, and  $\sigma_r(x)$  is the standard deviation for the errors which is representative of the error structure for the spectroscopy measurements and is assumed to be a continuous function of frequency. Under the assumption that the errors are uncorrelated with respect to frequency

$$\sigma_j^{*2}(\omega) = \sum_{m=1}^M \left\{ a_m [\sigma_r^2(\omega y_m) + \sigma_r^2(\omega/y_m)] \right\} \quad [15]$$

where the weighting factor is given by

$$a_m = \left[ \frac{W(y_m)}{1 - y_m^2} \right]^2 \quad [16]$$

In the limit that  $M \rightarrow \infty$ , the trapezoidal rule yields

$$a_m = \frac{4}{\pi^2} \frac{1}{(2m-1)^2} \quad [17]$$

and

$$\sum_{m=1}^{\infty} a_m = 0.5 \quad [18]$$

As shown in Fig. 3, the  $a_m$  coefficients decay rapidly away from  $y = 1$ . Beyond the first five terms, the individual contribution of each term is less than 1% of the first term. The series approaches its limiting value to within 1% when 20 terms are used. The error associated with using a finite number of terms in Eq. 15 therefore can be made to be negligibly small.

Under the assumption that  $\sigma_r^2(x)$  is continuous at  $x = \omega$ , a Taylor series expansion can be written in terms of frequency  $x$  which, when expressed in terms of the transformation variable  $x = \omega y_m$  (valid for  $x < \omega$ ), yields

$$\sigma_r^2(x) = \sigma_r^2(\omega) + \left[ \frac{d\sigma_r^2(x)}{dx} \right]_{x=\omega} [\omega(y_m - 1)] + O[(\omega(y_m - 1))^2] \quad [19]$$

Similarly, for the variable transformation  $x = \omega/y_m$  valid for  $x > \omega$

$$\sigma_r^2(x) = \sigma_r^2(\omega) + \left[ \frac{d\sigma_r^2(x)}{dx} \right]_{x=\omega} \omega \left( \frac{1}{y_m} - 1 \right) + O \left[ \left( \omega \left( \frac{1}{y_m} - 1 \right) \right)^2 \right] \quad [20a]$$

In the vicinity of  $y_m = 1$ , Eq. 20a can be expressed in a form similar to Eq. 19

$$\sigma_r^2(x) = \sigma_r^2(\omega) - \left[ \frac{d\sigma_r^2(x)}{dx} \right]_{x=\omega} \omega(y_m - 1) + O[(\omega(y_m - 1))^2] \quad [20b]$$

Equation 20b is justified because the major part of the contribution to the integral occurs within the range of  $y = 1$  to roughly  $y = 1 - 10^{-6}$ . The assumption that higher order terms in the expansion for  $\sigma_r^2(x)$  can be neglected is justified because the region over which linearization is

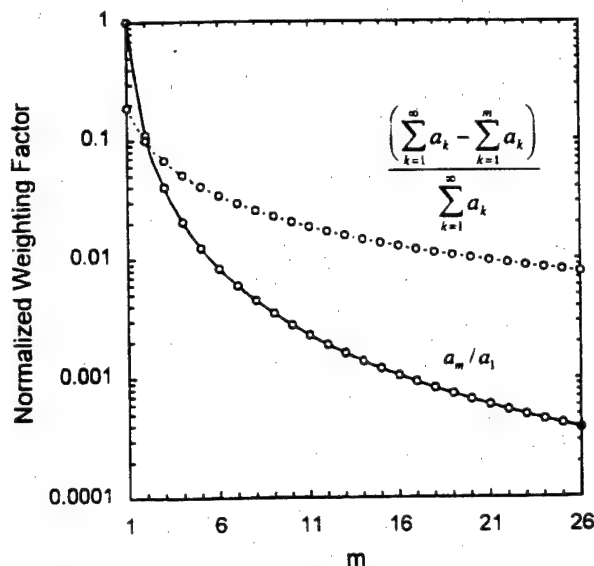


Fig. 3. Weighting factor for Eq. 16 as a function of  $m$  normalized to show relative contributions to the integral.

assumed to apply extends only 0.001 of the frequency  $\omega$ , e.g., 1 Hz at a frequency  $\omega$  of 1000 Hz.

Substitution of Eq. 19 and 20 into Eq. 15 yields

$$\sigma_j^{*2}(\omega) = \sigma_r^2(\omega) \sum_{m=1}^p 2a_m \quad [21]$$

where  $p \ll M$  and accounts for intervals in the vicinity of  $y = 1$ . Following Eq. 18

$$\sigma_j^{*2}(\omega) = \sigma_r^2(\omega) \quad [22]$$

This result is consistent with the results of Monte Carlo calculations for assumed error structures<sup>22,27</sup> but is obtained here without explicit assumption of an error structure. The only requirements are that the Kramers-Kronig relations be satisfied, that the errors be stationary in the sense of replication at each measurement frequency, that the errors be uncorrelated with respect to frequency, and that the derivative of the variance with respect to frequency exists.

**Transformation from imaginary to real.**—The Kramers-Kronig relations for obtaining the real part from the imaginary part of the spectrum can be expressed as Eq. 2b, which in terms of expectations becomes

$$E[Z_r(\omega) - Z_r(\infty)] = E \left[ \frac{2}{\pi} \int_0^\infty \frac{-xZ_i(x) + \omega Z_i(\omega) - x\epsilon_i(x) + \omega\epsilon_i(\omega)}{x^2 - \omega^2} dx \right] \quad [23]$$

Following the discussion in the earlier section, the necessary conditions for Kramers-Kronig transformability become Eq. 5b and

$$E \left[ \frac{2}{\pi} \int_0^\infty \frac{x\epsilon_i(x)}{x^2 - \omega^2} dx \right] = 0 \quad [24]$$

The variance of the error in the evaluation of Eq. 23 is given by

$$\text{var}(\epsilon_r^*) = \frac{1}{N-1} \sum_{k=1}^N \left[ \frac{2}{\pi} \int_0^\infty \frac{-x\epsilon_{j,k}(x)}{x^2 - \omega^2} dx \right]^2 \quad [25]$$

Under the transformation used in the earlier section

$$\int_0^{\infty} \frac{x \epsilon_{j,k}(x)}{x^2 - \omega^2} dx = - \int_0^1 \frac{y \epsilon_{j,k}(\omega y)}{1 - y^2} dy + \int_{y_2}^1 \frac{(1/y) \epsilon_{j,k}(\omega/y)}{1 - y^2} dy + \int_{x(y_2)}^{\infty} \frac{x \epsilon_{j,k}(x)}{x^2 - \omega^2} dx \quad [26]$$

where a point of singularity at  $y_m = 0$  (at  $\omega = \infty$ ) introduced by the transformation  $x = \omega/y$  was avoided by further subdivision of the integral. Since  $y_2$  can be chosen such that the third integral of Eq. 26 has negligible value and that the first integral has a negligible contribution from the range  $y = 0$  to  $y_2$ , Eq. 26 can be solved by following a procedure similar to that adopted in the earlier section. A form similar to Eq. 14 is obtained

$$\text{var}[\epsilon_r^*(\omega)] = \frac{4}{\pi^2} \frac{1}{N-1} \sum_{k=1}^N \left( \sum_{m=1}^M \left[ \frac{y_m \epsilon_{j,k}(\omega y_m) - (1/y_m) \epsilon_{j,k}(\omega/y_m)}{1 - y_m^2} W(y_m) \right]^2 \right) \quad [27]$$

In the region of interest ( $y_m \rightarrow 1$ ),  $y_m/(1 - y_m^2)$ , and  $1/y_m(1 - y_m^2)$  tend toward  $1/(1 - y_m^2)$ . Hence

$$\text{var}[\epsilon_r^*(\omega)] = \frac{4}{\pi^2} \frac{1}{N-1} \sum_{k=1}^N \left( \sum_{m=1}^p \left[ \frac{\epsilon_{j,k}(\omega y_m) - \epsilon_{j,k}(\omega/y_m)}{1 - y_m^2} W(y_m) \right]^2 \right) \quad [28]$$

where  $p \ll M$  and accounts for the intervals in the region of  $y \rightarrow 1$ . Equation 28 is directly analogous to Eq. 14. Following the discussion in the previous section

$$\sigma_r^2(\omega) = \sigma_i^2(\omega) \quad [29]$$

Thus, the variance of the real part of the impedance is equal to the variance of the imaginary part of the impedance, independent of the direction of the transformation, if the Kramers-Kronig relations are satisfied in an expectation sense. For the Kramers-Kronig relations to be satisfied, the conditions stated through Eq. 5, 7, and 24 must be satisfied. Equation 5a and b represent the usual constraints on the experimental stochastic errors; whereas Eq. 7 and 24 represent constraints on the integration procedure.

As summarized in the following section, the theoretical development presented here is supported by experimental observations for various physical systems that satisfy the conditions of Kramers-Kronig relations.

### Experimental

The equality of the standard deviations for real and imaginary parts of the impedance has been observed for the impedance response of solid-state systems (GaAs Schottky diodes, ZnO varistors, ZnS electroluminescent panels),<sup>15,16,33</sup> corrosion of copper in seawater (under either potentiostatic or galvanostatic modulation),<sup>16,33,34</sup> electrochemistry at metal hydride electrodes (LaNi<sub>5</sub> and misch metal),<sup>33,35</sup> the electrohydrodynamic impedance response for reduction of ferricyanide and oxidation of ferrocyanide on Pt rotating disks,<sup>17,26</sup> the impedance response of membranes for which the solution resistance is large,<sup>20</sup> and the impedance response of electrical circuits with a large leading resistance.<sup>20</sup>

A standard statistical criterion can be used to confirm the hypothesis that the standard deviations (or variances) of the real and imaginary parts of the impedance are equal.<sup>37</sup> A typical result is presented in Fig. 4 for the reduction of ferricyanide on a Pt disk rotating at 3000 rpm where three replicate impedance scans were obtained. The test criterion,  $F = \sigma_r^2/\sigma_i^2$ , is compared in Fig. 4 with 1 and 5% limits for three replicates. On a frequency-by-frequency basis,  $1/F_{0.01} < F < F_{0.01}$ ; therefore, the hypothesis

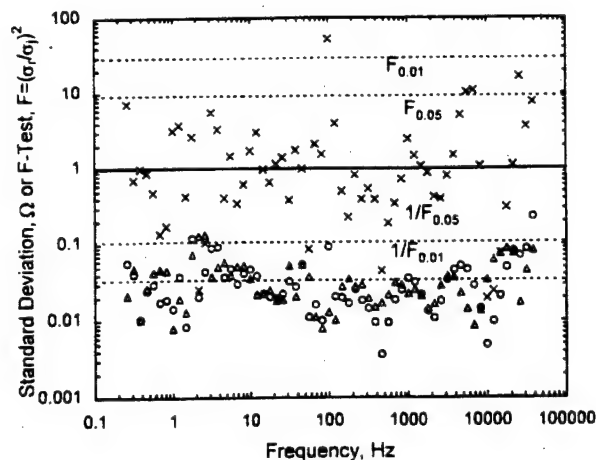


Fig. 4. Error structure obtained for reduction of ferricyanide on a platinum disk rotating at 3000 rpm in a 1 M KCl solution under potentiostatic modulation at one-half the limiting current value; (○) standard deviation for real part of the impedance response, (Δ) standard deviation for imaginary part of the impedance response, and (×)  $F$  test parameter  $F = \sigma_r^2/\sigma_i^2$ . Dashed lines correspond to significance levels for  $F$  for three replicates.

that the variance of the real part of the impedance is statistically different from the variance of the imaginary part over the measured frequency range can be rejected. The dispersion of  $F$  about one as a function of frequency further supports the conclusion that the variance of the real part of the impedance is equal to the variance of the imaginary part. The measurement model approach Agarwal *et al.*<sup>16,34,35,38</sup> showed that the data were consistent with the Kramers-Kronig relations.

The value of  $F_{0.01}$  for rejection of the null hypothesis (i.e.,  $\sigma_r^2 = \sigma_i^2$ ) approaches one when the number of replicated measurements is increased. Results are presented in Fig. 5 for the reduction of ferricyanide on a Pt disk rotating at 120 rpm where 25 replicate impedance scans were obtained. The test criterion,  $F = \sigma_r^2/\sigma_i^2$ , is compared in Fig. 5 with 1 and 5% limits for 25 replications. At frequencies below 100 Hz, the hypothesis that  $\sigma_r^2 = \sigma_i^2$  is confirmed. Above 100 Hz, the values for  $F$  and the trending as a func-

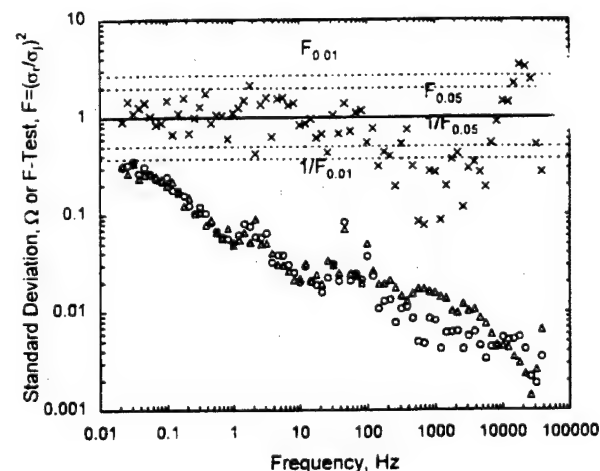


Fig. 5. Error structure obtained for reduction of ferricyanide on a platinum disk rotating at 120 rpm in a 1 M KCl solution under potentiostatic modulation at 0.25 of the limiting current value; (○) standard deviation for real part of the impedance response, (Δ) standard deviation for imaginary part of the impedance response, and (×)  $F$  test parameter  $F = \sigma_r^2/\sigma_i^2$ . Dashed lines correspond to significance levels for  $F$  for 25 replicates.

tion of frequency suggest that  $\sigma_r^2 \neq \sigma_i^2$ . For this experiment, however, the measurement model approach of Agarwal *et al.*<sup>18,34,35,38</sup> showed that the data collected at high frequency were inconsistent with the Kramers-Kronig relations.

The derivation presented here suggests that, if  $\sigma_r^2 = \sigma_i^2$  must be true for systems that satisfy the Kramers-Kronig relations, the experimental observation of the equality of the variance of the real and imaginary parts of the impedance cannot be attributed to unique features of electrochemical systems or of the frequency-response analyzer (FRA). This conclusion was subsequently tested by measuring the frequency-dependent complex viscosity of viscoelastic fluids using a Rheometrics RMS-800 parallel-plate viscometer.<sup>39</sup> This system is nonelectrochemical and does not employ an FRA. For measurements that satisfied the Kramers-Kronig relations, the standard deviations for real and imaginary parts of the viscosity were found to be equal.<sup>39</sup> Results are presented in Fig. 6a for the complex viscosity of a concentrated polyethylene oxide solution. The *F* test, presented in Fig. 6b, confirms that  $\sigma_r^2 = \sigma_i^2$ .

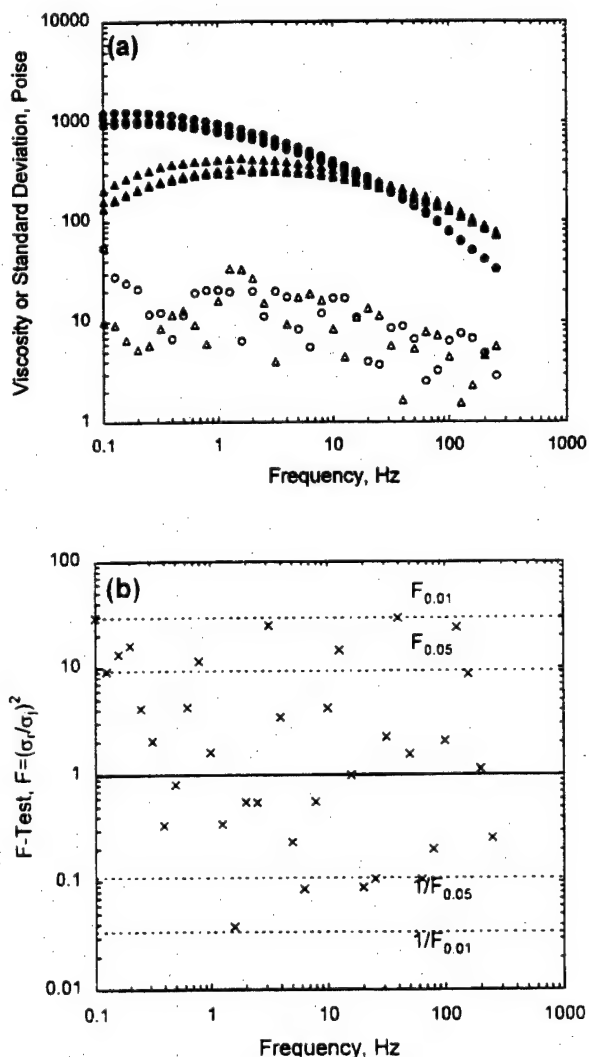


Fig. 6. (a) Complex viscosity and corresponding error structure obtained for a concentrated solution of polyethylene oxide (Mw 300,000) in water; filled symbols represent the measured complex viscosity, and open symbols correspond to the standard deviation; (○) the real part of the viscosity and (Δ) the imaginary part of the viscosity. (b) Test for inequality of the variance; (×) *F* test parameter  $F = \sigma_r^2/\sigma_i^2$ , and dashed lines correspond to significance levels for *F* for three replicates.

The results presented here demonstrate theoretically and experimentally that  $\sigma_r^2 = \sigma_i^2$  when the Kramers-Kronig relations are satisfied. Manuscripts are in preparation which describe in greater detail the results for the experimental systems presented in Fig. 4 to 6.

## Discussion

The result of the development presented here is that, for data that are consistent with the Kramers-Kronig relations in an expectation sense, the standard deviation of the real part of a complex spectrum at a given frequency must be equal to the standard deviation of the imaginary part. The development did not require any assumptions concerning analyticity of the stochastic noise with respect to frequency; therefore, the result applies to spectra in which data are collected sequentially as well as to spectra in which a single observation is used to resolve a spectrum, as is done, for example, by Fourier transformation of transient data.

The implications of this result are illustrated in Fig. 7, where the real and imaginary parts of an impedance spectrum are presented as functions of frequency. The probability distribution function for the data, corresponding to an equal standard deviation for the real and imaginary parts, is shown at a frequency of 0.03 Hz. The real part of the impedance at this frequency is roughly 100 Ω as compared to -3 Ω for the imaginary part, and the noise level therefore represents a much larger percentage of the imaginary signal than the real. This result, which has been

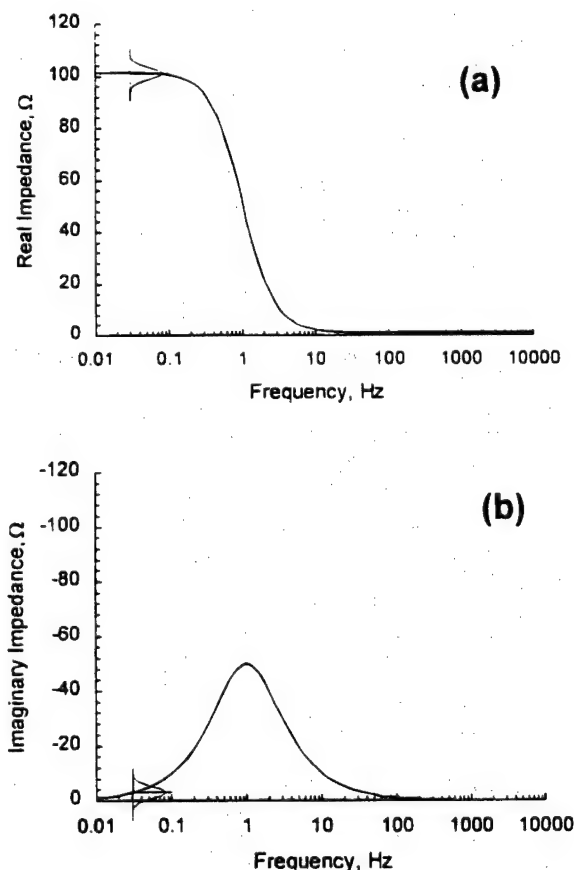


Fig. 7. Real (a) and imaginary (b) parts of a typical electrochemical impedance spectrum as a function of frequency. The normal probability distribution function, shown at a frequency of 0.03 Hz, shows that one consequence of the equality of the standard deviation for real and imaginary components is that the level of stochastic noise as a percentage of the signal can be much larger for one component than the other.

observed in many experimental systems,<sup>14-18,20,33-36</sup> is now shown to have a fundamental basis.

While the development presented here shows that the standard deviations for the real and imaginary parts of a Kramers-Kronig-transformable complex quantity are equal, the instantaneous realizations of the stochastic errors for the respective components have been shown experimentally to be uncorrelated.<sup>16,34</sup> The errors also were found to be uncorrelated with respect to frequency,<sup>16,34</sup> an observation that supports a key assumption made here. The assumption of the existence of the first derivative of the variance is supported by the identification of error structures presented in Fig. 4 to 6 and in Ref. 14-18, 20, and 33-36.

The need to identify an appropriate form for the impedance  $Z(x)$  in the presence of stochastic errors (e.g., Eq. 8 and 23) supports the use of measurement models composed of line shapes that themselves satisfy the Kramers-Kronig relations. The use of such measurement models is superior to the use of polynomial fitting because fewer parameters are needed to model complex behavior. Experimental data seldom contain a frequency range sufficient to approximate the range of integration of 0 to  $\infty$  required to evaluate the Kramers-Kronig integrals; therefore, extrapolation of the data set is required. Measurement models can be used to extrapolate the experimental data set, and the implications of the extrapolation procedure are quite different than from extrapolations with polynomials. The extrapolations done with measurement models are based on a common set of parameters for the real and imaginary parts and on a model structure that has been shown to represent the observations adequately. The confidence in the extrapolation using measurement models is, therefore, higher. In addition, as the line shapes used satisfy the Kramers-Kronig relations, experimental data may be checked for consistency with the Kramers-Kronig relations without actually integrating the equations over frequency, avoiding the concomitant quadrature errors.<sup>18,29,34-36,38,40</sup> The correlation and bias errors introduced by quadrature errors are discussed further in Ref. 22. The results presented here also indicate clearly the importance of identifying the nature of the error structure prior to application of the Kramers-Kronig transforms.

The analytic approach presented here establishes an explicit relationship between  $\sigma_r$  and  $\sigma_i$  with the only requirement that the errors be stationary in the sense of replication at each measurement frequency, that errors be uncorrelated with respect to frequency, that the derivative of the variance with respect to frequency exists, and that the Kramers-Kronig relations be satisfied. In addition, the conditions for the applicability of the Kramers-Kronig relations to experimental data have been identified, i.e., that Eq. 5, 7, and 24 be satisfied.

### Conclusion

Knowledge of the error structure plays a critical role in interpreting spectroscopic measurements. An assessment of the stochastic (or noise) component of the errors allows refinement of regression strategies and can guide design of experiments to improve signal-to-noise ratios. Assessment of consistency of data with the Kramers-Kronig relations is also important because inconsistencies can be attributed to experimental bias errors which must be accounted for during interpretation of measurements.

In this work, the experimental observation that real and imaginary parts of the impedance have the same standard deviation was found to have a fundamental basis for stationary error structures. The propagation of stochastic errors through the Kramers-Kronig relations in both directions (real-to-imaginary and imaginary-to-real) yielded standard deviations that were equal. This result appears to be general and should apply for all spectroscopic measurements in which real and imaginary components are obtained simultaneously and with the same instrumentation. Thus, the observations concerning the error structure of electrochemical, optical-electrochemi-

cal, and mechanical-electrochemical impedance spectra should apply as well to purely mechanical spectroscopic measurements.<sup>39</sup>

This work suggests also that evaluation of stochastic errors could provide insight into the degree of consistency with the Kramers-Kronig relations. The concept that there exists a relationship between stochastic error structure and bias errors is supported by repeated experimental observation that the standard deviation of real and imaginary parts of the impedance were equal except for spectra that were found to be inconsistent with the Kramers-Kronig relations.

### Acknowledgment

This work was supported in part by the U.S. Office of Naval Research under Grant No. N00014-93-1-0056 (A. J. Sedriks, Program Monitor), and by the Engineering Research Center (ERC) for Particle Science and Technology at the University of Florida, the National Science Foundation Grant No. EEC-94-02989, and the Industrial Partners of the ERC. Helpful conversations with Claude Deslouis and Bernard Tribollet (CNRS, Paris) and the assistance of Yudit Candocia are gratefully acknowledged.

Manuscript submitted March 7, 1996; revised manuscript received Sept. 27, 1996.

University of Florida assisted in meeting the publication costs of this article.

### LIST OF SYMBOLS

$a$	weighting factor defined by Eq. 16
$I$	current, A
$j$	the imaginary number, $\sqrt{-1}$
$M$	number of nodes used for numerical evaluation of integrals
$N$	number of observations for replicated experiments
$W$	weighting factor for numerical evaluation of integrals
$x$	frequency, rad/s
$y$	integration variable defined above Eq. 12
$Z$	complex impedance, $\Omega$
$\epsilon$	complex stochastic error
$\eta$	complex viscosity
$\omega$	frequency, rad/s
$\Omega$	rotation speed, rad/s
Subscripts	
$j$	imaginary part
$k$	observation number for replicated experiment
$m$	index number used for numerical evaluation of integrals
$r$	real part

### REFERENCES

1. G. E. P. Box and N. R. Draper, *Empirical Model-Building and Response Surfaces*, John Wiley & Sons, Inc., New York (1987).
2. H. W. Sorenson, *Parameter Estimation: Principles and Problems*, Marcel Dekker, Inc., New York (1980).
3. G. A. F. Seber, *Linear Regression Analysis*, pp. 330-334, John Wiley & Sons, New York (1977).
4. J. R. Macdonald and L. D. Potter, Jr., *Solid State Ionics*, **23**, 61 (1987).
5. J. R. Macdonald, *Electrochim. Acta*, **35**, 1483 (1990).
6. J. R. Macdonald and W. J. Thompson, *Commun. Statist. Simula.*, **20**, 843 (1991).
7. P. Zoltowski, *J. Electroanal. Chem.*, **178**, 11 (1984).
8. P. Zoltowski, *ibid.*, **260**, 269 (1989).
9. P. Zoltowski, *ibid.*, **260**, 287 (1989).
10. B. Robertson, B. Tribollet, and C. Deslouis, *This Journal*, **135**, 2279 (1988).
11. B. A. Boukamp, *Solid State Ionics*, **20**, 31 (1986).
12. R. W. Christy, *Am. J. Phys.*, **40**, 1403 (1972).
13. A. Jutan and L. H. Garcia-Rubio, *Process Control and Quality*, **4**, 235 (1993).
14. P. Agarwal, M. E. Orazem, and L. H. Garcia-Rubio, *This Journal*, **139**, 1917 (1992).
15. M. E. Orazem, P. Agarwal, A. N. Jansen, P. T. Wojcik, and L. H. Garcia-Rubio, *Electrochim. Acta*, **38**, 1903 (1993).
16. P. Agarwal, O. D. Crisalle, M. E. Orazem, and L. H. Garcia-Rubio, *This Journal*, **142**, 4149 (1995).

17. M. E. Orazem, P. Agarwal, C. Deslouis, and B. Tribollet, *ibid.*, **143**, 948 (1996).
18. P. Agarwal, M. E. Orazem, and L. H. García-Rubio, *ibid.*, **142**, 4159 (1995).
19. L. K. DeNoyer and J. G. Good, *American Laboratory*, March 1990. Software available from Spectrum Square Associates, Ithaca, NY, 114850.
20. M. E. Orazem, T. El Moustafid, C. Deslouis, and B. Tribollet, *This Journal*, **143**, 3880 (1996).
21. A. N. Jansen, Ph.D. Thesis, University of Florida, Gainesville, FL (1992).
22. C. Bacon, L. H. García-Rubio, and M. E. Orazem, *J. Phys. D: Appl. Phys.*, Submitted.
23. R. de L. Kronig, *J. Opt. Soc. Am. Rev. Sci. Instrum.*, **12**, 547 (1926).
24. R. de L. Kronig, *Phys. Z.*, **30**, 521 (1929).
25. H. A. Kramers, *ibid.*, p. 522.
26. H. W. Bode, *Network Analysis and Feedback Amplifier Design*, D. Van Nostrand Company, Inc., New York (1945).
27. J. R. Macdonald, *Electrochim. Acta*, **38**, 1883 (1993).
28. J. R. Macdonald, *J. Electroanal. Chem.*, **378**, 17 (1994).
29. B. A. Boukamp and J. R. Macdonald, *Solid State Ionics*, **74**, 85 (1994).
30. H. M. Nussenzveig, *Causality and Dispersion Relations*, Academic Press, New York (1972).
31. J. Killingbeck and G. H. A. Cole, *Mathematical Techniques and Physical Applications*, pp. 227-230, Academic Press, New York (1971).
32. I. S. Gradshteyn and I. M. Ryzhik, *Table of Integrals, Series, and Products*, Eq. [3.241.3], Academic Press, New York (1980).
33. P. Agarwal, Ph.D. Thesis, University of Florida, Gainesville, FL (1994).
34. P. Agarwal, O. C. Moghissi, M. E. Orazem, and L. H. García-Rubio, *Corrosion*, **49**, 278 (1993).
35. P. Agarwal, M. E. Orazem, and A. Hiser, in *Hydrogen Storage Materials, Batteries, and Electrochemistry*, D. A. Corrigan and S. Srinivasan, Editors, PV92-5, p. 120, The Electrochemical Society Proceedings Series, Pennington, NJ (1992).
36. P. Agarwal, M. E. Orazem, and L. H. García-Rubio, *Electrochim. Acta*, **41**, 1017, (1996).
37. G. W. Snedecor and W. G. Cochran, *Statistical Methods*, 6th ed., The Iowa State University Press, Ames, Iowa (1967).
38. P. Agarwal, M. E. Orazem, and L. H. García-Rubio, in *Electrochemical Impedance: Analysis and Interpretation*, ASTM STP 1188, J. Scully, D. Silverman, and M. Kendig, Editors, p. 115, ASTM, Philadelphia (1993).
39. M. Durbha, M. E. Orazem, and L. H. García-Rubio, in *New Directions in Electroanalytical Chemistry*, J. Leddy and R. M. Wightman, Editors, PV96-9, p. 385, The Electrochemical Society Proceedings Series, Pennington, NJ (1996).



# Experimental Study of the Erosion-Corrosion of Copper and Copper-Nickel Alloys at the Corrosion Potential and at Anodic Potentials<sup>1</sup>

Paul T. Wojcik,<sup>1</sup> Eric Charrière,<sup>2</sup> and Mark E. Orazem<sup>1</sup>

<sup>1</sup>Department of Chemical Engineering  
University of Florida  
Gainesville, FL 32611

<sup>2</sup>Swiss Federal Institute of Technology  
Materials Department, Metallurgical Chemistry  
MX-C Ecublens  
Lausanne, Switzerland

## ABSTRACT

The erosion-corrosion of copper and copper-nickel alloys in synthetic sea water was investigated using an impinging jet. Video microscopy, corrosion potential monitoring, and impedance spectroscopy were used to investigate the state of the system and the reactivity of the electrode surface. Shear-induced removal of salt films was observed and found to be associated with significant increases in surface reactivity. Direct shear-induced removal of oxide films, however, was not observed. Nevertheless, the protective oxide layer showed sensitivity in passively-aerated seawater to large fluid velocities and to small perturbations in potential. The films were stable under all conditions tested in continuously-aerated seawater.

## INTRODUCTION

Copper and copper alloys are widely used in marine environments because they are resistant to corrosion in seawater. This resistance is associated with formation of protective layers on the metal surface. However, copper and its alloys are known to be susceptible to enhanced corrosion in seawater when there is sufficient relative motion between the metal and the fluid.<sup>1-3</sup> The flow-enhanced corrosion of copper alloys in seawater has been attributed to erosion-corrosion.<sup>2</sup>

In the absence of suspended particles, erosion-corrosion is associated with mechanical disruption or removal of protective layers by hydrodynamic shear.<sup>2,4,5</sup> Protective layers are assumed to be removed when the shear force is greater than the binding force between the film and the substrate. Direct observation of shear-induced removal of films has been reported for some systems. Giralt and Trass<sup>6</sup> showed that removal of solid naphthalene and trans-cinnamic acid by a submerged impinging jet of saturated solution is proportional to the wall shear stress above a critical or threshold value. Steele and Geankoplis<sup>7</sup> reported removal of material by an apparent shear erosion mechanism. Esteban *et al.*<sup>8</sup> used an impinging jet system to identify shear

---

<sup>1</sup> P. T. Wojcik, E. Charrière, and M. E. Orazem, "Experimental Study of the Erosion-Corrosion of Copper and Copper-Nickel Alloys at the Corrosion Potential and at Anodic Potentials," *Proceedings of the Tri-Service Conference on Corrosion*, November 17-21, 1997.

induced removal of poorly adhered filming inhibitors on steel in chloride solutions. The removal of the inhibitor was associated with enhanced corrosion in regions of large hydrodynamic shear.

Efird reported critical values of shear stress for the erosion-corrosion of copper and some copper-based alloys in sea water (see Table 1).<sup>2</sup> His test apparatus consisted of a series of independent flow chambers with a rectangular cross section designed such that fresh sea water flowed parallel to the surface of the coupon. Flow establishment and disengagement regions were located up and downstream respectively to ensure a well-developed flow over the coupon. Coupons were removed and photographed after a thirty-day exposure. Accelerated corrosion was identified by the roughened appearance of corrosion products and of the metal surface after corrosion products were removed. A critical velocity for enhanced corrosion was identified which was correlated to shear stress. Onset of enhanced corrosion was consistently located at the leading edge of the coupon.

The experimental system used by Efird<sup>2</sup> was characterized by a uniform shear stress and a non-uniform mass transfer coefficient. The observation of a critical velocity for enhanced corrosion can therefore be attributed to either a shear-induced removal of protective films or to destabilization of the protective films by a differential mass transfer mechanism.

Using an impinging jet system for which mass transfer was uniform, Diem and Orazem<sup>9</sup> did not observe shear-induced corrosion on copper in alkaline chloride electrolytes for values of hydrodynamic shear which were as much as 10 times the critical shear stress reported by Efird.<sup>2</sup> In the alkaline chloride solutions used, passivation was observed in less than 100 seconds. The work of Diem and Orazem<sup>9</sup> cannot be compared directly to that of Efird<sup>2</sup> because the electrolyte was significantly different in composition from the seawater used in Efird's experiment. Steady-state films on copper alloys in seawater are reported to require 30 days or more to develop.<sup>10-13</sup>

The objective of this work was to determine whether shear-induced removal of protective films for copper and copper-nickel alloys could be observed in systems for which mass transfer is uniform. The exposure time for the coupons was up to 33 days, and ASTM standard synthetic seawater was used as the electrolyte.

## EXPERIMENTAL PROCEDURE

The hydrodynamics and the experimental design for the submerged axisymmetric impinging jet used in this study are presented in this section.

### Hydrodynamics of the Impinging Jet

The fluid mechanics within the region of the electrode is well-defined.<sup>14-18</sup> This geometry can be made to give uniform mass transfer rates across a disk electrode within the stagnation region. The stagnation region is defined to be the region surrounding the stagnation point in which the axial velocity, given by

$$v_z = -2\sqrt{av}\phi(\eta) \quad (1)$$

is independent of radial position, and the radial velocity is given by

$$v_r = ar \frac{d\phi(\eta)}{d\eta} \quad (2)$$

where  $a$  is the hydrodynamic constant which is a function only of geometry and fluid velocity,  $r$  and  $z$  are the radial and axial positions, respectively,  $\nu$  is the kinematic viscosity, and  $\phi$  is the stream function which is given in terms of dimensionless axial position  $\eta = z\sqrt{a/\nu}$  as<sup>18</sup>

$$\phi(\eta) = 0.656\eta^2 - 0.16667\eta^3 + 3.6444 \times 10^{-3}\eta^6 - 3.9682 \times 10^{-4}\eta^7 \quad (3)$$

Esteban *et al.* used ring electrodes to find that the stagnation region extends to a radial distance roughly equal to the inside radius of the nozzle.<sup>8</sup>

Within the stagnation region, the surface shear stress  $\tau_{rz}$  is given by

$$\tau_{rz} = -1.312r(\mu\rho)^{\frac{1}{2}}a^{\frac{3}{2}} \quad (4)$$

where  $\mu$  and  $\rho$  are the viscosity and density of the fluid, respectively. The hydrodynamic constant can be determined experimentally using ring or disk electrodes at the mass-transfer-limited condition and is proportional to the jet velocity.<sup>8,9</sup> The shear stress on the electrode surface is given in Figure 1 as a function of jet velocity for the range of velocities used in this work. The critical shear stress values reported by Efir<sup>2</sup> for copper (9.4 N/m<sup>2</sup>) and 70/30 copper nickel (47.9 N/m<sup>2</sup>) are provided for reference in Figure 1.

## Experimental Design

Because the mass transfer rate is uniform, differential mass transfer cells are not established for an electrode that lies entirely within the stagnation region. The impinging jet system can therefore be used in the absence of suspended particles to isolate the influence of the hydrodynamic shear stress. If the removal of protective layers by hydrodynamic shear is the primary cause of erosion-corrosion and the shear stress outside a certain critical radius is large enough to cause that removal, then the metal outside the critical radius will corrode at a significantly higher rate than the metal inside the critical radius. Since shear stress is a function of both radial position and jet velocity, the critical radius corresponding to the critical shear stress would be a function of jet velocity for fixed geometry.<sup>8</sup>

A schematic representation of the experimental setup is presented in Figure 2. The experimental impinging jet cell used for this work was a modification of the cell design used by Diem and Orazem.<sup>9</sup> The cell was enclosed completely to eliminate entrainment of air. The system was capable of continuous operation at a maximum mean jet velocity of 6.75 m/s which yielded a shear stress of 195 N/m<sup>2</sup> at 80% of the radius of a 0.635 cm (0.25 inch) diameter electrode. This value is 20 times larger than the critical shear stress of 9.8 N/m<sup>2</sup> reported by Efir<sup>2</sup> for copper.<sup>2</sup>

The system was configured with the jet positioned facing down. The top sides of the impinging jet cell were angled at 45° and 60° from vertical and an access port was centered in each side to allow in-situ observation of the working electrode. The port which supported the video microscope contained a sapphire window sealed with an o-ring and held in place by an aluminum retaining ring. The other access port housed a thermometer to monitor cell temperature

which was compared with reservoir temperature. At high flow rates, viscous dissipation caused the temperature in the cell to differ from that in the reservoir. The temperature in the cell was controlled at a desired value by adjusting the set-point temperature in the cooling bath.

Three *in-situ* experimental techniques were incorporated in this work. The corrosion potential with reference to a saturated calomel reference electrode was monitored continuously throughout the course of an experiment. Variable-amplitude galvanostatically-modulated (VAG) impedance spectroscopy was used at specified intervals to investigate the reactivity of the electrode surface.<sup>19,20</sup> The VAG technique allowed collection of impedance data without altering the natural evolution of the corrosion potential with time. Video microscopy complimented the two electrochemical techniques by providing a visual record of the state of the electrode surface. Digital images of the surface were used to detect velocity-enhanced phenomena which were manifested as rings or halos on the surface of the disk electrode.

The surface reactivity was quantified through use of the measurement model approach.<sup>21-26</sup> This quantification followed three steps:

1. The frequency-dependent error structure was identified following the method presented by Agarwal *et al.*<sup>23</sup>
2. The portion of the spectrum that is consistent with the Kramers-Kronig relations was identified following the method presented by Agarwal *et al.*<sup>24</sup> The error structure found in step 1 above was used to weight the regression. High-frequency data were found to be corrupted by instrumental artifacts. The low-frequency data were typically found to be consistent with the Kramers-Kronig relations except for data collected early in the experiment where the system was changing rapidly.
3. The measurement model was regressed to the portion of the spectrum found in step 2 to be consistent with the Kramers-Kronig relations. The regressed parameter values were used to extrapolate to the zero frequency limit, and Monte Carlo simulations were performed using the standard deviations of the regressed parameters to estimate the confidence interval for the extrapolation. The polarization impedance was obtained by subtracting the regressed solution resistance from the extrapolated zero-frequency value.<sup>26</sup>

## RESULTS

The experiments discussed here involved annealed electrodes made of 99.9% copper (CDA110) or a 70/30 copper/nickel alloy (CDA715). The electrolyte was ASTM-D-1141 synthetic sea water.

### Copper in Passively-Aerated Electrolyte

In the experiments presented in this section, the electrolyte was aerated only by passive diffusion of air through the exposed air-electrolyte interface in the reservoir. The pH was measured to be 8.05, and the oxygen content of the electrolyte was 6 ppm. In the subsequent section, results are presented for continuously-aerated electrolytes, for which the air used for aerating the electrolyte was scrubbed to remove CO<sub>2</sub>. Continuous aeration had no effect on the pH of the electrolyte, which remained at 8.2. The oxygen content of the continuously and passively-aerated electrolytes was 7 and 6 ppm, respectively.

Potentiostatic Experiments-The utility of the experimental setup for detecting shear-induced removal of films can be seen in the results of experiments conducted for 99.9% copper electrode in flowing (0.1 m/s) aerated synthetic sea water at anodic potentials. The current-time traces resulting from potentiostatic experiments are given in Figure 3 for values of 100, 200, and 400 mV (SCE). These potentials corresponded to regions of the polarization curve that were influenced by formation of salt films which, as seen in Figure 3, to decrease the current observed. The 200 mV (SCE) trace showed a decrease in the current followed by a sharp increase that was evident at roughly 300 seconds. Successive video images were collected at a rate of 2/second for this experiment. The dashed lines in Figure 3 are the times corresponding to the video images given in Figure 4 of the coupon during the 200 mV(SCE) experiment. At short times (33 and 61 seconds), growth of salt films reduced the magnitude of the current. Following the current distribution on a disk electrode below the limiting current,<sup>27</sup> salt films formed first as a ring on the periphery of a copper disk electrode and then grew inward. During the early stage of dissolution (0 to 160 seconds), the video images showed three waves corresponding to formation of salt films. At 160 seconds, the beginning stage of the mechanical removal of a salt film layer was evident at the periphery of the electrode. (see Figure 4). This removal was coincident with a slight increase in current evident in Figure 3. At 341 seconds, more of the film has been removed, and, at still longer times, the film was removed completely and a new salt film was precipitated. The removal of the salt film caused a 30 percent increase in the observed current. The removal process initiated at the periphery of the electrode where the shear stress is the largest, and mechanical removal of chunks of the film was evident in the video. This work demonstrated that the reactivity of the copper is sensitive to removal of salt films and that the experimental technique can be used to observe shear-induced removal of films.

Galvanostatic Experiments at the Corrosion Potential.-The working electrode was 99.9% copper immersed in ASTM-D-1141 synthetic sea water. The corrosion potential is presented in Figure 5 as a function of time for a period of 33 days. The initial corrosion potential behavior of all the copper and copper/nickel alloys studied for this work was similar in the sense that the corrosion potential, immediately after submersion, increased rapidly during the first few hours.<sup>28</sup> As the corrosion potential became more positive, the rate of change slowed until a constant value was reached. The difference between the initial value and the constant value was as much as 70 mV. Electrohydrodynamic impedance measurements conducted under similar conditions showed that the electrochemical behavior of copper in synthetic seawater became insensitive to convective diffusion within 24 hours; thus, the electrochemical behavior of the copper was controlled by surface films after the first day of immersion.

The jet velocity for the first seven days was controlled at 1 m/s. A pseudo-steady-state value of -283 mV for the corrosion potential was reached after approximately 48 hours, and this value fluctuated by only 2 mV over the next five days. Impedance spectra collected during this same seven day period showed an initial decrease in the impedance followed by an increase to a pseudo-steady-state value. Following the seventh day, the solution was kept quiescent for 16 days after which a series of impedance scans was conducted to investigate corresponding changes in the electrode reactivity. Impedance scans taken before and after the 16 day quiescent period revealed an increase in the polarization impedance during period of time the solution was stagnant. Video images of the copper surface revealed the presence of a thick film.

After 556.6 hours, a large cathodic potential on the order of -1.3 V(SCE) was applied to the system for approximately 2 minutes resulting in the evolution of hydrogen from the electrode surface and removal of copper oxides. The impedance values after the potential excursion were reduced by a factor of 10 as compared to the impedance scans prior to the upset. A noticeable change in the appearance of the electrode surface was evident, and the presence of hydrogen bubbles on the surface was observed in the video images. The decrease in the impedance observed after the potential disturbance is consistent with removal of a protective film. This hypothesis is supported by the digital images which showed that portions of a surface film were removed, leaving bare copper visible around the periphery of the electrode.

Approximately 25 minutes after the potential disturbance, flow was resumed. Air that had accumulated in the lines was removed, after which the jet velocity was adjusted to 1 m/s. Data collection resumed 25 minutes after flow was started, and the resulting corrosion potentials are presented in Figure 6. The corrosion potential returned to the value before the potential disturbance after a period of 120 hours and remained constant for several days. A small adjustment of pH by addition of NaOH had no discernible effect on the corrosion potential. The corrosion potential changed abruptly, however, following an increase in jet velocities of 1.0 to 6.75 m/s. The values for the shear stress corresponding to these velocities at a radial position of  $r/r_0 = 0.8$  are 14.5 and 195 N/m<sup>2</sup>, respectively.

Impedance data collected during this leg of the experiment are presented in Figure 7. The impedance increased steadily after the potential disturbance, showing a decrease in reactivity as the protective films became reestablished. The value for the impedance approached a constant value after an additional 150 hours. The influence of pH modification from 8.05 to 8.24 on the impedance response was not discernible when plotted in impedance plane format, however, the influence of a change in jet velocity from 1.0 to 6.75 m/s on the impedance of the electrode is easily seen in Figure 7.

The polarization impedance corresponding to Figure 7 is shown in Figure 8 as a function of time. The polarization impedance and the associated confidence intervals given in Figure 8 were obtained by the measurement model concept developed in this group as part of the infrastructure for the erosion-corrosion experiments.<sup>21-26</sup> The polarization impedance increased with time. The impedance response was found to be sensitive to the small adjustment of pH 161 hours after the potential swing, and also showed a large increase in the reactivity of the surface following the increase in jet velocity.

The video micrographs shown in Figure 9 can give insight on the evolution of the electrode surface. The copper electrode at  $t=0$ , immediately after submersion in solution, showed polishing marks left by the 0.05  $\mu\text{m}$  alumina powder used in the final stage of wet polishing. The presence of a uniform film at  $t=169$  hours is consistent with electrohydrodynamic impedance spectroscopy measurements that showed that the electrochemical properties of the copper were governed by surface films after 24 hours of immersion. A similar uniform film was observed at  $t=671$  hours after the system recovered from the potential excursion. After the increase in jet velocity, which resulted in a large reduction in the polarization impedance, a uniform film was still evident ( $t=814$  hours). The apparently increased sharpness as compared to the image at  $t=671$  hours is attributed to removal of a salt film, exposing the granular structure below. No ring-shaped features were evident in the micrographs.



## Copper and 70/30 Copper/Nickel in Continuously-Aerated Electrolyte at the Corrosion Potential

The abrupt increase in reactivity with increased jet velocity shown in Figure 8 was reproducible for passively-aerated electrolytes, but was not observed for copper in continuously-aerated electrolyte. The corrosion potential transients shown in Figure 10 are typical of the results obtained in aerated ASTM-D-1141 synthetic sea water. Effects of velocity on corrosion potential were not seen. The extrapolated polarization impedance values given in Figure 11 showed that the surface reactivity stabilized after a period of 10 days and that increases in jet velocity from 1 m/s to 2 m/s, from 2 m/s to 4 m/s, and from 4 m/s to 6.2 m/s had no discernible effect. Ex-situ analysis by XPS of the electrodes after immersion in continuously-aerated electrolyte revealed the presence of Mg and Fe salts that were not present on electrodes after immersion in passively-aerated electrolyte. These results, and observation of a small decrease in pH in the passively-aerated case, are consistent with the hypothesis that the nature of surface films formed had changed due to passive incorporation of CO<sub>2</sub> through the air-electrolyte interface in the reservoir.

The corrosion potential of the 70/30 copper nickel alloy in continuously aerated ASTM-D-1141 synthetic sea water reached a steady value within 5 days, though the measurement had considerably more scatter than observed for the copper system. The extrapolated polarization impedance values showed that surface reactivity stabilized after a period of 10 days, and that increases in jet velocity from 2 m/s to 6 m/s had no discernible effect.

## CONCLUSIONS

Fully-developed oxide layers were observed in earlier work to be sensitive to small amplitude (50 mV) perturbations in potential.<sup>19</sup> Flow conditions resulting in a variation of potential across a copper surface can therefore disrupt protective oxide layers, not by direct mechanical removal, but by inducing electrochemical instability. Salt films resulting from an applied anodic potential were observed to be removed by shear forces, and removal of such films increased the reactivity of copper. This removal of salt films on parts of the electrode and not on others could contribute to a potential gradient that would destabilize oxide layers. Oxygenation cells are another source of potential gradients which could form when using a channel flow cell such as used by Efird.<sup>2</sup> The present work suggests that the enhanced corrosion seen by Efird may not be due to a shear-induced mechanical removal of an oxide film but may be due instead to destabilization of the film by a potential gradient across the electrode surface. The enhanced corrosion observed by Efird at the leading edge of the coupon is consistent with distribution of mass transfer expected for a channel flow cell, and the observation of a critical velocity is consistent with our observation of a critical potential for destabilization of the oxide layer.

The coupling of the VAG impedance algorithm and the extrapolation of impedance spectra developed for this work provides a powerful tool for assessing changes in the reactivity of an electrode. By setting the current to be equal to zero, galvanostatic modulation allowed the system to be held at the open-circuit condition, and the variable-amplitude technique ensured that the potential swing the system experienced was sufficiently small to ensure a linear response. The latter is particularly important because, in earlier work, a potential perturbation of 50 mV was sufficient to disrupt the passive films formed on copper in passively-aerated ASTM-D-1141 synthetic sea water.<sup>19</sup> The VAG impedance technique used in this work did not appear to affect

the naturally occurring transients in the system associated with growth of surface films. The extrapolation technique developed here was intended to make maximum use of the available measurements by providing a convenient measure of reactivity. This was especially important in developing an assessment of the data presented in Figure 7 where the rapidly changing conditions made some low frequency data inconsistent with the Kramers-Kronig relations.

The films formed on copper in passively-aerated synthetic seawater appeared to be less stable than those formed in highly-aerated synthetic seawater. Such films were found here to be sensitive to changes in jet velocity. In earlier work, these films were found to be sensitive as well to changes in sinusoidal potential swings.<sup>19</sup> This result is consistent with the numerical simulations of Moghissi which predicted that the oxide layers on copper would be sensitive to pH and, in the pH ranges typical of seawater, could be unstable to small perturbations of potential.<sup>29</sup>

### ACKNOWLEDGMENTS

This research was supported by the Office of Naval Research under Grant Numbers N00014-93-I-0056 and N00014-93-I-1113 (Dr. A. J. Sedriks, program monitor).

### REFERENCES

- <sup>1</sup> F.L. LaQue, *Marine Corrosion: Causes and Prevention*, John Wiley and Sons, N.Y. (1975).
- <sup>2</sup> K.D. Eiford, *Corrosion*, **33** (1977), 3.
- <sup>3</sup> R.J.K. Wood, S.P. Hutton, and D.J. Schiffrin, *Corrosion Science*, **30** (1990), 1177.
- <sup>4</sup> H.R. Copson, *Corrosion*, **16** (1960), 86t.
- <sup>5</sup> D. C. Silverman, *Corrosion*, **40** (1984), 220-226.
- <sup>6</sup> F. Giralt, and O. Trass, *Canadian Journal of Chemical Engineering*, **53** (1975), 505.
- <sup>7</sup> L. R. Steele, and C. J. Geankoplis, *AIChE Journal*, **5** (1959), 178.
- <sup>8</sup> J. M. Esteban, G. Hickey, and M. E. Orazem, *Corrosion*, **46** (1990), 896.
- <sup>9</sup> C. B. Diem and M. E. Orazem, *Corrosion*, **50** (1994), 290.
- <sup>10</sup> H. P. Hack and J. P. Gudas, "Inhibition of Sulfide-Induced Corrosion by Clean Seawater Pre-exposure," Report DTNSRDC/SME-79-85, David Taylor Naval Ship Research and Development Center, 1979.
- <sup>11</sup> J. R. Scully, H. P. Hack, and D. G. Tipton, *Corrosion*, **42** (1986), 462.
- <sup>12</sup> H. P. Hack and J. R. Scully, *Corrosion*, **45** (1986), 79.
- <sup>13</sup> H.P. Hack and H.W. Pickering, *Journal of the Electrochemical Society*, **138** (1991), 690.
- <sup>14</sup> M. T. Scholtz, and O. Trass, *AIChE Journal*, **16** (1970), 82.
- <sup>15</sup> M. T. Scholtz, and O. Trass, *AIChE Journal*, **16** (1970), 90.

- <sup>16</sup> F. Giralt, C.-J. Chia, and O. Trass, *Industrial and Engineering Chemistry, Fundamentals*, **16** (1977), 21.
- <sup>17</sup> C.-J. Chia, F. Giralt, and O. Trass, *Industrial and Engineering Chemistry, Fundamentals*, **16** (1977), 28.
- <sup>18</sup> D.-T. Chin, and C.-H. Tsang, *Journal of the Electrochemical Society*, **125** (1978), 1461.
- <sup>19</sup> P.T. Wojcik, P. Agarwal, and M. E. Orazem, *Electrochimica Acta*, **41** (1996), 977-983.
- <sup>20</sup> P. T. Wojcik and M. E. Orazem, *Corrosion*, in press.
- <sup>21</sup> P. Agarwal, M. E. Orazem, and L. H. García-Rubio, *Journal of the Electrochemical Society*, **139** (1992), 1917-1927.
- <sup>22</sup> P. Agarwal, O. C. Moghissi, M. E. Orazem, and L. H. García-Rubio, *Corrosion*, **49** (1993), 278-289.
- <sup>23</sup> P. Agarwal, O. D. Crisalle, M. E. Orazem, and L. H. García-Rubio, *Journal of the Electrochemical Society*, **142** (1995), 4149-4158.
- <sup>24</sup> P. Agarwal, M. E. Orazem, and L. H. García-Rubio, *Journal of the Electrochemical Society*, **142** (1995), 4159-4168.
- <sup>25</sup> M. E. Orazem, P. Agarwal, and L. H. García-Rubio, *Materials Science Forum*, **192-194** (1995), 563-572.
- <sup>26</sup> M. E. Orazem, P. T. Wojcik, I. Frateur, and L. H. García-Rubio, "Application of Measurement Models for Interpretation of Impedance Spectra for Corrosion," to be presented at Electrochemical Methods for Corrosion Research, EMCR 97, Trento, Italy, August 25-29, 1997.
- <sup>27</sup> M. E. Orazem and M. G. Miller, *Journal of the Electrochemical Society*, **134** (1987), 392-399.
- <sup>28</sup> P. Agarwal, O. C. Moghissi, M. E. Orazem, and L. H. García-Rubio, *Corrosion*, **49** (1993), 278-289.
- <sup>29</sup> O. C. Moghissi, *The Electrochemical Behavior of Copper in Chloride Solutions*, PhD dissertation, University of Florida, May, 1993.

Table 1. Critical velocity and shear stress for copper-based alloys in sea water as reported by Efid.<sup>2</sup>

Alloy / main components	Critical Velocity, m/s	Temperature, °C	Critical Shear, Stress N/m <sup>2</sup>
CA 122 copper	1.3	17	9.6
CA 687 copper /zinc	2.2	12	19.2
CA 706 90/10 copper/nickel	4.5	27	43.1
CA 715 70/30 copper/nickel	4.1	12	47.9
CA 722 copper/nickel/chromium	12.0	27	296.9

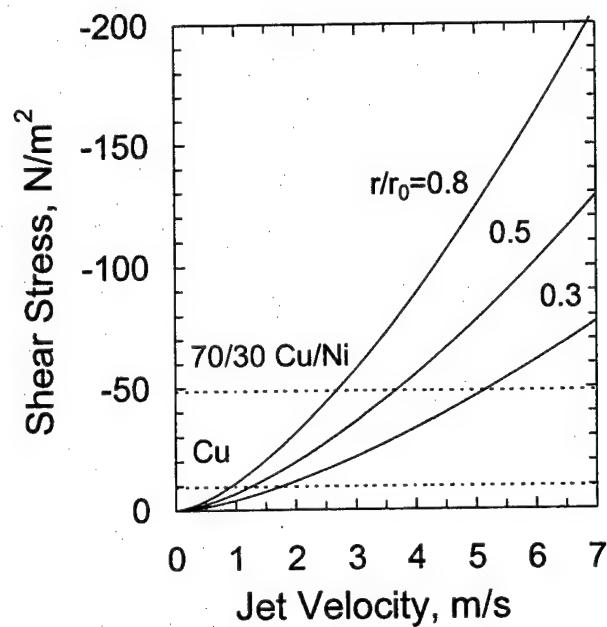


Figure 1. Shear stress as a function of jet velocity with dimensionless radial position on the electrode surface as a parameter for the impinging jet cell used in the present work. Critical shear stress values reported by Efird<sup>2</sup> are presented for reference.

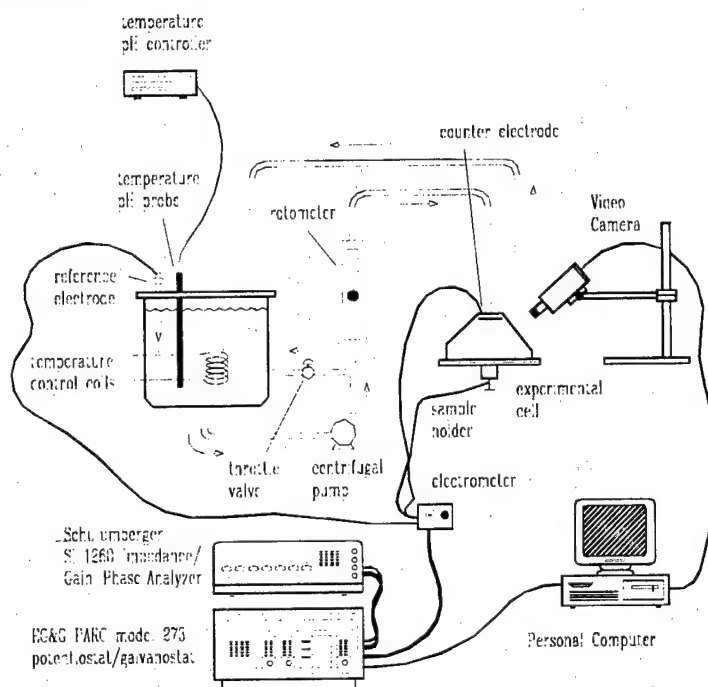


Figure 2. Experimental configuration used for measuring the influence of jet velocity on the corrosion of copper and copper alloys in synthetic sea water.

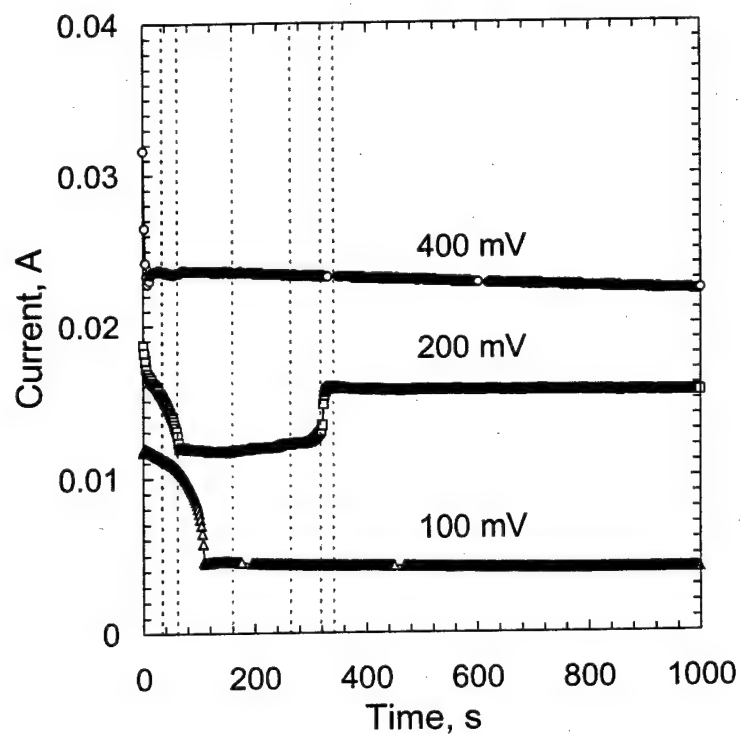


Figure 3. Current as a function of time for 99.9% copper in aerated synthetic sea water at a jet velocity of 0.1 m/s. The dashed lines correspond to the time at which images shown in Figure 4 were collected for the coupon held at 200 mV (SCE).

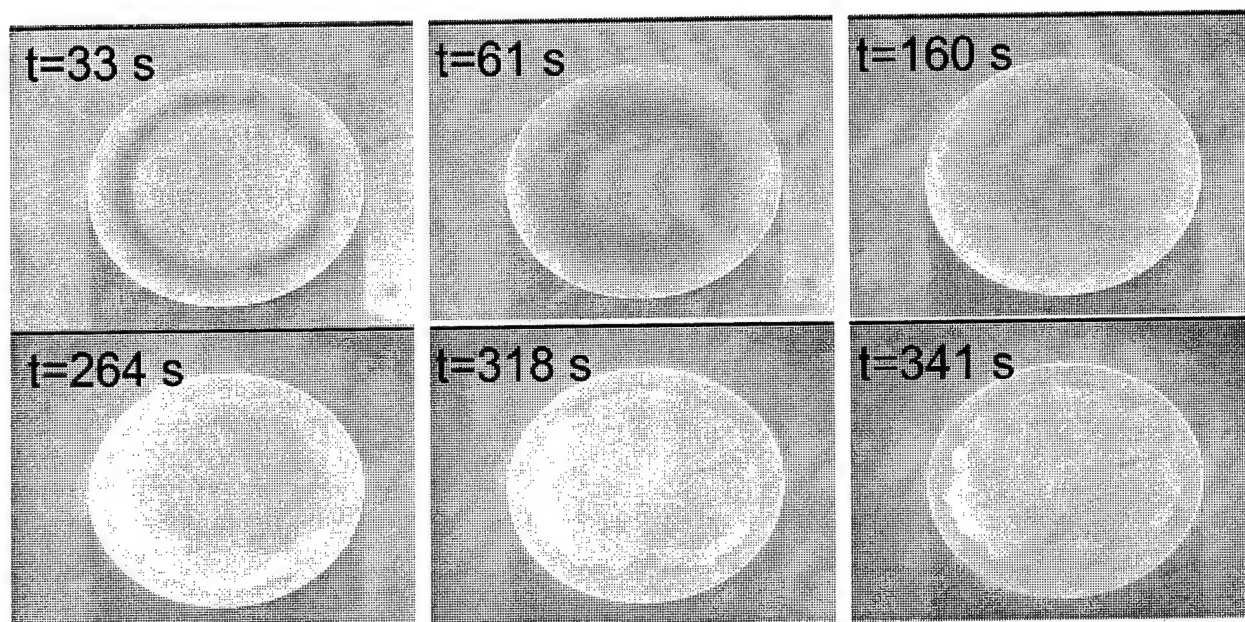


Figure 4. Video images collected for the coupon held at 200 mV(SCE) in Figure 3.

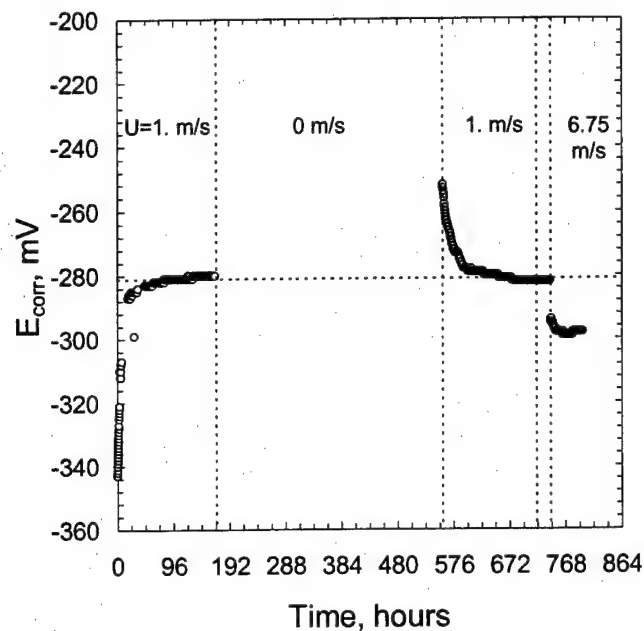


Figure 5. Corrosion potential as a function of time for 99.9% Cu in passively-aerated synthetic seawater. The time period for the experiment was 33 days. The electrode remained in stagnant fluid from  $t=190$  to 550 hours, a cathodic potential was applied at  $t=556$  hours, and flow was resumed at  $t=557$  hours.

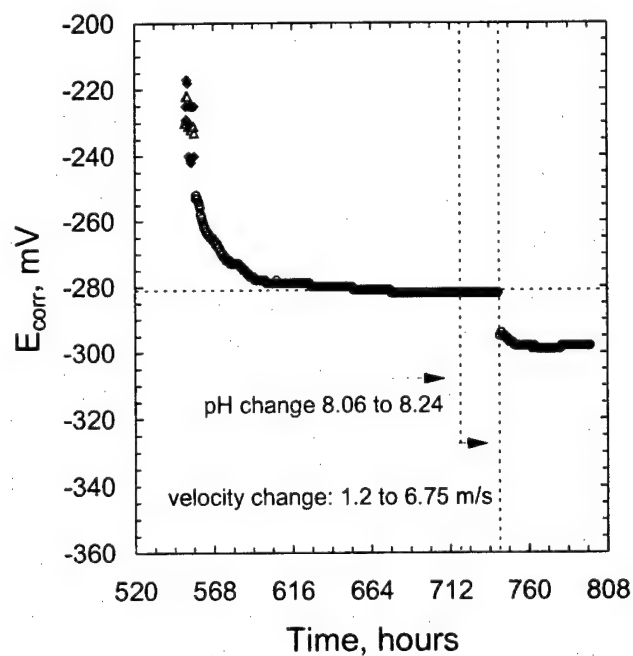


Figure 6. Corrosion potential as a function of time for the latter stage of the experiment presented in Figure 5.



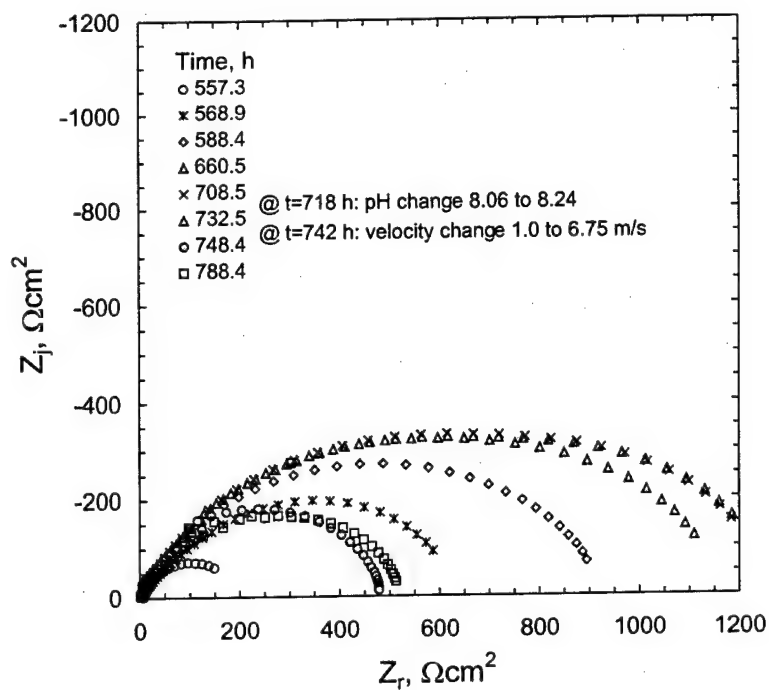


Figure 7. Impedance data collected for over the course of 231 hours corresponding to the corrosion potential data in Figure 6.

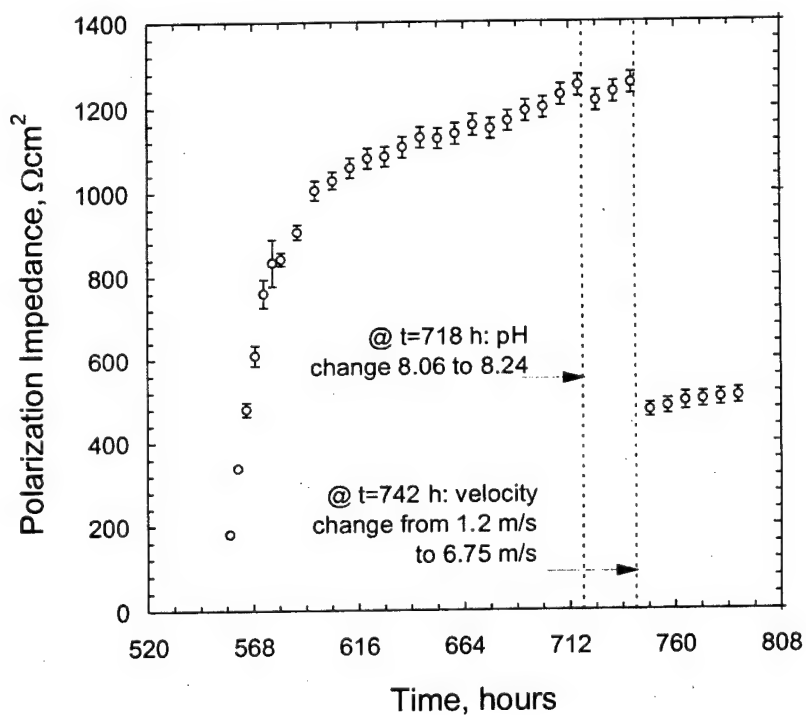


Figure 8. Polarization impedance for the impedance scans shown in Figure 7. Estimated values and associated standard deviation were obtained through the use of a measurement model.

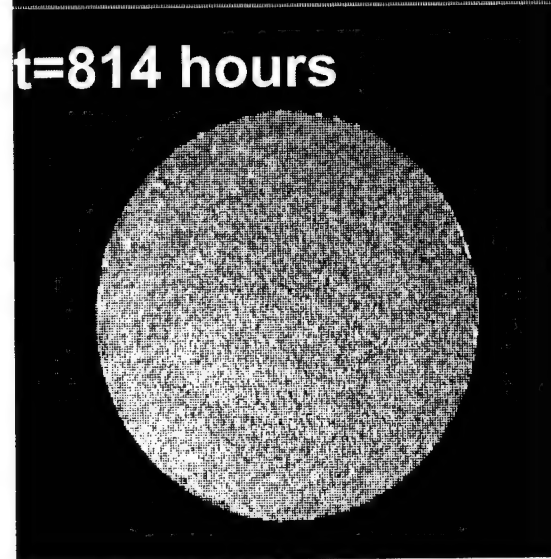
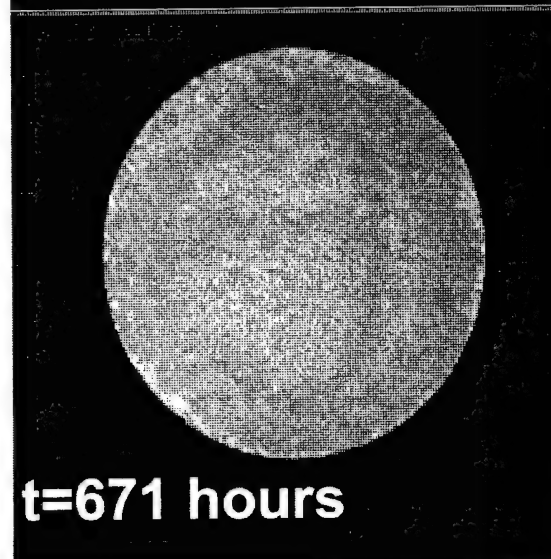
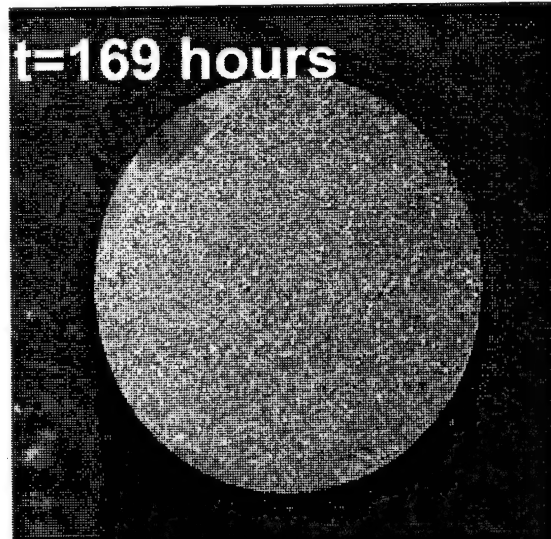
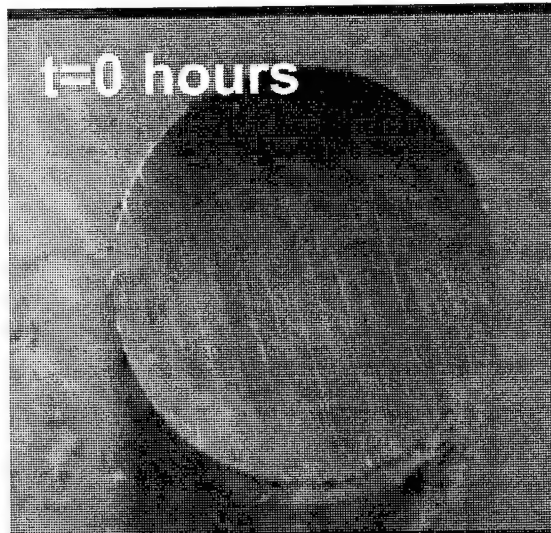


Figure 9. Video micrographs obtained for the experiment described in Table 1;  $t=0$  hours: the initial condition immediately after submersion;  $t=169$  hours: after steady flow at 1 m/s;  $t=671$  hours: before increase in jet velocity; and  $t=814$  hours: after increase in jet velocity.

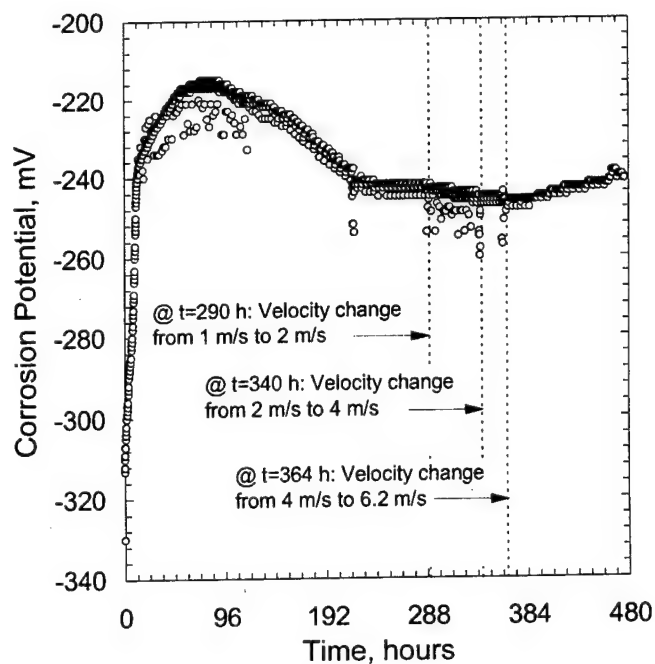


Figure 10. Corrosion potential as a function of time for 99.9% copper in continuously-aerated synthetic sea water electrolyte.

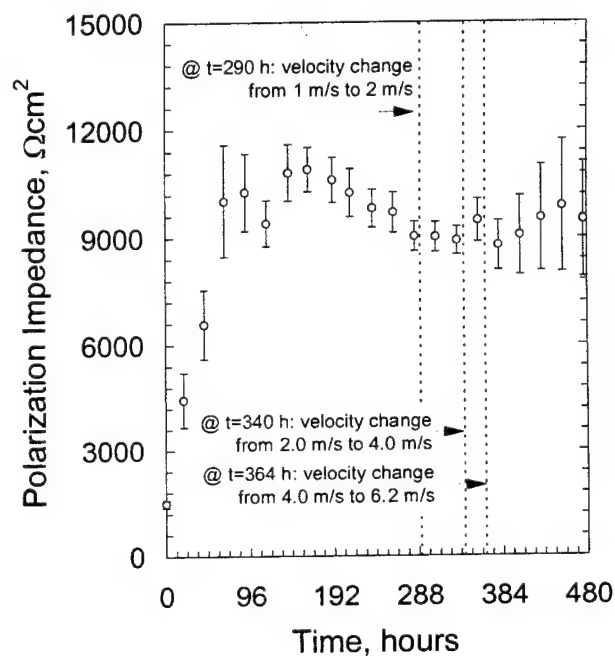


Figure 11. Polarization impedance for the impedance data collected during the experiment shown in Figure 10. Estimated values and associated standard deviation were obtained through the use of a measurement model.

# THE JOURNAL OF SCIENCE AND ENGINEERING CORROSION

## CORROSION SCIENCE

- 259** Elimination of Error from Nonuniform Current Distribution in Polarization Measurement by Boundary Element Inverse Analysis  
*S. Aoki, K. Amaya, A. Nakayama, and A. Nishikawa*
- 265** Scanning Microelectrode Studies of Early Pitting Corrosion of 18/8 Stainless Steel  
*C.J. Lin, J.L. Luo, X.D. Zhuo, and Z.W. Tian*
- 271** Effects of Cold Work, Sensitization Treatment, and the Combination on Corrosion Behavior of Stainless Steels in Nitric Acid  
*M. Mayuzumi, J. Ohta, and T. Arai*
- 281** Hydrogen-Facilitated Anodic Dissolution of Austenitic Stainless Steels  
*L.J. Qiao and J.L. Luo*
- 289** Variable-Amplitude Galvanostatically Modulated Impedance Spectroscopy as a Tool for Assessing Reactivity at the Corrosion Potential Without Distorting Temporal Evolution of the System  
*P.T. Wojcik and M.E. Orazem*
- 299** Oxide-Induced Initiation of Stress Corrosion Cracking in Irradiated Stainless Steel  
*J.M. Cookson, G.S. Was, and P.L. Andresen*
- 313** Surface Roughness and Metastable Pitting of Amorphous Nickel Alloy  
*Y. Zuo and S. Fu*

## CORROSION ENGINEERING

- 317** Sacrificial Anode Cathodic Polarization of Steel in Seawater: Part 2 — Design and Data Analysis  
*W.H. Hartt, S. Chen, and D.W. Townley*
- 323** A Mathematical Model for Electrochemical Removal of Chloride from Concrete Structures  
*A.M. Hassanein, G.K. Glass, and N.R. Buenfeld*

# Variable-Amplitude Galvanostatically Modulated Impedance Spectroscopy as a Tool for Assessing Reactivity at the Corrosion Potential Without Distorting Temporal Evolution of the System

P.T. Wojcik\* and M.E. Orazem\*\*

## ABSTRACT

An algorithm was developed in which galvanostatic regulation of electrochemical impedance measurements is conducted with an amplitude of current perturbation that is adjusted at each frequency to yield a desired variation in potential. Measurements of three previous frequencies are used to estimate the value of the impedance at the target frequency. The algorithm was implemented using a graphically based general interfacing software on a personal computer. Experimental results illustrated artifacts that can arise as a result of galvanostatic measurement with a fixed current amplitude or as a result of potentiostatic measurements for systems with a changing corrosion potential. A demonstration was presented of the use of variable-amplitude galvanostatically modulated impedance spectroscopy to monitor corrosion of copper in synthetic seawater.

**KEY WORDS:** copper, corrosion potential, current, impedance, linearity, potentiostatic testing, variable-amplitude galvanostatically modulated impedance spectroscopy

## INTRODUCTION

Electrochemical impedance measurements usually are performed under potentiostatic regulation. In these measurements, the potential is a fixed value with a superimposed (often sinusoidal) perturbation

of fixed amplitude. This approach is attractive because linearity in electrochemical systems is controlled by potential. For example, a Taylor series expansion for current density at the open-circuit condition using the Butler-Volmer equation:<sup>1</sup>

$$i = i_0 \left( e^{\alpha_a F \eta_s / RT} - e^{-\alpha_c F \eta_s / RT} \right) \quad (1)$$

yields:

$$i = i_0 \left\{ \left( \alpha_a + \alpha_c \right) \frac{F \eta_s}{RT} + \frac{\left( \alpha_a^2 - \alpha_c^2 \right)}{2} \left( \frac{F \eta_s}{RT} \right)^2 + \frac{\left( \alpha_a^3 - \alpha_c^3 \right)}{6} \left( \frac{F \eta_s}{RT} \right)^3 + O(\eta_s^4) \right\} \quad (2)$$

where  $i_0$  is the exchange current density;  $\alpha_a$  and  $\alpha_c$  are the apparent transfer coefficients for the anodic and cathodic reactions, respectively;  $\eta_s$  is the surface overpotential;  $F$  is Faraday's constant;  $R$  is the gas constant;  $T$  is absolute temperature; and the remaining terms are of the order of  $\eta_s^4$  or smaller. For typical parameter values for a symmetric reaction ( $\alpha_a = \alpha_c = 0.5$ ) and for  $T = 298$  K, the second term is equal to zero, and the third term is equal to 1% of the first (linear) term for potentials of  $\sim 13.0$  mV. Potential perturbations of 5 mV to 20 mV are used often.

Submitted for publication December 1996; in revised form, June 1997. Presented in part as paper no. 282 at CORROSION/97, March 1997, New Orleans, LA.

\* Department of Chemical Engineering, University of Florida, Gainesville, FL 32611. Present address: Merck & Co., Inc., 3517 Radium Springs Road, Albany, GA 32611.

\*\* Department of Chemical Engineering, University of Florida, Gainesville, FL 32611.

The need for a small-amplitude potential perturbation is even greater for typical corrosion studies using impedance measurements conducted at the corrosion potential. If hydrogen evolution can be neglected close to the corrosion potential, oxidation of the metal is balanced by the mass transfer-limited reduction of oxygen. Thus, total current density is:

$$i_n = i_{0,M} \exp \left[ \frac{\alpha_M F}{RT} (V - V_M) \right] - i_{O_2} \quad (3)$$

where  $\alpha_M$  is the apparent transfer coefficient for oxidation of the metal,  $i_{0,M}$  is the exchange current density for the oxidation of the metal,  $V_M$  is the equilibrium potential for the oxidation reaction,  $V$  is the applied potential, and  $i_{O_2}$  is the mass transfer-limited current density associated with reduction of oxygen ( $O_2$ ). At the corrosion potential  $V = V_{corr}$ , the net current  $i_n$  is equal to zero, and:

$$V_{corr} = V_M + \frac{RT}{\alpha_M F} \ln \left( \frac{i_{O_2}}{i_{0,M}} \right) \quad (4)$$

An increase in the mass transfer-limited current for oxygen reduction will shift the corrosion potential to more positive values and, thereby, increase the rate of corrosion. Equation (3) can be rewritten in terms of the corrosion potential as:

$$i_n = i_{O_2} \left\{ \exp \left[ \frac{\alpha_M F}{RT} (V - V_{corr}) \right] - 1 \right\} \quad (5)$$

At low current densities, linearization of the exponential term about the corrosion potential yields:

$$i_n = i_{O_2} \left\{ \left[ \frac{\alpha_M F}{RT} (V - V_{corr}) \right] + \frac{1}{2} \left[ \frac{\alpha_M F}{RT} (V - V_{corr}) \right]^2 + \dots \right\} \quad (6)$$

In contrast to the expansion for the Butler-Volmer reaction, the second term contributes to the expansion and is equal to 1% of the first (linear) term for potentials of 0.5 mV if  $\alpha_M = 1.0$ , corresponding to a Tafel slope of  $\sim 60$  mV/decade.

## MOTIVATION

The goal of the present work was to devise a method to use impedance spectroscopy to monitor the temporal evolution of a corroding system held at

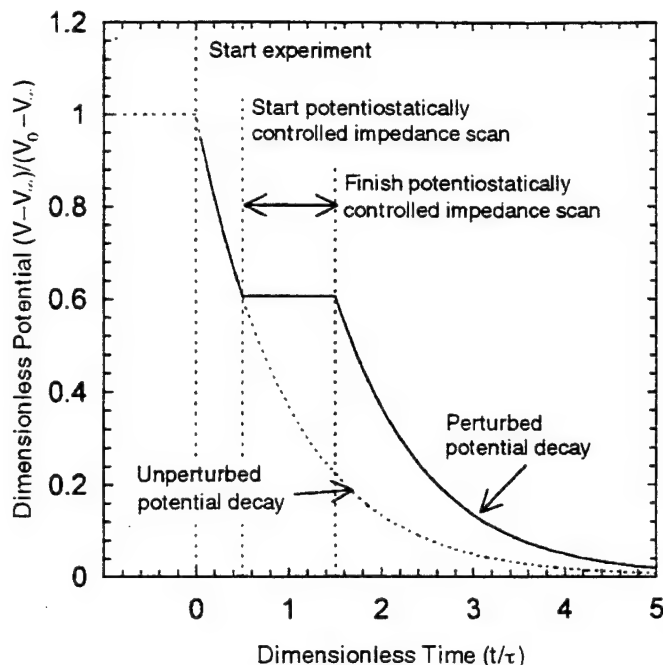


FIGURE 1. Schematic of the influence of a potentiostatically modulated impedance experiment on the observed corrosion potential for a system with a transient corrosion potential.

the corrosion potential. While the primary goal of the measurement was to assess the time-dependent electrochemical and physical properties of the system, a second critical concern was that the measurement technique should not interfere with the natural temporal evolution of the system. The conventional approach for measuring the impedance response uses potentiostatic regulation, in which the potential is set to the value of the corrosion potential at the beginning of the measurement, and the potential is perturbed by a value sufficiently small to ensure linearity.<sup>2,3</sup>

Potentiostatic regulation is satisfactory for measuring the impedance at the corrosion potential if the corrosion potential does not change during the course of the measurement. Under conditions where the corrosion potential changes with time, the potentiostatically controlled impedance scan alters the behavior of the system under study by forcing the potential to be constant during the period of the measurement. A schematic representation of the influence of potentiostatically controlled impedance spectroscopy on a system with a changing corrosion potential is given in Figure 1. The potential decay represented in Figure 1 could be the result of growth of surface films associated with corrosion products or calcareous deposits. The potentiostatically modulated impedance measurement in this case is invasive because the decay in potential is arrested during the measurement. As illustrated in Figure 2, one consequence of applying a fixed potential for a system in which the corrosion potential otherwise would be



changing is that the direct current (DC) component of the current becomes nonzero. For corrosion measurements, the resulting anodic or cathodic current can disrupt the growth of surface films and lead to current overloads.

Galvanostatic modulation of impedance experiments eliminates application of a potential that is anodic or cathodic to the true open-circuit potential. Under galvanostatic control, the desired zero-current base line condition is maintained throughout the impedance measurement, even when the corrosion potential drifts during the course of the measurement of a impedance spectrum. One difficulty with galvanostatic measurements is that the extent to which a true zero current is applied by the galvanostat depends upon the value of the current measuring resistor used. The error associated with imprecision in the applied current can be reduced by selecting a current measuring resistor appropriate for the smallest current range available. The more significant difficulty with galvanostatic measurements is that, with a fixed amplitude for the current perturbation, such measurements can result in severe swings in potential, especially at low frequencies where the impedance is large. The amplitude of the potential variation ( $\Delta\tilde{V}$ ) associated with a perturbation amplitude of current ( $\Delta\tilde{I}$ ) is given by:

$$\Delta\tilde{V} = \Delta\tilde{I} |Z(\omega)| \quad (7)$$

where  $|Z(\omega)|$  is the magnitude of the impedance at frequency  $\omega$ . A current perturbation as small as 10  $\mu\text{A}$  can result in potential swings of 1 V for systems with a polarization resistance of  $10^5 \Omega$ , a value typical of many membranes and some slowly corroding systems with well-developed, dense films.

The potential swing associated with galvanostatically modulated impedance measurements with a fixed perturbation amplitude can be significant, even for systems with a small polarization impedance. The potential perturbations resulting from three fixed-amplitude current perturbations on an electrical circuit consisting of a 10- $\Omega$  leading resistor in series with a parallel resistor (90  $\Omega$ )-capacitor (88  $\mu\text{F}$ ) combination are shown in Figure 3. The impedance for this system changed only one order of magnitude over the entire frequency range. The 1-mA perturbation amplitude (triangles) was sufficiently large to ensure an acceptable signal-to-noise ratio at high frequency (10 mV) but yielded a potential swing of 100 mV at low frequency. For most electrochemical systems governed by kinetics, a 100-mV potential perturbation lies well above the threshold defining linearity. Conversely, if care is taken to choose a current perturbation that will ensure that the low-frequency potential perturbation is within the limits of linearity, the high-frequency potential response

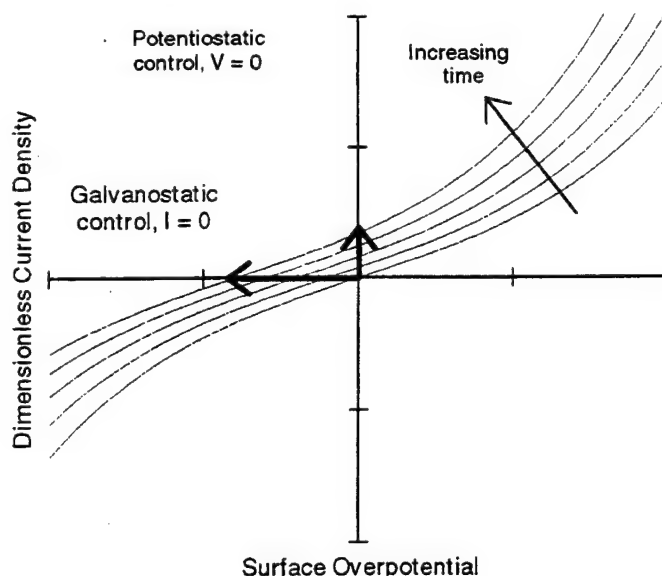


FIGURE 2. Schematic of the manner in which application of potentiostatic control to a system with a transient corrosion potential can cause excursions into an anodic regime of the polarization curve.

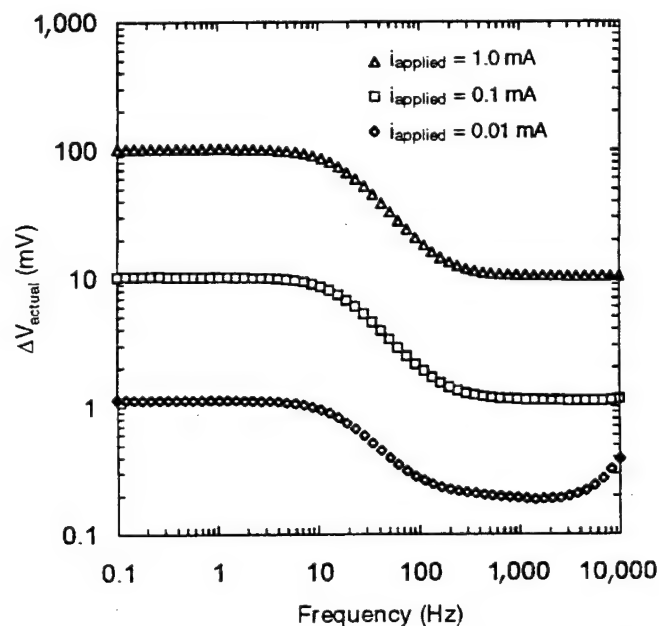


FIGURE 3. Potential perturbation for a test circuit resulting from traditional galvanostatic impedance measurements using fixed-amplitude current perturbations.

can fall below the resolution limits of the potentiostat, as demonstrated by the results obtained with a 0.01-mA current perturbation.

The need to adjust the amplitude of the current perturbation has been addressed in some frequency response analyzers by incorporation of an amplitude compression feature.<sup>4-5</sup> Amplitude compression provides a linear prediction of the current perturbation amplitude. While amplitude compression does not incorporate automated selection of current measur-

ing resistors, it provides current perturbation amplitudes in agreement with the preliminary algorithm developed by Wojcik, et al., in which galvanostatic regulation is conducted with an amplitude of current perturbation that is adjusted at each frequency to yield a desired variation in potential.<sup>6</sup> The algorithm of Wojcik, et al., can be applied for any frequency response analyzer because it does not rely on special nonstandard features of the instrument.<sup>6</sup> The prediction approach also allows selection of an optimal current measuring resistor. This approach retains the advantage of galvanostatic modulation in that the experiment does not disturb the transients that otherwise would exist in the system while ensuring the maximum signal-to-noise ratio for perturbations that stay within the linear regime.

The objective of the present work was to present recent improvements to the variable-amplitude galvanostatic modulation (VAG) algorithm and to demonstrate its utility for monitoring transient corrosion processes.

## VAG MODULATION

The VAG algorithm consists of a method to select an appropriate amplitude for the current perturbation and for the current measuring resistor. The algorithm was implemented using a general graphical interfacing software on a personal computer (PC).

### *Prediction of the Amplitude of the Current Perturbation*

Measurements at previous frequencies were used to estimate the value of the impedance at the target frequency. The current perturbation to be used was given by:

$$\Delta \bar{I}(\omega) = \frac{\Delta \bar{V}_{\text{target}}}{|Z(\omega)|_{\text{estimated}}} \quad (8)$$

where  $\Delta \bar{I}(\omega)$  is the current perturbation at a given frequency,  $\Delta \bar{V}_{\text{target}}$  is the desired potential perturbation at the surface of the electrode, and  $|Z(\omega)|_{\text{estimated}}$  is the magnitude of the impedance taken from the preceding measurement. In this approach, the magnitude of the impedance at the frequency to be measured was predicted from values obtained at previously measured frequencies. This prediction, therefore, was obtained without additional probing of the system. A sequential collection of data in logarithmic increments of decreasing frequency was assumed.

In previous work, a one-point prediction algorithm was used:<sup>6</sup>

$$Z(\omega_k) = Z(\omega_{k-1}) + O \left[ \log \left( \frac{\omega_k}{\omega_{k-1}} \right) \right] \quad (9)$$

where the impedance at frequency  $\omega_k$  was assumed to be equal to the impedance obtained at the previous frequency  $\omega_{k-1}$ . The error in Equation (9), as given by:

$$O \left[ \log \left( \frac{\omega_k}{\omega_{k-1}} \right) \right] \quad (10)$$

is of the order of the inverse number of points per decade. The error in Equation (9) is the same as would be obtained by using the amplitude compression algorithm available on a few frequency response analyzers.<sup>4,5</sup>

In the present work, Equation (9) was replaced by:

$$Z(\omega_k) = 3Z(\omega_{k-1}) - 3Z(\omega_{k-2}) + Z(\omega_{k-3}) + O \left[ \log \left( \frac{\omega_k}{\omega_{k-1}} \right) \right]^2 \quad (11)$$

The error in Equation (11) is of the order of the square of the inverse number of points per decade. For 10 points per decade, an order of magnitude improvement is expected when Equation (11) is used as compared to Equation (9).

At the first measured frequency, the initial guess for the impedance was used. The estimated solution resistance provided a good initial guess for impedance scans made from high frequency to low. At the second measured frequency, Equation (9) was used. At the third measured frequency, the estimated impedance was obtained from a two-point formula:

$$Z(\omega_k) = 2Z(\omega_{k-1}) - Z(\omega_{k-2}) + O \left[ \log \left( \frac{\omega_k}{\omega_{k-1}} \right) \right]^2 \quad (12)$$

which has an accuracy of the order of the square of the inverse number of points per decade. The three-point algorithm given as Equation (11) provided a refinement to the two-point algorithm (Equation [12]) by including an estimate for the second derivative of impedance with the log of frequency.

A comparison of the one-point and three-point algorithms is presented in Figure 4 for the test cell used to generate Figure 3. The largest errors in the prediction algorithm appeared at frequencies where the impedance was a strong function of frequency. For a 10-mV target perturbation, the one-point technique, displayed by triangles, resulted in a maximum perturbation of 11.7 mV. The maximum error in the three-point variable-amplitude prediction was 0.2 mV for the one-point method as compared to 1.7 mV for the one-point algorithm. The largest error for the three-point algorithm was at the first measured frequency where an initial guess was used to predict the appropriate current perturbation.

### Prediction of the Value for the Current Measuring Resistor

The value of the current perturbation obtained from Equation (8) also was used to guide automated selection of the current measuring resistor. Automated selection of current measuring resistors is not new,<sup>7</sup> but its implementation is an essential feature of the algorithm. Several changes of the current measuring resistor often were needed when the current perturbation varied over several orders of magnitude during a scan.

The current measuring resistors available for the potentiostat used in this work are presented in Table 1, along with the nominal current ranges for each selection. The nominal current range was 15% to 190% of the posted current with the exception of the 1- $\Omega$  resistor, which had an upper limit of 200% of the posted current. Selection of the proper current measuring resistor was crucial to ensure reliable data collection. Selection of too large a current measuring resistor resulted in a current overload in the potentiostat, and too small a current measuring resistor resulted in a poor signal-to-noise ratio. An overlap in the current ranges is evident in Table 1. Measurements conducted toward the full-scale-limit side of the current range tended to be more sensitive than those taken at the lower limits of the allowable range (e.g., a current value of 12 mA was measured more accurately using the 10- $\Omega$  rather than the 100- $\Omega$  current measuring resistor).

However, there were situations where the current from an electrochemical experiment was augmented by an additional current resulting from noise, external perturbation, or change in the system under study. When the selection of the optimum current measuring resistor was based solely on the perturbation being applied, the additional currents, in many instances, caused a current overload. With the current measuring resistor selection algorithm described below, a more conservative approach could be taken in situations where overloads are common.

The algorithm for selecting the proper current measuring resistor was based on calculation of:

$$\log \left| \frac{i_{\text{predict}}}{i_{\text{min}}} \right| = x.y \quad (13)$$

where  $x$  and  $y$  are the characteristic and mantissa of the logarithm, respectively;  $i_{\text{predict}}$  is the predicted value for the current; and  $i_{\text{min}}$  is the nominal minimum measurable current for the instrument, given in Table 1 to be 100 nA. A switch-over factor ( $y_c$ ) was defined as having a value between 1.5 and 1.9. If  $y \leq y_c$ , the current measuring resistor index ( $k_R$ , Table 1) was obtained from  $k_R = 7 - x$ . If  $y > y_c$ ,  $k_R = 6 - x$ . This algorithm does not depend upon past history, and increases or decreases in current measuring

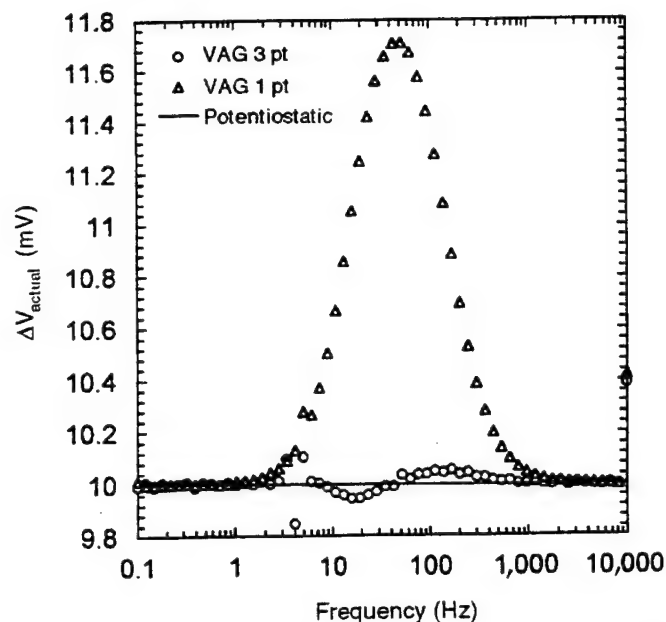


FIGURE 4. Comparison between the one-point and three-point prediction methods for the VAG algorithm with a 10-mV target potential perturbation.

TABLE 1  
Current Measuring Resistor Ranges for the Potentiostat/Galvanostat Used<sup>a</sup>

Current Nominal Resistor Index ( $k_R$ )	Measuring Resistor Value	Nominal Current Value	Nominal Current Range
0	1 $\Omega$	1 A	150 mA – 2 A
1	10 $\Omega$	100 mA	15 mA – 190 mA
2	100 $\Omega$	10 mA	1.5 mA – 19 mA
3	1,000 $\Omega$	1 mA	150 $\mu$ A – 1.9 mA
4	10,000 $\Omega$	100 $\mu$ A	15 $\mu$ A – 190 $\mu$ A
5	100,000 $\Omega$	10 $\mu$ A	1.5 $\mu$ A – 19 $\mu$ A
6	1 M $\Omega$	1 $\mu$ A	150 nA – 1.9 $\mu$ A
7	100 M $\Omega$	100 nA	15 nA – 190 nA

resistor values are possible based upon the predicted current value.

The method for calculating a value for  $i_{\text{predict}}$  depended upon the mode of regulation used. For galvanostatic regulation,  $i_{\text{predict}}$  was calculated by:

$$i_{\text{predict}} = \frac{V_{\text{target}}}{Z_{\text{predict}}} + i_{\text{bias}} \quad (14)$$

and under potentiostatic regulation by:

$$i_{\text{predict}} = \frac{V_{\text{perturb}}}{Z_{\text{predict}}} + i_{\text{pol}} \quad (15)$$

where  $V_{\text{target}}$  is the desired potential perturbation at the electrode surface,  $Z_{\text{predict}}$  is the value predicted for

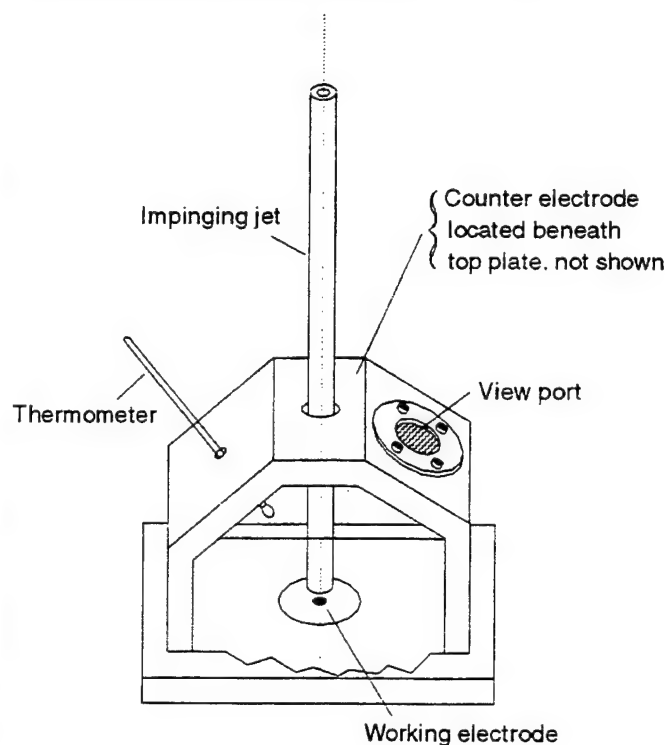


FIGURE 5. Schematic of the impinging jet cell.

the impedance by the prediction algorithm.  $i_{\text{bias}}$  is a current bias applied by the potentiostat, and  $i_{\text{pol}}$  is any DC present after a potential bias is set.

#### APPLICATION TO CORROSION MEASUREMENTS

The copper/synthetic seawater system chosen to illustrate the benefits of the VAG algorithm is affected strongly by the formation of salt and oxide films.<sup>8</sup> The corrosion potential of a freshly polished copper electrode submerged in electrolyte changes rapidly at first as a result of the removal and formation of surface films, then reaches a pseudo steady-state condition after several days.<sup>8-9</sup>

Details of the experimental design have been presented previously,<sup>9-10</sup> and a schematic of the impinging jet cell is shown in Figure 5. An annealed copper cylinder (0.3175-cm [0.125 in.] radius) was embedded in an inert epoxy resin puck designed to expose the disk-shaped face with an area of 0.317 cm<sup>2</sup> (0.049 in.<sup>2</sup>) to flow from the submerged impinging jet. The cell configuration was designed to ensure that the flow near the working electrode was in the stagnation regime. The cell design provided uniform accessibility of the electrode to mass transfer. The experimental system was controlled and data was collected by a PC. The program used to run the experiments was constructed using a commercially

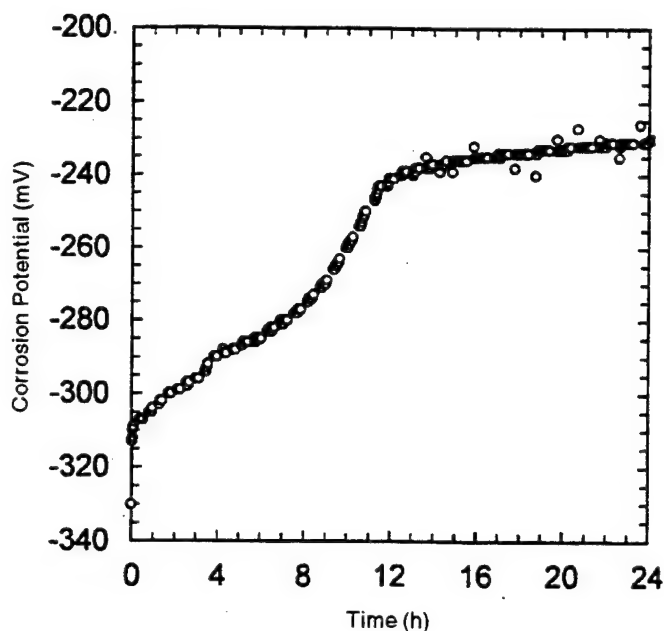


FIGURE 6. Corrosion potential as a function of time for a copper disk subjected to an impinging jet of synthetic seawater with a jet velocity of 1 m/s.

available graphical interfacing software. A potentiostat/galvanostat and an impedance/gain-phase analyzer were connected to the PC via a general purpose interface bus (GPIB) connection. Impedance measurements were collected frequency-by-frequency from high frequency to low. The long-integration feature of the frequency response analyzer was used, which terminated measurement at a given frequency when a 1% closure error was achieved on the measured channel.

#### Comparison of Modulation Techniques

The change in the corrosion potential as a function of time, as evident in Figure 6 for the copper synthetic seawater system, created problems using the impedance spectroscopy under potentiostatic modulation. The data presented were obtained after 12 h of immersion in order to bypass initial transients. Impedance spectra collected under potentiostatic and VAG modulation are presented in Figure 7. The reproducibility of the three sequential VAG scans showed that, during the 30-min period required to collect the three scans, the system impedance did not change. The subsequent three potentiostatic scans demonstrated significant differences, caused by imposition of a small anodic bias as the system changed with time (Figure 2). The data collected under potentiostatic modulation were shown by the measurement model technique to be inconsistent with the Kramers-Kronig relations at low frequencies,<sup>11-14</sup> whereas the low-frequency data collected under VAG modulation were consistent with the Kramers-Kronig relations. The low-frequency

inconsistency with the Kramers-Kronig relations of the data obtained under potentiostatic modulation supported the conclusion that potentiostatically modulated impedance experiments changed the behavior of the copper electrode.

The VAG modulation technique was compared to use of constant-amplitude galvanostatic modulation. The large range of impedance values seen for this system as a function of frequency made it impossible to collect consistent data using the conventional constant-amplitude galvanostatic techniques. The problem was that, to retain an acceptable signal-to-noise ratio at high frequencies, the perturbation had to be sufficiently large to cause a nonlinear response at low frequencies. The problem is demonstrated in Figure 8, where spectra collected with the conventional galvanostatic, conventional potentiostatic, and VAG modulation are presented. A fixed current amplitude of 0.01 mA yielded errors at high frequency which, surprisingly, had the appearance of a bias error rather than that of a stochastic noise. Comparison of the galvanostatic results to those obtained under VAG modulation (Figures 9 and 10 for real and imaginary components, respectively) revealed that the spectrum obtained under galvanostatic modulation with 0.01-mA amplitude was in good agreement with VAG results at low frequency but showed large discrepancies at high frequency. The high-frequency errors were reduced (but not eliminated) by increasing the current perturbation amplitude to a value of 0.1 mA. Violation of linearity constraints were evident at low frequency.

Consistent with the results presented in Figure 7, the data presented in Figures 8 through 10 revealed that results obtained under conventional potentiostatic modulation (triangles) were not as reproducible as those obtained under the VAG method (squares). Slight drifts in the corrosion potential created DC conditions that perturbed the system and caused errors in the impedance results.

#### Application as a Monitor for Corrosion Systems

The manner in which VAG impedance spectroscopy can be used to monitor the reactivity of a corrosion system as a function of time was considered. The corrosion potential is presented in Figure 11 for a copper disk subjected to a submerged impinging jet of aerated synthetic seawater. The transient presented in Figure 6 represented the first 24 h of the 480-h duration experiment in Figure 11. The initial jet velocity was 1 m/s, and the jet velocity was changed from 1 m/s to 2 m/s after 290 h, from 2 m/s to 4 m/s after 340 h, and from 4 m/s to 6.2 m/s after 364 h. The velocities and corresponding time intervals are indicated in Figure 11. The objective was to explore the reactivity of the copper coupon as a function of time and as a function of jet velocity. The VAG method was used to monitor the

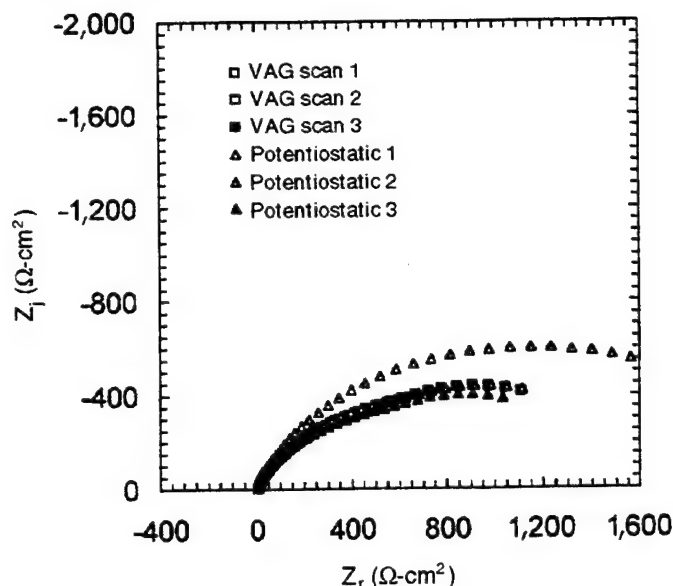


FIGURE 7. Impedance plane plots (imaginary impedance [ $Z_i$ ] as a function of real impedance [ $Z_r$ ]) for three consecutive VAG scans followed by three consecutive potentiostatic scans for a copper disk electrode immersed in synthetic seawater.

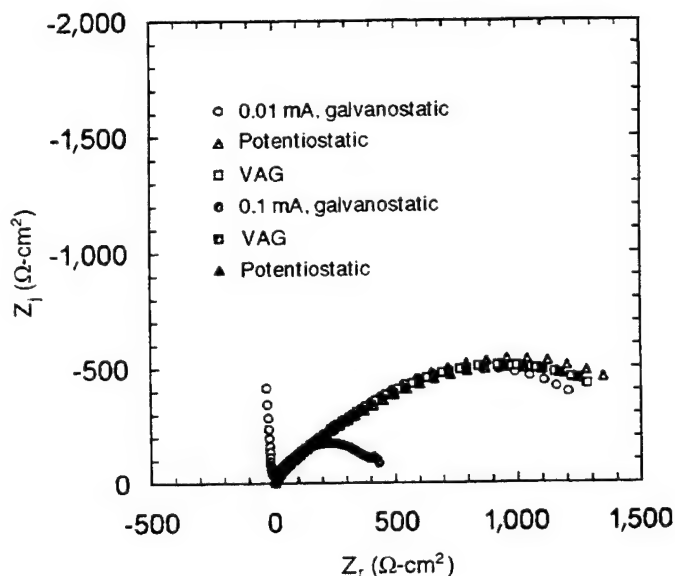


FIGURE 8. Comparison of conventional potentiostatic, conventional galvanostatic, and VAG techniques for a copper electrode in synthetic seawater.

corrosion system at the open-circuit condition at regular intervals. Typical results are presented in Figure 12 for the time frame in which changes in jet velocity were made. Small differences in features were evident in the impedance plane format.

Results demonstrated that the VAG impedance technique satisfied the requirement that the impedance method not distort the transients associated with a freely corroding system. To be useful as a monitor of corrosion processes, the data obtained



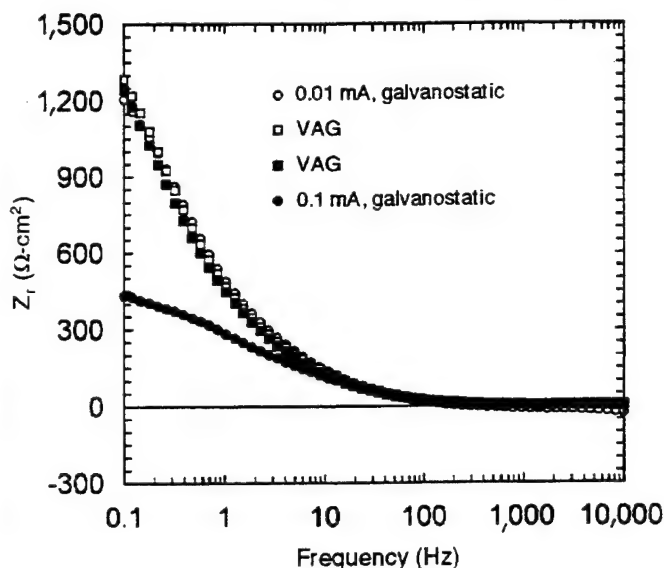


FIGURE 9. Real component of impedance for data in Figure 8.

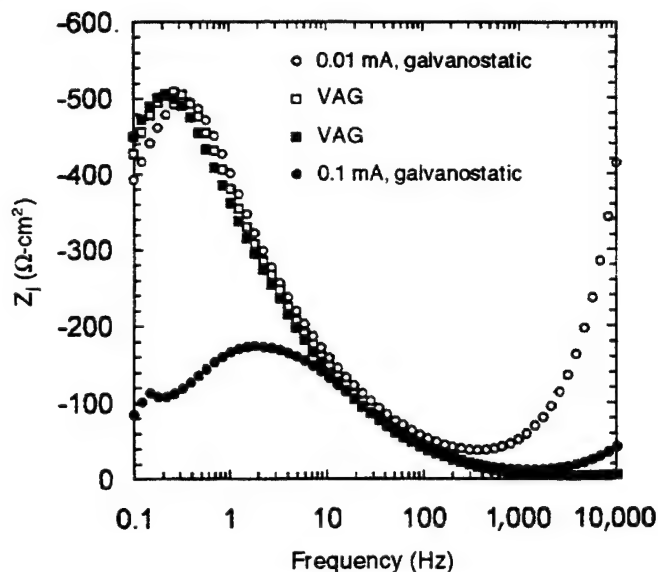


FIGURE 10. Imaginary component of impedance for data in Figure 8.

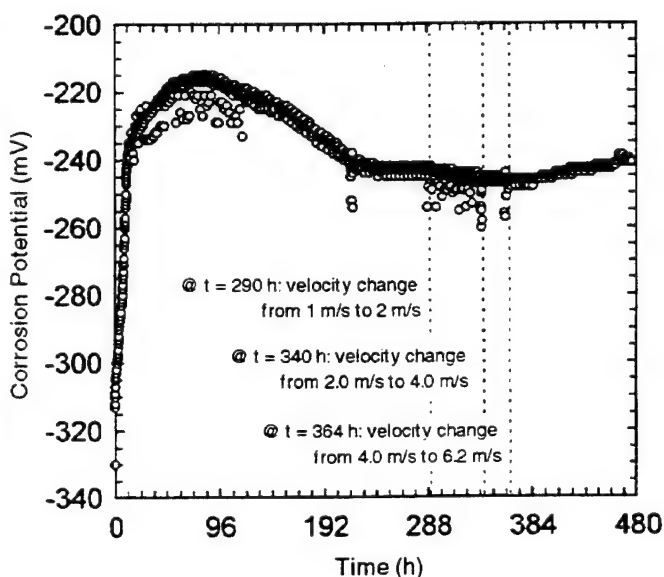


FIGURE 11. Corrosion potential measured as a function of time for a copper disk copper disk subjected to an impinging jet of synthetic seawater with jet velocity as indicated. Data presented in Figure 6 represent the short-time behavior of the data presented here.

also should allow ready interpretation in terms of physical properties. If the time constant for the transient process is of the same order as the time required for the impedance scan, the nonstationarity of a system will introduce bias errors in the impedance measurement and will cause the data to be inconsistent with the Kramers Kronig relations. The use of the measurement model concept to assess the error structure of the impedance scans allowed identification of the portion of the measurement that was unaffected by bias errors.<sup>11-14</sup> Thus, the VAG imped-

ance technique allowed measurements that did not distort the transients associated with a freely corroding system, and the measurement model allowed identification of the portion of the measurement that could be used to extract physical properties.

In addition to its use to assess consistency with the Kramers-Kronig relations, the measurement model approach was used to quantify differences in surface reactivity.<sup>15</sup> Interpretation of the spectra presented here followed:

- Identification of the frequency-dependent stochastic component of the error structure following the method presented by Agarwal, et al.<sup>13</sup> This information was used to weight subsequent regressions.

- Identification of the portion of the spectrum that was consistent with the Kramers-Kronig relations following the method presented by Agarwal, et al.<sup>14</sup> The error structure found in the previous step was used to weight the regression. High-frequency data were corrupted by instrumental artifacts. The low-frequency data typically were consistent with the Kramers-Kronig relations except for data collected early in the experiment where the system was changing rapidly. Nevertheless, a significant portion of even the first impedance measurements was consistent with the Kramers-Kronig relations, and acceptable values of polarization impedance were obtained.

- Regression of the measurement model to the part of the spectrum found to be consistent with the Kramers-Kronig relations. The regressed parameter values were used to extrapolate the zero-frequency limit and Monte Carlo simulations were performed using the standard deviations of the regressed parameters to estimate the confidence interval for the extrapolation. The polarization impedance



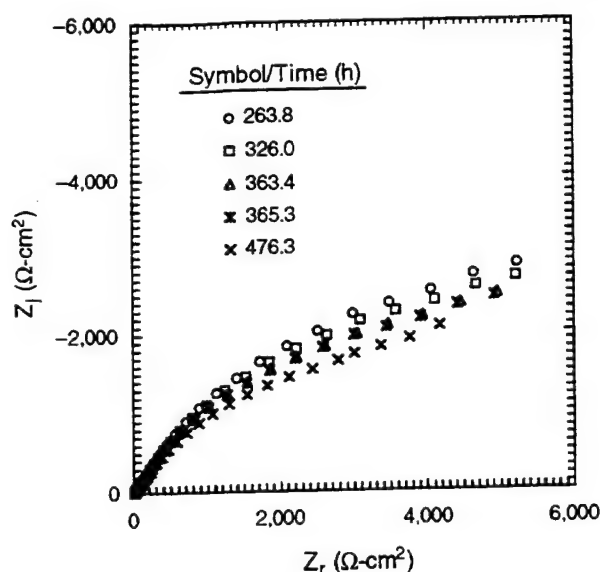


FIGURE 12. Impedance spectra corresponding to measurements of Figure 11. Spectra correspond to times before and after changes in jet velocity.

was obtained by subtracting the regressed solution resistance from the extrapolated zero-frequency value.

Results are presented in Figure 13 for the polarization impedance as a function of time for the impedance data shown in Figure 12. The polarization impedance increased from an initial value of roughly  $1,600 \Omega\text{-cm}^2$  to  $10,000 \Omega\text{-cm}^2$ . Results showed that, for this experiment, there was no dramatic change in the surface reactivity associated with changes in jet velocity. Other examples of the use of VAG modulated impedance spectroscopy for monitoring reactivity changes have been presented elsewhere.<sup>9-10</sup>

The utility of the VAG method was emphasized by its use for monitoring the short-term behavior shown in Figure 6. As shown, the trends in corrosion potential were unaffected by the impedance scans. The impedance scans given in Figure 14 showed that the surface reactivity changed dramatically over the course of 24 h. The resulting polarization impedance values are given in Figure 15. The impedance decreased initially as a result of removal of the native oxide layer and then increased as the films associated with the corrosion products formed and grew. The role of the measurement model for evaluating consistency with the Kramers-Kronig relations was evident in that the apparent zero-frequency asymptote of the scan obtained at 0.2 h (Figure 14) was  $1,800 \Omega\text{-cm}^2$ ; whereas, the corresponding polarization impedance shown in Figure 15 obtained by the analysis outlined above was  $1,500 \Omega\text{-cm}^2$ . The low-frequency data were corrupted by nonstationary behavior, but a polarization impedance still could be obtained from the portion of the data that satisfied the Kramers-Kronig relations.

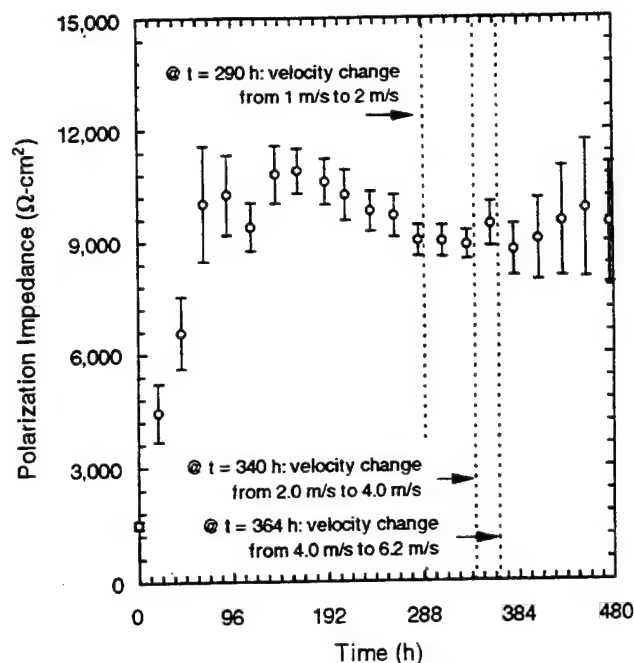


FIGURE 13. Extrapolated polarization impedance for the system presented in Figure 11.

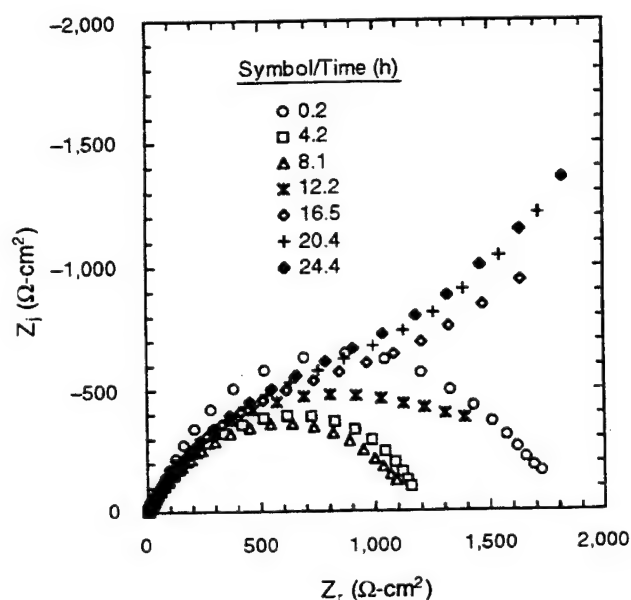


FIGURE 14. Impedance spectra corresponding to the data presented in Figure 6.

## CONCLUSIONS

- ❖ Impedance spectroscopy can be used to follow the temporal evaluation of surface properties at the corrosion potential, but the perturbation must be small and the modulation must not distort transients associated with the freely corroding system.
- ❖ Galvanostatic regulation is ideal for the use of impedance spectroscopy to observe periodically the

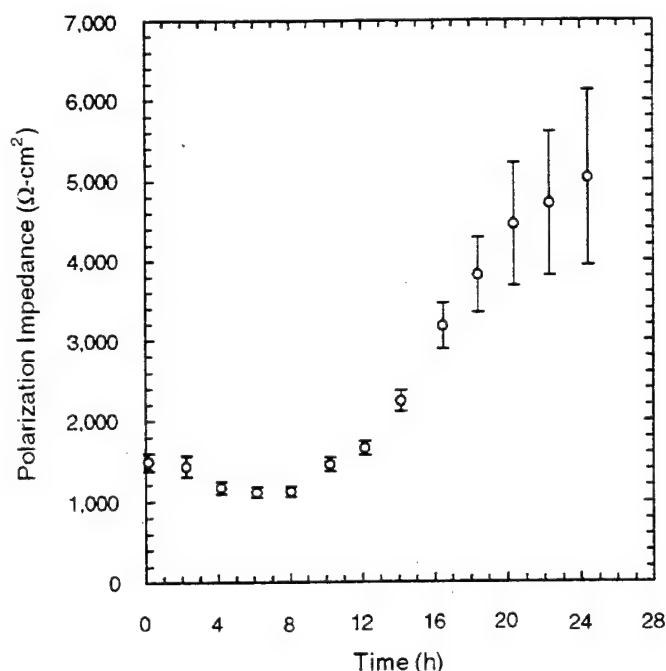


FIGURE 15. Extrapolated polarization impedance for the system presented in Figure 6.

condition of a metal held at the corrosion potential because the required zero-current condition is maintained even when the corrosion potential is a strong function of time.

❖ While galvanostatic measurements with a fixed amplitude for the current perturbation can result in severe swings in potential, the algorithm described provides a good means for adjusting the modulation amplitude for current to prevent large perturbations to the system.

❖ Measurement of an impedance spectrum with this technique does not distort the natural evolution of a system, even under conditions where rapid evolution

of surface properties distorts the resulting impedance scan. Use of the measurement model concept to assess the error structure of the impedance scans allows use of the uncorrupted portion of the measurement to evaluate physical properties.

## ACKNOWLEDGMENTS

This work was supported by the U.S. Office of Naval Research under grant nos. N00014-93-1-0056 and N00014-93-1-1113 (A.J. Sedriks, program monitor).

## REFERENCES

1. J.A.V. Butler, *Trans. Faraday Soc.* 19 (1924): p. 729-734.
2. "Model 273 Potentiostat/Galvanostat," operation manual (Princeton, NJ: EG&G Princeton Applied Research, 1985).
3. "Operating Manual for the 1260 Impedance/Gain-Phase Analyser" (Farnborough, U.K.: Schlumberger-Solartron, 1993).
4. "Operating manual for the 1250 Frequency Response Analyzer", Schlumberger-Solartron: Farnborough (UK) 1982.
5. P. Bernard, H. Takenouti, "Manual of Program FRACOM 2.1," UPR 15 du CNRS (Paris, France: 1991).
6. P.T. Wojcik, P. Agarwal, M.E. Orazem, *Electrochim. Acta* 41 (1996): p. 977-983.
7. M.W. Kendig, A.I. Allen, F. Mansfeld, *J. Electrochem. Soc.* 131 (1984): p. 935-936.
8. F. LaQue, *Marine Corrosion: Causes and Prevention* (New York, NY: John Wiley and Sons, 1975).
9. P.T. Wojcik, M.E. Orazem, "Experimental Study of the Erosion-Corrosion of Copper and Copper-Nickel Alloys Using a Submerged Impinging Jet," *CORROSION/97*, paper no. 435 (Houston, TX: NACE, 1997).
10. P.T. Wojcik, "Electrochemical Behavior of Copper and Copper-Nickel Alloys in Synthetic Seawater" (Gainesville, FL: University of Florida, 1997).
11. P. Agarwal, M.E. Orazem, L.H. Garcia-Rubio, *J. Electrochem. Soc.* 139 (1992): p. 1,917-1,927.
12. P. Agarwal, O.C. Moghissi, M.E. Orazem, L.H. Garcia-Rubio, *Corrosion* 49 (1993): p. 278-289.
13. P. Agarwal, O.D. Crisalle, M.E. Orazem, L.H. Garcia-Rubio, *J. Electrochem. Soc.* 142 (1995): p. 4,149-4,158.
14. P. Agarwal, M.E. Orazem, L.H. Garcia-Rubio, *J. Electrochem. Soc.* 142 (1995): p. 4,159-4,168.
15. M.E. Orazem, P.T. Wojcik, M. Durbba, I. Frateur, L.H. Garcia-Rubio, "Application of Measurement Models for Interpretation of Impedance Spectra for Corrosion," *Mat. Sci. Forum*, in press.

# Application of Measurement Models for Interpretation of Impedance Spectra for Corrosion

M.E. Orazem<sup>1</sup>, P.T. Wojcik<sup>1</sup>, M. Durbha<sup>1</sup>,  
I. Frateur<sup>2</sup> and L.H. Garcia-Rubio<sup>3</sup>

<sup>1</sup> Department of Chemical Engineering, University of Florida, Gainesville, Florida 32611, USA

<sup>2</sup> UPR 15 du CNRS "Physique des Liquides et Electrochimie", Université Pierre et Marie Curie, Tour 22, 4 Place Jussieu, F-75252 Paris Cedex 05, France

<sup>3</sup> Department of Chemical Engineering, University of South Florida, Tampa, Florida 33620, USA

**Keywords:** Impedance Spectroscopy, Measurement Models, Error Analysis, Polarization Resistance

This material may be protected by  
copyright law (Title 17 U.S. Code).

## Abstract

Experimental identification of errors has allowed enhanced interpretation of a wide variety of spectroscopy techniques, including measurements for electrochemical systems for which detailed process models are available. The physicochemical models available for corrosion systems, however, are typically not sufficiently detailed to represent adequately impedance data to within the experimentally determined noise level of the measurement. Even in the absence of detailed physicochemical models, enhanced interpretation of corrosion processes is possible through the use of measurement models which can account quantitatively for differences in surface reactivities. In this paper, the necessary steps for the quantification of corrosion processes using the measurement model approach of Agarwal *et al.* are described. The stationary stochastic error contribution to impedance spectra is identified from replicated measurements. Presence of a bias error contribution, caused, for example, by instrumental artifacts and non-stationary behavior, is identified from application of the Kramers-Kronig transforms. The zero and high frequency limits obtained through the measurement model are used to determine the polarization resistance in a way that accounts for the experimentally determined error structure. The results of this procedure, weighted by an appropriate statistical analysis, can be used to monitor electrochemical systems as functions of time or process conditions. The approach described herein is validated for model systems, such as the reduction of ferricyanide on platinum for which accurate process models are available. The corrosion examples presented here involve the transient growth of corrosion-product films on copper in synthetic seawater and on cast iron in Evian water.

## Introduction

Interpretation of impedance data requires, in principle, both a model which describes the physics of the system under study and a quantitative assessment of the error structure of the measurement.[1-3] The experimental difficulty of quantifying the error structure for electrochemical impedance spectroscopy had, until recently, prevented application of an error analysis approach for interpretation of spectra. The error structure for most radiation-based spectroscopic measurements such as absorption spectroscopy and light scattering can be readily identified.[4-6] The error analysis approach has been successful for some optical spectroscopy techniques because these systems lend themselves to replication and, therefore, to the independent identification of the different errors that contribute to the total variance of the measurements. In contrast, the stochastic contribution to the error structure of electrochemical impedance spectroscopy measurements cannot generally be obtained from the standard deviation of repeated measurements because even a mild non-stationary behavior introduces a significant time-varying bias contribution to the error. Recent

advances in the use of measurement models for filtering lack of replicacy have made possible experimental determination of the stochastic and bias contributions to the error structure for impedance measurements.[7-16]

The measurement model approach for identification of error structure, previously used for optical spectroscopies,[4-6] has recently been applied to electrochemical systems.[7-16] Enhanced interpretation of impedance spectra was demonstrated for some systems for which detailed process models were available. For example, using normal weighting strategies impedance spectra for n-GaAs diodes, information concerning deep-level states could not be obtained; whereas, evaluation of the error structure allowed interpretation in terms of concentrations and energy levels of deep-level electronic states.[8,17,18] Similar improvement was demonstrated for interpretation of electrohydrodynamic impedance spectra in terms of transport properties.[16]

Such enhanced interpretation was possible for the GaAs system and the electrohydrodynamic impedance system because sophisticated process models were available which could be used to interpret the measurements in terms of well-defined physical properties. The objective of this work was to explore how the error analysis approach made possible by use of the measurement model can be used for corrosion systems for which detailed process models are often unavailable.

### Classification of Measurement Errors

The residual errors  $\epsilon_{\text{res}}$  that arise when a model is regressed to experimental data have systematic and stochastic contributions, *i.e.*, [1-3]

$$\epsilon_{\text{res}} = Z_{\text{exp}} - Z_{\text{mod}} = \epsilon_{\text{systematic}} + \epsilon_{\text{stochastic}} \quad (1)$$

The contribution to the total variance of the stochastic errors is in two parts: a stationary component with mean zero and a frequency-dependent variance and a non-stationary component that may result in bias or drift. The stationary stochastic errors were assumed in this work to have a Gaussian distribution around a mean value of zero. Systematic errors can arise from model inadequacies or from experimental bias. The error analysis employed in this work involves quantification of stationary stochastic errors and experimental bias errors. Experimental bias errors were assumed to be those errors which cause the data to be inconsistent with the Kramers-Kronig relations. As defined, the term experimental bias error does not include contributions from model inadequacy, but does include contributions from non-stationary stochastic errors and both stationary and non-stationary systematic experimental errors. Changes in the system characteristics during the course of the measurement can cause non-stationary experimental bias errors, and instrumental artifacts can cause stationary experimental bias errors. As described in the subsequent section, the measurement model was used to filter lack of replicacy between repeated measurements and to identify consistency with the Kramers-Kronig relations.

### Applications of Measurement Models to Corrosion

The measurement model facilitates design of experiments and, for systems for which detailed process models are unavailable, can be used to obtain asymptotic values which provide rough estimations of corrosion rates.

#### Experimental Design

To be useful as a monitor of corrosion processes, the impedance data obtained should allow ready interpretation in terms of physical properties. If the time constant for the transient process is of the same order as the time required for the impedance scan, the non-stationarity of the system will introduce bias errors in the impedance measurement and will cause the data to be inconsistent with

the Kramers-Kronig relations. The use of the measurement model concept to assess the error structure of the impedance scans allows identification of the portion of the measurement that is unaffected by experimental bias errors.[14] The second benefit of the error analysis approach is identification of the stationary stochastic component of the error structure.[13] This information can be used to direct modification of the experimental design to minimize bias and stochastic errors. For example, bias errors caused by nonstationarity can be reduced by decreasing the time required for the measurement. One approach is to decrease the integration time at each frequency, but this reduction of bias errors is at the expense of increasing the noise level of the measurement. Another approach is to reduce the number of frequencies sampled, but this strategy has the effect of reducing the degree of freedom for the regression. A third approach is to eliminate a source of noise in the system, for example, by using a low-pass filter to reduce the high-frequency noise in the signals input to the frequency response analyzer. Selection of an appropriate strategy to reduce experimental time requires quantitative assessment of the effect of each strategy on the error characteristics, and this assessment is provided by the measurement model approach.[7,13,14] The above discussion was oriented towards use of digital frequency response analyzers such as the Solartron series, but similar arguments can be developed for other impedance measurement techniques such as phase-sensitive detection (using lock-in amplifiers) and applications of fast Fourier transforms.

### **Estimation of Asymptotic Values**

In addition to its use to quantify the noise level of the measurement and to assess consistency with the Kramers-Kronig relations, the measurement model approach can be used as follows to quantify differences in surface reactivity.

1. The frequency-dependent stationary stochastic component of the error structure was identified following the method presented by Agarwal *et al.*[13] This information was used to weight subsequent regressions.
2. The portion of the spectrum that is consistent with the Kramers-Kronig relations was identified following the method presented by Agarwal *et al.*[14] The error structure found in part 1 above was used to weight the regression. High-frequency data were found in some cases to be corrupted by instrumental artifacts. The low-frequency data were typically found to be consistent with the Kramers-Kronig relations except for data collected under conditions where the system was changing rapidly.
3. The measurement model was regressed to the part of the spectrum found to be consistent with the Kramers-Kronig relations. The regressed parameter values were used to extrapolate the measurement model to the zero frequency limit, and Monte Carlo simulations were performed using the standard deviations of the regressed parameters to estimate the confidence interval for the extrapolation.[14] The polarization impedance was obtained by subtracting the regressed solution resistance from the extrapolated zero frequency value.

## **Results and Discussion**

The emphasis of the present work is on the use of the measurement model for determining zero and high-frequency asymptotes for the impedance response. In this section, an experimental system is described that was used to validate the procedure and examples of its implementation are given.

### **Verification of Procedure**

Data obtained for the reduction of ferricyanide on a Pt rotating disk electrode were used to verify that the procedure described above provides adequate estimation of the polarization impedance.[19,20] The data set used for this purpose was collected at a rotation speed of 120 rpm,

at one quarter of the mass-transfer-limited current, and at a temperature of 25°C. As this system was controlled by mass transfer, it provided a good test of the algorithm. While, in theory, an infinite number of Voigt elements are needed to approximate a Warburg impedance, only a finite number can be obtained from the regression of a Voigt model to the data because stochastic errors (or noise) in the measurement limit the information content of the data.

A process model for the impedance response associated with convective diffusion to a rotating disk, developed by Tribollet and Newman,[21] was modified by Orazem *et al.*[22]

$$Z(\omega) = R_e + \frac{R_i + z_d(\omega)}{1 + (j\omega C)^{1-\alpha} (R_i + z_d(\omega))} \quad (2)$$

where

$$z_d(\omega) = z_d(0) \left( -\frac{1}{\theta'_0 (pSc)^{1/3}} + \frac{Z_1 (pSc^{1/3})}{Sc^{1/3}} + \frac{Z_2 (pSc^{1/3})}{Sc^{2/3}} \right) \quad (3)$$

The model includes 6 parameters ( $R_e$ ,  $R_i$ ,  $C$ ,  $\alpha$ ,  $z_d(0)$ , and  $Sc$ ) which were obtained by regression to the data. The methods of Agarwal *et al.*[7,13,14] were used to identify the frequency-dependent standard deviation of repeated measurements and to remove data influenced by bias errors that caused inconsistencies with the Kramers-Kronig relations. A weighted non-linear least squares regression was used to fit the process model to the data, and the weighting was provided by the inverse of the experimentally determined variance of the data.

The results of the regression are provided in Fig. 1. The data and the model reveal a high frequency loop associated with the electrode reaction and a low frequency loop corresponding to Warburg behavior. The residual errors for the regression show that the fitting errors are of the order of the noise level of the measurement. The larger deviation and trending evident at frequencies above 100 Hz are attributed to the approximate constant-phase-element model used to account for the electrochemical reaction. The dashed lines in Figs. 1b and 1c represent 95.4 percent confidence intervals (2 times the experimentally determined standard deviation of the measurement) scaled to the real and imaginary parts of the impedance, respectively. The standard deviations of the real and imaginary parts were found to be equal, as reported for other spectroscopy systems,[23] and the different appearance of the confidence interval lines in Figs. 1b and 1c are caused by the different scaling used. The 95.4 percent confidence intervals for the data are of the order of 0.3 percent of the real part of the impedance and 1 percent of the imaginary part. As seen in Table 1, the Schmidt number obtained was  $1163 \pm 39$  which is close to the value of  $1100 \pm 4$  obtained by Robertson *et al.* using DC methods and  $1155 \pm 43$  using electrohydrodynamic impedance methods.[24] The residual sum of squares for this fit was 1.561 times the sum of variances. In the context of an F-Test for comparison of variance,[1] the ratio is less than  $F_{0.01} = 1.754$  which suggests that the hypothesis that the residual sum of squares is statistically different from the sum of variances for the measurement can be rejected. The trending of the residual errors at frequencies above 100 Hz suggests, however, that the model does not adequately describe the high frequency behavior.

Monte Carlo simulations were performed to extrapolate the process model to the zero frequency asymptote. The resulting value of  $188.6 \pm 0.9 \Omega$  is shown as a diamond in Fig. 1a. The corresponding value obtained by regression of the measurement model, shown in Fig. 2, was  $188.3 \pm 0.6 \Omega$ . The number of Voigt elements used was the largest that yielded parameter estimates that did not include zero within their 95.4% confidence interval. The regression of the measurement model yielded a normalized residual sum of squares of 1.8691, which was larger than that obtained by the process model. The residual errors shown in Figs. 2b and 2c fell roughly within the confidence interval of the data. In spite of the fact Voigt elements provide only an approximate representation of Warburg



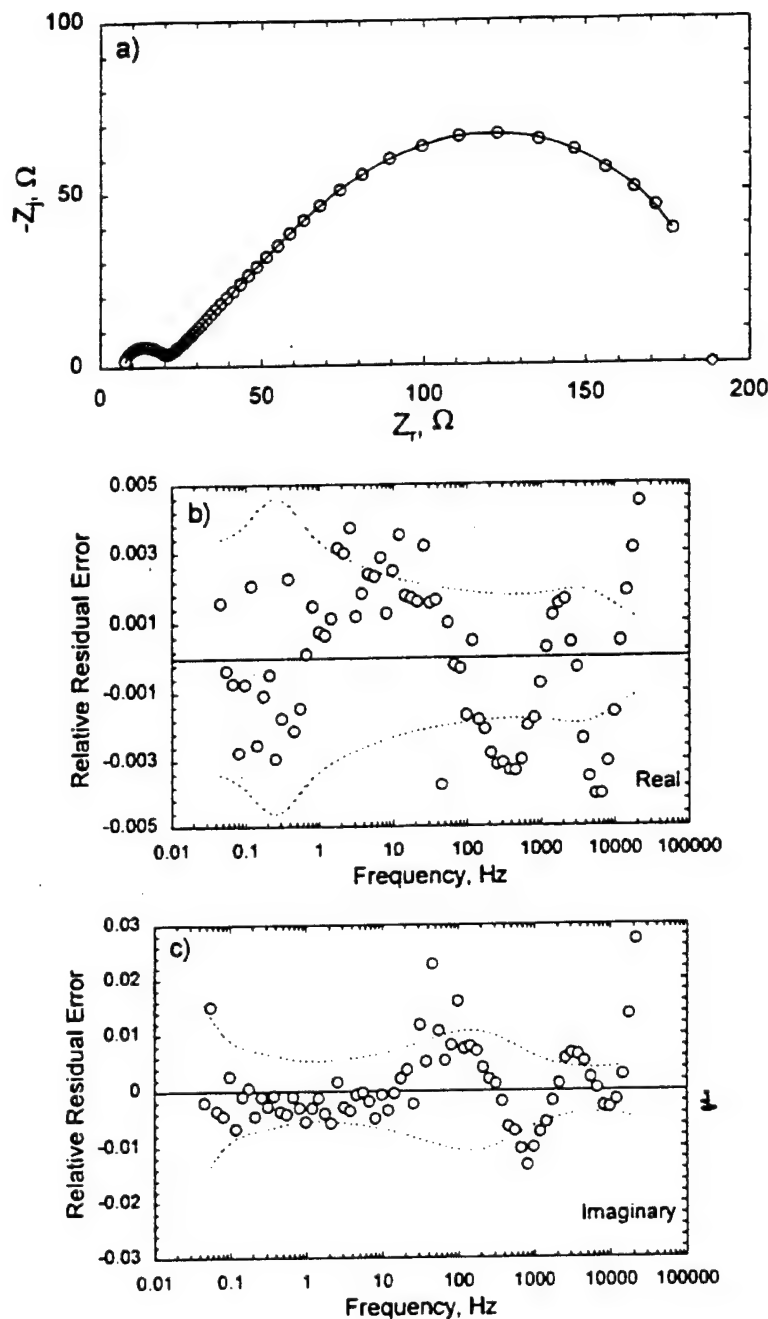


**Figure 1.** Results of the regression of the process model (equations (2) and (3)) to the data obtained for the reduction of ferricyanide on a Pt disk rotating at 120 rpm and held at  $\frac{1}{4}$  of the mass-transfer-limited current. The regression was weighted by the experimentally determined variance, and data shown by the measurement model to be inconsistent were removed from the regressed data set. The frequency range was 0.0461 Hz to 21.4 kHz. a) impedance plane representation where  $\circ$  represents data used in the regression,  $\diamond$  represents the predicted zero-frequency asymptote, and the line is the regressed fit. b) and c) relative residual error for the regression where the dashed lines represent the bounds for the 95.4% confidence interval for the measurement (i.e.,  $\pm 2\sigma/\hat{Z}_r$ , and  $\pm 2\sigma/\hat{Z}_i$ , respectively).

**Table 1.** Comparison of regression results obtained using the measurement and process models. The shaded area represents conditions under which both models could be regressed to the data.

Measurement Model					Process Model				
#data	Lowest Frequency, Hz	#Volgt elements	NSSQ*	$R_{\text{vol}}, \Omega$	$Z(0), \Omega$	NSSQ*	$R_{\text{rel}}, \Omega$	$Z(0), \Omega$	Error %
69	0.0461	9	1.8691	$6.96 \pm 0.03$	$188.3 \pm 0.6$	1.561	$7.2548 \pm 0.0071$	$188.6 \pm 0.9$	-0.19
63	0.146	9	1.8109	$6.95 \pm 0.04$	$187.4 \pm 0.6$	1.434	$7.2548 \pm 0.0075$	$188.7 \pm 1.9$	-0.66
58	0.381	11	0.8424	$6.70 \pm 0.12$	$184.2 \pm 1.7$	2.739	$7.2548 \pm 0.0078$	$187.8 \pm 5.4$	-1.94
57	0.461	11	0.8744	$6.72 \pm 0.11$	$185.6 \pm 2.2$	2.99	$7.2548 \pm 0.0079$	$188.5 \pm 6.9$	-1.55
56	0.559	11	0.9977	$6.73 \pm 0.11$	$182.5 \pm 3.1$	...Regression Failed...			
53	0.993	9	1.895	$6.81 \pm 0.07$	$151.0 \pm 2.5$				
48	2.59	9	1.3026	$6.80 \pm 0.07$	$139 \pm 38$				
43	6.77	8	1.6767	$6.84 \pm 0.06$	$104 \pm 23$				
38	17.7	7	1.7196	$6.78 \pm 0.08$	$54.5 \pm 1.6$				
33	46.1	7	0.9235	$6.70 \pm 0.10$	$40.9 \pm 1.2$				
28	120	6	0.4807	$6.46 \pm 0.19$	$30.7 \pm 0.6$				
23	314.08	5	0.7675	$6.70 \pm 0.10$	$25.9 \pm 0.3$				

\* Residual sum of squares normalized by the independently determined sum of variances for the measurement.

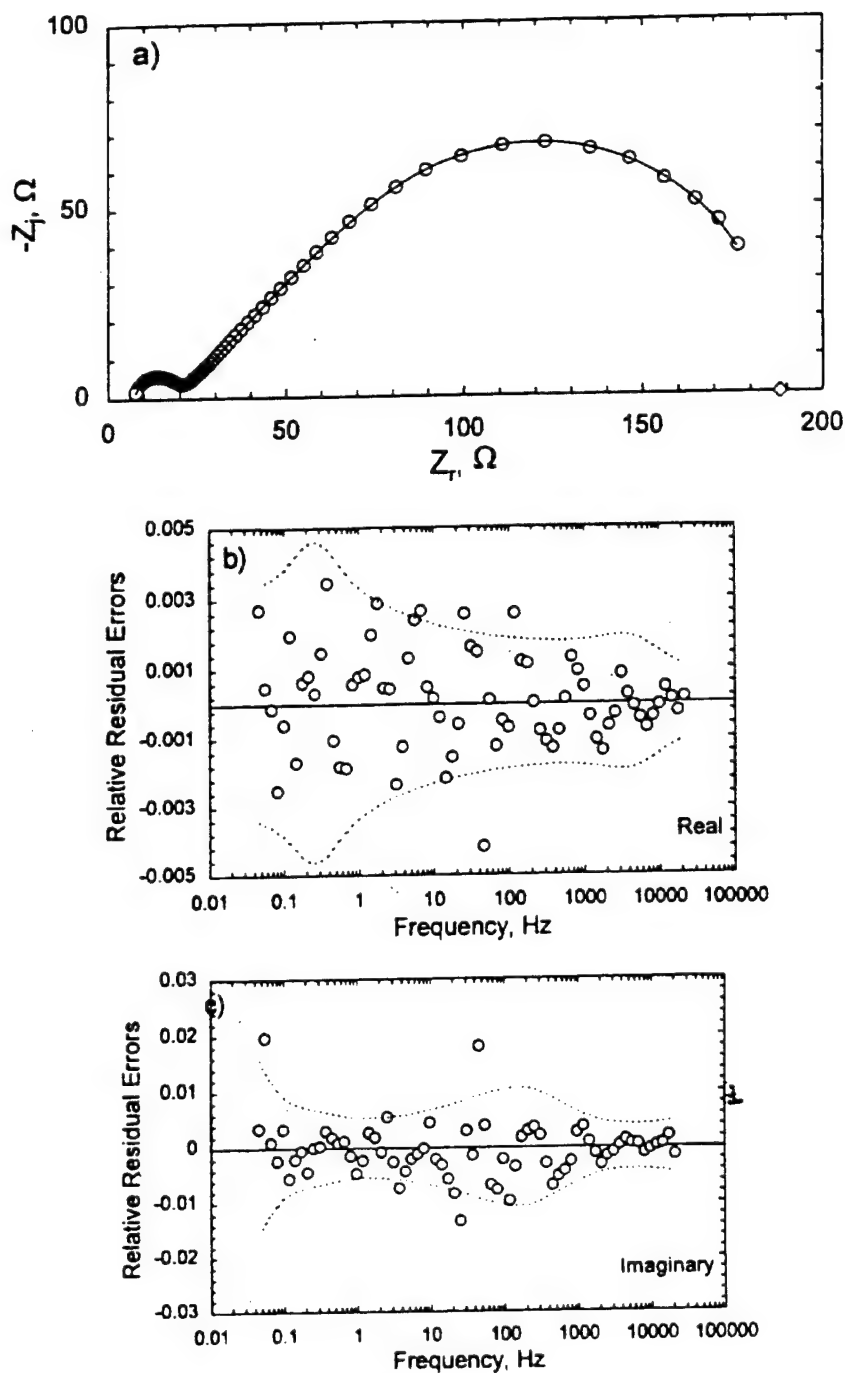


**Figure 2.** Results of the regression of the measurement model to the data presented in Figure 1. The frequency range was 0.0461 Hz to 21.4 kHz. a) impedance plane representation where  $\circ$  represents data used in the regression,  $\diamond$  represents the predicted zero-frequency asymptote, and the line is the regressed fit. b) and c) relative residual error for the regression where the dashed lines represent the bounds for the 95.4% confidence interval for the measurement (i.e.,  $\pm 2\sigma / \hat{Z}_r$  and  $\pm 2\sigma / \hat{Z}_i$ , respectively).

behavior, the zero frequency asymptotes and solution resistances obtained by the two models were in good agreement. The solution resistance obtained by using the process (Warburg) model was  $7.2548 \pm 0.0071 \Omega$ ; whereas that obtained using the measurement model was  $6.96 \pm 0.03 \Omega$ .

The fit and extrapolation of the process model to a reduced data set is shown in Fig. 3. The lowest frequency included in the regression was 0.461 Hz. The corresponding results from regression of the measurement model with eleven Voigt elements are shown in Fig. 4. The regression results are shown in Table 1. Both process and measurement models could be used successfully to extrapolate the data, and the results obtained agreed to within 1.55 percent.

The process model could not be used to obtain a full set of parameters with a data set reduced further than that shown in Figs. 3 and 4 because the resulting confidence interval for the Schmidt number included zero. As the measurement model based on a superposition of Voigt elements is more general, it could be used to provide extrapolations of more severely reduced data sets, as shown in Figs. 5a and 5b. A summary of the comparison between asymptotic values predicted by the process and measurement models is shown in Fig. 6. As the process model describes more completely the low-frequency behavior of the system, the results obtained from the process model are considered to be more reliable. Within the frequency range that was sufficiently complete as to allow use of the process model for extrapolations, the measurement model gave asymptotic values that were in good agreement with those obtained from the process model. The asymptotic values obtained by fitting the measurement model to a more severely truncated data set, however, were lower than the expected value. This result can be expected because deletion of low-frequency data results in a loss of information from low-frequency processes. It should be noted that the confidence interval for the extrapolated values, obtained using the standard deviations of regressed parameters, did not provide an accurate indication of the uncertainty associated with missing data.

This work shows that, in spite of the fact Voigt elements provide only an approximate representation of Warburg behavior, when sufficient low-frequency data were included that the Warburg model could be regressed to the data, the zero and high frequency asymptotes obtained by the two models were in good agreement. The measurement model therefore provides a useful tool for approximate analysis of impedance data under conditions that an appropriate process model is unavailable. The measurement model does not, however, provide an alternative to collecting data over a frequency range sufficient to sample all relevant electrochemical phenomena.

### **Corrosion of Copper in Synthetic Seawater**

The objective of the experiment was to explore the reactivity of the copper coupon as a function of time and as a function of jet velocity.[25-27] A PAR 273 potentiostat was used to monitor the corrosion potential and, at regular intervals, to conduct impedance scans. The impedance measurements were conducted using a Solartron 1260 frequency response analyzer, and the impedance scans were obtained at the zero-current condition using the variable-amplitude galvanostatically-modulated impedance technique.[27]

The corrosion potential is presented in Fig. 7a for a copper disk subjected to a submerged impinging jet of aerated synthetic sea-water at 1 m/s. The transient presented in Fig. 7a represents the first 24 hours of a 480 hour duration experiment. The variable-amplitude galvanostatic method was used to monitor the corrosion system at the open-circuit condition at regular intervals. Impedance data are presented in Fig. 7b. As shown in Fig. 7a, the trends in corrosion potential were unaffected by the impedance scans. The impedance scans given in Fig. 7b show that the surface reactivity changed dramatically over the course of 24 hours.

The polarization impedance and its confidence interval were obtained by Monte Carlo simulations using the parameters and associated confidence intervals obtained by regression of the measurement model. The goal of this effort was to assess the reactivity of the corrosion system in the absence of a

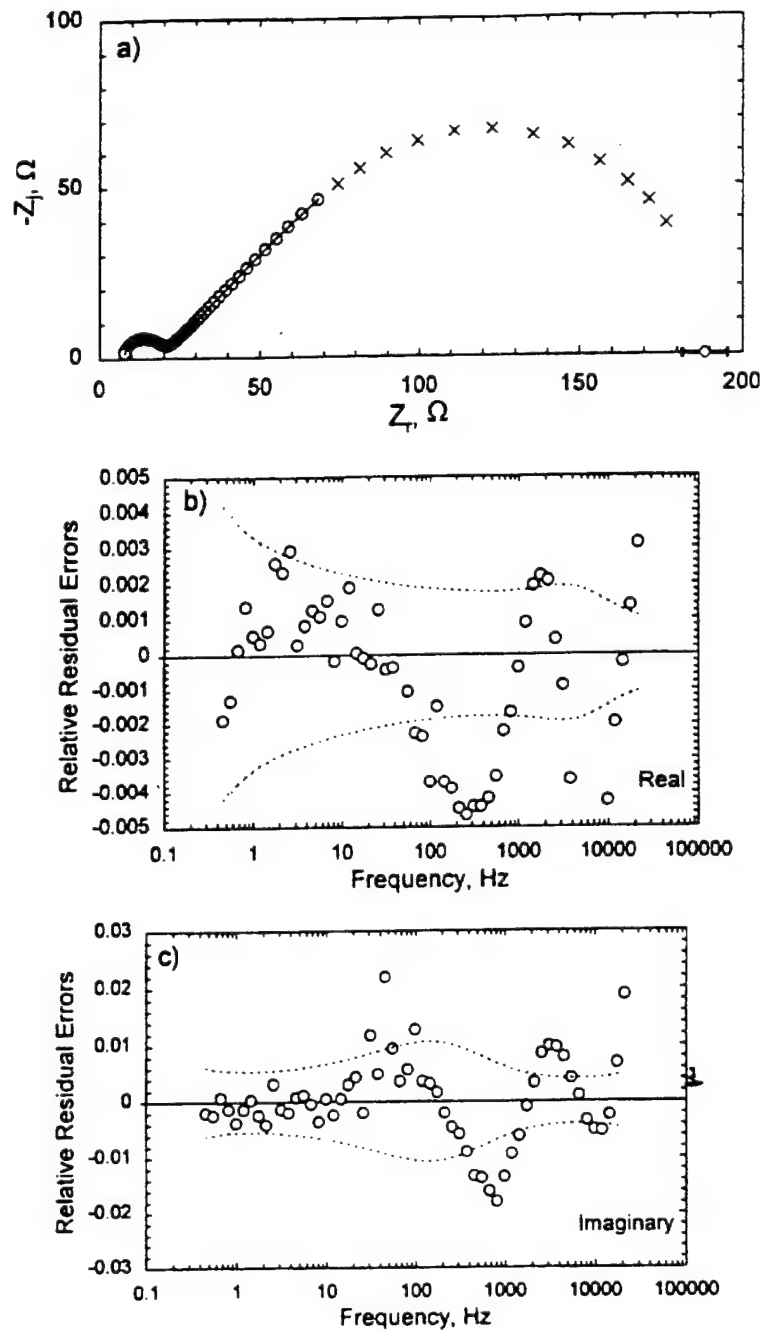


**Figure 3.** Results of the regression of the process model (equations (2) and (3)) to the data presented in Figure 1. The frequency range was 0.461 Hz to 21.4 kHz. a) impedance plane representation where  $\circ$  represents data used in the regression,  $\times$  represents data removed from the regression,  $\diamond$  represents the predicted zero-frequency asymptote, and the line is the regressed fit. b) and c) relative residual error for the regression where the dashed lines represent the bounds for the 95.4% confidence interval for the measurement (i.e.,  $\pm 2\sigma / \hat{Z}_r$  and  $\pm 2\sigma / \hat{Z}_i$ , respectively).

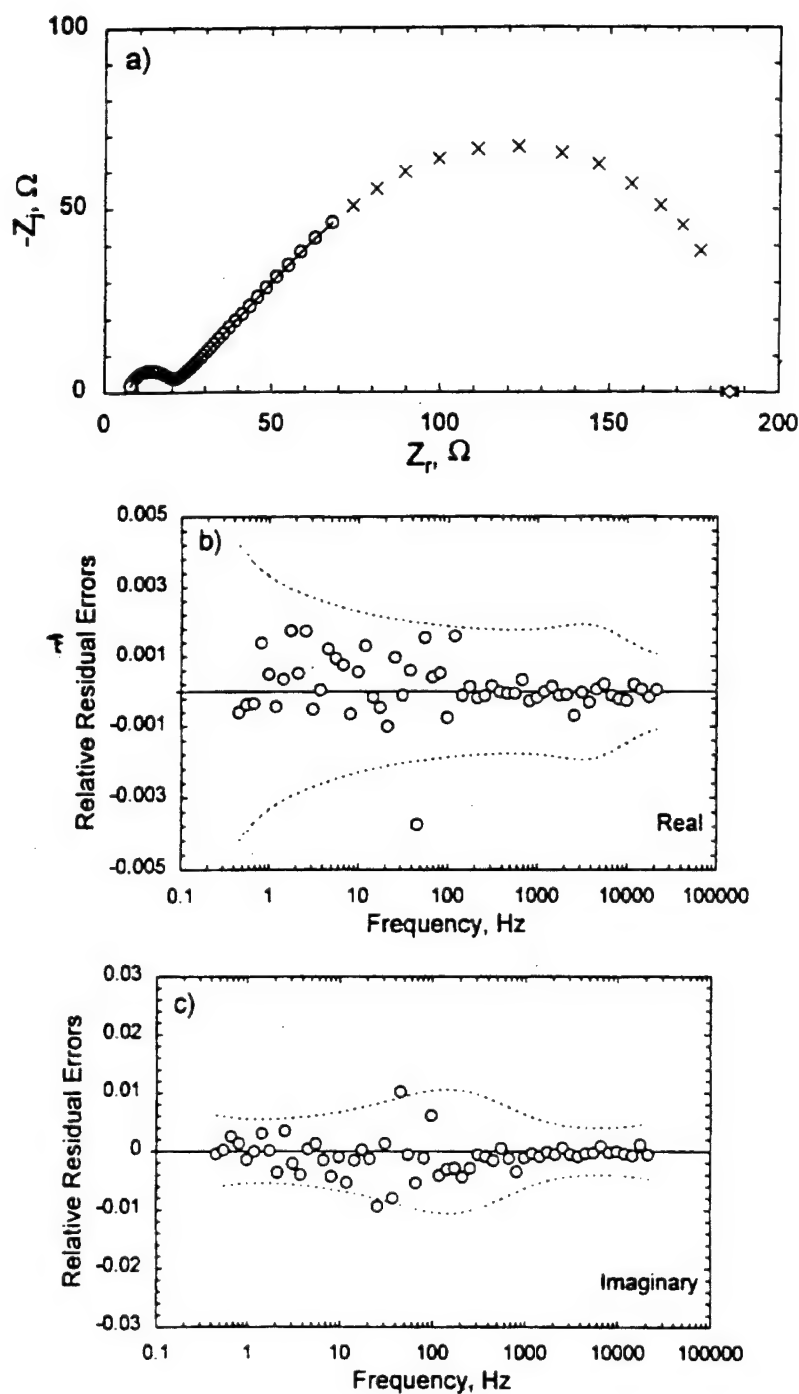


**Figure 4.** Results of the regression of the measurement model to the data presented in Figure 3. The frequency range was 0.461 Hz to 21.4 kHz. a) impedance plane representation where O represents data used in the regression, x represents data removed from the regression,  $\diamond$  represents the predicted zero-frequency asymptote, and the line is the regressed fit. b) and c) relative residual error for the regression where the dashed lines represent the bounds for the 95.4% confidence interval for the measurement (i.e.,  $\pm 2\sigma / \hat{Z}_r$  and  $\pm 2\sigma / \hat{Z}_i$ , respectively).



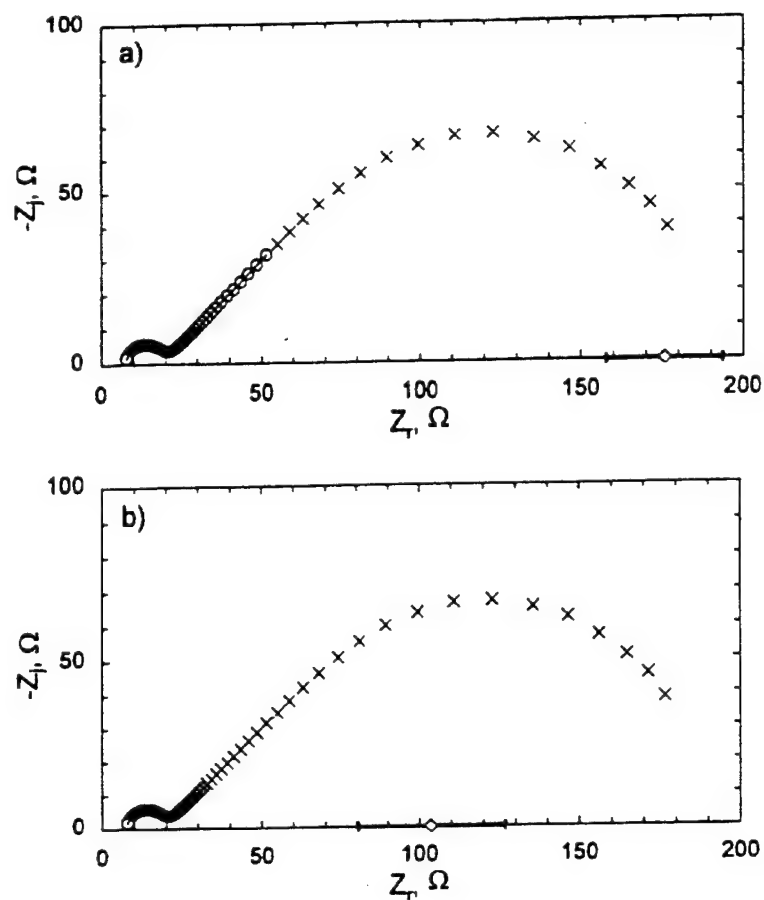


**Figure 5.** Results of the regression of the measurement model to the data presented in Figure 1 where O represents data used in the regression, x represents data removed from the regression,  $\diamond$  represents the predicted zero-frequency asymptote, and the line is the regressed fit. a) The regressed frequency range was 0.993 Hz to 21.4 kHz. b) The regressed frequency range was 6.77 Hz to 21.4 kHz.

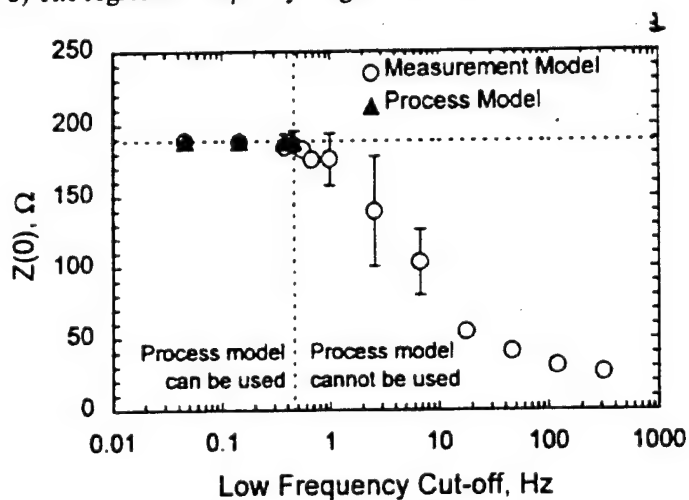


**Figure 6.** Comparison of the asymptotic values obtained by the measurement model to those obtained using the established process model for this system as a function of the lowest frequency used in the regression.

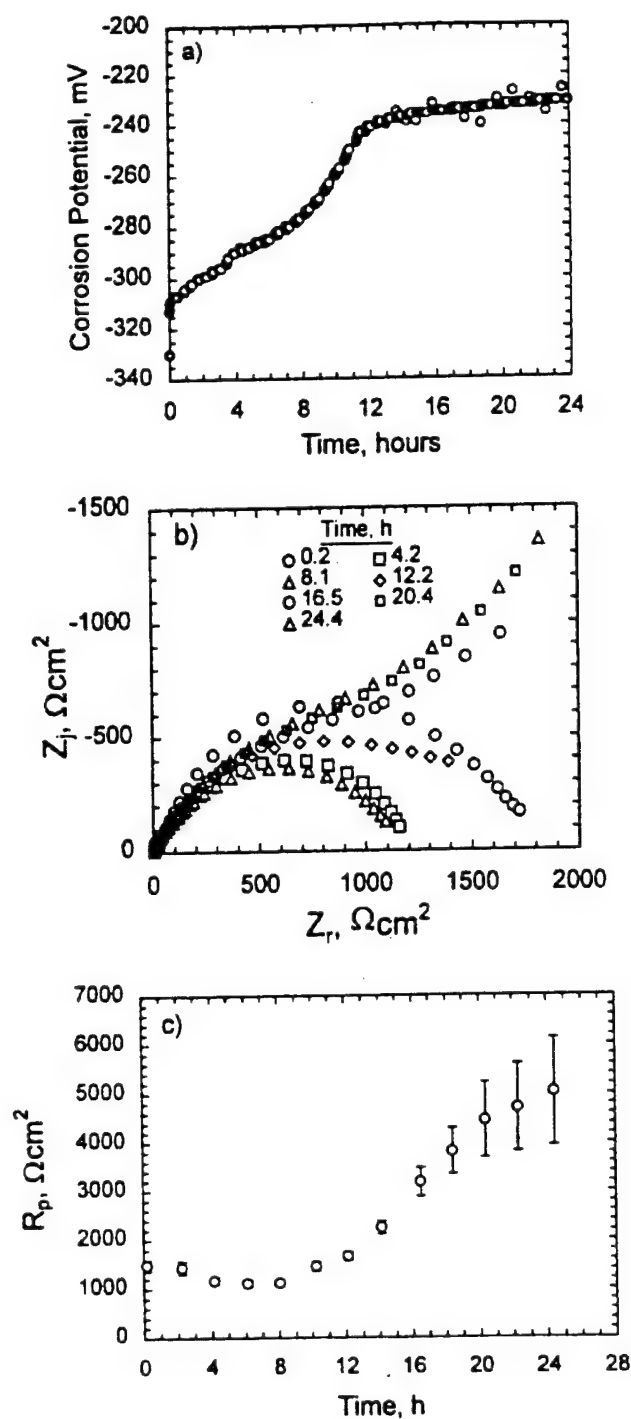


**Figure 7.** Results obtained for a copper disk subjected to an impinging jet of synthetic sea water with a jet velocity of 1 m/s for 24 hours. a) corrosion potential as a function of time, b) impedance plane representations of impedance spectra obtained using the variable-amplitude galvanostatic modulation, and c) polarization impedance obtained using the techniques presented in this paper.

detailed process model. Results are presented in Fig. 7c for the polarization impedance as a function of time for the impedance data shown in Fig. 7b. The polarization impedance increased from an initial value of roughly 1,500 to 10,000  $\Omega\text{cm}^2$ . The impedance decreased initially due to removal of the native oxide layer and then increased as the films associated with the corrosion products formed and grew. The role of the measurement model for evaluating consistency with the Kramers-Kronig relations is evident in that the apparent zero frequency asymptote of the scan obtained at 0.2 hours (Fig. 6b) was 1,800  $\Omega\text{cm}^2$ ; whereas, the corresponding polarization impedance shown in Fig. 7c obtained by the analysis outlined above was 1,500  $\Omega\text{cm}^2$ . The low frequency data were corrupted by nonstationary behavior, but a polarization impedance could still be obtained from the portion of the data that satisfied the Kramers-Kronig relations. The use of polarization impedance to monitor the influence of changes in pH and jet velocity for this system is illustrated by Fig. 8.

### ***Cast Iron in Evian Water***

The objective of this work was to study the effect of chlorination on the corrosion of cast iron pipes containing municipal drinking water.[28] The electrochemical instrumentation consisted of a Solartron 1287 potentiostat-galvanostat and a Solartron 1250 Frequency Response Analyzer. The frequency range used was 64 kHz to a few mHz. The experiments were performed with a rotating disk electrode machined from a cast iron potable water pipe. The electrolyte was the commercial Evian water, used as delivered. The temperature was fixed at 20°C. Other experimental details are presented in reference 28. Results obtained in the absence of chlorination are presented in Fig. 9. The polarization resistance obtained using the measurement model technique is in good agreement with that obtained using a 9-parameter process model which included the influence of a porous film on anodic and cathodic reactions. The Ohmic resistance obtained from the measurement model was in good agreement with that obtained from independent measurements.

### **Conclusions**

Even in the absence of detailed physicochemical models, the enhanced error analysis made possible by use of measurement models can play a significant role in the interpretation of impedance spectra. The identification of stochastic and bias errors allows a rational approach toward experimental design which takes into account the various contributions to the error structure. The zero and high-frequency limits obtained through the measurement model were used to determine the polarization resistance in a way that accounted for the experimentally determined error structure. The results of this procedure, weighted by an appropriate statistical analysis, can be used to monitor electrochemical systems as functions of time or process conditions. The approach was validated for the reduction of ferricyanide on platinum, for which accurate process models are available, and demonstrated for the corrosion of copper in synthetic seawater and of cast iron in Evian water.

### **Acknowledgements**

The work was supported by the Office of Naval Research under Grant Numbers N00014-93-I-0056 and N00014-93-I-1113 (A.J. Sedriks, Program Monitor). This work was also supported in part by the National Science Foundation under a US-France Cooperative Research Grant INT-9416713.

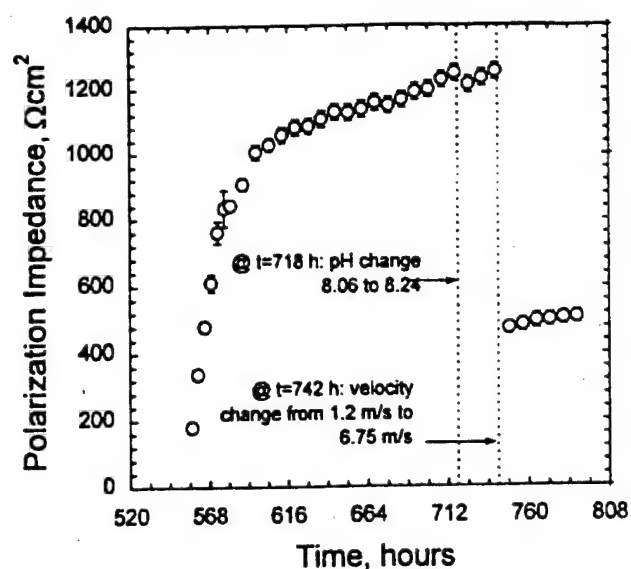


Figure 8. Polarization resistance obtained for a copper disk subjected to an impinging jet of synthetic sea water. The polarization resistance shows a small effect of changing pH at 718 hours and of changing jet velocity at 742 hours.

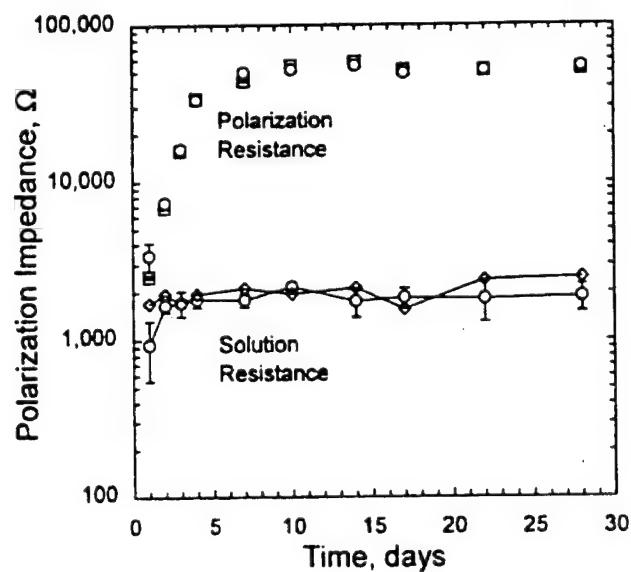


Figure 9. Polarization and solution resistance obtained for a cast iron rotating disk. (O) values obtained from measurement model, (□) values obtained from a preliminary process model, (◇) independently measured solution resistance.

## References

- [1] G. E. P. Box and N. R. Draper, *Empirical Model-Building and Response Surfaces*, John Wiley & Sons, Inc., New York, 1987.
- [2] Harold W. Sorenson, *Parameter Estimation: Principles and Problems*, Marcel Dekker, Inc., New York, 1980.
- [3] G. A. F. Seber, *Linear Regression Analysis*, John Wiley & Sons, New York, 1977, pp. 330-334.
- [4] R. W. Christy, *American Journal of Physics*, 40, 1403 (1972).
- [5] A. Jutan and L. H. Garcia-Rubio, *Process Control and Quality*, 4, 235 (1993).
- [6] L. K. DeNoyer and J. G. Good, *American Laboratory*, March, 1990. Software available from Spectrum Square Associates, Ithaca, NY, 114850.
- [7] P. Agarwal, M. E. Orazem, and L. H. Garcia-Rubio, *J. Electrochem. Soc.*, 139, 1917 (1992).
- [8] M. E. Orazem, P. Agarwal, A. N. Jansen, P. T. Wojcik, and L. H. Garcia-Rubio, *Electrochimica Acta*, 38, 1903 (1993).
- [9] P. Agarwal, O. C. Moghissi, M. E. Orazem, and L. H. Garcia-Rubio, *Corrosion*, 49, 278 (1993).
- [10] M. E. Orazem, P. Agarwal, L. H. Garcia-Rubio, *J. Electroanal. Chem.*, 378, 51 (1994).
- [11] B. A. Boukamp and J. R. Macdonald, *Solid State Ionics*, 74, 85 (1994).
- [12] B. A. Boukamp, *J. Electrochem. Soc.*, 142, 1885 (1995).
- [13] P. Agarwal, O. D. Crisalle, M. E. Orazem, and L. H. Garcia-Rubio, *J. Electrochem. Soc.*, 142, 4149 (1995).
- [14] P. Agarwal, M. E. Orazem, and L. H. Garcia-Rubio, *J. Electrochem. Soc.*, 142, 4159 (1995).
- [15] P. Agarwal, M. E. Orazem, and L. H. Garcia-Rubio, *Electrochimica Acta*, 41, 1017, (1996).
- [16] M. E. Orazem, P. Agarwal, C. Deslouis, and B. Tribollet, *J. Electrochem. Soc.*, 143, 948 (1996).
- [17] A. N. Jansen, P. T. Wojcik, P. Agarwal, and M. E. Orazem, *J. Electrochem. Soc.*, 143 (1996), 4066-4074.
- [18] A. N. Jansen and M. E. Orazem, *J. Electrochem. Soc.*, 143 (1996), 4074-4080.
- [19] M. Durbha, *Influence of Non-Uniform Current and Potential Distributions on the Interpretation of Impedance Spectra*, Ph.D. dissertation, University of Florida, Gainesville, 1998.
- [20] M. Durbha, M. E. Orazem, C. Deslouis, H. Takenouti, and B. Tribollet, "Current Distribution on a Rotating Disk Electrode Below the Mass-Transfer Limited Current: Influence on the Reduction of Ferricyanide on Pt," in preparation.
- [21] B. Tribollet and J. Newman, *J. Electrochem. Soc.*, 130, 2016 (1983).
- [22] M. E. Orazem, C. Deslouis, and B. Tribollet, "Comparison of Impedance Models for Mass Transfer to a Disk Electrode," presented at the 191<sup>st</sup> Meeting of the Electrochemical Society, Montreal, Canada, May 4-9, 1997, paper in preparation.
- [23] M. Durbha, M. E. Orazem, and L. H. Garcia-Rubio, *J. Electrochem. Soc.*, 144 (1997), 48-55.
- [24] B. Robertson, B. Tribollet, and C. Deslouis, *J. Electrochem. Soc.*, 135 (1988), 2279.

- 
- [25] P. T. Wojcik and M. E. Orazem, Paper #97-435, National Association of Corrosion Engineers, Houston, Texas, 1997.
- [26] P. T. Wojcik, E. Charrière, and M. E. Orazem, "Experimental Study of the Erosion-Corrosion of Copper and Copper-Nickel Alloys at the Corrosion Potential and at Anodic Potentials," to be presented at the *Tri-Service Conference on Corrosion*, November 17-21, 1997.
- [27] P. T. Wojcik and M. E. Orazem, "Variable-Amplitude Galvanostatically-Modulated Impedance Spectroscopy as a Tool for Assessing Reactivity at the Corrosion Potential without Distorting the Temporal Evolution of the System," *Corrosion*, in press.
- [28] C Deslouis, I. Frateur, L. Kiene, Y. Levi, and B. Tribollet, "Corrosion Study of Cast Iron Pipes in Water Distribution Systems by Impedances: Application to Chlorine Consumption," presented at *Electrochemical Methods for Corrosion Research, EMCR 97*, Trento, Italy, August 25-29, 1997.



# Current Distribution on a Rotating Disk Electrode below the Mass-Transfer-Limited Current

## Correction for Finite Schmidt Number and Determination of Surface Charge Distribution

Madhav Durbha\* and Mark E. Orazem\*\*

Department of Chemical Engineering, University of Florida, Gainesville, Florida 32611, USA

### ABSTRACT

The two-dimensional model for the current distribution on a rotating disk below the mass-transfer-limited current developed by Newman is extended here to account for the influence of a finite Schmidt number and to provide the charge distribution in the diffuse part of the double layer. A polynomial expansion in terms of  $Sc^{-1/3}$  is developed for the dimensionless concentration derivative at the electrode surface. The charge distribution is estimated under the assumption that specific adsorption can be neglected. This approach requires introduction of only one additional parameter corresponding to the distance between the metal surface and the plane of closest approach for solvated ions. Zero-frequency asymptotes for the local impedance values, determined from the steady-state calculations, are used to establish the need for a two-dimensional model for the impedance response of a disk electrode.

### Introduction

The rotating disk electrode is an effective tool for the identification of mechanisms and associated rate constants for electrode reactions, for studying homogeneous reactions accompanied by electrode processes, and for the measurement of diffusion coefficients of dissolved species because the fluid flow is well defined and the uniform axial velocity yields a uniform mass-transfer-limited current density. The popularity of the rotating disk for experimental electrochemistry has motivated development of mathematical models which describe the physics of the system.

The Levich equation for mass-transfer-limited current<sup>1</sup> was obtained under the assumption that the Schmidt number is infinitely large. Newman<sup>2</sup> provided a correction to the Levich equation which accounted for a finite value of the Schmidt number. Newman's correction amounted to a 3% reduction in the value of the mass-transfer-limited current obtained for a Schmidt number of 1000, typical of electrolytic systems. In subsequent work, he relaxed the assumption of a mass-transfer-limited condition by coupling convective diffusion in radial and axial directions in an inner diffusion-layer region with Laplace's equation for potential in an outer domain.<sup>3</sup> The cathodic Tafel limit of a Butler-Volmer expression was used to account for metal deposition kinetics. Appel extended this model to account for redox reactions as, in principle, Newman's model was developed for deposition reactions.<sup>4</sup>

The focus in later years was on frequency domain techniques. A significant effort has been expended on developing analytic formulae for the impedance response of a rotating disk electrode.<sup>5-16</sup> A comparative study of the application of these models to interpretation of impedance spectra has been presented by Orazem et al.<sup>17</sup> A one-dimensional numerical model for the impedance response of a rotating disk electrode which accounted for the influence of a finite Schmidt number was presented by Tribollet and Newman.<sup>18</sup> The first two terms in the Cochran expansion<sup>19</sup> for the axial component of fluid velocity were included in the convective diffusion equation. Tribollet et al.<sup>15</sup> reported that the errors caused by neglecting the second term in the axial velocity expansion could be as high as 24% for a Schmidt number of 1000. This result was confirmed by regression of various mass-transfer models to impedance data.<sup>17</sup> Mathematical models have been developed which account for frequency dispersion associated with the nonuniform potential distribution on the disk electrode,<sup>20-23</sup> but, to date, no comparable model has been developed for the influence of nonuniform mass transfer on the impedance response. Appel and

Newman<sup>24</sup> provided a preliminary mathematical development that they proposed would be used to develop a model for the influence of radially dependent convective diffusion on the impedance response under the assumption that the Schmidt number is infinitely large. Later Appel provided a model to calculate the radial distribution of impedance under the assumption that the Schmidt number is infinitely large.<sup>4</sup> In this work he used a total overpotential without accounting separately for the surface, concentration, and zeta overpotentials.

Though the errors resulting from neglecting the finite Schmidt number correction are not so significant for steady-state calculations, they have been shown to be significant in the frequency domain.<sup>15,17</sup> The objective of the present work is to develop a steady-state treatment of current and potential distributions on a rotating disk electrode that accounts for a finite Schmidt number and for the distribution of charge in the diffuse part of the double layer. This work provides a foundation for the subsequent development of a mathematical model that would account for the influence of nonuniform mass transfer on the impedance response of a rotating disk electrode.<sup>25</sup> The present work also provides a means of interpreting anomalous values of Schmidt numbers obtained from impedance data collected for the reduction of ferricyanide on a Pt disk electrode in terms of the competing roles of surface poisoning and the influence of nonuniform current distribution.<sup>7,26,27</sup>

### Theoretical Development

The domain of interest was divided into an outer region where electroneutrality was assumed to apply and the concentration was assumed to be uniform, an inner boundary-layer region where electroneutrality and the convective diffusion equation for the reacting species were assumed to apply, and an inner diffuse part of the double layer where the assumption of electroneutrality was relaxed. The entire electrode surface was assumed to be active; thus, local passivation and partial blocking phenomena were not included in the model.

**Diffusion layer.**—The development in this part follows that presented by Newman<sup>3</sup> with the exception that a correction is made for a finite Schmidt number by incorporating three-term expansions appropriate near the electrode surface for axial and radial velocity. A critical assumption in the development of this work was that the current densities at the inner limit of the diffusion layer and at the inner limit of the outer region are equal to the current density at the electrode surface. This assumption is valid if the diffusion layer is thin compared to the electrode radius. The validity of this assumption is implicit for

\* Electrochemical Society Student Member.

\*\* Electrochemical Society Active Member.

an infinite Schmidt number because the diffusion layer is infinitely thin.

For a finite Schmidt number, the diffusion layer is still small as compared to typical disk dimensions. The thickness of the boundary layer  $\delta$  is given by

$$\delta = \left( \frac{3D_r}{av} \right)^{1/3} \left( \frac{\nu}{\Omega} \right)^{1/2} \quad [1]$$

The boundary-layer thickness for the copper deposition system considered by Newman<sup>3</sup> is determined by the diffusivity of the cupric ion ( $D_{Cu^{2+}} = 0.642 \times 10^{-5} \text{ cm}^2/\text{s}$ ) and by the kinematic viscosity ( $\nu = 0.94452 \times 10^{-2} \text{ cm}^2/\text{s}$ ). For a rotation rate of 300 rpm,  $\delta$  has a value of 13.76  $\mu\text{m}$ , which is small as compared to the disk radius of 0.25 cm, yielding an aspect ratio  $\delta/r_0 = 0.0055$ . The corresponding value for the ferricyanide system treated in a later section of this paper is 0.012. The solution of the convective diffusion equation can, in these cases, be decoupled from the solution of Laplace's equation for potential in the region of uniform composition.

Under the assumption of a steady state, the convective diffusion equation is given by

$$v_r \frac{\partial c_R}{\partial r} + v_z \frac{\partial c_R}{\partial z} = D_R \frac{\partial^2 c_R}{\partial z^2} \quad [2]$$

where R in the subscript corresponds to the reacting species, and other symbols are defined in the list of symbols. A separation of variables can be applied as shown below

$$c_R = c_\infty \left[ 1 + \sum_{m=0}^{\infty} \left( A_m (r/r_0)^{2m} \theta_m(\xi) \right) \right] \quad [3]$$

where

$$\xi = z \left( \sqrt{av/(3D_R)} \right) \sqrt{\Omega/\nu} \quad [4]$$

For  $\theta_m = 1$  at  $\xi = 0$ , the radial concentration distribution on the electrode surface can be written as

$$c_0 = c_\infty \left[ 1 + \sum_{m=0}^{\infty} \left( A_m (r/r_0)^{2m} \right) \right] \quad [5]$$

The expressions for the radial and axial components of the velocity resulting from Cochran three-term expansion<sup>19</sup> are given by

$$v_r = arz \frac{\Omega^{3/2}}{\nu^{1/2}} - \frac{1}{2} rz^3 \frac{\Omega^2}{\nu} - \frac{b}{3} rz^3 \frac{\Omega^{5/2}}{\nu^{3/2}} \quad [6]$$

and

$$v_z = -az^2 \frac{\Omega^{3/2}}{\nu^{1/2}} + \frac{1}{3} z^3 \frac{\Omega^2}{\nu} + \frac{b}{6} z^4 \frac{\Omega^{5/2}}{\nu^{3/2}} \quad [7]$$

respectively. Application of Eq. 3, 4, 6, and 7 in Eq. 2 yields

$$\sum_{m=0}^{\infty} A_m (r/r_0)^{2m} \theta_m''(\xi) + \frac{3\xi^2}{a} \left\{ a - \frac{\xi}{3} \left( \frac{3D_R}{av} \right)^{1/3} - \frac{b\xi^2}{6} \left( \frac{3D_R}{av} \right)^{2/3} \right\} \theta_m'(\xi) - \frac{3\xi}{a} \left\{ a - \frac{\xi}{2} \left( \frac{3D_R}{av} \right)^{1/3} - \frac{b\xi^2}{3} \left( \frac{3D_R}{av} \right)^{2/3} \right\} \sum_{m=0}^{\infty} 2mA_m (r/r_0)^{2m} \theta_m(\xi) = 0 \quad [8]$$

By equating the coefficients of  $(r/r_0)^{2m}$  Eq. 8 can be rewritten as

$$\theta_m'' - \frac{3}{a} \xi^2 \left[ -a + \frac{1}{3} \xi \left( \frac{3}{a} \right)^{1/3} Sc^{-1/3} + \frac{b}{6} \xi^2 \left( \frac{3}{a} \right)^{2/3} Sc^{-2/3} \right] \theta_m' - \frac{6m\xi}{a} \left[ a - \frac{1}{2} \xi \left( \frac{3}{a} \right)^{1/3} Sc^{-1/3} - \frac{b}{3} \xi^2 \left( \frac{3}{a} \right)^{2/3} Sc^{-2/3} \right] \theta_m = 0 \quad [9]$$

The primes in the superscripts refer to derivatives with respect to  $\xi$ . Equation 9 can be compared to

$$\theta_m'' + 3\xi^2 \theta_m' - 6m\xi \theta_m = 0 \quad [10]$$

obtained by Newman for the case of infinite Schmidt number. The boundary conditions for Eq. 9 are  $\theta_m = 1$  at  $\xi = 0$ , and  $\theta_m = 0$  at  $\xi = \infty$ . For the numerical calculation presented here, a value of  $\xi = 20$  was used for approximation of the boundary condition at  $\infty$ . The choice of this value is justified as a value of  $\xi = 10$  resulted in the same values of  $\theta_m$  to within 15 significant digits and the derivative of  $\theta_m$  with respect to  $\xi$  at  $\xi = 20$  yielded a value identically equal to 0. Equation 9 exhibits a functional dependence on the Schmidt number. The numerical procedure that was used to solve the convective diffusion equation is presented in a subsequent section.

The current distribution on the electrode surface at steady state depends only on the dimensionless concentration gradient at the electrode surface  $\theta_m'(0)$  and not on the  $\theta_m$  values at the other axial positions, i.e.

$$\frac{i}{nF} = \frac{D_R}{1 - t_R} \frac{\partial c_R}{\partial z} \bigg|_{z=0} = \frac{D_R c_\infty}{1 - t_R} \left( \frac{av}{3D} \right)^{1/3} \sqrt{\frac{\Omega}{\nu}} \sum_{m=0}^{\infty} A_m (r/r_0)^{2m} \theta_m'(0) \quad [11]$$

where  $t_R$  is the transference number of the reacting species. The interfacial overpotential resulting from convective diffusion is the concentration overpotential given by

$$\eta_c = -\frac{RT}{ZF} \left[ \ln \left( \frac{c_z}{c_0} \right) - t_R \left( 1 - \frac{c_0}{c_z} \right) \right] \quad [12]$$

**Outer region: Laplace's equation.**—The approach taken followed that developed by Newman.<sup>3</sup> In the outer region, concentrations were assumed to be uniform, and, under the assumption that there is no charge distribution within the bulk of the solution, the potential in this region satisfies Laplace's equation. Hence

$$\nabla^2 \Phi = 0 \quad [13]$$

where  $\Phi$  is the potential referenced to infinity. The solution of Eq. 13 after transformation to rotational elliptic coordinates  $(\eta, \mu)$  where  $z = r_0 \mu \eta$  and  $r = r_0 \sqrt{(1 + \mu^2)(1 - \eta^2)}$  and after applying appropriate boundary conditions is

$$\Phi_0 = \frac{RT}{ZF} \sum_{n=0}^{\infty} B_n P_{2n}(\eta) \quad [14]$$

on the electrode surface ( $\mu = 0$ ), where  $Z = -z_z/(z_z - z_-)$  for single salt and  $Z = -n$  with supporting electrolyte. The current density obtained from the derivative of the potential just outside the diffusion layer is assumed to be equal to that obtained from Eq. 11; thus a relationship between coefficients  $B_n$  and  $A_m$  is found as

$$B_n = \frac{\pi}{4} N \sum_{m=0}^{\infty} (Q_{n,m} A_m) \quad [15]$$

where

$$Q_{n,m} = (4n + 1) \frac{4\theta_m'(0)}{\pi M_{2n}'(0)} \int_0^1 \eta (1 - \eta^2)^m P_{2n}(\eta) d\eta \quad [16]$$

$$M'_{2n}(0) = -\frac{2}{\pi} \frac{(2^n n!)^4}{[(2n)!]^2} \quad [17]$$

and

$$N = -\sqrt{\frac{r_0^2 \Omega}{v}} \left( \frac{av}{3D} \right)^{1/3} \frac{nZF^2 D c_\infty}{RT(1-t)\kappa_\infty} \quad [18]$$

The  $A_m$  coefficients were determined using an iterative procedure. A more detailed discussion of the solution procedure can be found in Ref. 3.

**Diffuse part of the double layer.**—The method used to account for the two-dimensional diffuse part of the double layer followed the approach suggested by Frumkin<sup>28</sup> in which the kinetic expression was written in terms of a surface overpotential adjusted by the zeta potential and the concentrations were replaced by the concentrations at the inner limit of the diffuse double layer.

**Solution of Poisson's equation.**—Under the assumption that the double layer is unaffected by the passage of current (see, e.g., Ref. 29) the concentration at the inner limit of the diffuse part of the double layer is given by

$$c_{i,ddl} = c_{i,0} \exp\left(-\frac{z_i F \zeta}{RT}\right) \quad [19]$$

where  $c_{i,0}$  is the concentration of species  $i$  at the outermost part of the diffuse part of the double layer (the innermost part of the diffusion layer),  $c_{i,ddl}$  is the concentration of species at the innermost part of the diffuse part of the double layer (the plane of closest approach to the metal surface), and  $\zeta$  is the zeta potential. The values of concentration at the inner limit of the diffusion layer  $c_{i,0}$  were obtained under the assumptions that the solution at this location is electrically neutral, that the diffusion coefficients of the reactant and product ions are equal, and that the diffusion coefficients of the cation and anion from the supporting electrolyte are equal. Thus, a decrease in the concentration of the reactants was offset by an equal increase in the product concentration. The above assumptions are appropriate for the case of the reduction of ferricyanide on a Pt electrode as discussed in a subsequent section. The diffusion coefficients of the ferricyanide and ferrocyanide ions are  $0.896 \times 10^{-5}$  and  $0.739 \times 10^{-5}$  cm<sup>2</sup>/s, respectively, and the diffusion coefficients for K<sup>+</sup> and Cl<sup>−</sup> ions are  $1.957 \times 10^{-5}$  and  $2.032 \times 10^{-5}$  cm<sup>2</sup>/s, respectively. The above assumptions could be relaxed following the ordinary perturbation approach of Levich.<sup>1,30</sup>

Under the assumption that the diffuse part of the double layer is thin, Poisson's equation

$$\frac{d^2 \psi}{dy^2} = -\frac{F}{\epsilon} \sum_i z_i c_i \exp\left(-\frac{z_i F \psi}{RT}\right) \quad [20]$$

can be solved in the axial dimension subject to the boundary conditions

$$\psi \rightarrow 0 \text{ as } y \rightarrow \infty \text{ and } \frac{d\psi}{dy} = \frac{q_2}{\epsilon} \text{ at } y = y_2 \quad [21]$$

where  $\psi$  is the potential within the diffuse part of the double layer measured relative to the outermost region of this diffuse part and  $q_2$  is the charge held within the diffuse part of the double layer at a given radial position. The use of Eq. 21 requires introduction of a geometric parameter  $y_2$  corresponding to the distance between the electrode surface and the plane of closest approach for ionic species. Solution of Eq. 20 yields

$$q_2 = \left\{ 2RT\epsilon \sum_i c_{i,0} \left[ \exp\left(-\frac{z_i F \zeta}{RT}\right) - 1 \right] \right\}^{1/2} \quad [22]$$

where  $\zeta$  is the zeta potential given by the value of  $\psi$  at  $y = y_2$ .

The total applied potential

$$V - \Phi_{ref} = \Phi_0 + \eta_c + \eta_s^* + \zeta \quad [23]$$

is sum of the ohmic potential drop, concentration overpotential, surface overpotential, and zeta potential. The Butler-Volmer expression for the normal current density as a function of surface overpotential and concentration was modified to account for the potential and concentration of reacting species at the plane of closest approach; thus

$$i = i_0 \left\{ \frac{c_0 \exp(-z_r F \zeta / RT)}{c_\infty} \right\} \left[ \exp\left\{ \frac{\alpha Z F}{RT} \eta_s^* \right\} - \exp\left\{ -\frac{\beta Z F}{RT} \eta_s^* \right\} \right] \quad [24]$$

where  $z_r$  is the charge number of the reacting species. In principle such an expression for the reaction kinetics is valid only in case of deposition reactions. However Appel showed that this expression can still be used for redox reactions when the current is a significant fraction of the mass-transfer limiting current.<sup>4</sup>

Within this approach,  $q_2$ ,  $c_{i,0}$ ,  $c_{i,ddl}$ ,  $i$ ,  $\zeta$ ,  $\eta_c$ ,  $\Phi_{ohmic}$ , and  $\eta_s^*$  are functions of radial position. Assumption that the interface taken as a whole is electrically neutral yields

$$q_2 + q_m = 0 \text{ or } q_m = -q_2 \quad [25]$$

where  $q_m$  is the charge density associated with the concentration of electrons on the metal surface. Because the diffuse double layer is thin in comparison to electrode dimensions, Eq. 25 was assumed to apply at each radial position. Under the assumption that specific adsorption can be neglected, charge is not present between the metal surface and the plane of closest approach of the solvated ions. The potential profile in this region can be assumed to be linear with respect to the axial position; hence

$$\frac{\eta_s^*}{y_2} = \frac{q_m}{\epsilon} \quad [26]$$

The development presented to this point constitutes the mathematical model for convective diffusion to a rotating disk electrode that accounts for finite Schmidt numbers, the influence of the diffuse double layer, and currents below the mass-transfer-limited current. Solution of this set of equations can be used to obtain such measurable properties as the double-layer capacitance.

**Calculation of double-layer capacitance.**—The double-layer capacitance is given by

$$\begin{aligned} C_{dl} &= \frac{dq_m}{d(\eta_s^* + \zeta)} \\ &= \frac{1}{(d\eta_s^*/dq_m) + (d\zeta/dq_m)} \\ &= \frac{1}{(1/C_2) + (1/C_{ddl})} \end{aligned} \quad [27]$$

where  $C_2$  is the capacitance between the electrode surface and the plane of closest approach and  $C_{ddl}$  is the capacitance across the diffuse part of the double layer. From Eq. 26

$$C_2 = \frac{dq_m}{d\eta_s^*} = \frac{\epsilon}{y_2} \quad [28]$$

$C_{ddl}$  can be calculated as  $C_{ddl} = dq_m/d\zeta$ . The double-layer capacitance can be expressed as a function of zeta potential by introducing Eq. 22 and 25

$$C_{\text{ddl}} = -\{2RT\epsilon\}^{1/2} \frac{d}{d\zeta} \left[ \sum_i c_{i0} \left[ \exp\left\{\frac{-z_i F \zeta}{RT}\right\} - 1 \right] \right]^{1/2}$$

$$= F \sqrt{\frac{\epsilon}{RT}} \frac{\sum_i z_i c_{i0} \exp\left\{\frac{-z_i F \zeta}{RT}\right\}}{\sqrt{\sum_i 2c_{i0} \left[ \exp\left\{\frac{-z_i F \zeta}{RT}\right\} - 1 \right]}} \quad [29]$$

### Numerical Procedure

In the following sections the numerical procedure employed to solve the convective diffusion equation and a step-by-step algorithm for the implementation of the steady-state model are presented.

**Solution to the convective diffusion equation.**—Calculation of the steady-state current and potential distributions on the electrode surface requires accurate values for  $\theta'_m(0)$ . A finite-difference scheme using central difference formulae accurate to the order of the square of the element length was used to solve Eq. 9 for  $m = 0$  to 10 at different values of the Schmidt number. A tridiagonal system of equations was obtained and solved by employing the Thomas algorithm.<sup>31</sup> To reduce the error caused by the choice of the step size, calculated values of  $\theta'_m(0)$  for different element lengths were extrapolated to zero element length by linear regression. The 95% confidence interval for the intercept was used to estimate the precision of the result. In all cases, nine significant digits were obtained. For example, the value for  $\theta'_m(0)$  obtained by extrapolation was  $-1.119846522$ . This result is consistent with the corresponding value of  $-1.11984652$  reported by Newman.<sup>3</sup> The same results were obtained by approximating the solution by a series of Chebyshev polynomials.<sup>25</sup> For the number of significant digits reported here,  $\theta'_m(0)$  was not sensitive to the use of more decimal places for constants  $a$  and  $b$  in Cochran's velocity expansions.<sup>19</sup>

Similar extrapolations were made for  $m = 1$  to 10 and for various values of Schmidt number. The  $\theta'_m(0)$  values obtained for different values of  $m$  were regressed to a sixth degree polynomial as given by

$$\theta'_m(0) = \sum_{k=0}^6 a_{m,k} Sc^{-k/3} \quad [30]$$

A sixth-order expansion was used because the 95% confidence intervals for the regressed parameters did not include zero and because smaller order expansions did not provide a sufficiently accurate representation of the numerical results. The residual errors for the expansion were randomly distributed and had magnitudes of roughly  $10^{-11}$ .

The mass-transfer limited current density is uniform and is given by

$$i_{\text{lim}} = -\frac{nFDc_\infty}{1-t} \left( \frac{av}{3D} \right)^{1/3} \sqrt{\frac{\Omega}{v}} \theta'_0(0) \quad [31]$$

Equation 30 yields a value for  $\theta'_m(0)$  at a Schmidt number of 1000 of  $-1.085880341$  as compared to  $-1.119846522$  for an infinite Schmidt number. Assumption of an infinite Schmidt number results in a relative error of 3.1% which is in agreement with the value reported by Newman.<sup>3</sup> The largest error expected for aqueous electrolytes may be seen for hydrogen ion which yields a Schmidt number of the order of 100, resulting in a relative error of 7.1% in the calculated value of the mass-transfer-limited current. While the influence of the finite Schmidt number correction on the calculated mass-transfer-limited current is small, the errors associated with neglecting this correction are more significant in the frequency domain.<sup>15,17</sup>

**Algorithm for implementation of the model.**—The numerical procedure employed in this work to handle the diffusion layer and the outer region with the ohmic drop is similar to the one implemented by Newman<sup>3</sup>; however, introduction of the diffuse part of the double layer required modification of the kinetic boundary condition in order to accommodate the zeta potential. An algorithm for implementation of the numerical scheme is provided below:

1. The values for  $\theta'_m(0)$  resulting from the convective diffusion equation were determined for a given value of Schmidt number from the polynomial expression in Eq. 30 and by using Table I for the values of  $a_{m,k}$ .

2. A value for  $A_m$  coefficients was assumed, or, in other words, the concentration distribution was assumed on the electrode surface as per Eq. 5.

3. The current distribution resulting from mass transport was calculated as per Eq. 11.

4. The current distribution obtained from the derivative of the potential just outside the diffusion layer was equated to that from step 3 to obtain the  $B_n$  coefficients. The relation used to obtain these coefficients was provided in Eq. 15.

5. The  $\Phi_0$  distribution was obtained from Eq. 14.

6. A value for  $\eta^*$  was substituted in terms of  $\zeta$  from the Eq. 22, 25, and 26, and the value of  $\zeta$  was obtained by using a Newton-Raphson technique to solve the nonlinear Eq. 24.

7. The  $\eta^*$  distribution was calculated from the  $\zeta$ -potential distribution obtained from step 5 by employing Eq. 22, 25, and 26.

8. The  $\eta_c$  distribution was calculated from Eq. 23.

9. The concentration distribution was calculated from Eq. 12.

10. The  $A_m$  coefficients were obtained again from the concentration distribution from step 8. The new values for the  $A_m$  coefficients are the weighted sum of those obtained from the present iteration and from the previous iteration.

11. Steps 3 through 10 were repeated until convergence was achieved.

12. Once the convergence criteria were met, the charge distribution was obtained from Eq. 22, and the double-layer capacitance was obtained from Eq. 27, 28, and 29.

### Application to Experimental Systems

The systems treated in this work included electrodeposition of copper and reduction of ferricyanide on platinum.

Table I. Polynomial coefficients in the expansion for  $\theta'_m(0)$  resulting from the solution of the convective diffusion equation. The numbers of significant digits reported are based on the respective confidence intervals from the regression.

	$a_0$	$a_1$	$a_2$	$a_3$	$a_4$	$a_5$	$a_6$
$m = 0$	-1.119846522	0.333723494	0.0630655	-0.02483	-0.1009	-0.1539	-0.361
1	-1.532987928	0.348508169	0.0563987	-0.01244	-0.0557	-0.0760	-0.184
2	-1.805490584	0.351502095	0.0501466	-0.008443	-0.03678	-0.0463	-0.1034
3	-2.015723734	0.352526040	0.0456708	-0.006567	-0.02707	-0.0321	-0.0647
4	-2.189982747	0.352984907	0.0423604	-0.005472	-0.02132	-0.0240	-0.0441
5	-2.340450747	0.353227157	0.0398003	-0.004743	-0.01758	-0.0187	-0.0323
6	-2.473842754	0.353369827	0.0377463	-0.004220	-0.01493	-0.0153	-0.0247
7	-2.594287242	0.353460658	0.03605028	-0.003823	-0.01295	-0.0128	-0.0194
8	-2.704520850	0.353521951	0.03461769	-0.0035106	-0.01141	-0.01114	-0.0154
9	-2.806460253	0.35356522	0.0333854	-0.00326	-0.0102	-0.010	-0.013
10	-2.901505453	0.35359688	0.03230943	-0.003038	-0.00927	-0.00841	-0.0109

**Electrodeposition of copper.**—To validate the numerical approach used in this work, calculations were performed corresponding to the 0.1 M copper sulfate system studied by Newman.<sup>3</sup> This part of the study did not incorporate the diffuse part of the double layer. Newman's results for an infinite Schmidt number were reproduced. The concentration and current distributions obtained for infinite and finite Schmidt number for this system are compared in Fig. 1 with applied potential as a parameter. For a given value of applied potential, the distributions resulting from both these cases differed most significantly as the mass-transfer-limited condition was approached. The largest deviation was seen at the center of the disk. The differences seen between the calculated distributions for infinite and finite Schmidt number are due to differences in the corresponding values of the mass-transfer-limited cur-

**Table II.** Input parameters used for the ferricyanide/ferrocyanide in 1 M KCl system reacting on the Pt disk electrode.

$\nu = 0.951 \times 10^{-2} \text{ cm}^2/\text{s}$	$D = 0.896 \times 10^{-5} \text{ cm}^2/\text{s}$
$F = 96487 \text{ C/eq}$	$c_s = 10^{-5} \text{ mol/cm}^3$
$Z = 1$	$T = 298 \text{ K}$
$\alpha = 0.5$	$\beta = 0.5$
$\epsilon = 6.933 \times 10^{-12} \text{ C/V-cm}$	$n = 1$
$r_0 = 0.25 \text{ cm}$	$t = 0.04$
$R = 8.314 \text{ J/mol-K}$	$i_0 = 0.3 \text{ A/cm}^2$
$\kappa_s = 0.1 \Omega^{-1} \text{ cm}^{-1}$	$y_2 = 10 \text{ Å}$
$\gamma = 1.0$	

rent. When distributions were presented at the same fraction of the mass-transfer-limited current, the differences were not perceptible.

**Reduction of ferricyanide on Pt.**—The motivation for this study was to explore the influence of the nonuniform current and potential distributions on interpretation of the impedance data obtained for the reduction of ferricyanide on a Pt rotating disk electrode. The electrolytic solution consisted of 0.01 M  $\text{K}_3\text{Fe}(\text{CN})_6$ , 0.01 M  $\text{K}_4\text{Fe}(\text{CN})_6$ ,

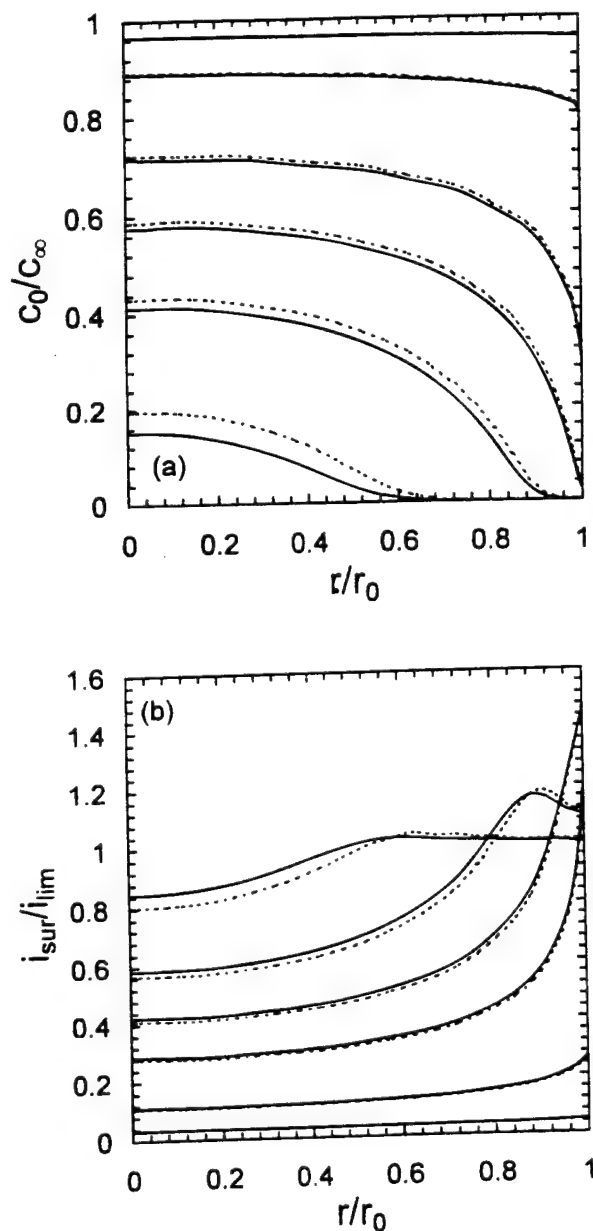


**Fig. 1.** Calculated (a) concentration and (b) current distribution on the surface of the disk electrode for deposition of copper under the condition corresponding to Fig. 6 and 7 of Ref. 3 with  $N = 50$ . Adjacent infinite  $Sc$  (dashed lines) and finite  $Sc$  (solid lines) are for same applied potential. In the order of decreasing concentration, the applied potentials ( $V - \Phi_{ref}$ ) used were  $-0.08$ ,  $-0.28$ ,  $-0.68$ ,  $-0.98$ ,  $-1.28$ , and  $-1.58 \text{ V}$ .

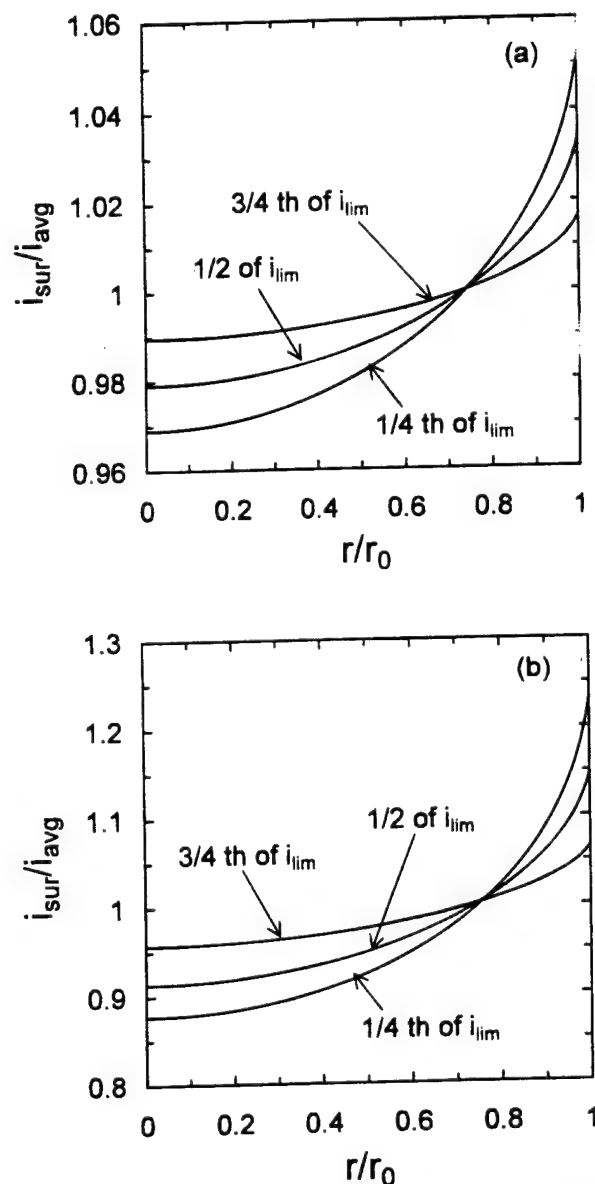


**Fig. 2.** Calculated current distributions for the reduction of ferricyanide on a Pt disk electrode rotating at (a) 120 rpm and (b) 3000 rpm. System properties are given in Table II.

and 1 M KCl. Experimental details are presented in Ref. 25 and 27. The one-dimensional impedance model developed by Tribollet and Newman<sup>18</sup> was used to analyze the data obtained. It was observed that the regressed values for Schmidt number increased with an increase in rotation speed. As the Schmidt number is an electrolytic property independent of rotation speed, this result points to the inadequacy of the one-dimensional model used. To motivate development of a two-dimensional model, current, potential, and charge distributions for this system were obtained as functions of rotation speed and fraction of the mass-transfer-limited current.

**Current, potential, and charge distributions.**—The numerical values of various parameters used for this particular system are listed in Table II. The rate constant for reduction of ferricyanide on Pt is very large;<sup>32,33</sup> thus, the surface overpotential can be expected to be small. Due to the use of excess supporting electrolyte, the contribution of ohmic drop can also be expected to be small. Thus, mass transport being the predominate factor, the current distribution is expected to be uniform. Calculated current distributions are presented in Fig. 2 for rotation rates of 120 and

3000 rpm. A uniform calculated current distribution was indeed observed at low rotation speeds, but at large rotation speeds the current distribution was less nonuniform. These distributions can be contrasted with the extreme case of a primary current distribution where  $i_{\text{sur}}/i_{\text{avg}} = 0.5$  at the center of the electrode and is equal to  $\infty$  at the periphery. As shown in Fig. 2b for one-fourth of the limiting current at 3000 rpm, the current distribution varies from a value of 0.88 at the center to 1.23 at the edge of the electrode.

The nonuniformity in calculated current distribution shown in Fig. 2b was obtained in spite of the use of excess supporting electrolyte. The calculated overpotentials shown in Fig. 3 and 4 show that at both 120 and 3000 rpm, the surface overpotential, and the zeta potential are small. The applied potential, by virtue of the large metal conductivity, is uniform. Thus, a nonuniform distribution in ohmic potential is compensated by an opposing distribution in concentration overpotential. The potential distributions are more uniform for the 120 rpm case and are less so for the 3000 rpm case. A large rotation speed increases the value of the mass-transfer-limited current and, therefore, increases the influence of the ohmic potential drop.

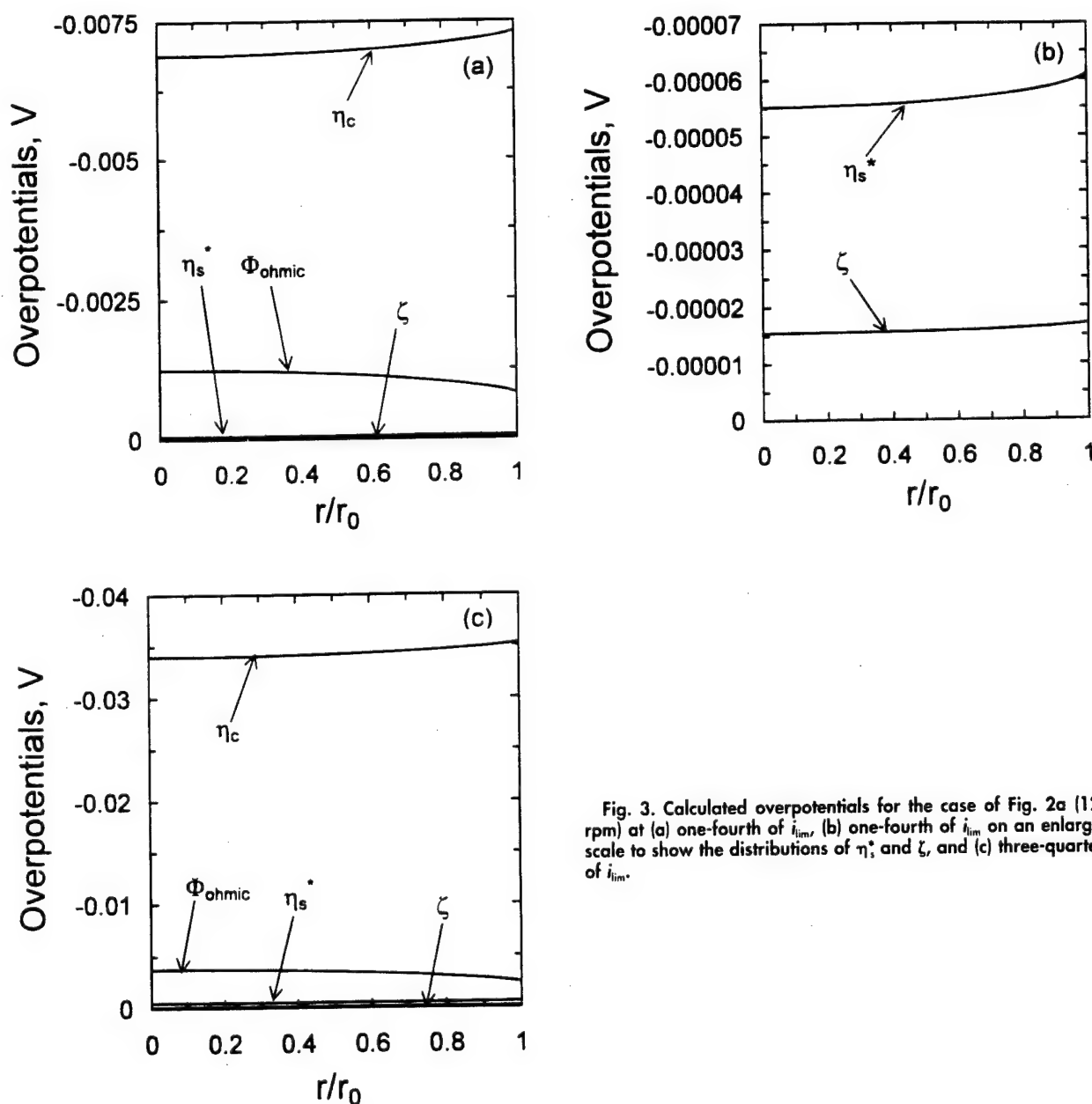


Fig. 3. Calculated overpotentials for the case of Fig. 2a (120 rpm) at (a) one-fourth of  $i_{\text{lim}}$ , (b) one-fourth of  $i_{\text{lim}}$  on an enlarged scale to show the distributions of  $\eta_s^*$  and  $\zeta$ , and (c) three-quarters of  $i_{\text{lim}}$ .



The concentration overpotential increases to be a more significant fraction of the applied potential as current approaches mass-transfer limitation. The ohmic potential drop, therefore, becomes less significant. Thus, the current distribution is more uniform at three-fourths of the mass-transfer-limited current than at one-fourth (see Fig. 2).

Although, as seen in Fig. 3 and 4, the zeta potential obtained does not contribute significantly to the overall potential, calculation of the zeta potential allows determination of the charge distribution from Eq. 22. As can be seen from Fig. 5, the charge distribution calculated for this system is less nonuniform at 3000 rpm than at 120 rpm. The charge distribution follows the distribution of surface overpotential (see Eq. 26).

The charge distribution thus obtained was used to calculate the radial distribution of the double-layer capacitance from Eq. 27 and 29. The calculated capacitance was found to be independent of rotation rate and to be uniformly distributed with a value of  $55 \mu\text{F}/\text{cm}^2$  for  $y_2 = 10 \text{ \AA}$ . This value is in reasonable agreement with the experimental value of  $35 \mu\text{F}/\text{cm}^2$  obtained by Deslouis and Tribollet for the same system.<sup>34</sup> They obtained the same value of capacitance from measurements on disk and ring-disk electrodes. This result is in agreement with the calculations from the present work, which show that the capaci-

tance has no radial distribution. The value of the double-layer capacitance is sensitive to the choice of  $y_2$ . By choosing  $y_2 = 17 \text{ \AA}$ , a value of  $35 \mu\text{F}/\text{cm}^2$  was obtained for double-layer capacitance.

**Zero frequency asymptotes of local impedance.**—As a preliminary step toward formulating a detailed two-dimensional model for the impedance analysis explicitly accounting for various phenomena, the zero frequency asymptotes for the local impedances for the ferri/ferrocyanide system were obtained from steady-state distributions calculated at two applied potentials separated by 5 mV. The ratio of the difference in overpotential with respect to the difference in current density calculated locally provides the contribution of the respective phenomena to overall impedance response. The radial distributions of these values are presented in Fig. 6 and 7 for 120 and 3000 rpm, respectively. The zero frequency asymptotes for the local impedance are more uniform for the case of 120 rpm and are less so for 3000 rpm. This is a strong indication that a two-dimensional model is necessary for obtaining reliable information from impedance data. At higher fractions of the limiting current, the local impedance resulting from the concentration overpotential dominates. The local impedance values resulting from the ohmic drop are estimated to be about  $2 \Omega \text{ cm}^2$ ,

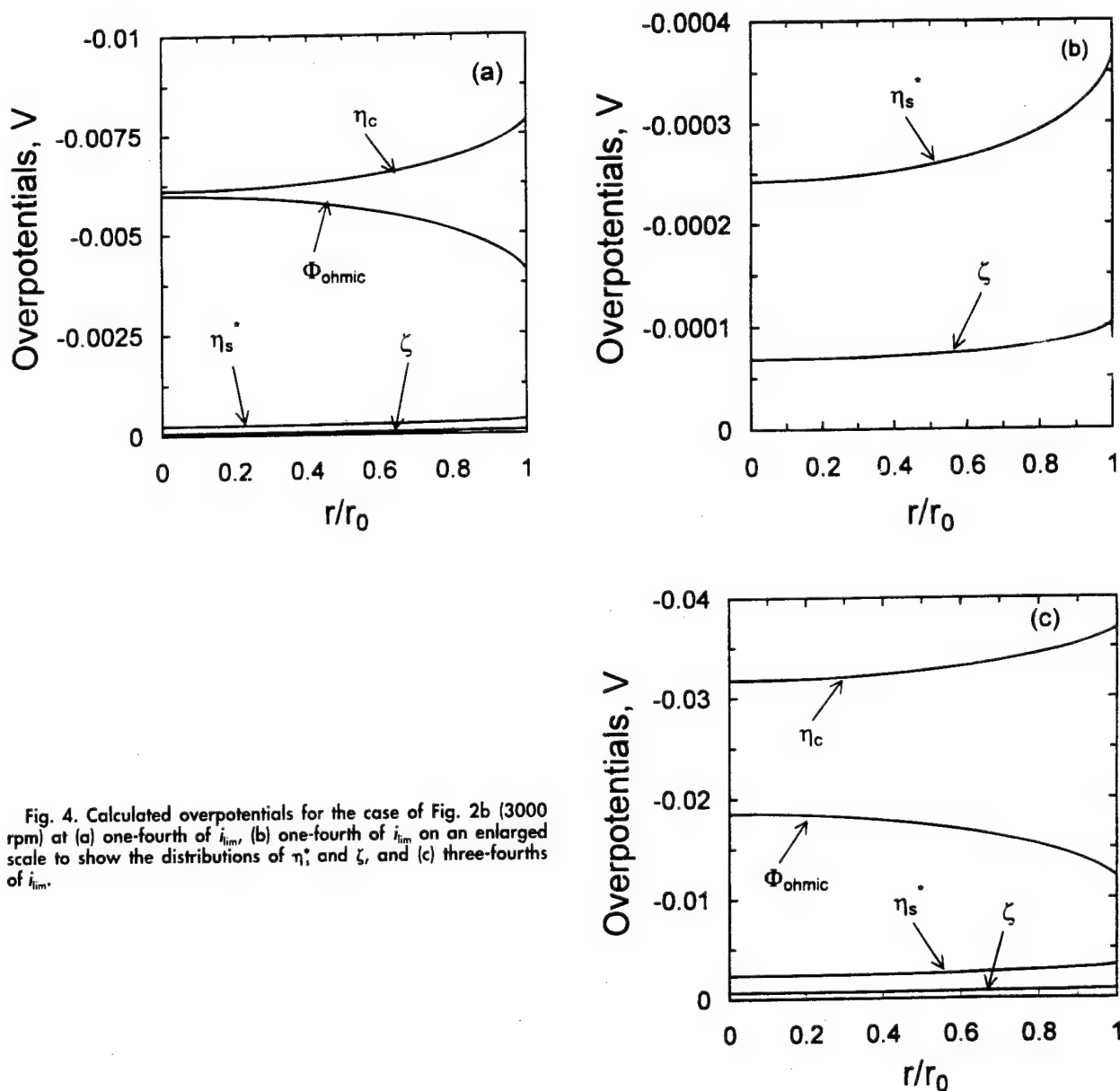


Fig. 4. Calculated overpotentials for the case of Fig. 2b (3000 rpm) at (a) one-fourth of  $i_{lim}$ , (b) one-fourth of  $i_{lim}$  on an enlarged scale to show the distributions of  $\eta_s^*$  and  $\zeta$ , and (c) three-fourths of  $i_{lim}$ .

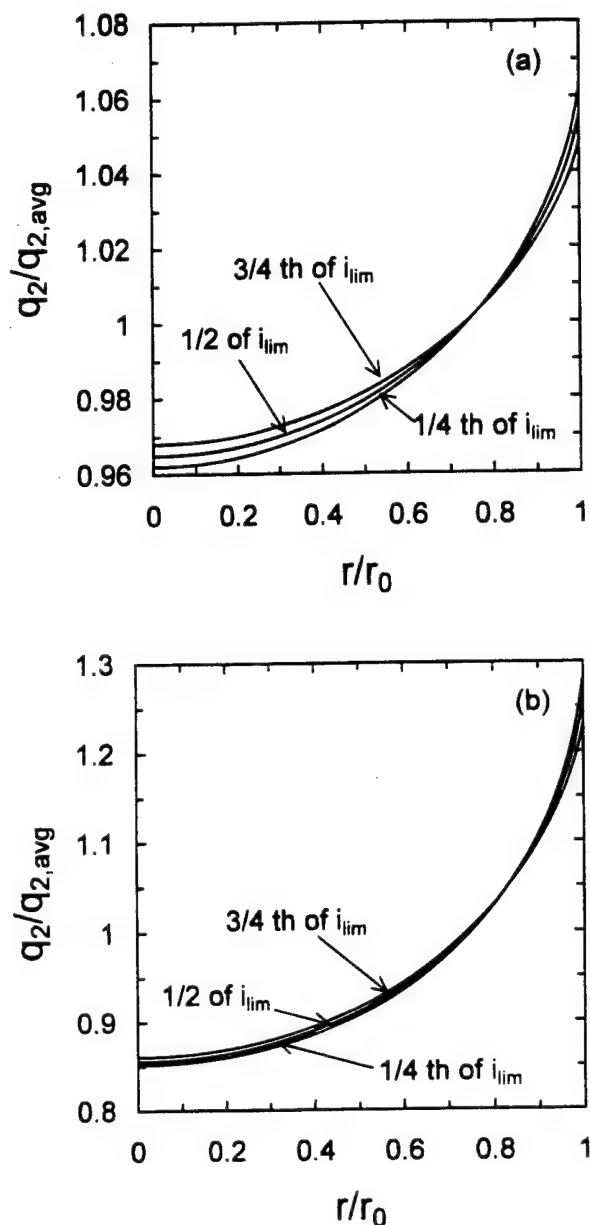


Fig. 5. Calculated charge distributions for the cases of (a) Fig. 2a (120 rpm) and (b) Fig. 2b (3000 rpm).

which corresponds to  $10 \Omega$  for a disk with a surface area of  $0.2 \text{ cm}^2$ , in agreement with experiment.<sup>25,27</sup> Appel reported the radial distributions of the impedance calculations for a single dimensionless frequency of 0.1 applied to 0.0001 M equimolar solution of sodium ferrocyanide and sodium ferricyanide with a 0.1 M sodium fluoride supporting electrolyte.<sup>1</sup> Similar nonuniformities were observed from his calculations.

### Conclusions

A finite Schmidt number correction was applied to the steady-state model for the rotating disk electrode below the mass-transfer-limited current. The result of the convective diffusion equation accounting for this correction was expressed as a polynomial expansion of  $Sc^{-1/3}$ , and the coefficients of the polynomial expansion were tabulated. The model was then extended to incorporate the diffuse part of the double layer. Results provided by Newman for deposition of copper were reproduced. The distributions of current, potential, and charge were assessed for the reduction of ferricyanide on Pt. The double-layer capacitance and the zero-frequency asymptotes of the local impedances were evaluated. Surface nonuniformities were observed for the

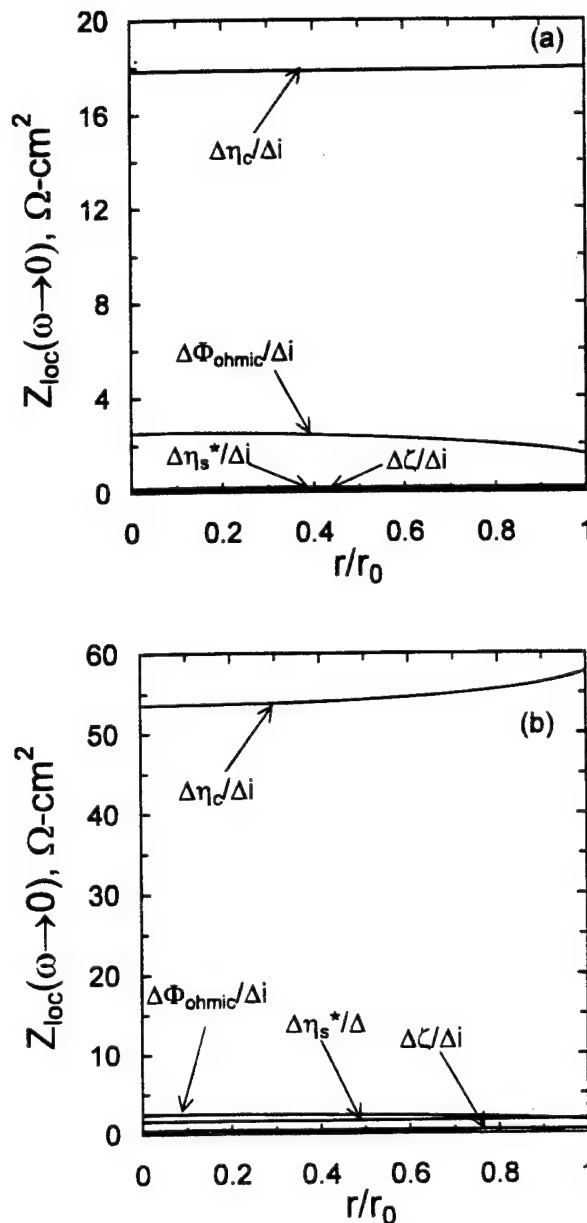


Fig. 6. Calculated local impedance distributions corresponding to Fig. 2a (120 rpm) for (a) one-fourth of  $i_{lim}$  and (b) three-fourths of  $i_{lim}$ .

distribution of various parameters. The zero frequency asymptotes of the local impedances were calculated, and nonuniformities were observed. The results of this work support the need for a two-dimensional impedance model accounting for a finite Schmidt number correction. Development of such a two-dimensional impedance model is in progress.

### Acknowledgments

This research received support from the Office of Naval Research under grant no. N00014-93-I-0056 and N00014-93-I-1113 (Dr. A. J. Sedriks, program monitor) and from the National Science Foundation under the U.S.-France Cooperative Research Grant INT-9416713. The authors would also like to thank Bernard Tribollet, Hisasi Takenouti, and Claude Deslouis of CNRS, Paris, for their helpful suggestions.

Manuscript submitted September 22, 1997; revised manuscript received December 19, 1997. This was in part Paper 52 presented at the Memorial Symposium in honor of Professor Charles W. Tobias at the Montréal, Québec, Canada, Meeting of the Society, May 4-9, 1997.

The University of Florida assisted in meeting the publication costs of this article.

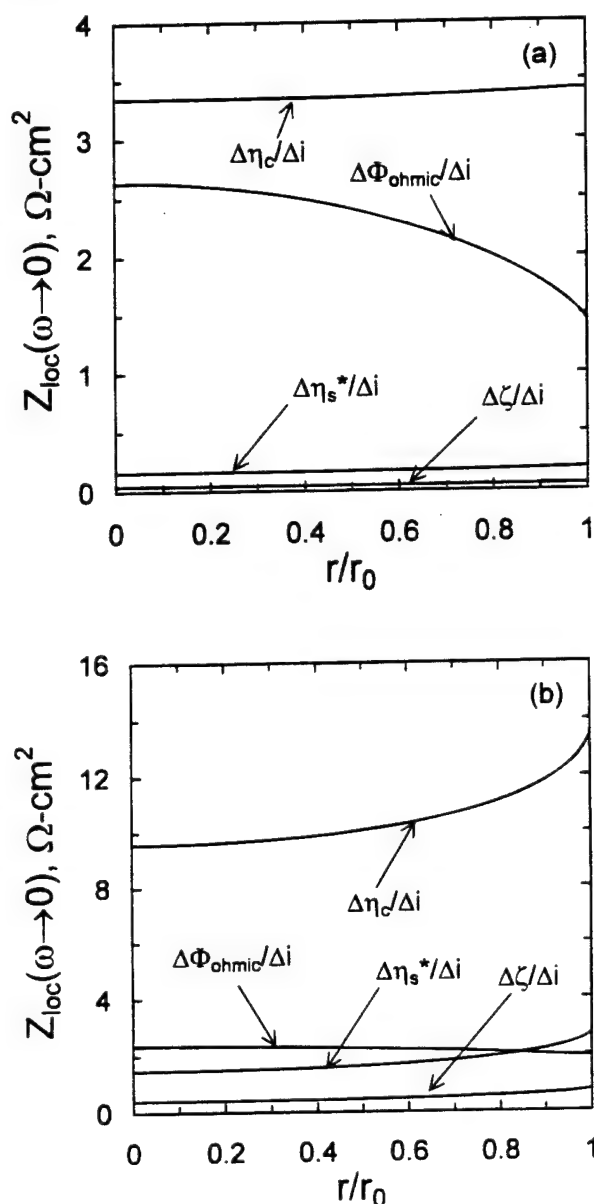


Fig. 7. Calculated local impedance distributions corresponding to Fig. 2b (3000 rpm) for (a) one-fourth of  $i_{lim}$  and (b) three-fourths of  $i_{lim}$ .

#### LIST OF SYMBOLS

$A_m$	coefficients in series for concentration (see Eq. 5)
$a, b$	coefficients in Cochran expansion for velocity terms. 0.51023 and -0.61592, respectively
$a_{m,k}$	coefficients in the polynomial expansion for $\theta'_m(0)$ (see Eq. 30)
$C_2$	capacitance between the electrode surface and the closest plane of approach, F/cm <sup>2</sup>
$C_{ddi}$	capacitance across the diffuse part of double layer, F/cm <sup>2</sup>
$C_{dl}$	overall double-layer capacitance, F/cm <sup>2</sup>
$c_i$	concentration of species $i$ , mol/cm <sup>3</sup>
$c_R$	concentration of reacting species, mol/cm <sup>3</sup>
$c_s$	concentration of the reactant on the electrode surface, mol/cm <sup>3</sup>
$c_s$	bulk concentration of the reacting species, mol/cm <sup>3</sup>
$c_{i,0}$	concentration of species $i$ at the outermost part of the diffuse part of the double layer
$c_{i,ddl}$	concentration of species $i$ at the innermost part of the double layer
$D$	diffusion coefficient of the reacting species, cm <sup>2</sup> /s
$D_R$	diffusion coefficient of the reacting species, cm <sup>2</sup> /s
$F$	Faraday's constant, C/equiv
$i_{avg}$	average surface current density, A/cm <sup>2</sup>
$i_{lim}$	limiting current density, A/cm <sup>2</sup>

$i_{sur}$	local surface current density, A/cm <sup>2</sup>
$N$	parameter related to the significance of mass-transfer (see Eq. 18)
$n$	number of electrons produced when one reactant ion or molecule reacts
$P_{2n}$	Legendre polynomial of order $2n$
$q_2$	charge density distribution within the diffuse part of double layer, C/cm <sup>2</sup>
$q_{2,avg}$	average charge density within the diffuse part of the double layer, C/cm <sup>2</sup>
$q_m$	charge on the surface of the electrode, C/cm <sup>2</sup>
$R$	universal gas constant, J/mol-K
$r$	radial coordinate, cm
$r_0$	radius of disk, cm
$Sc$	Schmidt number
$T$	electrolyte temperature, K
$t_R$	transference number of the reacting species
$V$	Electrode potential
$v_r, v_z$	radial and axial velocity components, cm/s
$y_2$	distance between the electrode surface and the closest plane of approach, 10 <sup>-7</sup> cm
$Z$	number of equivalents of reactant used up for one electron produced/consumed
$Z_{loc}$	value of local impedance in $\Omega$ -cm <sup>2</sup>
$z$	normal distance from disk, cm

#### Greek

$\alpha, \beta, \gamma$	parameters in kinetics expression (see Eq. 24)
$\epsilon$	permittivity of electrolyte, $6.93 \times 10^{-12}$ C/V cm
$\delta$	thickness of the diffusion layer, cm
$\zeta$	potential drop across the diffuse part of double layer, V
$\eta, \mu$	parameters in the rotational elliptic coordinate transformation used in solving the Laplace's equation
$\eta_c$	concentration overpotential, V
$\eta_s$	surface overpotential, V
$\eta_s^*$	surface overpotential adjusted by the zeta potent. V
$\theta_m$	axial-dependent term in the concentration series
$\kappa_s$	solution conductivity ( $\Omega$ cm) <sup>-1</sup>
$\nu$	kinematic viscosity, cm <sup>2</sup> /s
$\xi$	normalized axial position
$\Phi$	ohmic potential drop, V
$\Phi_{ref}$	reference potential, V
$\psi$	potential at any position within the diffuse part of the double layer measured relative to the outermost region of the diffuse part, V
$\Omega$	rotation speed, rad/s
$\omega$	frequency of perturbation, Hz

#### REFERENCES

1. B. Levich, *Acta Physicochim. URSS*, **17**, 257 (1942).
2. J. Newman, *J. Phys. Chem.*, **70**, 1327 (1966).
3. J. Newman, *J. Electrochem. Soc.*, **113**, 1235 (1966).
4. P. W. Appel, Ph.D. Thesis, University of California, Berkeley, CA (1976).
5. Yu. Filinovsky and V. A. Kir'yanov, *Dokl. Akad. Nauk. SSSR*, **156**, 1412 (1964).
6. D. Schumann, *C. R. Acad. Sci. Paris*, **262C**, 624 (1966).
7. C. Deslouis, E. Epelboin, M. Keddam, and J. C. Lestrade, *J. Electroanal. Chem. Interfacial Electrochem.*, **28**, 57 (1970).
8. E. Levart and D. Schuhmann, *J. Electroanal. Chem. Interfacial Electrochem.*, **53**, 77 (1974).
9. V. Homay and J. Newman, *J. Electrochem. Soc.*, **121**, 521 (1974).
10. E. Levart and D. Schuhmann, *J. Electrochem. Soc.*, **122**, 1082 (1975).
11. D. A. Scherson and J. Newman, *J. Electrochem. Soc.*, **127**, 110 (1980).
12. E. Levart and D. Schuhmann, *J. Electrochem. Soc.*, **127**, 2649 (1980).
13. B. Tribollet and J. Newman, *J. Electrochem. Soc.*, **130**, 822 (1983).
14. C. Deslouis, C. Gabrielli, and B. Tribollet, *J. Electrochem. Soc.*, **130**, 2044 (1983).
15. B. Tribollet, J. Newman, and W. H. Smyrl, *J. Electrochem. Soc.*, **135**, 134 (1988).
16. C. Deslouis and B. Tribollet, *Electrochim. Acta*, **35**, 1637 (1990).
17. M. E. Orazem, C. Deslouis, and B. Tribollet, Abstract 120, p. 139, The Electrochemical Society Meeting Abstracts, Vol. 97-1, Montréal, Québec, Canada, May 4-9, 1997; Paper in preparation.
18. B. Tribollet and J. Newman, *J. Electrochem. Soc.*, **130**,

- 2016 (1983).
19. M. Cochran, *Proceedings of the Cambridge Philosophical Society*, **30**, 365 (1935).
  20. J. Newman, *J. Electrochem. Soc.*, **117**, 198 (1970).
  21. K. Nisançioğlu, *Corrosion*, **43**, 258 (1987).
  22. K. Nisançioğlu, *The Measurement and Correction of Electrolyte Resistance in Electrochemical Tests*, ASTM STP 1056, p. 61, American Society for Testing and Materials, Philadelphia, PA (1990).
  23. K. Nisançioğlu and J. Newman, *J. Electrochem. Soc.*, **121**, 523 (1974).
  24. P. W. Appel and J. Newman, *J. Electrochem. Soc.*, **124**, 1864 (1977).
  25. M. Durbha, Ph.D. Thesis, University of Florida, Gainesville, FL (1998).
  26. C. Deslouis and B. Tribollet, Paper B2-9 presented at the 35th meeting of the International Society of Electrochemistry, Berkeley, CA, Aug 5-10, 1984.
  27. M. Durbha, M. E. Orazem, C. Deslouis, H. Takenouti, and B. Tribollet, In preparation.
  28. A. Frumkin, *Z. Phys. Chem.*, **164**, 121 (1933).
  29. J. Newman, *Trans. Faraday Soc.*, **61**, 2229 (1965).
  30. J. Newman, *Electrochemical Systems*, 2nd ed., pp. 250-252, Prentice Hall Publications, Englewood Cliffs, NJ (1991).
  31. S. C. Chapra and R. P. Canale, *Numerical Methods for Engineers*, 2nd ed., pp. 286-287, McGraw-Hill Pub. Co., New York (1988).
  32. D. Jahn and W. Vielstich, *J. Electrochem. Soc.*, **109**, 849 (1962).
  33. W. Huang and R. McCreery, *J. Electroanal. Chem.*, **326**, 1 (1992).
  34. C. Deslouis and B. Tribollet, *Electrochim. Acta*, **23**, 935 (1978).



# A Mathematical Model for the Radially Dependent Impedance of a Rotating Disk Electrode

Madhav Durbha,<sup>a,\*</sup> Mark E. Orazem<sup>a,\*\*</sup> and Bernard Tribollet<sup>b,\*\*</sup>

<sup>a</sup>Department of Chemical Engineering, University of Florida, Gainesville, Florida 32611, USA

<sup>b</sup>UPR 15 du CNRS, Laboratoire "Physique des Liquides et Electrochimie," Université Pierre et Marie Curie, 75252 Paris Cedex 05, France

A mathematical model was developed which accounts for the influence of nonuniform current distribution on the impedance response of a rotating disk electrode. Results obtained using this two-dimensional model were compared against those using the one-dimensional model for impedance developed by Tribollet and Newman. The one-dimensional model was found to be adequate when kinetic limitations cause the current to be uniformly distributed. Significant differences between the one-dimensional and two-dimensional models were seen for fast reaction kinetics where the nonuniform ohmic potential distribution is balanced by a nonuniform concentration overpotential.

© 1999 The Electrochemical Society. S0013-4651(98)05-102-7. All rights reserved.

Manuscript submitted May 29, 1998; revised manuscript received February 26, 1999.

Frequency-domain techniques are commonly employed in the study of electrode kinetics and mass transfer in electrolytic solutions. While the information obtained is similar to that from transient techniques, better resolution of physical processes can be achieved because the noise level in frequency-domain measurements can be made extremely small.<sup>1-3</sup> A second advantage of the frequency domain techniques over transient techniques is that the Kramers-Kronig relations can be used to identify instrumental artifacts or changes in base line properties.<sup>4,7</sup>

The uniform accessibility of the rotating disk at the mass-transfer-limited current makes it an attractive tool for frequency-domain techniques. Significant effort has been expended on developing analytic formulae for the impedance response of a rotating disk electrode.<sup>8-19</sup> A comparative study of the application of these models to interpretation of impedance spectra has been presented by Orazem et al.<sup>20</sup> A one-dimensional numerical model for the impedance response of a rotating disk electrode which accounted for the influence of a finite Schmidt number was presented by Tribollet and Newman.<sup>21</sup> This model accounts for effects associated with kinetics, mass-transport, and ohmic potential drop within the bulk of the solution under the assumption that the disk can be treated as being uniform. The first two terms in the Cochran<sup>22</sup> expansion for the axial component of fluid velocity were included in the convective diffusion equation. Tribollet et al.<sup>18</sup> reported that the errors in the calculated Schmidt numbers caused by assuming an infinite Schmidt number, i.e., by neglecting the second and higher terms in the axial velocity expansion, could be as high as 24% for a Schmidt number of 1000. This result was confirmed by regression of various mass-transfer models to impedance data.<sup>20</sup>

Mathematical models have been developed which account for frequency dispersion associated with the nonuniform potential distribution on the disk electrode,<sup>23-26</sup> but to date, no comparable model has been developed for the influence of nonuniform mass transfer on the impedance response. Appel and Newman<sup>27</sup> provided a preliminary mathematical development, valid for an infinite Schmidt number, that could be used as part of a model for the influence of radially dependent convective diffusion on the impedance response. Appel used this approach to calculate the radial distribution of impedance, but results were presented only for a single dimensionless frequency due to numerical difficulties associated with implementation of the model.<sup>28</sup>

The growing popularity of the rotating disk electrode system in the use of frequency-domain techniques motivates development of sophisticated models for interpretation of experimental data. For

some systems, even in the presence of excess supporting electrolyte, the distributions of current and overpotential on the electrode surface can be significantly nonuniform in the steady-state domain.<sup>29</sup> The objective of this work was to provide development of a two-dimensional model for electrochemical impedance response of a rotating disk electrode that accounts for nonuniform ohmic potential drop, and surface and concentration overpotentials.

## Theoretical Development

The formulation for the two-dimensional impedance model results from applying a sinusoidal perturbation about the steady-state solution presented in reference Ref. 29. The development that follows is valid under the assumptions of either a binary electrolyte or an excess of supporting electrolyte. The capacitance was assumed to be uniformly distributed across the surface of the disk electrode throughout the present analysis. This assumption was justified by calculation, in the absence of specific adsorption, of a uniform capacitance for the ferri/ferrocyanide redox system considered for this work.<sup>29</sup> Assumption of a uniform capacitance is also consistent with the experimental results reported by Deslouis and Tribollet.<sup>30</sup>

**Convective diffusion.**—For a small sinusoidal perturbation in potential of frequency  $\omega$ , the response can be assumed to be linear, and all the variables involved oscillate with the same frequency of  $\omega$ . Each variable  $\chi$  can be written in the form

$$\chi = \bar{\chi} + \text{Re}\{\tilde{\chi}e^{j\omega t}\} \quad [1]$$

where  $\bar{\chi}$  is the steady-state or base line value of  $\chi$ ,  $\tilde{\chi}$  is the complex amplitude of perturbation, which is a function only of position,  $t$  is time,  $\omega$  is frequency, and  $j = \sqrt{-1}$ . Thus, the concentration of the reacting species can be written as

$$c(r, z, t) = \bar{c}(r, z) + \text{Re}\{\tilde{c}(r, z)e^{j\omega t}\} \quad [2]$$

where  $\bar{c}$  and  $\tilde{c}$  are functions of radial and axial position but are not functions of time. Incorporation of concentration perturbation terms in the unsteady-state convective diffusion equation and cancellation of the steady-state terms yields

$$j\omega\tilde{c} + v_r\frac{\partial\tilde{c}}{\partial r} + v_z\frac{\partial\tilde{c}}{\partial z} = D\frac{\partial^2\tilde{c}}{\partial z^2} \quad [3]$$

where  $v_r$  and  $v_z$  are the radial and axial components of the velocity of the fluid and  $D$  is the diffusion coefficient of the species of interest. The velocity components,  $v_r$  and  $v_z$  were given by

$$v_r = ar\omega\frac{\Omega^{3/2}}{\nu^{1/2}} - \frac{1}{2}r\omega^2\frac{\Omega^2}{\nu} - \frac{b}{3}r\omega^3\frac{\Omega^{5/2}}{\nu^{3/2}} \quad [4a]$$

\* Electrochemical Society Student Member.

\*\* Electrochemical Society Active Member.

<sup>a</sup> Present address: I2 Technologies, Incorporated, Irving, Texas 75039, USA.

and

$$v_z = -az^2 \frac{\Omega^{3/2}}{\nu^{1/2}} + \frac{1}{3}z^3 \frac{\Omega^2}{\nu} + \frac{b}{6}z^4 \frac{\Omega^{5/2}}{\nu^{3/2}} \quad [4b]$$

where  $a$  and  $b$  are the coefficients from Cochran's expansion for the radial and axial velocities for the rotating disk electrode system,  $\Omega$  is the rotation rate of the disk electrode, and  $\nu$  is the kinematic viscosity of the electrolyte.

Upon substitution of Eq. 4a, b, and 8 into Eq. 3

$$jK\bar{c} + \left(3r\xi - \frac{3}{2}r\xi^2 BSc^{-1/3} - 2Cr\xi^3 Sc^{-2/3}\right) \frac{\partial \bar{c}}{\partial r} + \left(3\xi^2 + B\xi^3 Sc^{-1/3} + C\xi^4 Sc^{-2/3}\right) \frac{\partial \bar{c}}{\partial \xi} = \frac{\partial^2 \bar{c}}{\partial \xi^2} \quad [5]$$

where  $Sc$  is the Schmidt number of the species of interest, the dimensionless frequency  $K$  is given by

$$K = \frac{\omega}{\Omega} \left( \frac{9\nu}{a^2 D} \right)^{1/3} \quad [6]$$

and coefficients  $B$  and  $C$  are given by

$$B = \left( \frac{3}{a^4} \right)^{1/3} \quad \text{and} \quad C = \frac{b}{6} \left( \frac{3}{a} \right)^{5/3} \quad [7]$$

respectively. The dimensionless axial distance,  $\xi$ , is given by

$$\xi = z \left( \frac{a\nu}{3D} \right)^{1/3} \sqrt{\frac{\Omega}{\nu}} \quad [8]$$

For the steady-state case, a series expansion,<sup>31,29</sup> was used for the expression of concentration of the reacting species,  $\bar{c}(r, \xi)$ , such that

$$\bar{c}(r, \xi) = c_\infty \left[ 1 + \sum_{m=0}^{\infty} \left\{ A_m \left( \frac{r}{r_0} \right)^{2m} \theta_m(\xi) \right\} \right] \quad [9]$$

where  $c_\infty$  is the bulk concentration of the reacting species,  $A_m$  values are the coefficients to be determined from the steady-state calculations, and  $\theta_m(\xi)$  is the axially dependent function obtained from the steady-state solution. A similar expansion, employed in the present work, was obtained from Eq. 9 by a small perturbation analysis which ignored second and higher-order terms, i.e.

$$\bar{c} = c_\infty \sum_{m=0}^{\infty} \left\{ \left[ \tilde{A}_m \theta_m(\xi) + A_m \tilde{\theta}_m(\xi) \right] \left( \frac{r}{r_0} \right)^{2m} \right\} \quad [10]$$

where  $\tilde{A}_m$  are coefficients that account for the radial dependence of the frequency response and  $\tilde{\theta}_m$  is a function of axial position. Upon introduction of Eq. 10 into 5, cancellation of terms resulting from the steady-state part of the convective diffusion given by

$$\theta_m'' + (3\xi^2 - B\xi^3 Sc^{-1/3} - C\xi^4 Sc^{-2/3}) \theta_m' + 2m \left( -3\xi + \frac{3}{2}\xi^2 BSc^{-1/3} + 2C\xi^3 Sc^{-2/3} \right) \theta_m = 0 \quad [11]$$

and equating the coefficients of  $(r/r_0)^{2m}$  on either side of the resulting equation, the expression

$$A_m \left\{ \begin{aligned} &\tilde{\theta}_m'' + (3\xi^2 - B\xi^3 Sc^{-1/3} - C\xi^4 Sc^{-2/3}) \tilde{\theta}_m' \\ &+ 2m \left( -3\xi + \frac{3}{2}\xi^2 BSc^{-1/3} + 2C\xi^3 Sc^{-2/3} \right) \tilde{\theta}_m - jK\tilde{\theta}_m \\ &- jK\tilde{A}_m \theta_m = 0 \end{aligned} \right\} \quad [12]$$

is obtained in which primes in the superscripts refer to derivatives with respect to  $\xi$ . The real and imaginary parts of Eq. 12 provide two ordinary differential equations which must be solved simultaneously.

Equation 12 and the concentration given in Eq. 10 are functions of both radial and axial perturbation terms,  $\tilde{A}_m$  and  $\tilde{\theta}_m$ , respectively. To facilitate identification of appropriate boundary conditions on the axial perturbation term  $\tilde{\theta}_m$ , a new function

$$\tilde{\theta}_m(\xi) = \frac{K\tilde{A}_m}{A_m} \tilde{\Psi}_m(\xi) \quad [13]$$

can be defined. In terms of Eq. 13, Eq. 12 becomes

$$\begin{aligned} &\tilde{\Psi}_m'' + (3\xi^2 - B\xi^3 Sc^{-1/3} - C\xi^4 Sc^{-2/3}) \tilde{\Psi}_m' \\ &+ 2m \left( -3\xi + \frac{3}{2}\xi^2 BSc^{-1/3} + 2C\xi^3 Sc^{-2/3} \right) \tilde{\Psi}_m - jK\tilde{\Psi}_m = j\theta_m \end{aligned} \quad [14]$$

Equation 14 shows that  $\tilde{\Psi}_m(\xi)$  is independent of  $\tilde{A}_m$ . With this notation, Eq. 10 becomes

$$\bar{c} = c_\infty \sum_{m=0}^{\infty} \left\{ \tilde{A}_m \left[ \theta_m(\xi) + K\tilde{\Psi}_m(\xi) \right] \left( \frac{r}{r_0} \right)^{2m} \right\} \quad [15]$$

In particular, for  $\xi = 0$ , Eq. 15 is

$$\bar{c}_0 = c_\infty \sum_{m=0}^{\infty} \left\{ \tilde{A}_m \left[ \theta_m(0) + K\tilde{\Psi}_m(0) \right] \left( \frac{r}{r_0} \right)^{2m} \right\} \quad [16]$$

The boundary condition from the steady-state calculations is that  $\theta_m(0) = 1$ . The condition that surface concentration  $\bar{c}_0$  be independent of frequency is obtained with  $\tilde{\Psi}_m(0) = 0$ .

The function  $\tilde{\Psi}_m(\xi)$  modifies the concentration field with respect to the steady-state concentration field. At zero frequency, the concentration field is exactly the steady-state concentration field. At intermediate frequencies the effect of the second term in Eq. 15 is increasingly important. When the frequency tends toward infinity, the first term is negligible with respect to the second, and the usual Warburg behavior is obtained. The boundary conditions for Eq. 14 are

$$\tilde{\Psi}_m = 0 \quad \text{at} \quad \xi = 0 \quad [17]$$

and

$$\tilde{\Psi}_m = 0 \quad \text{at} \quad \xi \rightarrow \infty \quad [18]$$

The boundary condition at  $\xi \rightarrow \infty$  results from the observation that the imposed perturbation should have no effect on the parameter values far away from the electrode surface.

The boundary conditions for the homogeneous part of Eq. 14 are given by

$$\tilde{\Psi}_{m,h} = 1 \quad \text{at} \quad \xi = 0 \quad [19]$$

and

$$\tilde{\Psi}_{m,h} = 0 \quad \text{at} \quad \xi \rightarrow \infty \quad [20]$$

Following the approach of Levart and Schuhmann,<sup>13</sup> the solution to the homogeneous part can be expressed as a polynomial series of  $Sc^{-1/3}$ . By retaining two terms accounting for the finite  $Sc$  correction,  $\tilde{\Psi}_{m,h}$  can be represented by

$$\tilde{\Psi}_{m,h} = \tilde{\Psi}_{0,mh} + \tilde{\Psi}_{1,mh} Sc^{1/3} + \tilde{\Psi}_{2,mh} Sc^{2/3} \quad [21]$$

Hence, the homogeneous part of Eq. 14 can be expressed by three ordinary differential equations, i.e.

$$\tilde{\Psi}_{0,mh}'' + 3\xi^2 \tilde{\Psi}_{0,mh}' - 6m\xi \tilde{\Psi}_{0,mh} - jK\tilde{\Psi}_{0,mh} = 0 \quad [22a]$$



$$\tilde{\Psi}_{1,mh}'' + 3\xi^2\tilde{\Psi}_{1,mh}' - B\xi^3\tilde{\Psi}_{0,mh}' - 6m\xi\tilde{\Psi}_{1,mh} + 3mB\xi^2\tilde{\Psi}_{0,mh} - jK\tilde{\Psi}_{1,mh} = 0 \quad [22b]$$

$$\tilde{\Psi}_{2,mh}'' + 3\xi^2\tilde{\Psi}_{2,mh}' - B\xi^3\tilde{\Psi}_{1,mh}' - C\xi^4\tilde{\Psi}_{0,mh}' - 6m\xi\tilde{\Psi}_{2,mh} + 3mB\xi^2\tilde{\Psi}_{1,mh} + 4mC\xi^3\tilde{\Psi}_{0,mh} - jK\tilde{\Psi}_{2,mh} = 0 \quad [22c]$$

The real and imaginary parts of Eq. 22a-c comprise a system of six simultaneous ordinary differential equations subject to boundary conditions

$$\tilde{\Psi}_{0,mh} = 1 \text{ at } \xi = 0 \text{ and } \tilde{\Psi}_{0,mh} \rightarrow 0 \text{ as } \xi \rightarrow \infty \quad [23a]$$

$$\tilde{\Psi}_{1,mh} = 0 \text{ at } \xi = 0 \text{ and } \tilde{\Psi}_{1,mh} \rightarrow 0 \text{ as } \xi \rightarrow \infty \quad [23b]$$

and

$$\tilde{\Psi}_{2,mh} = 0 \text{ at } \xi = 0 \text{ and } \tilde{\Psi}_{2,mh} \rightarrow 0 \text{ as } \xi \rightarrow \infty \quad [23c]$$

Equations 22a-c were solved using Newman's BAND algorithm.<sup>32</sup>

The solution to the nonhomogeneous equation, Eq. 14, was obtained in terms of the homogeneous solution,  $\tilde{\Psi}_{m,h}$ , by the reduction-of-order method.<sup>33</sup> i.e.

$$\tilde{\Psi}_m(\xi) = \tilde{\Psi}_{m,h} \int_0^\xi \frac{jP(\xi)\theta_m \tilde{\Psi}_{m,h} d\xi}{P(\xi)(\tilde{\Psi}_{m,h})^2} d\xi + K_1 \tilde{\Psi}_{m,h} \int_0^\xi \frac{1}{P(\xi)(\tilde{\Psi}_{m,h})^2} d\xi + K_2 \tilde{\Psi}_{m,h} \quad [24]$$

where

$$P(\xi) = \exp\left(\xi^3 - \frac{B\xi^4}{4} S_c^{-1/3} - \frac{C\xi^5}{5} S_c^{-2/3}\right) \quad [25]$$

and where  $K_1$  and  $K_2$  are constants to be determined by evaluation of the boundary conditions. Equation 24 can be written as

$$\tilde{\Psi}_m = \tilde{\Psi}_{m,h} \left[ K_2 + \int_0^\xi \frac{K_1 + j \int_0^\xi P(\xi)\theta_m \tilde{\Psi}_{m,h} d\xi}{P(\xi)(\tilde{\Psi}_{m,h})^2} d\xi \right] \quad [26]$$

From boundary condition 17,  $K_2 = 0$ . From boundary condition 18,

$$K_1 = -j \int_0^\infty P(\xi)\theta_m \tilde{\Psi}_{m,h} d\xi \quad [27]$$

Equation 27 could also be obtained by requiring that the solution be finite as  $\xi \rightarrow \infty$ .

Evaluation of the impedance response requires the derivative of  $\tilde{\Psi}_m$  with respect to  $\xi$  at the electrode surface, which is given by

$$\left. \frac{d\tilde{\Psi}_m}{d\xi} \right|_{\xi=0} = \frac{K_1}{\tilde{\Psi}_{m,h}(0)} = -j \frac{1}{\tilde{\Psi}_{m,h}(0)} \int_0^\infty P(\xi)\theta_m \tilde{\Psi}_{m,h} d\xi \quad [28]$$

or, in terms of  $\tilde{\theta}_m$

$$\left. \frac{d\tilde{\theta}_m}{d\xi} \right|_{\xi=0} = \frac{K\tilde{A}_m}{\tilde{A}_m} \left. \frac{d\tilde{\Psi}_m}{d\xi} \right|_{\xi=0} = -j \frac{K\tilde{A}_m}{\tilde{A}_m \tilde{\Psi}_{m,h}(0)} \int_0^\infty P(\xi)\theta_m \tilde{\Psi}_{m,h} d\xi \quad [29]$$

The remaining development is given in terms of  $\tilde{\theta}_m(0)$ .

**Conditions on current.**—The current density on the electrode surface is constrained by mass-transfer and kinetic considerations.

**Mass transport.**—The normal current density resulting from the concentration gradients at the electrode surface for the steady-state case is given by

$$\frac{\tilde{i}_f}{nF} = \frac{D}{1-t_R} \left. \frac{\partial \tilde{c}}{\partial z} \right|_{z=0} = \frac{Dc_\infty}{1-t_R} \left( \frac{av}{3D} \right)^{1/3} \sqrt{\frac{\Omega}{v}} \sum_{m=0}^{\infty} A_m(r/r_0)^{2m} \theta'_m(0) \quad [30]$$

where  $\tilde{i}_f$  is the normal current density from concentration gradients or from the mass transport,  $t$  is the transference number of the reacting species,  $n$  is the number of electrons produced when one reactant ion or molecule reacts, and  $F$  is Faraday's constant. Similarly, the fluctuation in normal current density is given by

$$\frac{\tilde{i}_f}{nF} = \frac{D}{1-t_R} \left. \frac{\partial \tilde{c}}{\partial z} \right|_{z=0} = \frac{Dc_\infty}{1-t_R} \left( \frac{av}{3D} \right)^{1/3} \sqrt{\frac{\Omega}{v}} \sum_{m=0}^{\infty} \left\{ [\tilde{A}_m \theta'_m(0) + A_m \tilde{\theta}'_m(0)] (r/r_0)^{2m} \right\} \quad [31]$$

where  $\tilde{\theta}'_m(0)$  is given by Eq. 29.

The interfacial overpotential resulting from convective diffusion is the concentration overpotential given by

$$\eta_c = -\frac{RT}{N_{er}F} \left[ \ln\left(\frac{c_\infty}{c_0}\right) - t_R \left(1 - \frac{c_0}{c_\infty}\right) \right] \quad [32]$$

where  $\eta_c$  is the concentration overpotential,  $R$  is the universal gas constant,  $T$  is the temperature of the electrolyte in kelvin, and  $N_{er}$  is the number of equivalents of reactant per electron produced/consumed. In the case of sinusoidal perturbation

$$\tilde{\eta}_c = -\frac{RT}{N_{er}F} \left[ \frac{1}{c_0} - \frac{t_R}{c_\infty} \right] \tilde{c}_0 \quad [33]$$

**Kinetics.**—The current resulting from the kinetic contribution can be equated to the current resulting from the mass transport, as was done for the steady-state case. The steady-state expression for the current due to kinetic contribution is

$$i_f = i_0 \left( \frac{c_0}{c_\infty} \right)^\gamma \left[ \exp\left(\frac{\alpha N_{er}F}{RT} \eta_s\right) - \exp\left(\frac{\beta N_{er}F}{RT} \eta_s\right) \right] \quad [34]$$

where  $i_0$  is the exchange current density,  $\alpha$  and  $\beta$  are the anodic and cathodic transfer coefficients, respectively, and  $\gamma$  is the composition dependence of the exchange current density. The corresponding expression for the response to a sinusoidal perturbation is given by

$$\tilde{i}_f = \frac{\gamma i_f}{c_0} \tilde{c}_0 + i_0 \left( \frac{c_0}{c_\infty} \right)^\gamma \frac{N_{er}F}{RT} \left[ \alpha \exp\left(\frac{\alpha N_{er}F}{RT} \eta_s\right) + \beta \exp\left(-\frac{\beta N_{er}F}{RT} \eta_s\right) \right] \tilde{\eta}_s \quad [35]$$

The capacitive contribution to the current density is given by

$$\tilde{i}_C = j\omega C_{dl} (\tilde{\eta}_c + \tilde{\eta}_s) \quad [36]$$

In this work,  $C_{dl}$  was assumed to be independent of radial position.

**Potential.**—Far from the electrode surface, Laplace's equation

$$\nabla^2 \Phi = 0 \quad [37]$$

applies, where  $\Phi$  is the ohmic potential. Hence, for the perturbed case, the equation transforms to

$$\nabla^2 \tilde{\Phi} = 0 \quad [38]$$

Because the solution is assumed to be electrically neutral, Laplace's equation is not a function of time. The method of solution followed that developed for the steady state.<sup>29,31</sup> Under a rotational elliptic coordinate transformation ( $\mu, \eta$ ), Eq. 38 becomes

$$\frac{\partial}{\partial \mu} \left[ (1 + \mu^2) \frac{\partial \tilde{\Phi}}{\partial \mu} \right] + \frac{\partial}{\partial \eta} \left[ (1 - \eta^2) \frac{\partial \tilde{\Phi}}{\partial \eta} \right] = 0 \quad [39]$$

where  $z = r_0 \mu \eta$  and  $r = r_0 \sqrt{(1 + \mu^2)(1 - \eta^2)}$ . The boundary conditions for Eq. 39 were that  $\partial \tilde{\Phi} / \partial \eta = 0$  at  $\eta = 0$  (on the annulus),  $\tilde{\Phi} = 0$  at  $\mu = \infty$  (far from the disk), and  $\tilde{\Phi}$  is well defined at  $\eta = 1$  (on the axis of disk). The solution of Eq. 39 satisfying these boundary conditions can be expressed as

$$\tilde{\Phi} = \frac{RT}{N_{\text{er}} F} \sum_{n=0}^{\infty} \tilde{B}_n P_{2n}(\eta) M_{2n}(\mu) \quad [40]$$

where  $\tilde{B}_n$  are coefficients to be determined,  $P_{2n}(\eta)$  are Legendre polynomials of order  $2n$ , and  $M_{2n}(\mu)$  are Legendre polynomials of an imaginary argument satisfying

$$\frac{d}{d\mu} \left[ (1 + \mu^2) \frac{dM_{2n}}{d\mu} \right] = 2n(2n + 1) M_{2n} \quad [41]$$

and the boundary conditions,  $M_{2n} = 1$  at  $\mu = 0$  and  $M_{2n} = 0$  at  $\mu = \infty$ . On the surface of the disk electrode, i.e., at  $\mu = 0$

$$\tilde{\Phi}_0 = \frac{RT}{N_{\text{er}} F} \sum_{n=0}^{\infty} \tilde{B}_n P_{2n}(\eta) \quad [42]$$

Under the assumption of a steady state, the current density was related to the normal component of the potential gradient at the electrode surface<sup>29,31</sup>

$$i = -\kappa_{\infty} \frac{\partial \tilde{\Phi}}{\partial z} \bigg|_{z=0} = -\frac{\kappa_{\infty}}{r_0 \eta} \frac{\partial \tilde{\Phi}}{\partial \mu} \bigg|_{\mu=0} \quad [43]$$

Similarly

$$\tilde{i} = -\kappa_{\infty} \frac{\partial \tilde{\Phi}}{\partial z} \bigg|_{z=0} = -\frac{\kappa_{\infty}}{r_0 \eta} \frac{\partial \tilde{\Phi}}{\partial \mu} \bigg|_{\mu=0} \quad [44]$$

From Eq. 40

$$\tilde{i} = \frac{-\kappa_{\infty}}{r_0 \eta} \frac{RT}{N_{\text{er}} F} \sum_{n=0}^{\infty} \tilde{B}_n P_{2n}(\eta) M'_{2n}(0) \quad [45]$$

From the properties of the Legendre functions it can be seen that

$$M'_{2n}(0) = -\frac{2}{\pi} \frac{(2^n n!)^4}{[(2n)!]^2} \quad [46]$$

The total current density is given by

$$\tilde{i} = \tilde{i}_c + i_f \quad [47]$$

where  $\tilde{i}_c$  is given by Eq. 36 and the total potential is given by

$$\tilde{V} = \tilde{\Phi}_0 + \tilde{\eta}_s + \tilde{\eta}_c \quad [48]$$

where  $\tilde{V}$  is the perturbation in potential applied to the system.

### Numerical Procedure

The numerical procedure adopted for obtaining current and potential distributions in the frequency domain is discussed in this section. The steps provided were used to obtain distributions for a given frequency, and the calculations were repeated over a range of frequencies of interest:

1. The steady-state distributions for concentration, current, various overpotentials, and other parameters of interest such as  $A_m$ ,

$\theta'_m(0)$ , etc., were calculated using the steady-state model without accounting explicitly for the charge distribution.<sup>29</sup> This calculation included correction for a finite Schmidt number.

2. The solution to the homogeneous part of the convective diffusion equation was obtained adopting Newman's BAND algorithm for a given set of frequencies. A Simpson's 1/3<sup>rd</sup> rule in combination with Simpson's 3/8<sup>th</sup> rule was used to evaluate the integral in Eq. 28, and a value of  $\xi = 10.0$  was used to represent the value for  $\infty$ , as the perturbations dissipate at this distance. The accuracy of the solution can be increased using an adaptive integration technique. Use of adaptive integration should be especially important for calculations at high frequencies.

3. In a manner consistent with the approach used for the steady-state solution, guessed values for  $\tilde{A}_m$  were introduced. The power series was truncated at  $m = 10$ . The converged answer did not depend on the initial values. A uniform initial guessed value of  $-0.01$  for both real and imaginary components for  $m = 0, \dots, 10$  provided good convergence.

4. The values for  $\tilde{c}_0$  were calculated from

$$\tilde{c}_0 = c_{\infty} \sum_{m=0}^{\infty} \left\{ \tilde{A}_m \left( \frac{r}{r_0} \right)^m \right\} \quad [49]$$

obtained from Eq. 16 under the boundary conditions used. The values of  $r/r_0$  used were chosen to be the values of abscissa ranging between 0 and 1 used for the Gauss-Legendre quadrature.

5. The values for  $\theta'_m(0)$  were determined from Eq. 29.

6. The  $\tilde{i}_f$  distribution was obtained from Eq. 31 using values for  $\tilde{A}_m$  and  $\theta'_m(0)$ .

7. The  $\tilde{\eta}_s$  distribution was calculated using Eq. 35.

8. The total current density  $\tilde{i}$  was determined from Eq. 47.

9. The  $\tilde{B}_n$  coefficients were calculated by expressing  $\tilde{i}$  resulting from step 8 as a linear combination of Legendre polynomials of  $\eta$ , the rotational elliptic transformation variable, i.e.

$$\tilde{i} = \sum_{l=0}^{\infty} \tilde{\eta}_l P_{2l}(\eta) \quad [50]$$

where  $l$  is varied from 0 to 10 and  $\tilde{\eta}_l$  are complex coefficients. By making use of the orthogonal properties of Legendre polynomials,  $\tilde{\eta}_l$  coefficients were obtained as

$$\tilde{\eta}_l = (4l + 1) \int_0^1 \tilde{i} P_{2l}(\eta) d\eta \quad [51]$$

From Eq. 45 and 50

$$\frac{-\kappa_{\infty}}{r_0 \eta} \frac{RT}{N_{\text{er}} F} \sum_{n=0}^{\infty} \tilde{B}_n P_{2n}(\eta) M'_{2n}(0) = \sum_{l=0}^{\infty} \tilde{\eta}_l P_{2l}(\eta) \quad [52]$$

From Eq. 52

$$\tilde{B}_n = -\frac{r_0 \eta}{\kappa_{\infty}} \frac{N_{\text{er}} F}{RT} \frac{1}{M'_{2n}(0)} \tilde{\eta}_n \quad [53]$$

10. From the values of  $\tilde{B}_n$  coefficients thus obtained, the  $\tilde{\Phi}_0$  values were found from Eq. 42.

11. The  $\tilde{\eta}_c$  distribution was obtained from Eq. 48.

12. The  $\tilde{c}_0$  distribution was recalculated from Eq. 33. At convergence, the distribution obtained during this step should match with that obtained from step 4.

13. The  $\tilde{c}_0$  distribution resulting from step 12 was expressed as a linear combination of Legendre polynomials of  $\eta$ , the rotational elliptic transformation variable, i.e.

$$\tilde{c}_0 = c_{\infty} \sum_{l=0}^{\infty} \tilde{a}_l P_{2l}(\eta) \quad [54]$$

where  $l$  is varied from 0 to 10 and  $\tilde{a}_l$  are complex coefficients. By making use of the orthogonal properties of Legendre polynomials,  $\tilde{a}_l$  coefficients were obtained as

$$\tilde{a}_l = (4l + 1) \int_0^1 (\tilde{c}_0/c_\infty) P_{2l}(\eta) d\eta \quad [55]$$

14. From Eq. 49 and 54, a relationship between  $\tilde{A}_m$  and  $\tilde{a}_l$  was established and a new set of  $\tilde{A}_m$  values was obtained.

15. The new  $\tilde{A}_m$  values were averaged with the  $\tilde{A}_m$  values from previous iteration using a weighting factor which was chosen to have a value near 0.95 at low frequencies and near 0.05 at high frequencies. The convergence criterion was scaled by the weighting factor used.

16. Steps 5-15 were repeated until convergence was obtained. The convergence criterion used provided 5 significant digits in the value for  $\tilde{A}_m$ .

### Results and Discussion

Direct comparison can be made for the same set of parameters between the results of the two-dimensional model developed in the present work and those for a one-dimensional model developed by Tribollet and Newman.<sup>21</sup> For all calculations presented in this section, a value of  $35 \mu\text{F}/\text{cm}^2$  was used for the double-layer capacitance. This value is consistent with experimental results.<sup>30</sup> Other physical parameters used are given in the subsequent sections. Agreement between the two models is expected under conditions for which the current distribution is uniform (slow kinetics or near mass-transfer limitation). The one-dimensional model is expected to be inadequate for nonuniform current distributions.

**Uniform current distribution.**—From steady-state calculations, an a priori assessment of the uniformity of current distribution can be obtained from dimensionless parameters

$$J = \frac{i_0 r_0 N_{\text{er}} F}{RT \kappa_\infty} \quad [56]$$

which provides the relative value of kinetic and ohmic contributions to the system resistance, and

$$N = -\sqrt{\frac{r_0^2 \Omega}{\nu}} \left( \frac{av}{3D} \right)^{1/3} \frac{n N_{\text{er}} F^2 D c_\infty}{RT(1-t)\kappa_\infty} \quad [57]$$

which provides the relative value of mass-transfer and ohmic contributions. The influence of these parameters on the uniformity of distributions can be seen in Fig. 8 of Ref. 31. The current distribution is uniform for small values of  $J$  and  $N$ .

Calculated results are presented in Fig. 1 for an exchange current density of  $3 \text{ mA}/\text{cm}^2$  and a diffusion coefficient value of  $0.3095 \times 10^{-5} \text{ cm}^2/\text{s}$ . Other parameters used in these simulations are those corresponding to the values for the reduction of ferricyanide system as reported in Ref. 29. Equations 56 and 57 yield  $J = 0.225$  and  $N = 0.0695$ . From the calculations presented in Fig. 1, it can be seen that a significant high-frequency loop results due to the kinetic effect. Steady-state calculations for this case showed that the current distribution had less than a 1% variation across the electrode surface.

For small values of  $J$  and  $N$ , it is expected that results from the two-dimensional model developed here should be in agreement with the calculations performed for the one-dimensional case. Comparisons between the one-dimensional model of Tribollet and Newman<sup>21</sup> and the present two-dimensional model are presented in Fig. 2. The discrepancy between the two models at high frequencies was attributed to numerical instabilities seen in the two-dimensional model at high frequencies. However, for most of the frequency spectrum, the normalized differences were less than 3%. This result illustrates that the one-dimensional model is adequate for cases where kinetic effects play a dominant role. Similar agreement between the one and two-dimensional model was seen for larger exchange current densities (larger values of  $J$ ) as the mass-transfer-limited current density is approached ( $N \rightarrow 0$ ).

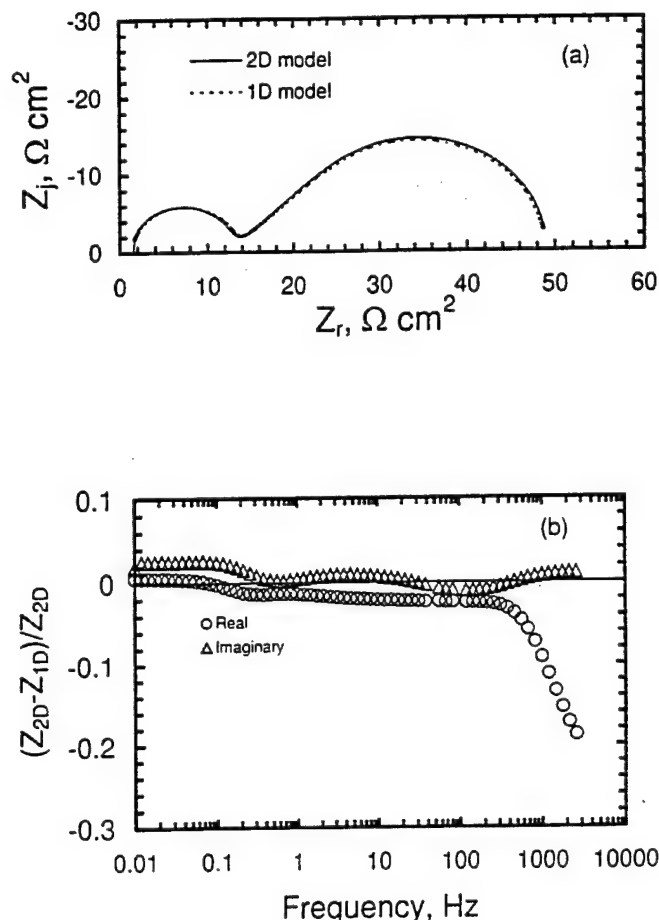


**Figure 1.** (a) Comparison between one-dimensional and two-dimensional models for the slow kinetics case at  $1/4^{\text{th}}$  of  $i_{\text{lim}}$  and  $\Omega = 120 \text{ rpm}$  with  $i_0 = 3 \text{ mA}/\text{cm}^2$ ,  $D = 0.3095 \times 10^{-5} \text{ cm}^2/\text{s}$ ,  $J = 0.225$ ,  $N = 0.0695$ , and  $Sc = 2730$ . In this case, steady-state distributions tend to be highly uniform. (b) Differences between the calculations from two-dimensional and one-dimensional model normalized with respect to the two-dimensional model as a function of frequency.

**Nonuniform current distribution.**—The one-dimensional model did not provide an adequate representation of the impedance response for a disk electrode below the mass-transfer-limited current for large exchange current densities. The values for the exchange current densities and the diffusion coefficients used in this section are those required to match the values of experimentally obtained impedance spectra.<sup>34</sup>

A comparison between the two models is presented in Fig. 3 for a rotation speed of 120 rpm at one quarter of the mass-transfer-limited current density ( $J = 2.247$  and  $N = 0.0695$ ). Even at this low rotation speed, where the steady-state current density at the center of the disk is 97% of the average value, considerable disparity was observed between the one-dimensional and two-dimensional models. This result is consistent with the observation that even small nonuniformities in the steady-state domain can become significantly important in the frequency domain. The one-dimensional model did not adequately describe the system behavior as reaction kinetics became fast. A similar comparison is presented in Fig. 4 for 3000 rpm at one quarter of the mass-transfer-limited current ( $J = 7.489$  and  $N = 0.3552$ ). The discrepancy is larger due to the increased value of  $N$ .

For the same value of  $J$  as was used in Fig. 3, the disparity between the two models for a rotation speed of 120 rpm was reduced significantly when calculations were obtained at three-quarters of the mass-transfer-limited current, as shown in Fig. 4. The agreement is observed because the distributions are more uniform near mass-

transfer limitation. At 3000 rpm, however, the two models do not agree, even near the mass-transfer-limited current (see Fig. 5). In this case,  $J = 5.617$  and  $N = 0.5874$ . The discrepancy between the two models can be attributed to the larger value of  $N$ . The influence of nonuniformities becomes more significant with an increase in rotation speed.

Another perspective on the two-dimensional character of the disk impedance response at large  $N$  can be seen from the radial distributions of the real and imaginary parts of local impedance given in Fig. 6 for the conditions of Fig. 4 and 5. The distributions are shown for dimensionless frequencies  $K = 1$  and  $K = 2.8$ . The increased nonuniformity of the local impedance at 3000 rpm results in the discrepancy seen between the one- and two-dimensional models.

A surprising result of the work presented by Orazem et al.<sup>20</sup> was that the one-dimensional model of Tribollet and Newman<sup>21</sup> for impedance of a rotating disk fit the data to almost within the noise level of the measurement, even for conditions where the present work would indicate that a two-dimensional model would be required. Their result can be explained by regressing the one-dimensional model to impedance spectra calculated using the two-dimensional model presented in the present work. The results of the regression are presented in Fig. 7 for the 120 rpm, three-quarters of mass-transfer-limited current comparison shown in Fig. 4. The quality of the fit was extremely good. The relative residual errors are compared to the noise

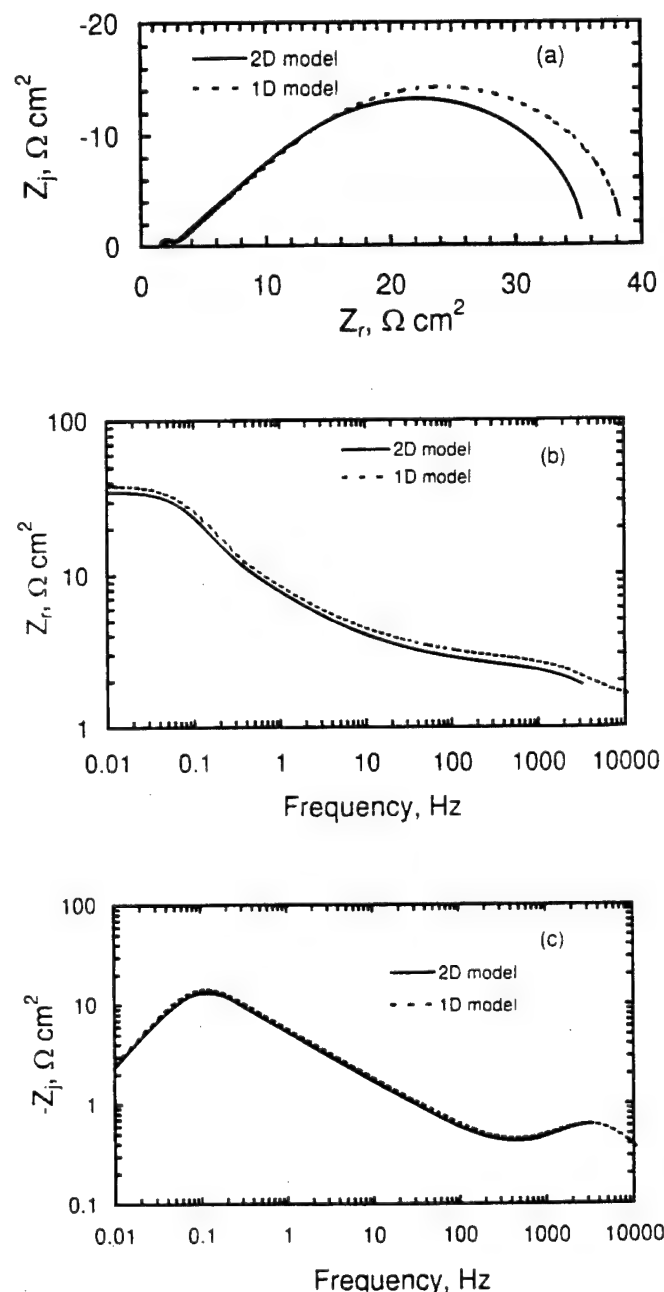


**Figure 2.** Comparison between the impedance spectra generated by 1D and 2D models for 120 rpm,  $1/4^{\text{th}}$  of  $i_{\text{lim}}$ ,  $i_0 = 30 \text{ mA/cm}^2$ ,  $D = 0.3095 \times 10^{-5} \text{ cm}^2/\text{s}$ ,  $J = 2.247$ ,  $N = 0.0695$ , and  $Sc = 2730$ . Results presented for (a) impedance plane plot; (b) real part as a function of frequency; and (c) imaginary part as a function of frequency.

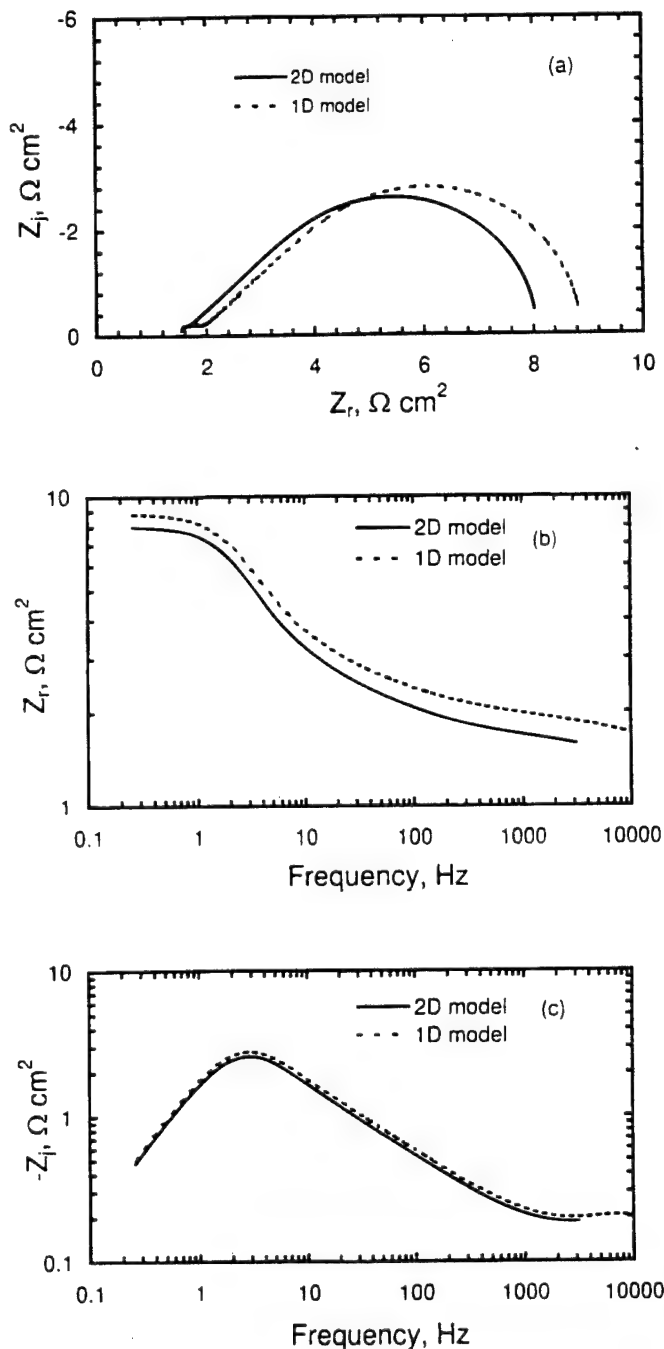


**Figure 3.** Comparison between the impedance spectra generated by 1D and 2D models for 3000 rpm,  $1/4^{\text{th}}$  of  $i_{\text{lim}}$ ,  $i_0 = 100 \text{ mA/cm}^2$ ,  $D = 0.3195 \times 10^{-5} \text{ cm}^2/\text{s}$ ,  $J = 7.489$ ,  $N = 0.3552$ , and  $Sc = 2650$ . Results presented for (a) impedance plane plot; (b) real part as a function of frequency; and (c) imaginary part as a function of frequency.

level of the measurements in Fig. 7d and e. The relative residual error for the imaginary part is on the order of 1% of the imaginary impedance and on the order of 0.4% for the real part. The quality of the fit is such that it would be difficult to use regression to experimental data to distinguish between the two- and one-dimensional models. The principal difference between the two models was that the one-dimensional model provided a Schmidt number 7% higher (1780 as opposed to 1660 for the two-dimensional model). Similar results were obtained for all examples presented here. The regressed Schmidt numbers were as much as 22% higher than the expected value in cases where the discrepancy between models was very significant.<sup>34</sup> The

present work illustrates that a good fit for the one-dimensional model does not imply that the model is adequate to describe the physics of the system. Due importance should be attached to the role of nonuniform current distributions for the assessment of electrochemical impedance data for cases where  $J$  and  $N$  are large.

### Conclusions

A two-dimensional mathematical model for the impedance response of a disk electrode was developed on the basis of the coupling

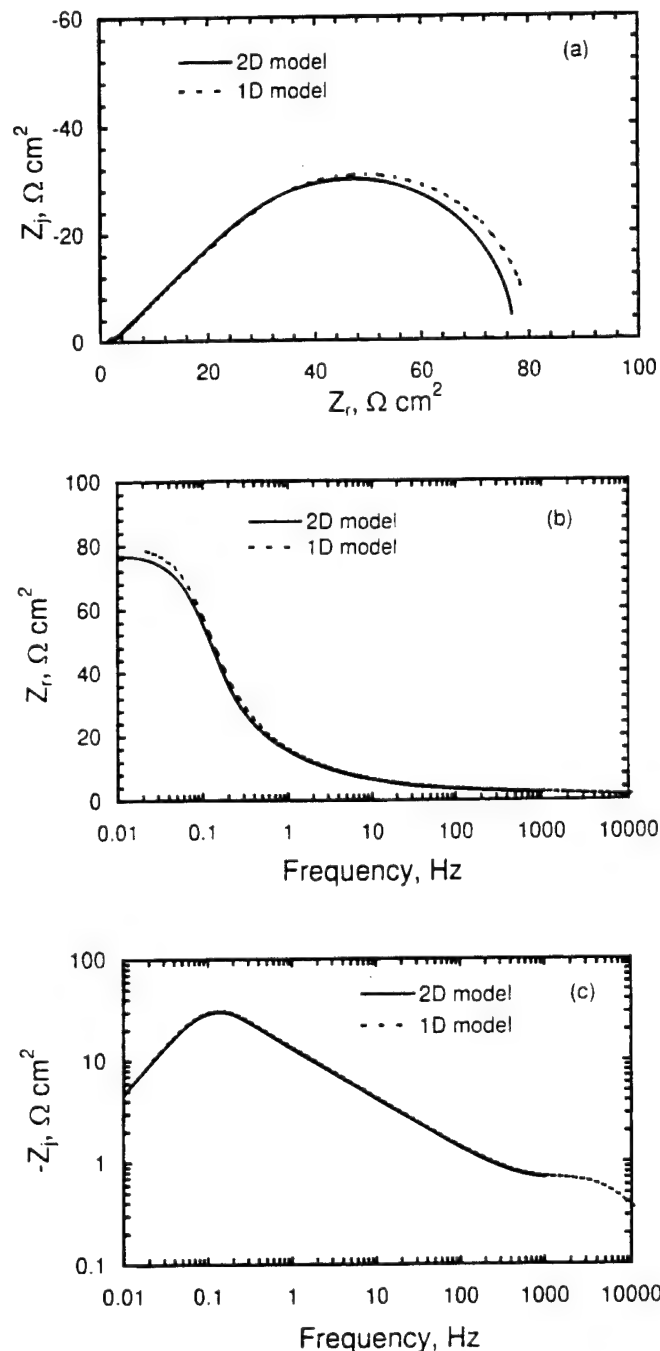


**Figure 4.** Comparison between the impedance spectra generated by 1D and 2D model for 120 rpm,  $3/4^{\text{th}}$  of  $i_{\text{lim}}$ ,  $i_0 = 100 \text{ mA/cm}^2$ ,  $D = 0.5095 \times 10^{-5} \text{ cm}^2/\text{s}$ ,  $J = 7.489$ ,  $N = 0.0970$ , and  $Sc = 1660$ . Results presented for (a) impedance plane plot; (b) real part as a function of frequency; and (c) imaginary part as a function of frequency.

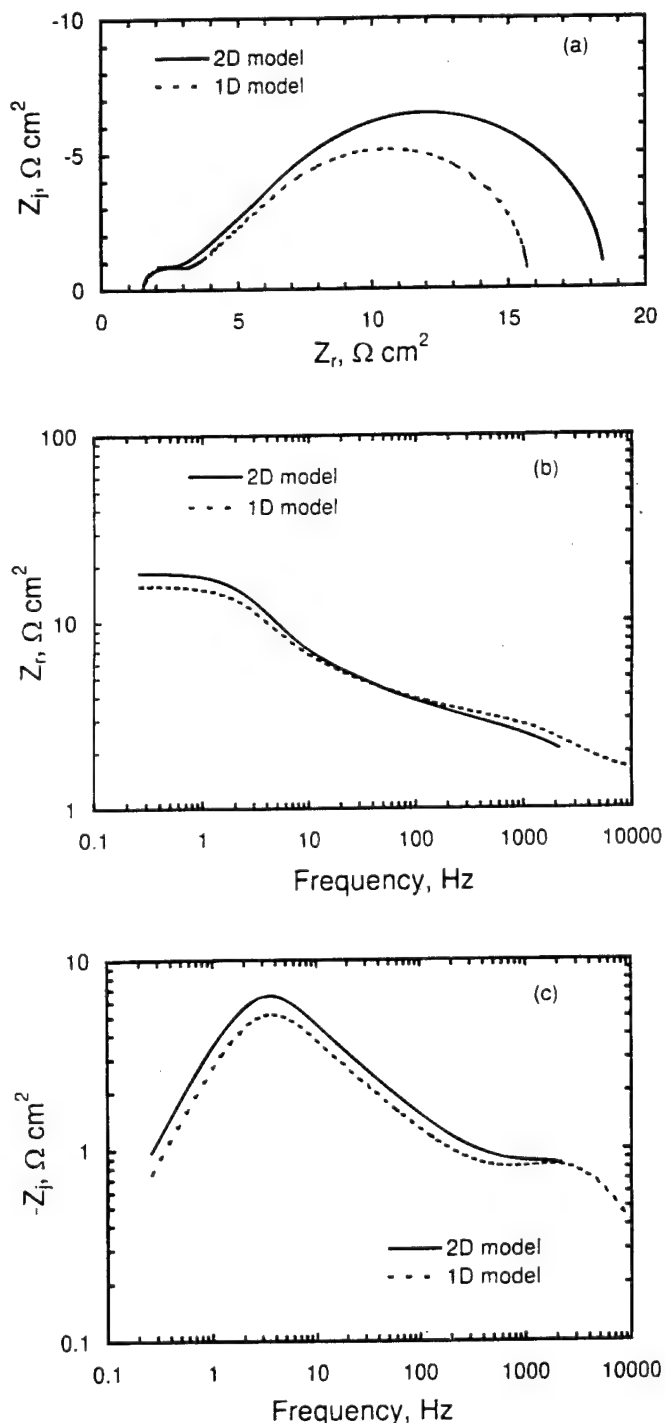


**Figure 5.** Comparison between the impedance spectra generated by 1D and 2D model for 3000 rpm,  $3/4^{\text{th}}$  of  $i_{\text{lim}}$ ,  $i_0 = 75 \text{ mA/cm}^2$ ,  $D = 0.6795 \times 10^{-5} \text{ cm}^2/\text{s}$ ,  $J = 5.617$ ,  $N = 0.5874$ , and  $Sc = 1250$ . Results presented for (a) impedance plane plot; (b) real part as a function of frequency; and (c) imaginary part as a function of frequency.

between convective diffusion in a thin diffusion layer, Laplace's equation for potential in an outer region, and electrode kinetics. The influence of a finite Schmidt number, which is critical in the frequency domain, was taken into account by including three terms in the axial and radial velocity expansions. A uniform distribution of capacitance was assumed in the development of the model, and this assumption was supported by experimental observations reported in the literature for ring-disk measurements<sup>30</sup> and by preliminary calculations.<sup>29</sup> Reliable results were obtained for dimensionless frequencies less than 1000. Use of improved integration strategies could extend the frequency range.

The nonuniform current distribution observed below the mass-transfer-limited current has a significant effect on the impedance response of a rotating disk electrode when electrode kinetics are fast. One-dimensional models apply when kinetic or mass-transfer limitations make the current distribution more uniform. Discrepancies between the one- and two-dimensional models were observed under conditions where the steady-state current density at the center of the disk was 97% or less of the average value.

Under conditions yielding a nonuniform current distribution, the one-dimensional model may provide an adequate fit to the data, but the physical parameters obtained by regression will be incorrect. In

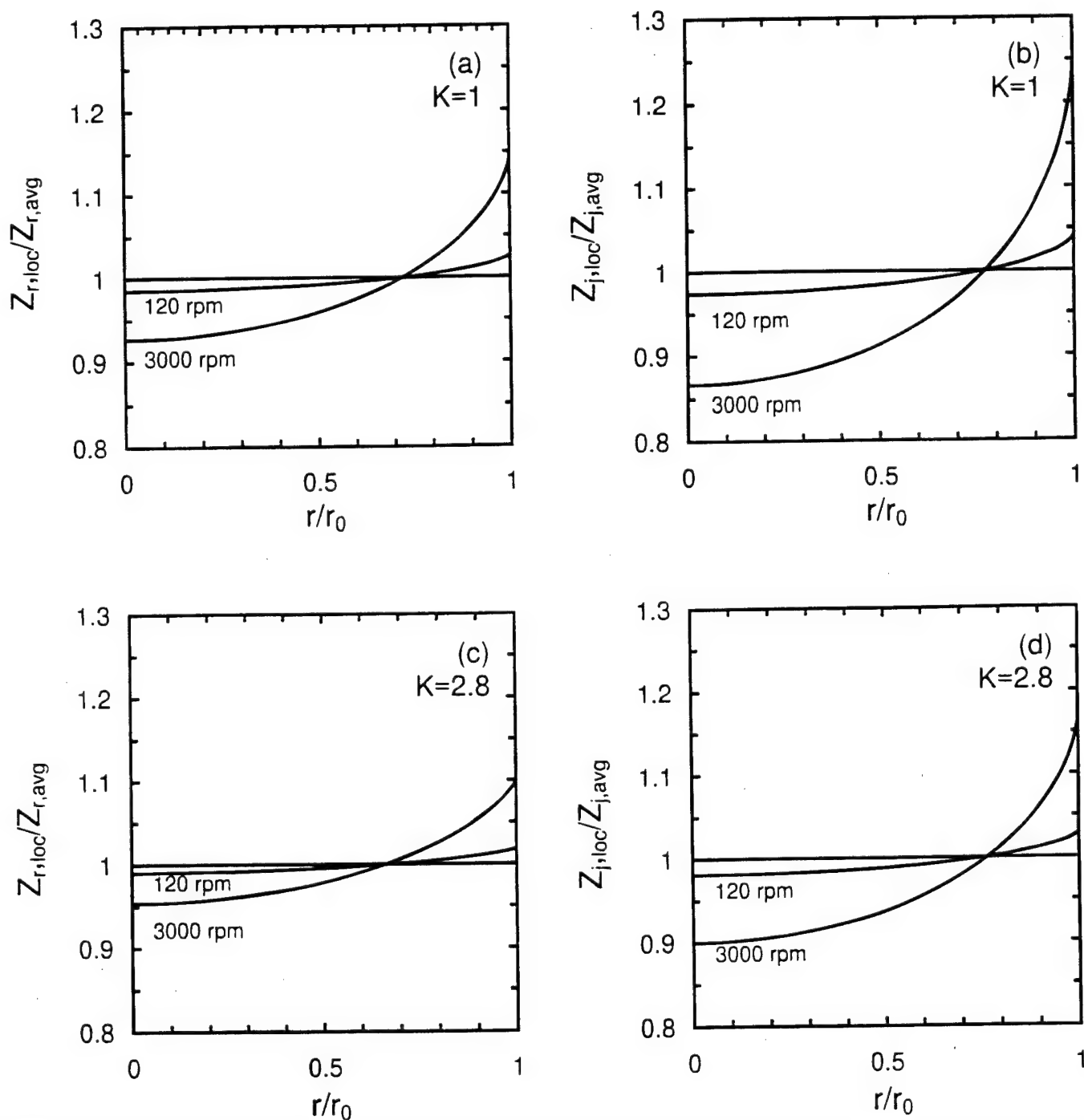
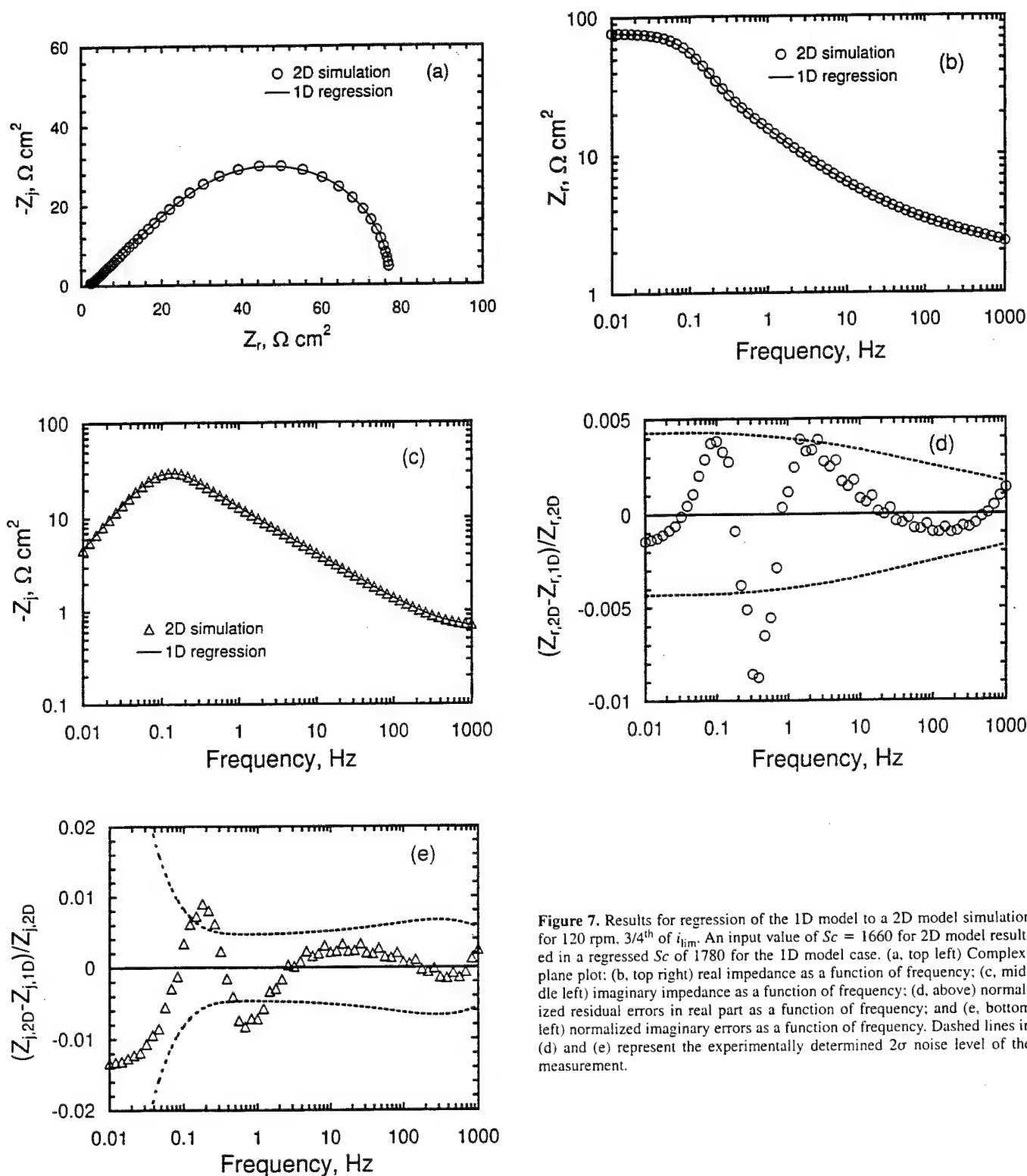


Figure 6. Distributions for local impedance values for a dimensionless frequencies of  $K = 1$  and  $K = 2.8$ . The parameter values are those given in Fig. 4 and 5.





**Figure 7.** Results for regression of the 1D model to a 2D model simulation for 120 rpm,  $3/4$ th of  $i_{lim}$ . An input value of  $Sc = 1660$  for 2D model resulted in a regressed  $Sc$  of 1780 for the 1D model case. (a, top left) Complex-plane plot; (b, top right) real impedance as a function of frequency; (c, middle left) imaginary impedance as a function of frequency; (d, above) normalized residual errors in real part as a function of frequency; and (e, bottom left) normalized imaginary errors as a function of frequency. Dashed lines in (d) and (e) represent the experimentally determined  $2\sigma$  noise level of the measurement.

such cases, nonuniform current distributions should be taken into account. For the fast reaction kinetics associated with the reduction of ferricyanide, the effect of nonuniform current distributions on impedance was seen at 120 rpm and was even greater at larger rotation speeds.

#### Acknowledgments

This research received support from the Office of Naval Research under Grant No. N000149310056 and N000149311113 (Dr. A. J.

Sedriks, program monitor) and from the National Science Foundation under the US-France Cooperative Research Grant INT-9416713.

#### List of Symbols

$a$	coefficient in the Cochran expansion for velocity, $a=0.51023$ (see Eq. 4a)
$A_m$	coefficients in series for concentration (see Eq. 9)
$\tilde{A}_m$	coefficients in series for concentration (see Eq. 10)

$B$	constant given in Eq. 7
$b$	coefficient in the Cochran expansion for velocity, $b = -0.61592$ (see Eq. 4a)
$c$	concentration of reacting species, mol/cm <sup>3</sup>
$c_0$	concentration of the reactant on the electrode surface, mol/cm <sup>3</sup>
$c_\infty$	bulk concentration of the reacting species, mol/cm <sup>3</sup>
$C$	constant given in Eq. 7
$C_{dl}$	double-layer capacitance, F/cm <sup>2</sup>
$D$	diffusion coefficient of the reacting species, cm <sup>2</sup> /s
$F$	Faraday's constant, C/equiv
$i_f$	faradaic current density, A/cm <sup>2</sup>
$i_0$	exchange current density, A/cm <sup>2</sup>
$J$	dimensionless parameter related to the significance of kinetics (see Eq. 56)
$j$	imaginary number, $\sqrt{-1}$
$K$	dimensionless frequency (see Eq. 6)
$K_1, K_2$	constants of integration in Eq. 24
$N$	parameter related to the significance of mass transfer (see Eq. 57)
$N_{er}$	number of equivalents of reactant used per one electron produced/consumed
$n$	number of electrons produced when one reactant ion or molecule reacts
$R$	universal gas constant, J/mol/K
$r$	radial coordinate, cm
$r_0$	radius of disk, cm
$\tilde{r}_k$	Complex coefficients used in Eq. 50
$Sc$	Schmidt number
$T$	electrolyte temperature, K
$t$	time, s
$t_R$	transference number of the reacting species
$v_r, v_z$	radial and axial velocity components, respectively, cm/s
$Z$	impedance, ohms
$z$	normal distance from disk, cm

# Greek

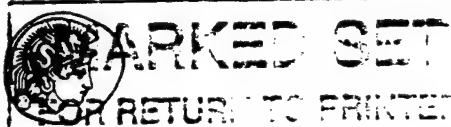
$\alpha, \beta, \gamma$	parameters in kinetic expression (see Eq. 34)
$\chi$	dummy variable
$\bar{\chi}$	steady-state value corresponding to $\chi$
$\tilde{\chi}$	amplitude of perturbation corresponding to $\chi$
$\eta, \mu$	parameters in the rotational elliptic coordinate transformation used in solving Laplace's equation
$\eta_c$	concentration overpotential, V
$\eta_s$	surface overpotential, V
$\theta_m$	axial-dependent term in the concentration series
$\bar{\theta}_{m,h}$	homogeneous solution for convective diffusion equation
$\kappa_\infty$	solution conductivity, $\Omega \text{ cm}^{-1}$
$\nu$	kinematic viscosity, cm <sup>2</sup> /s
$\xi$	normalized axial position

$\Phi$	ohmic potential drop, V
$\omega$	frequency of perturbation, s <sup>-1</sup>
$\Omega$	rotation speed, s <sup>-1</sup>

## References

1. *Impedance Spectroscopy Emphasizing Solid Materials and Analysis*, J. Ross Macdonald, Editor, John Wiley and Sons, New York (1987).
2. M. E. Orazem, P. Agarwal, C. Deslouis, and B. Tribollet, *J. Electrochem. Soc.*, **143**, 948 (1996).
3. M. E. Orazem, T. El Moustafid, C. Deslouis, and B. Tribollet, *J. Electrochem. Soc.*, **143**, 3880 (1996).
4. P. Agarwal, M. E. Orazem, and L. H. García-Rubio, *J. Electrochem. Soc.*, **142**, 4159 (1995).
5. P. Agarwal, O. C. Moghissi, M. E. Orazem, and L. H. García-Rubio, *Corrosion*, **49**, 278 (1993).
6. P. Agarwal, M. E. Orazem, and A. Hiser, in *Hydrogen Storage Materials, Batteries, and Chemistry*, D. A. Corrigan and S. Srinivasan, Editors, PV 92-5, p. 120, Electrochemical Society Proceedings Series, Pennington, NJ (1991).
7. P. Agarwal, M. E. Orazem, and L. H. García-Rubio, in *Electrochemical Impedance: Analysis and Interpretation*, ASTM STP 1188, J. Scully, D. Silverman, and M. Kendig, Editors, p. 115, American Society for Testing and Materials, Philadelphia, PA (1993).
8. Yu. Filinovsky and V. A. Kiriyanov, *Dokl. Akad. Nauk. SSSR*, **156**, 1412 (1964).
9. D. Schumann, *Compt. Rend. Acad. Scientifique Paris*, **262C**, 624 (1966).
10. C. Deslouis, I. Epelboin, M. Keddam, and J. C. Lestrade, *J. Electroanal. Chem.*, **28**, 57 (1970).
11. E. Levart and D. Schuhmann, *J. Electroanal. Chem.*, **53**, 77 (1974).
12. V. Homsy and J. Newman, *J. Electrochem. Soc.*, **121**, 521 (1974).
13. E. Levart and D. Schuhmann, *J. Electrochem. Soc.*, **122**, 1082 (1975).
14. D. A. Scherson and J. Newman, *J. Electrochem. Soc.*, **127**, 110 (1980).
15. E. Levart and D. Schuhmann, *J. Electrochem. Soc.*, **127**, 2649 (1980).
16. B. Tribollet and J. Newman, *J. Electrochem. Soc.*, **130**, 822 (1983).
17. C. Deslouis, C. Gabrielli, and B. Tribollet, *J. Electrochem. Soc.*, **130**, 2044 (1983).
18. B. Tribollet, J. Newman, and W. H. Smyrl, *J. Electrochem. Soc.*, **135**, 134 (1988).
19. C. Deslouis and B. Tribollet, *Electrochim. Acta*, **35**, 1637 (1990).
20. M. E. Orazem, C. Deslouis, and B. Tribollet, Paper 120 presented at The Electrochemical Society Meeting, Montreal, Canada, May 4-9, 1997. Paper in preparation.
21. B. Tribollet and J. Newman, *J. Electrochem. Soc.*, **130**, 2016 (1983).
22. W. G. Cochran, *Proc. Cambridge Philos. Soc.*, **30**, 365 (1935).
23. J. Newman, *J. Electrochem. Soc.*, **117**, 198 (1970).
24. K. Nisancioglu, *Corrosion*, **43**, 258 (1987).
25. K. Nisancioglu, in *The Measurement and Correction of Electrolyte Resistance in Electrochemical Tests*, ASTM STP 1056, p. 61, American Society for Testing and Materials, Philadelphia, PA (1990).
26. K. Nisancioglu and J. Newman, *J. Electrochem. Soc.*, **121**, 523 (1974).
27. P. W. Appel and J. Newman, *J. Electrochem. Soc.*, **124**, 1864 (1977).
28. P. W. Appel, Ph.D. Dissertation, University of California, Berkeley, Berkeley, CA (1976).
29. M. Durbha and M. E. Orazem, *J. Electrochem. Soc.*, **145**, 1940 (1998).
30. C. Deslouis and B. Tribollet, *Electrochim. Acta*, **23**, 935 (1978).
31. J. Newman, *J. Electrochem. Soc.*, **113**, 1235 (1966).
32. J. Newman, *Industrial and Engineering Chemistry Fundamentals*, **7**, 514 (1968).
33. F. B. Hildebrand, *Advanced Calculus for Engineers*, 1st ed., Prentice Hall Publications, pp. 32-33, Englewood Cliffs, NJ (1948).
34. M. Durbha, Ph.D. Thesis, University of Florida (1998).

Ref. 34  
Gainesville, FL?



PERGAMON

Electrochimica Acta 00 (1999) 1-10

ELECTROCHIMICA

Acta

# Influence of surface phenomena on the impedance response of a rotating disk electrode

M.E. Orazem<sup>a,\*</sup>, M. Durbha<sup>a</sup>, C. Deslouis<sup>b</sup>, H. Takenouti<sup>b</sup>, B. Tribollet<sup>b</sup>

<sup>a</sup>Department of Chemical Engineering, University of Florida, Gainesville, Florida, 32611-6005, USA

<sup>b</sup>UPR 15 du CNRS, Laboratoire "Physique des Liquides et Electrochimie", Université Pierre et Marie Curie, 75252, Paris Cedex 05, France

Received 7 August 1998; accepted 2 December 1998

## Abstract

The objective of this work was to explore the role of surface blocking on the impedance response associated with reduction of ferricyanide on a Pt rotating disk electrode. The analysis took into account the possible role of non-uniform current distribution on the impedance response. The results suggest that the time-dependent change to the Pt surface contributes to both a decrease of rate constant that hinders electrode kinetics and a blocking of the electrode surface that hinders mass transfer. © 1999 Elsevier Science Ltd. All rights reserved.

## 1. Introduction

The rotating disk electrode is attractive for determination of the diffusion coefficient of electro-active ionic species because the flow is well defined in the laminar regime and because the disk is uniformly accessible at the mass-transfer limited condition [1]. A one-dimensional model for transport can therefore be used to interpret experimental results at the mass-transfer-limited condition. In the steady state, uniform accessibility has allowed development of the Levich equation, which takes into account the first term of the expansion appropriate for the axial velocity close to the electrode surface [2]. This approach is strictly appropriate for infinite Schmidt (Sc) numbers. Treatments have been developed which include higher-order terms in the velocity expansion, thereby correcting for the finite value of the Schmidt number. For typical electrolytic solutions, the correction for the finite Schmidt number can be 2 to 4% [3].

A parallel development has been made in the frequency domain for the Warburg impedance associated with convective diffusion to a disk. In principle, the equation governing mass transfer to the disk is

$$\frac{\partial c_i}{\partial t} + v_r \frac{\partial c_i}{\partial r} + v_z \frac{\partial c_i}{\partial z} = D_i \left\{ \frac{\partial}{\partial r} \left( \frac{1}{r} \frac{\partial r c_i}{\partial r} \right) + \frac{\partial^2 c_i}{\partial z^2} \right\} \quad (1)$$

where  $c_i$  and  $D_i$  are the concentration and diffusivity of the limiting species, respectively, and the velocity is given by

$$v_z = \sqrt{v\Omega} \left\{ -\frac{a\Omega}{v} z^2 + \frac{1}{3} \left( \frac{\Omega}{v} \right)^{3/2} z^3 + \frac{b}{6} \left( \frac{\Omega}{v} \right)^2 z^4 + \dots \right\} \quad (2)$$

for the axial component and by

\* Corresponding author.

$$v_r = r\Omega \left\{ a \left( \frac{\Omega}{v} \right)^{1/2} z - \left( \frac{\Omega}{v} \right) \frac{z^2}{2} - \frac{b}{3} \left( \frac{\Omega}{v} \right)^{3/2} z^3 + \dots \right\} \quad (3)$$

for the radial component. The radial terms can be neglected under mass-transfer or kinetically limited conditions for which the current distribution may be assumed to be uniform. Numerical and analytic solutions have been obtained for the Warburg impedance at the limiting current, with a considerable effort expended on obtaining analytic expressions appropriate for regression to impedance data (see, e.g., [4–8]). These works make use of only the first term in the velocity expansions, and thus are appropriate for an infinite Schmidt number. The correction for finite values of the Schmidt number can be more significant for impedance data than for steady state measurements. The error caused by neglecting these corrections for a Schmidt number of 1000 can be as high as 24% [9].

Tribollet and Newman have developed a general numerical solution for the Warburg impedance associated with convective diffusion to the disk electrode where the axial velocity (Eq. (2)) is treated by a two-term expansion, thus accounting for the influence of a finite Schmidt number [10]. One attractive feature of their approach was that the solution was presented in the form of a table from which appropriate values could be obtained by interpolation, thereby greatly speeding up regression to experimental data. Their model was extended to account for the third term in the velocity expansion [11].

The analytic and numerical solutions reported in the literature are strictly valid only at the limiting current where the concentration and flux to the disk electrode are uniform and radial variations can be neglected. Unfortunately, impedance techniques that rely on perturbation of current or potential cannot be applied at this plateau because the current density in this regime is not dependent upon potential. The model of Tribollet and Newman has been applied to the results of electrohydrodynamical impedance spectroscopy (EHD) which, by modulation of the disk rotation speed at a constant potential, can be used to access the mass-transfer-limited plateau [10,12]. The value obtained for the Schmidt number for ferricyanide ions was in good agreement with accepted values [13]. No similar confirmation was obtained for standard electrochemical impedance spectroscopy (EIS) measurements. Such experiments conducted below the limiting current plateau yielded values for the Schmidt number that were higher than expected values by 200% or more, even when the models are corrected for the finite Schmidt number [14]. EHD measurements conducted

below the limiting current plateau also yielded similarly incorrect values for the Schmidt number [14]. The discrepancies in the values of *Sc* determined by EHD and EIS were too large to be attributed to the influence of migration on mass transfer.

While it was suggested that these discrepancies could be attributed to a frequency-dependent relaxation of adsorbed poisons, the impedance spectra show qualitatively the form expected for convective diffusion impedance [14]. In fact, the data conformed to the model for convective diffusion so well that these experiments were used to demonstrate the inadequacies of using the Warburg impedance based on assumption of a Nernst stagnant diffusion layer [15]. The only discrepancy was that the Schmidt number required to achieve this excellent fit was two or three times the reported value. Similar results were seen for reduction of ferricyanide on both nickel in a NaOH supporting electrolyte and on platinum in a KCl supporting electrolyte [14]. In recent experiments, the Schmidt number obtained for the ferricyanide ion using electrohydrodynamic impedance spectroscopy was found to be a function of duration of the experiment [16]. This result is consistent with recent reports of the formation of surface films that influence the behavior of this system, either through a blocking effect or through reduction of the rate constant for the reduction of ferricyanide.

Stieble and Jüttner reported that, depending on the defined prepolarization conditions, a partial blocking of the electrode surface was observed as indicated by distinct changes of the impedance spectra [17]. They reported blocking index values as high as 30 in some cases, which results in just 3% of the total surface area of the electrode being active. The blocking index is defined as the ratio of the area of inactive portion of the surface to the area of active portion. Voltammetric techniques were applied to study the effect of surface blocking [18–20]. It was observed that the irreversibility of the heterogeneous kinetics increased with the surface coverage, and the apparent charge transfer resistance was found to be higher. The film formation was attributed to the adsorption of certain compounds on to the surface of the Pt disk electrode. However, there is no agreement between the authors about the composition and structure of the compounds adsorbed on to the electrode surface. Some suggested that ferri and ferrocyanide ions are adsorbed on the Pt surface [21–23]. Others suggested that iron cyanide complexes are decomposed resulting in the formation of species that are adsorbed on the electrode surface (e.g.,  $\text{CN}^-$  and  $\text{Fe}(\text{CN})_3$ ) [24–26]. It was also believed that coexistence of different oxidation states of iron as in ferri and ferrocyanide may lead to a bonding between the two species thus forming a Prussian blue layer on the electrode surface.

A second possible explanation for the anomalous

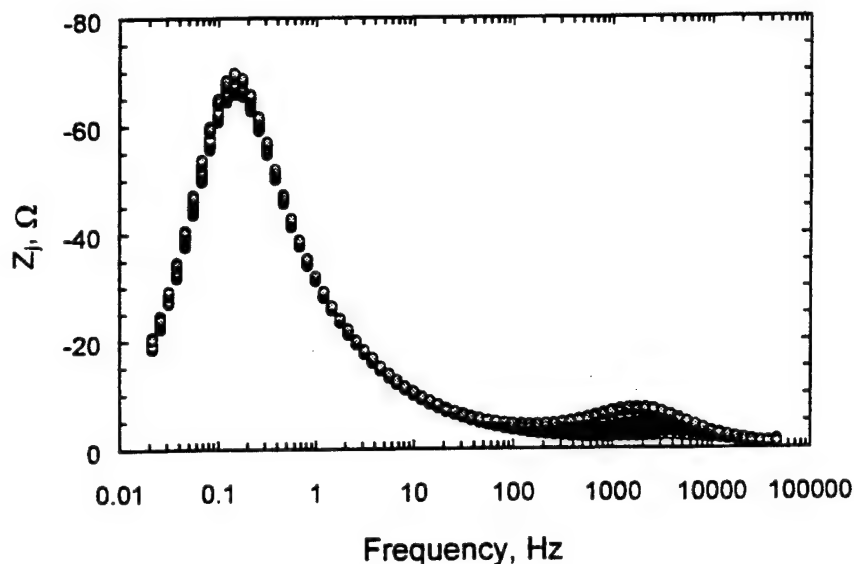


Fig. 1. Imaginary part of the impedance for reduction of ferricyanide on a Pt disk rotating at 120 rpm with time as a parameter.

results is that the frequency dependence of the non-uniform current and potential distribution causes the observed discrepancies in the value for the Schmidt number. While the current distribution is uniform on a disk electrode at the mass-transfer-limited plateau where EHD measurements are performed, the current distribution below the plateau is non-uniform [27–29]. The non-uniform current and potential distributions were shown to have a significant effect on the impedance response for this system at large rotation speeds ( $> 600$  rpm) [30], but at low rotation speeds (e.g. 120 rpm), the current distribution was determined to be relatively uniform [31]. Thus, the one-dimensional analysis of Tribollet and Newman [10] can be assumed to be valid for some experimental conditions.

A third possible explanation for the anomalous results is that the model used to extract Schmidt number values did not provide a statistically adequate fit. The level of stochastic noise in impedance experiments can be very small, as shown by Orazem et al. [32], and it is possible that refinements in the process model could influence the value of the Schmidt number obtained.

The objective of this work was to explore the role of surface blocking on the impedance response associated with reduction of ferricyanide on a Pt rotating disk electrode. This work also provides a demonstration of the application of the error analysis techniques described by Agarwal et al. [33–35] to a physical system.

## 2. Experimental procedure

The potentials and currents were measured and controlled by a Solartron 1286 potentiostat for EIS measurements and a Solartron 1287 potentiostat for EHD measurements. A Solartron 1250 frequency response analyzer (FRA) was used to apply the sinusoidal perturbation and to calculate the resulting transfer function. A matched two-channel Kemo type VBF8 48 low-pass Butterworth analog filter was used to reduce the noise level of the input signals to the FRA ~~in case~~ <sup>for</sup> ~~of the EIS.~~ <sup>measure</sup> No filter was employed for the EHD <sup>measurements.</sup> as it was shown earlier that for the EHD measurements at the limiting current, the noise level in the measurement was unaffected by employing a filter and the time required for collecting data increased slightly by employing the filter [32].

The data were collected from high frequency to low frequency with 12 logarithmically spaced frequencies per decade for the EIS measurements. ~~In case of EHD~~ <sup>For</sup> measurements, 20 frequencies per decade were used, and the scans were made for low frequency to high frequency. The reason for beginning with low frequencies is that, in case of EHD, the signal to noise ratio at the high frequency end of the spectrum is low, and measurements with good confidence typically take longer than is needed for the low frequency end. The first measurement in each spectrum obtained was discarded in the analysis because the start-up transient often influenced the value of impedance reported by the instrumentation. The long (1% closure error) auto-integration option of the frequency-response analyzer was used, and the channel used for integration was

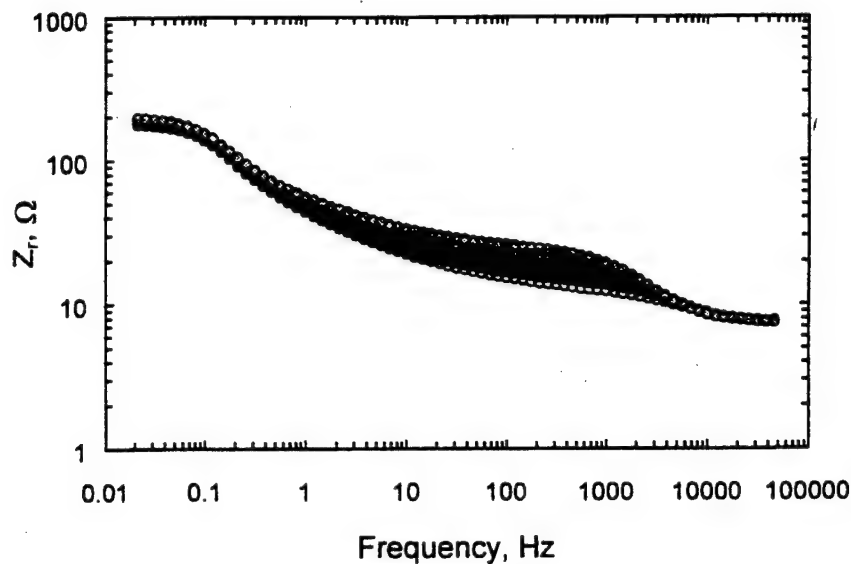


Fig. 2. Real part of the impedance with time as a parameter.

that corresponding to current. The solution was not deaerated, but experiments were performed at a polarization potential of 0 V (SCE) in order to minimize the influence of oxygen on the reduction of ferricyanide.

✓ FRA COM software developed in-house at CNRS by H. Takenouti was used to control the experiments and collect the data.

✓ The electrolyte consisted of 0.01 M  $K_3Fe(CN)_6$  and 0.01 M  $K_4Fe(CN)_6$  in 1 M KCl. The temperature was controlled at  $25.0 \pm 0.1^\circ C$ . Temperature control is

a very important factor as the diffusion coefficients of the various species involved exhibit a very strong functional dependence on temperature of the electrolyte and a small change in temperature could influence the results to a great extent.

The electrode diameter was 5 mm, yielding a surface area of  $0.1963 \text{ cm}^2$ . A polishing technique was selected for the Pt disk electrode that provided the maximum steady mass-transfer-limited current. The electrode was polished with a 1200 grit emery cloth, washed in deio-

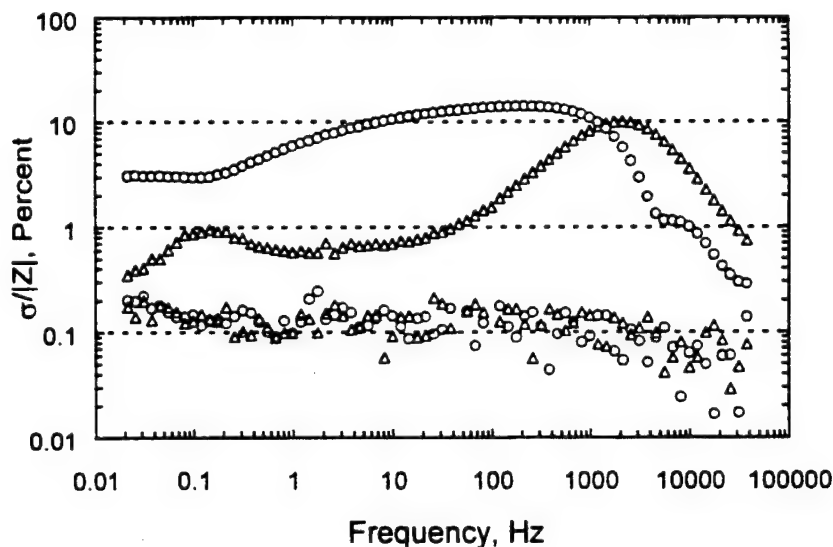


Fig. 3. Error structure for the data presented in Figs. 1 and 2: filled symbols are standard deviation of repeated measurements; open symbols were calculated using the measurement model approach.



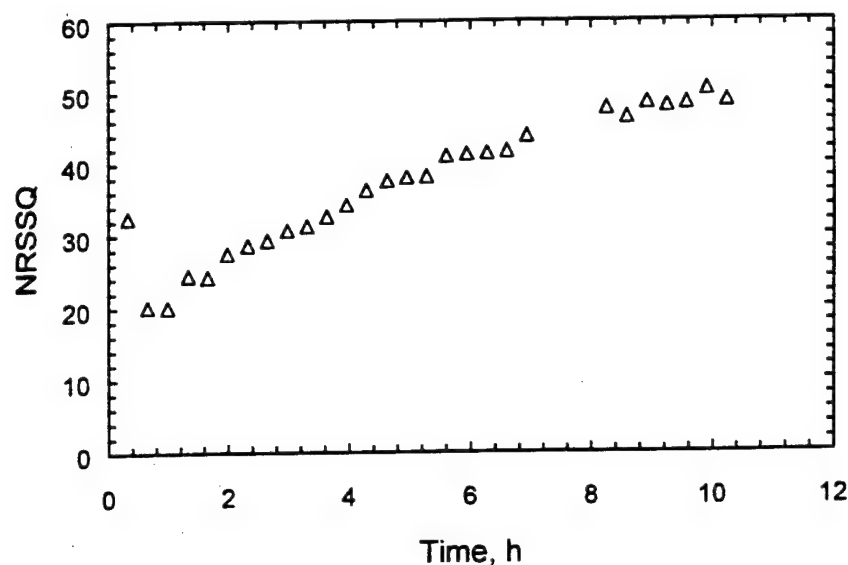


Fig. 4. Normalized residual errors for regression of Eq. (4) to the data presented in Figs. 1 and 2.

nized water, polished with alumina paste, and subjected to ultrasound cleaning in a 1:1 solution of water and ethyl alcohol.

Experiments conducted at 1/4, 1/2, and 3/4 of the mass-transfer-limited current were replicated to allow use of the statistical analysis of Agarwal et al. [33–35]. The data used for the present analysis were collected at a rotation speed of 120 rpm. At this low rotation speed and at low fractions of the mass-transfer-limited current, the distribution of current density and local impedance was determined to be relatively uniform

[30,31], and the one-dimensional analysis of Tribollet and Newman [10] could be assumed to be valid.

### 3. Results and discussion

The results presented in Figs. 1 and 2 for 28 repeated impedance scans at a current equal to 1/4 the mass-transfer-limited current reflect time-dependent changes to the Pt surface that have maximum effect at a frequency of 2000 Hz. The standard deviations of

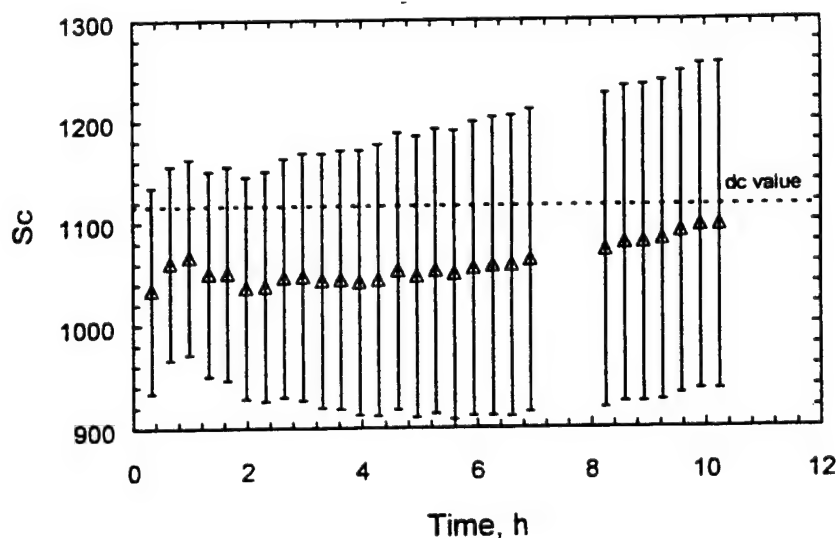


Fig. 5. Schmidt number obtained by regression of Eq. (4) to the data presented in Figs. 1 and 2.

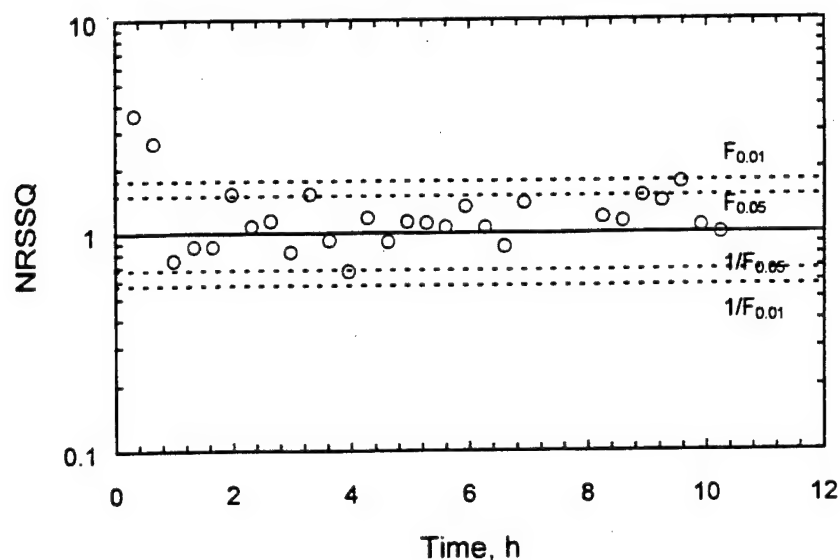


Fig. 6. Normalized residual errors for regression of Eq. (5) to the data presented in Figs. 1 and 2.

the repeated measurements given in Fig. 3 reflect contributions from bias errors caused by transient changes in electrode conditions. The real and imaginary parts of the standard deviation calculated directly were correlated but not equal. The standard deviations of the stochastic part of the measurement, obtained by use of the measurement model to filter bias errors [34], were much smaller, and the real and imaginary parts of the standard deviation were found to be statistically equal. The standard deviation of the stochastic part of the measurement (open symbols in Fig. 3) ranged from 0.2% to 0.04% of the modulus. The stochastic noise level of the measurements shown in Figs. 1 and 2 was therefore much less than the 3 to 5% of the modulus often assumed for impedance measurements.

The mathematical model developed by Tribollet and Newman [10]

$$Z(\omega) = R_e + \frac{R_i + z_d(\omega)}{1 + j\omega C(R_i + z_d(\omega))} \quad (4)$$

was regressed to the data using a weighting strategy based on the experimentally determined error structure. The normalized residual sum of squares for the regression of Eq. (4) to a series of sequential impedance measurements is presented in Fig. 4 as a function of the time at which the respective measurements were completed. The normalized residual sum of squares, which should have a value near 1 for a good fit, are very large and increase with time. The Schmidt number obtained by the regression was in good agreement with the accepted value of 1100 and was independent of the duration of the experiment (see Fig. 5).

although the 95.4% confidence interval for the estimate was large.

In order to obtain a better fit to the data, Eq. (4) was modified by treating the capacitance as a constant phase element, i.e.,

$$Z(\omega) = R_e + \frac{R_i + z_d(\omega)}{1 + (j\omega C)^{1-\alpha}(R_i + z_d(\omega))} \quad (5)$$

where  $\alpha$  is a number less than 1. Several qualitative justifications have been advanced in the literature for the use of a constant phase element, including surface roughness [36,37], coupled reaction mechanisms, and non-uniform current distribution [38]. The motivation for applying Eq. (5) was to account for the more complicated electrode kinetics associated with poisoning of the electrode surface.

Eq. (5) provided a much better fit to the data than did Eq. (4). The residual sum of squares normalized by the sum of variances for the measurement given in Fig. 6 represents an F-test for comparison of variance. The dashed lines are 0.01 and 0.05 limits for accepting the hypothesis that residual sum of squares differs from the sum of variances for the measurement. In spite of the low noise levels evident in Fig. 3, with the exception of the first two measurements the process model yielded residual errors that fell within the noise level of the measurement. The larger residual errors seen for the first two scans were shown by the methods of Agarwal et al. [35] to be the result of inconsistency of the data with the Kramers-Kronig relation.

The success of the regression of Eq. (5) for the subsequent measurements allowed determination of the role of the surface phenomena evident in Figs. 1 and

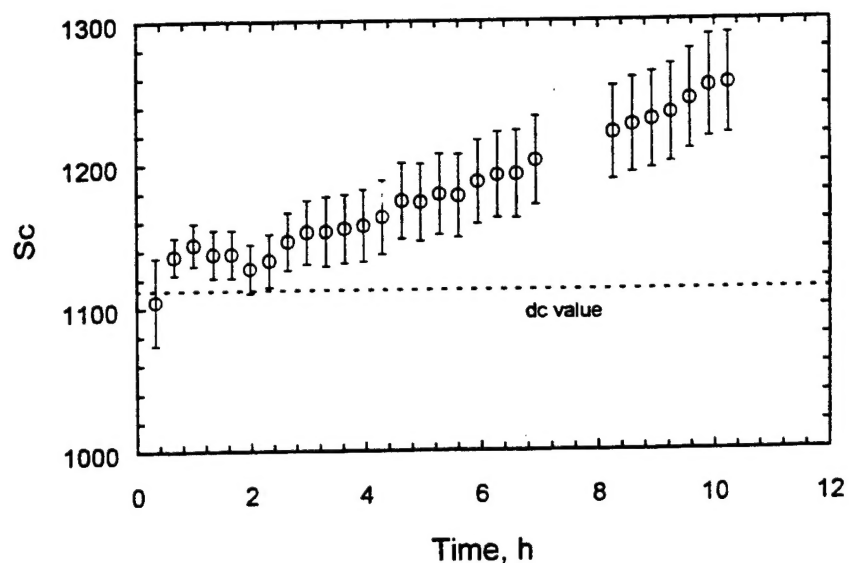


Fig. 7. Schmidt number obtained by regression of Eq. (5) to the data presented in Figs. 1 and 2.

2. The Schmidt number obtained by regression is presented in Fig. 7. For the first 2 h of the sequential impedance scans, the Schmidt number obtained was in good agreement with the value obtained by d.c. techniques given by the dashed line in Fig. 7. After this time, the apparent Schmidt number increased with time. As the residual errors for these regressions (Fig. 6) were of the order of the noise of the measurement, the increase of Schmidt number suggests that the effective diffusion coefficient decreased with time. The charge transfer resistance also increased with time, as

shown in Fig. 8. The increase of the mass transfer resistance shown in Fig. 9 is consistent with the decrease of diffusion coefficient suggested by Fig. 7. The double layer capacitance, shown in Fig. 10, and the exponent for the constant phase element, not shown, approached constant values.

The apparent variation in  $Sc$  cannot be attributed to degradation of the electrolytic solution because the original value for  $Sc$  was consistently obtained after repolishing the electrode.

The increase in charge transfer resistance and the

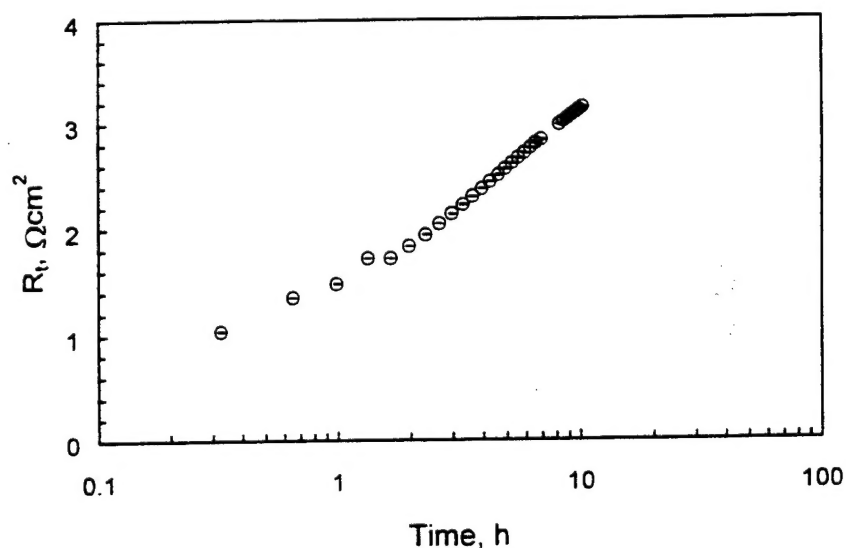


Fig. 8. Charge transfer resistance obtained by regression of Eq. (5) to the data presented in Figs. 1 and 2.

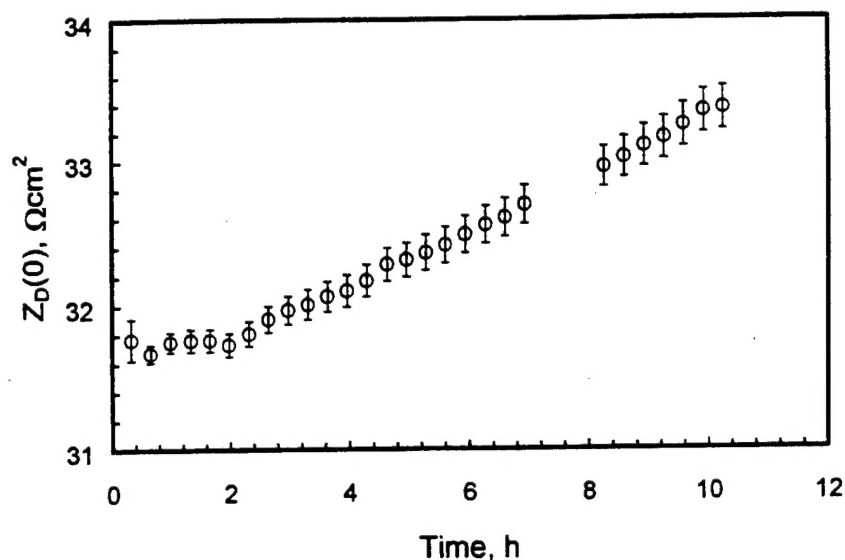


Fig. 9. Mass transfer resistance obtained by regression of Eq. (5) to the data presented in Figs. 1 and 2.

zero frequency limit of the mass transfer impedance are suggestive of a poisoning of the electrode surface. Similar changes were seen when Eq. (4) was regressed to the data. The poor quality of the fit seen in Fig. 4 shows that Eq. (4) is an inappropriate model for this system, and Eq. (4) becomes increasingly inappropriate as the poisoning becomes more severe. The excellent fit indicated in Fig. 6 shows that Eq. (5) provides a good accounting for the poisoning of the surface at the expense of an increased value for  $Sc$ .

The influence of blocking on the Schmidt number,

surmised from interpretation of regression to EIS data, can also be demonstrated by EHD measurements that showed an increasing value of  $Sc$  with time [16]. The current distribution is uniform for EHD measurements conducted at the mass-transfer-limited plateau; thus the one-dimensional model of Tribollet and Newman applies [10]. The increase in  $Sc$  with time cannot, therefore, be attributed to a non-uniform current distribution and must be attributed to a partial blocking of the surface.

The results of d.c. measurements shown in Fig. 11

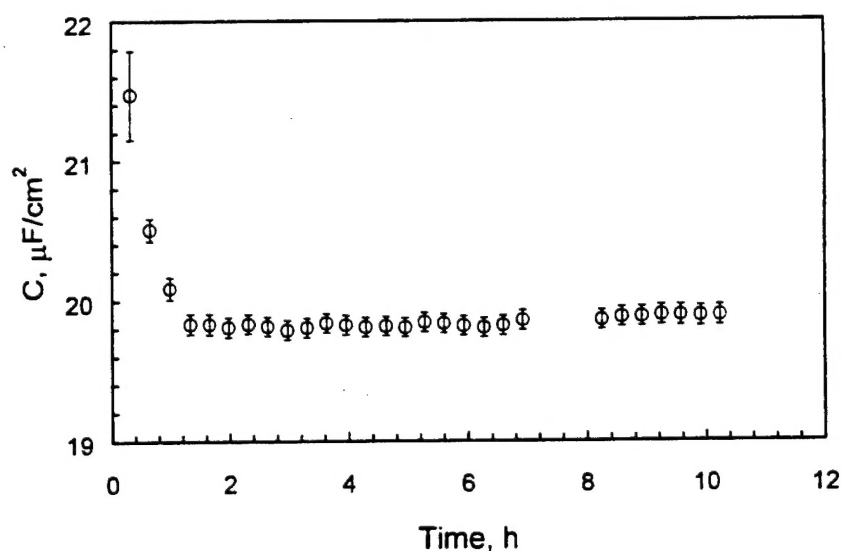


Fig. 10. Double layer capacitance obtained by regression of Eq. (5) to the data presented in Figs. 1 and 2.

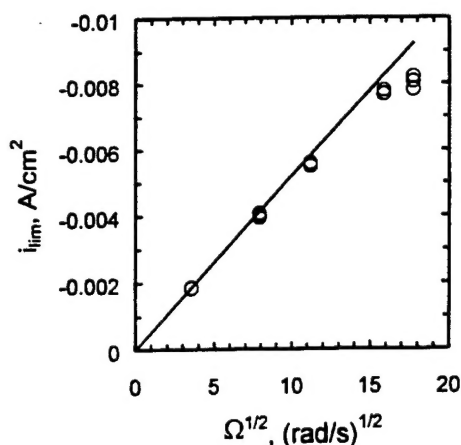


Fig. 11. Mass-transfer-limited current density as a function of rotation speed.

reveal that the blocking effect increases with rotation speed. The mass-transfer-limited current values were obtained within 3 min of completion of the polishing procedure. The Schmidt numbers obtained from the values of the mass-transfer limited currents are given in Table 1.

These results suggest that the time-dependent change to the Pt surface contributes to both a decrease of rate constant that hinders electrode kinetics and a blocking of the electrode surface that hinders mass transfer.

#### 4. Conclusions

Identification of error structure is critical to interpretation of regressed results. In this case, assessment of the experimental values of the stochastic part of the measurement showed that Eq. (4) did not provide an adequate description of the impedance response for the system. The data selected for the present analysis were collected at a low rotation speed and at a low fraction of the mass-transfer-limited current because modeling efforts showed that the non-uniform

current distribution normally seen on disk electrodes below the mass-transfer-limited current would have a minimal influence on the impedance response. The analysis of the impedance response presented here suggests that the formation of surface films influence the reduction of ferricyanide on Pt both through a blocking effect and through reduction of the rate constant for the electrochemical reaction.

#### Acknowledgements

This work was supported by the US Office of Naval Research under Grant Numbers N00014-93-1-0056 and N00014-93-1-1113 (A.J. Sedriks, Program Monitor) and by the National Science Foundation under a US–France Cooperative Research Grant INT-9416713.

#### References

- [1] A.C. Riddiford, 1966, *Advances in Electrochemistry and Electrochemical Engineering*, 4, 47–116.
- [2] B. Levich, *Acta Physicochimica URSS* 17 (1942) 257–307.
- [3] J. Newman, *Journal of Physical Chemistry* 70 (1966) 1327–1328.
- [4] V. Yu Filinovskii, V.A. Kir'yanov, *Dokl. Akad. Nauk. SSSR* 156 (1964) 1412.
- [5] E. Levart, D. Schuhmann, *J. Electrochem. Soc* 122 (1975) 1082–1083.
- [6] D.A. Scherson, J. Newman, *J. Electrochem. Soc* 127 (1980) 110–113.
- [7] C. Deslouis, C. Gabrielli, B. Tribollet, *J. Electrochem. Soc* 130 (1983) 2044–2046.
- [8] B. Tribollet, J. Newman, *J. Electrochem. Soc* 130 (1983) 822–824.
- [9] B. Tribollet, J. Newman, W.H. Smyrl, *J. Electrochem. Soc* 135 (1988) 134–138.
- [10] B. Tribollet, J. Newman, *J. Electrochem. Soc* 130 (1983) 2016.
- [11] M.E. Orazem, C. Deslouis, B. Tribollet 1997. Presented at the 191st Meeting of the Electrochemical Society, Montreal, Canada, May 6.
- [12] C. Deslouis, B. Tribollet, C.W. Tobias, H. Gerischer (Eds.), *Advances in Electrochemical Science and Engineering*, 2, VCH Weinheim, New York, 1991, pp. 205–263.
- [13] C. Deslouis, B. Tribollet, *Electrochimica Acta* 35 (1990) 1637.
- [14] C. Deslouis, B. Tribollet, 1984, Paper B2-9 presented at the 35th Meeting of the International Society of Electrochemistry, Berkeley, CA August 5–10.
- [15] C. Deslouis, I. Epelboin, M. Keddam, J.C. Lestrade, *Electroanalytical Chemistry and Interfacial Electrochemistry* 28 (1970) 57–63.
- [16] M.E. Orazem, P. Agarwal, C. Deslouis, B. Tribollet, *J. Electrochem. Soc* 143 (1996) 948.

Table 1  
Schmidt number values obtained from the mass-transfer-limited current presented in Fig. 11 as a function of rotation speed

$\Omega$ (in rpm)	Sc
120	1114
600	1158
1200	1195
2400	1222
3000	1362

the

- [17] M. Stieble, K. Jüttner, J. Electroanal. Chem 290 (1990) 163.
- [18] T. Gueshi, K. Tokuda, H. Matsuda, Voltammetry at Partially Covered Electrodes: Part I. Chronopotentiometry and Chronoamperometry at Model Electrodes, J. Electroanal. Chem 89 (1978) 247.
- [19] T. Gueshi, K. Tokuda, H. Matsuda, J. Electroanal. Chem 101 (1979) 29.
- [20] K. Tokuda, T. Gueshi, H. Matsuda, J. Electroanal. Chem 102 (1979) 41.
- [21] J.O'M Bockris, B. Yang, J. Electroanal. Chem 252 (1988) 209.
- [22] P.A. Christensen, A. Hamnett, P.R. Trevellick, J. Electroanal. Chem 242 (1988) 23.
- [23] H. Baltruschat, F. Lu, D. Song, S.K. Lewis, D.C. Zapien, D.G. Frank, G.N. Salaita, A.T. Hubbard, J. Electroanal. Chem 234 (1987) 229.
- [24] K. Winkler, J. Electroanal. Chem 388 (1995) 151.
- [25] W. Huang, R. McCreery, J. Electroanal. Chem 326 (1992) 1.
- [26] K. Kunitatsu, Y. Shigematsu, K. Uosaki, H. Kita, J. Electroanal. Chem 262 (1989) 195.
- [27] Newman, J. Electrochem. Soc 113 (1966) 1235–1241.
- [28] Nanis, W. Kesselman, J. Electrochem. Soc 118 (1971) 454–461.
- [29] J. Newman, J. Electrochem. Soc 113 (1966) 501.
- [30] M. Durbha, M.E. Orazem, ~~submitted~~ J. Electrochem. Soc., **146 (1999), 2199.**
- [31] M. Durbha, M.E. Orazem, J. Electrochem. Soc 145 (1998) 1940–1949.
- [32] M.E. Orazem, T. El Moustafid, C. Deslouis, B. Tribollet, J. Electrochem. Soc 143 (1996) 3880–3890.
- [33] P. Agarwal, M.E. Orazem, L.H. Garcia-Rubio, J. Electrochem. Soc 139 (1992) 1917.
- [34] P. Agarwal, O.D. Crisalle, M.E. Orazem, L.H. Garcia-Rubio, J. Electrochem. Soc 142 (1995) 4149.
- [35] P. Agarwal, M.E. Orazem, L.H. Garcia-Rubio, J. Electrochem. Soc 142 (1995) 4159.
- [36] R. de Levie 1967 Advances in electrochemistry and electrochemical engineering, 6, 329.
- [37] J.R. Macdonald (Ed.), Impedance Spectroscopy: Emphasizing Solid Materials and Systems, John Wiley & Sons, New York, 1987.
- [38] H.H. Bauer, M.S. Spritzer, P.J. Elving, J. Electroanal. Chem 17 (1968) 299.